

Optimal Filtering, Localized Analysis and Multiscale Representations on the Sphere

A Dissertation
Presented by

ADEEM ASLAM

In Partial Fullfilment
of the Requirements for the Degree of
Doctor of Philosophy in
Electrical Engineering

SUPERVISOR: DR. ZUBAIR KHALID



Syed Babar Ali School of Science and Engineering
Lahore University of Management Sciences
June 2021

© 2021 Adeem Aslam

Declaration

I, the undersigned, declare that this dissertation has been compiled by myself and its contents have not been presented for a higher degree at any other institute. The work in this dissertation is a result of original research carried out by myself under the supervision of Dr. Zubair Khalid (Lahore University of Management Sciences, Pakistan), in joint collaboration with Prof. Dr. Rodney A. Kennedy (The Australian National University, Australia) and Prof. Dr. Jason D. McEwen (University College London, U.K.).

Most of the work in this dissertation has either been published as journal papers (**J**) and conference proceedings (**C**), or is currently in peer review, as detailed below:

- (C1) **Adeem Aslam**, Zubair Khalid and Rodney A. Kennedy, “Efficient Sampling on HEALPix Grid,” *2018 IEEE International Conference on Acoustics, Speech and Signal Processing (ICASSP)*, Calgary, AB, 2018, pp. 4589–4593.
- (C2) **Adeem Aslam** and Zubair Khalid, “Construction of Overcomplete Multiscale Dictionary of Slepian Functions on the Sphere,” *ICASSP 2019 - 2019 IEEE International Conference on Acoustics, Speech and Signal Processing (ICASSP)*, Brighton, United Kingdom, 2019, pp. 5137–5141.
- (C3) **Adeem Aslam** and Zubair Khalid, “Optimal Window Design for Joint Spatial-Spectral Domain Filtering of Signals on the Sphere,” *ICASSP 2020 - 2020 IEEE International Conference on Acoustics, Speech and Signal Processing (ICASSP)*, Barcelona, Spain, 2020, pp. 5785–5789.
- (J1) **Adeem Aslam** and Zubair Khalid, “Localized Analysis of Signals on the

Sphere Over Polygon Regions,” in *IEEE Transactions on Signal Processing*, vol. 68, pp. 4568–4582, 2020.

- (J2) **Adeem Aslam** and Zubair Khalid, “Joint $\mathbb{SO}(3)$ -Spectral Domain Filtering of Spherical Signals in the Presence of Anisotropic Noise,” in *IEEE Signal Processing Letters*, vol. 27, pp. 2109–2113, 2020.
- (J3) **Adeem Aslam**, Zubair Khalid and Jason D. McEwen, “Multiscale Optimal Filtering on the Sphere,” in *IEEE Signal Processing Letters*, vol. 28, pp. 394–398, 2021.
- (J4) **Adeem Aslam** and Zubair Khalid, “Spatial-Slepian Transform on the Sphere,” in *IEEE Transactions on Signal Processing* (accepted with minor revision for English usage, revision submitted on May 16, 2021).
- (J5) **Adeem Aslam** and Zubair Khalid, ”Linear Transformations and Signal Estimation in the Joint Spatial-Slepian Domain,” submitted to *IEEE Signal Processing Letters* (accepted for publication).
- (J6) **Adeem Aslam** and Zubair Khalid, ”Optimal Window Design For Joint $\mathbb{SO}(3)$ -Spectral Domain Filtering of Signals on the Sphere,” submitted to *IEEE Signal Processing Letters*.

Some of the work in this dissertation is being compiled for submission to a peer-reviewed journal with the following details:

- (J7) **Adeem Aslam** and Zubair Khalid, “Overcomplete Multiscale Dictionary of Slepian Functions for HEALPix on the Sphere,” manuscript under preparation for submission to *IEEE Transactions on Signal Processing*.

A significant portion of this research is my own work.

Adeem Aslam
Syed Babar Ali School of Science and Engineering,
Lahore University of Management Sciences,
Lahore, Punjab 54792, Pakistan.

Acknowledgements

All praise be to ALLAH Almighty, the most Benevolent, the most Gracious Creator, Who shows the right path and guides man in all his endeavors.

Darood and Salaam (Salutations and Divine blessings) on Prophet Muhammad (peace be upon him), the best of His creations, the best mentor and guide till the end of times.

Adoration and high esteem for my dear parents who have been a supporting shadow all these years, whose love, guidance and prayers have made this day possible.

Profound gratitude for my respected supervisor Dr. Zubair Khalid, who has always encouraged me to do better, helped me explore my capacity, mentored me to the best of his abilities, showed unfaltering confidence in me and motivated me during tough times.

Deepest appreciation for Lahore University of Management Sciences (LUMS) for providing me with a wonderful opportunity to experience multi-disciplinary studies, fair competition, ergonomic environment and professional exposure. Also, I would like to thank the university for supporting my research through the inaugural Syed Babar Ali Research Awards.

Huge bundle of thanks to Higher Education Commission Pakistan for arranging a research placement at Mullard Space Science Laboratory (MSSL), University College London (UCL), UK. This additional research opportunity has broadened my horizon,

given me international exposure and helped me establish healthy research collaboration. I would also like to thank Prof. Dr. Jason D. McEwen for graciously hosting me at MSSL and providing me with an opportunity to work with him, which was an immense learning experience in itself.

Respect and gratitude for all of my teachers, who have taught, mentored and counseled me to this day. Whatever my accomplishments today are, I owe it to them.

I would also like to thank my friends and colleagues from the Signal, Image and Video Processing (SIVP) group, that I have been a part of during my doctoral studies at LUMS, for providing a friendly and supportive atmosphere. Special thanks to my dear friend Dr. Faran Awais Butt, for encouraging me to pursue doctoral studies from LUMS.

Many thanks to my dear sisters for the prayers, deep care and treasured memories through all these years.

And last but not the least, much love and affection for my beautiful family: my beloved wife Masooma, for her staunch support and companionship through thick and thin, who has talked me through turmoils, laughed with me at the falters, celebrated with me on each success and had my back at every step; our darling daughter Aroush, who is the light in our lives, whose laughter makes everyday beautiful and worth living, and whose nonstop chatter is therapeutic after long working hours; our handsome little prince Muhammad Mus'ab, one of Allah's biggest, most beautiful blessings to brighten up our lives, whose sight makes our hearts melt and a lifetime of dreams transpire in our souls. These are the people in my life whose love is what keeps me moving forward.

Dedicated to my late mother who, without a doubt, would have been the happiest person for me.

She was my first friend and confidante, my guide and support, who nurtured me with her undying love, helped me understand the true meaning of Tawakkal on ALLAH SWT and made me realize that there's no time as beautiful and precious as the moments spent with loved ones.

Abstract

The work in this dissertation is related to the development of novel techniques for processing of signals defined on the sphere. Known as spherical signals, these are encountered in areas of science and engineering where the underlying configuration of the problem has a spherical geometry, e.g., in astronomy, cosmology, acoustics, medical imaging, geophysics and wireless communication. In most of these areas, acquired signals are almost always marred with unwanted, yet unavoidable noise due to different sources of interference, which places signal filtering and estimation at the heart of signal processing methods. In this context, the first part of the dissertation addresses the problem of signal filtering and estimation on the sphere in the presence of random anisotropic noise. In particular, filters are designed in the joint $\mathbb{SO}(3)$ -spectral domain, rendered by the directional spatially localized spherical harmonic transform, and the joint $\mathbb{SO}(3)$ -scale domain, yielded by the scale-discretized wavelet transform on the sphere. Additionally, optimal window signals are designed to enhance the performance of the joint spatial-spectral domain filter and the proposed joint $\mathbb{SO}(3)$ -spectral domain filter. The utility of these filtering frameworks is demonstrated on bandlimited Earth and Mars topography maps.

The second part of this dissertation is focused on the use of Slepian functions, which are obtained as a solution of the Slepian spatial-spectral concentration problem on the sphere, to support localized signal analysis. Such analysis is motivated by the unavailability or unreliability of the spherical data over some region on the sphere. In this respect, an analytical formulation for the (i) surface integration of signals, and (ii) computation of Slepian basis functions, over regions represented by simple spherical polygons, is presented. Through a polygon right-angled triangulation algorithm, the problem of localized signal analysis over simple spherical polygon is broken down into simpler analyses over spherical right-angled triangles. Using appropriate rotation angles and Wigner- D functions, the computations for spherical right-angled triangles, which span the spherical polygon, are combined to yield the results for the polygon. Slepian functions are also employed to formulate a new joint spatial-Slepian domain representation of spherical signals through the novel spatial-Slepian transform. The joint spatial-Slepian domain representation is given by the spatial-Slepian coefficients, which are analyzed for their spatial localization on the sphere. Spatial-Slepian transform is utilized for detecting the presence of hidden and weak localized variations in a signal. Furthermore, a framework for generalized linear transformations in the joint spatial-Slepian domain is presented, which is exemplified through particular forms of the underlying spatial-Slepian transformation kernel. All of these formulations are validated using bandlimited Earth and Mars topography maps.

The third part of the dissertation considers the use of Slepian functions for the framework of multiscale (multiresolution) analysis of spherical signals through hierarchical partitioning of the sphere into pixels of varying spatial extent. In this context, different sampling and partitioning methods on the sphere are reviewed and Hierarchical Equal Area iso-Latitude iso-Longitude Pixelization (HEALLPix) scheme is proposed. Employing the formulation available in the literature, Slepian functions for the HEALLPix pixels are computed and an overcomplete multiscale dictionary

of Slepian functions is constructed. Additionally, a framework for analytical computation of Slepian functions for pixels generated using Hierarchical Equal Area iso-Latitude Pixelization (HEALPix) scheme is formulated. Exploiting the symmetries between HEALPix pixels, an efficient framework for the construction of an overcomplete multiscale dictionary of Slepian functions for HEALPix is presented. Elements of both dictionaries are shown to span the space of bandlimited functions on the sphere, while most of the elements of both dictionaries are also shown to exhibit negligibly small mutual coherence. As an outcome of the review of sampling schemes on the sphere, an efficient and accurate spherical harmonic transform is also formulated for HEALPix.

List of acronyms

1D	1 dimensional
2D	2 dimensional
3D	3 dimensional
CMB	cosmic microwave background
SHT	spherical harmonic transform
SLSHT	spatially localized spherical harmonic transform
SNR	signal to noise ratio
GW	Gauss-Weierstrass
GWKS	Gauss-Weierstrass kernel smoothing
GL	Gauss-Legendre
SST	spatial-Slepian transform
FFT	fast Fourier transform
SVR	signal to variation ratio
HEALPix	Hierarchical Equal Area iso-Latitude Pixelization
HEALPix	Hierarchical Equal Area iso-Latitude iso-Longitude Pixelization

Notation

On some rare occasions, a symbol is used to represent more than one mathematical quantity across different chapters. Hence, the scope of mathematical notation should be considered local to the chapters in order to avoid any confusion. As an exception, same symbol θ_0 has been used to represent the angle of a polar cap region as well as focus colatitude of a spherical ellipse throughout the dissertation.

x	scalar
\mathbf{x}	2D or 3D Euclidean column vector
$\hat{\mathbf{x}}$	3D Euclidean unit column vector (representing points on the sphere)
\mathbf{x}	column vector
\mathbf{X}	matrix
x_k	k^{th} element of the column vector \mathbf{x}
$X_{k,k'}$	element in row k and column k' of the matrix \mathbf{X}
$\text{trace}(\mathbf{X})$	trace of the matrix \mathbf{X}
\mathbb{S}^2	2-sphere or unit sphere or sphere
A_R	area of a spherical region $R \subset \mathbb{S}^2$
$\Delta(\hat{\mathbf{x}}, \hat{\mathbf{y}})$	Angular distance between points $\hat{\mathbf{x}}$ and $\hat{\mathbf{y}}$ on the sphere
$\langle f, g \rangle_R$	inner product between functions $f(\hat{\mathbf{x}})$, $g(\hat{\mathbf{x}})$ over a region $R \subset \mathbb{S}^2$
$\langle f, g \rangle_{\mathbb{S}^2}$	inner product between functions $f(\hat{\mathbf{x}})$, $g(\hat{\mathbf{x}})$ over the sphere
$\ \cdot\ _R$	L_2 norm of a function over a region $R \subset \mathbb{S}^2$
$\ \cdot\ _{\mathbb{S}^2}$	L_2 norm of a function over the sphere
$L^2(\mathbb{S}^2)$	Hilbert space of functions on the sphere
\mathcal{H}_L	Hilbert space of bandlimited functions on the sphere

\mathcal{H}_0	Hilbert space of azimuthally symmetric functions on the sphere
Y_ℓ^m	spherical harmonic function of degree ℓ and order m
$\mathbb{SO}(3)$	$\mathbb{SO}(3)$ rotation group
ρ	3-tuple of Euler angles $(\varphi, \vartheta, \omega)$
$\langle f, g \rangle_{\mathbb{SO}(3)}$	inner product between functions $f(\rho), g(\rho)$ over $\mathbb{SO}(3)$
$\ \cdot\ _{\mathbb{SO}(3)}$	L_2 norm of a function over the $\mathbb{SO}(3)$ rotation group
$L^2(\mathbb{SO}(3))$	Hilbert space of functions on the $\mathbb{SO}(3)$ rotation group
$D_{m,m'}^\ell$	Wigner- D function of degree ℓ and orders m, m'
$d_{m,m'}^\ell$	Wigner- d function of degree ℓ and orders m, m'
$\Delta_{m,m'}^\ell$	Wigner- d function of degree ℓ and orders m, m' , evaluated at $\pi/2$
$T(\cdot; \cdot; \cdot)$	spherical harmonic triple product
$ \cdot $	absolute value of the scalar or norm of the Euclidean vector
$\text{Re}\{\cdot\}$	real part of the parameter
$\overline{(\cdot)}$	complex conjugate operation
$(\cdot)^T$	vector transpose operation
$(\cdot)^H$	conjugate transpose operation
N_R	spherical Shannon number for a region $R \subset \mathbb{S}^2$
$\lfloor \cdot \rfloor$	integer floor function
$\lceil \cdot \rceil$	integer ceiling function
$\delta_{\ell,p}$	Kronecker delta function
$\delta(\cdot)$	Dirac delta function
$*$	convolution of Euclidean domain signals
\star	convolution of spherical signals
\circledast	convolution of signals defined on $\mathbb{SO}(3)$ rotation group
$\max\{\cdot\}$	maximum of the parameters
$\min\{\cdot\}$	minimum of the parameters
j	scale-discretized wavelet scale
J	maximum scale-discretized wavelet scale
\mathbb{E}	statistical expectation
\mathbf{C}^d	spectral covariance matrix of a spherical signal d

\mathcal{F}	joint spatial-spectral domain filter function
ζ	joint $\mathbb{SO}(3)$ -spectral domain filter function
Ξ	multiscale optimal filter function
\mathcal{E}_{mse}	mean square error
\mathcal{E}_{se}	squared error
K_{GW}	Gauss-Weierstrass kernel
\mathcal{E}_{KS}	squared error for Gauss-Weierstrass kernel smoothing
var	spatial variance
$\#\{\cdot\}$	number of elements satisfying the logical condition inside the braces
\mathbf{r}	fractional ratio of the number of spatial-Slepian coefficients having smaller spatial variance than the scale-discretized wavelet coefficients
Σ^2	sample variance
$\zeta_{\alpha,\beta}$	spatial-Slepian transformation kernel
\mathfrak{S}	spatial-Slepian transformation operator
ζ^{M}	multiplicative spatial-Slepian transformation kernel
ζ^{\otimes}	convolutive spatial-Slepian transformation kernel
\mathfrak{L}	resolution parameter for HEALPix scheme
N_{side}	resolution parameter for HEALPix scheme
N_{pix}	number of pixels for HEALPix scheme
h_{T}	quaternary tree level
\mathfrak{H}	height of the quaternary tree
\mathfrak{D}	overcomplete multiscale dictionary of well-optimally concentrated Slepian functions
J_n	Bessel function of first kind and order n
M_{C}	mutual coherence
$N_{\text{sig},M_{\text{C}}}$	number of inner products between dictionary elements which result in significant mutual coherence

Contents

Declaration	i
Acknowledgements	iii
Abstract	vii
List of acronyms	ix
Notation	xi
List of Figures	xxi
List of Tables	xxxiii
1 Introduction	1
1.1 Background and motivation	1
1.1.1 Signal filtering and estimation	2
1.1.2 Localized signal analysis	3
1.1.3 Sampling of signals on the sphere	4
1.1.4 Multiresolution (multiscale) analysis	5
1.2 Scope of the dissertation	6
1.2.1 Summary of research contributions	6
1.3 Organization	10
2 Signal analysis on the sphere and $\mathbb{SO}(3)$ rotation group	13
2.1 2-sphere	13

2.1.1	Spherical coordinates	15
2.1.2	Regions on the sphere	15
2.1.3	Rotations on the sphere	17
2.2	Signal analysis on the sphere	18
2.2.1	Spherical harmonics	19
2.2.2	Space of bandlimited signals on the sphere	21
2.2.3	Space of azimuthally symmetric signals on the sphere	22
2.3	Signal analysis on the $\mathbb{SO}(3)$ rotation group	23
2.3.1	Wigner- D functions	24
2.3.2	Space of bandlimited signals on $\mathbb{SO}(3)$ rotation group	25
2.4	Rotation of signals on the sphere	25
2.5	Localized basis on the sphere	27
2.5.1	Spatial concentration of bandlimited signals on the sphere	28
2.6	Convolution of signals on the sphere	31
2.6.1	Spherical convolution of type 1	31
2.6.2	Spherical convolution of type 2	32
2.6.3	Spherical convolution of type 3	33
2.6.4	Commutative anisotropic spherical convolution	33
2.6.5	Harmonic multiplication	34
2.7	Convolution of signals on $\mathbb{SO}(3)$ rotation group	34
2.8	Spatial-spectral analysis on the sphere	36
2.8.1	SLSHT	37
2.8.2	SLSHT – Inverse transform	39
2.9	Multiscale representation for signals on the sphere	40
2.9.1	Scale-discretized wavelet transform on the sphere	41
3	Joint domain optimal filtering on the sphere	49
3.1	Joint domain filtering – Problem formulation	51
3.1.1	Real bandlimited Gaussian noise	52

3.1.2	Real bandlimited white Gaussian noise	53
3.2	Window design for joint spatial-spectral domain filter	54
3.2.1	Joint spatial-spectral domain filter	55
3.2.2	Normalized axisymmetric optimal window design	57
3.2.3	Axisymmetric optimal window design – Alternative formulation	61
3.2.4	Illustrations	62
3.3	Joint $\mathbb{SO}(3)$ -spectral domain filtering	65
3.3.1	Joint $\mathbb{SO}(3)$ -spectral domain filter design	65
3.3.2	Signal estimation	69
3.3.3	Analysis	72
3.4	Optimal window design for joint $\mathbb{SO}(3)$ -spectral domain filter	75
3.4.1	Directional optimal window design – Alternative formulation	78
3.4.2	Illustrations	79
3.5	Multiscale optimal filter	81
3.5.1	Analysis	85
3.6	Performance comparison of joint domain optimal filters	89
4	Localized analysis over spherical polygons	93
4.1	Spherical polygon	94
4.1.1	Polygon right-angled triangulation	95
4.2	Localized signal analysis over simple polygons on the sphere	99
4.2.1	Integration of signals over a spherical polygon	100
4.2.2	Slepian functions over a spherical polygon	102
4.2.3	Evaluation of the integral of complex exponential functions	103
4.2.4	Rotation of spherical right-angled triangles	107
4.2.5	Computational considerations	109
4.3	Numerical validation and illustrations	111
5	Spatial-Slepian transform on the sphere	119
5.1	Spatial-Slepian transform (SST)	120
5.1.1	SST formulation	120

5.1.2	Inverse SST	122
5.1.3	Fast computation of spatial-Slepian transform	122
5.1.4	SST using zonal Slepian functions	123
5.2	Analysis	125
5.2.1	Inverse SST validation	125
5.2.2	Computational complexity analysis	126
5.2.3	Localization of spatial-Slepian coefficients	128
5.3	Localized variation analysis	132
5.3.1	Motivation	133
5.3.2	Mathematical framework	134
5.3.3	Illustration	134
5.4	Generalized linear transformations in the joint spatial-Slepian domain	137
5.4.1	Admissibility condition	139
5.4.2	Least square signal estimation	140
5.4.3	Filters in the joint spatial-Slepian domain	144
5.4.4	Illustrations	147
6	Sampling on the sphere	151
6.1	Equiangular sampling	152
6.2	Equal area and hierarchical sampling	153
6.2.1	HEALPix	154
6.3	Optimal dimensionality sampling scheme	157
6.4	Efficient sampling on HEALPix grid	158
6.4.1	Spherical harmonic transform for optimal dimensionality sam- pling scheme – A quick review	159
6.4.2	Proposed sampling scheme – Requirements	162
6.4.3	Proposed sampling scheme – Design	163
6.4.4	Multipass SHT	164
6.4.5	Evaluation	164

7	Multiscale analysis on the sphere	169
7.1	HEALLPix	170
7.1.1	Placement of iso-latitude rings	171
7.1.2	Placement of iso-longitude rings	171
7.1.3	Area of a pixel	172
7.1.4	Pixel centers	173
7.1.5	Quaternary tree structure	176
7.2	Overcomplete multiscale dictionary of Slepian functions	178
7.2.1	Fixed N_{SF} for each tree node	179
7.2.2	Varying N_{SF} for nodes at different tree levels	180
7.2.3	Dictionary	181
7.2.4	Computation of Slepian functions	182
7.3	Analysis	182
7.3.1	Range of \mathfrak{D}	183
7.3.2	Mutual coherence	185
7.4	Multiscale analysis for HEALPix	189
7.4.1	Geometry of HEALPix	191
7.5	Slepian functions for HEALPix pixels	195
7.5.1	North polar pixels	196
7.5.2	Equatorial pixels (centered either above or at equator)	200
7.5.3	North polar-equatorial pixels	204
7.5.4	Pixels centered below equator	206
7.6	Multiscale dictionary of Slepian functions for HEALPix	206
7.6.1	Construction of overcomplete multiscale dictionary	208
7.7	Numerical considerations	211
7.7.1	Generalized binomial series expansions	211
7.7.2	Infinite Maclaurin series expansions	214
7.8	Analysis	214
7.8.1	Range of \mathfrak{D}	215
7.8.2	Mutual coherence	217

8 Summary and future work	221
8.1 Summary of dissertation	221
8.2 Future research directions	222
 Appendices	
 Appendix A	 225
A.1 Integration of $e^{iq\phi}e^{im\theta}$ over spherical right-angled triangle in standard orientation	225
A.1.1 $q = 0, m = 0, 0 \leq \theta_{b,t} < \pi/4$:	226
A.1.2 $q = 0, m = 0, \pi/4 \leq \theta_{b,t} < \pi/2$	228
A.1.3 $q = 0, m \neq 0, q \neq 0, m = 0$ and $q \neq 0, m \neq 0$	228
 Appendix B	 233
B.1 Placement of iso-latitude rings for HEALPix	233
B.2 Placement of iso-longitude rings for HEALPix	235
 Appendix C	 237
C.1 Evaluating Slepian sub-integral for HEALPix north polar pixels	237
C.1.1 $q - m \neq 0$:	238
C.1.2 $q - m = 0$:	241
C.2 Evaluating Slepian sub-integral for HEALPix equatorial pixels	242
C.2.1 $q - m \neq 0$:	243
C.2.2 $q - m = 0$:	246

List of Figures

1-1	Flowchart of the organization of dissertation.	11
2-1	2-sphere embedded in \mathbb{R}^3 with a point on its surface represented by a unit vector $\hat{\mathbf{x}}(\theta, \phi)$, where $\theta \in [0, \pi]$ is the colatitude and $\phi \in [0, 2\pi)$ is the longitude.	14
2-2	North and south polar cap regions shown as shaded areas on the surface of the sphere.	16
2-3	Spherical elliptical region, centered at the north pole and aligned with x -axis, with focus colatitude $\theta_0 = 35^\circ$ and semi-major axis $a = 40^\circ$	17
2-4	Tiling of the spherical harmonic degree space using $\Gamma_\Psi^{(j)}(\ell)$ and $\Gamma_\Phi(\ell)$ for bandlimit $L = 64$, $\epsilon = 2$ and $j_2 = J = 6$	46
3-1	Azimuthally symmetric optimal window signal, bandlimited to degree $L_h = 16$, is constructed for the Mars topography map ($L_f = 32$) and zero-mean, uncorrelated, anisotropic Gaussian noise process at SNR = 0 dBs. (a) Magnitude of the azimuthally symmetric optimal window signal plotted against the colatitude, $\theta \in [0, \pi]$. (b) Magnitude of the axisymmetric optimal window signal on the sphere.	62

3-2 Joint spatial-spectral domain filtering using azimuthally symmetric optimal window signal ($L_h = 16$), resulting in an SNR improvement of 13 dBs. Figure shows magnitude plots of (a) the Mars topography map, $s(\hat{\mathbf{x}})$ ($L_f = 32$), (b) the zero mean, uncorrelated and anisotropic Gaussian noise signal, $z(\hat{\mathbf{x}})$, (c) the noise-contaminated observation, $f(\hat{\mathbf{x}}) = s(\hat{\mathbf{x}}) + z(\hat{\mathbf{x}})$, with $\text{SNR}^f = 0.32$ dBs, and (d) the source signal estimate, $\tilde{s}(\hat{\mathbf{x}})$, with $\text{SNR}^{\tilde{s}} = 13.33$ dBs. 63

3-3 Joint spatial-spectral domain filtering of the bandlimited Mars topography map using the axisymmetric optimal window signal and rank 1 Slepian window signals for the north polar cap regions of angles $\theta_0 = 2^\circ, 10^\circ, 20^\circ$. Output SNR, $\text{SNR}^{\tilde{s}}$, averaged over 100 realizations of a zero-mean, uncorrelated and anisotropic Gaussian noise process, is plotted against the average input SNR. Axisymmetric optimal window signal can be seen to perform better than the rank 1 axisymmetric Slepian window signals, specially at high noise levels. Also shown in the bottom right corner is the magnified plot at low noise levels. . . . 64

3-4 (a) Earth topography map, bandlimited to degree $L_f = 64$, used as the source signal $s(\hat{\mathbf{x}})$, (b) most well-optimally concentrated azimuthally symmetric Slepian window signal, bandlimited to degree $L_{h_0} = 20$, computed for the north polar cap region R_{15° , and (c) most well-optimally concentrated directional Slepian window signal, bandlimited to degree $L_h = 20$, computed for the spherical ellipse $R_{(15^\circ, 16^\circ)}$. Boundary of the north polar cap region and spherical ellipse is shown in black. 72

3-5	(a) Zero-mean, uncorrelated and anisotropic Gaussian noise $z(\hat{\mathbf{x}})$, (b) noise-contaminated observation $f(\hat{\mathbf{x}})$ with $\text{SNR}^f = 0.001$ dBs, (c) signal estimate obtained from the joint $\mathbb{SO}(3)$ -spectral domain filtering framework $\tilde{s}(\hat{\mathbf{x}})$, (d) signal estimate obtained from the joint spatial-spectral domain filtering framework $\tilde{s}_0(\hat{\mathbf{x}})$. Figures (e)–(g) show the magnitude plots of $s(\hat{\mathbf{x}})$, $\tilde{s}(\hat{\mathbf{x}})$ and $\tilde{s}_0(\hat{\mathbf{x}})$. Joint $\mathbb{SO}(3)$ -spectral domain filtering, with $\text{SNR}^{\tilde{s}} = 18.33$ dBs, outperforms the joint spatial-spectral domain filtering by 8 dBs. Moreover, magnitude plots show much better reconstruction of the directional features, such as the dark blue contours marking the boundary between land and water, using the joint $\mathbb{SO}(3)$ -spectral domain filter.	73
3-6	Mean output SNR plotted against mean input SNR for 100 realizations of a zero-mean, uncorrelated and anisotropic Gaussian noise process. Blue and black curves show the results for the estimation of Earth topography map, bandlimited to degree $L_f = 64$, using the joint $\mathbb{SO}(3)$ -spectral domain and the joint spatial-spectral domain filtering frameworks respectively.	74
3-7	(a) Energy per degree plot of the directional optimal window signal for the Earth topography map, bandlimited to degree $L_f = 32$, constructed for a zero-mean, uncorrelated and anisotropic Gaussian noise process at $\text{SNR} = 0$ dBs. (b) Magnitude of the directional optimal window signal on the sphere. Directional optimal window signal is bandlimited to degree $L_h = 16$	79
3-8	Mean output SNR plotted against mean input SNR for 100 realizations of zero-mean, uncorrelated and anisotropic Gaussian noise process. Blue and black curves quantify the performance of the joint $\mathbb{SO}(3)$ -spectral domain filter using directional optimal window signal and rank 1 Slepian window signal (computed for the spherical ellipse $R_{(15^\circ, 16^\circ)}$) respectively, on the Earth topography map, bandlimited to degree $L_f = 32$	80

3-9	Joint $\mathbb{SO}(3)$ -spectral domain filtering of the Earth topography map $s(\hat{\mathbf{x}})$, bandlimited to degree $L_f = 32$, contaminated by a realization of a zero-mean, uncorrelated and anisotropic Gaussian noise process $z(\hat{\mathbf{x}})$ at $\text{SNR}^f = -0.15$ dBs, resulting in an SNR gain of 20.37 dBs for the signal estimate $\tilde{s}(\hat{\mathbf{x}})$, compared to an SNR gain of 16.39 dBs for $\tilde{s}_1(\hat{\mathbf{x}})$.	81
3-10	Multiscale optimal filtering of the Earth topography map $s(\hat{\mathbf{x}})$, bandlimited to degree $L_f = 64$, which is contaminated by zero-mean, uncorrelated and white Gaussian noise $z(\hat{\mathbf{x}})$ at $\text{SNR}^f = -0.057$ dBs. Output SNR obtained from the source signal estimate $\tilde{s}(\hat{\mathbf{x}})$ is 9.68 dBs, resulting in SNR improvement of 9.7 dBs.	86
3-11	Output SNR, averaged over 100 realizations of a zero-mean, uncorrelated and white Gaussian noise process, is plotted versus average input SNR for the estimation of Earth topography map, bandlimited to degree $L_f = 64$, through multiscale optimal filtering framework (blue curve), hard thresholding method (black curve), and weighted-SPHARM based GWKS at different values of κ .	89
3-12	Output SNR, averaged over 100 realizations of a zero-mean, uncorrelated and anisotropic Gaussian noise process, is plotted against average input SNR for filtering and estimation of the Earth topography map, bandlimited to degree $L_f = 32$. Signal estimate is computed using joint spatial-spectral domain filter with axisymmetric optimal window signal, joint $\mathbb{SO}(3)$ -spectral domain filter with rank 1 Slepian window signal for the spherical ellipse $R_{(15^\circ, 16^\circ)}$, joint $\mathbb{SO}(3)$ -spectral domain filter with directional optimal window signal and multiscale optimal filter employing directional wavelet functions with dilation parameter $\epsilon = 2$ and largest wavelet scale set to $J = 5$. All the window signals are bandlimited to degree $L_h = 16$.	90

4-1	Right-angled triangulation of a spherical polygon which is located in the longitudinal quadrants 2 and 3. Vertices shown in yellow are created as a result of either limiting the edges to respective quadrants or dividing the spherical triangles into spherical right-angled triangles. Thick black dot marks the centroid of the polygon.	99
4-2	Spherical right-angled triangle in standard orientation with vertices $\hat{\mathbf{a}}(\pi/2, 0)$, $\hat{\mathbf{b}}(\theta_{b,t}, 0)$ and $\hat{\mathbf{c}}(\pi/2, \phi_{c,t})$, where $\theta_{b,t} = 5\pi/18$ and $\phi_{c,t} = 2\pi/9$.	100
4-3	Possible orientations of a randomly oriented spherical right-angled triangle after first pass of zyz rotation by angles $\varphi_1 \vartheta_1 \omega_1$ (in the order from right to left in zyz -convention).	108
4-4	Geographical region of Australia (shown in blue) and its down-sampled version (shown in black), excluding Tasmania and neighboring islands.	112
4-5	Simple polygon, which encloses the volcanic plateau of Tharsis on the Mars topography map, and its right-angled triangulation. Boundary of the polygon is shown in black. Thick black dot marks the centroid of the polygon.	112
4-6	(a) Earth topography map, bandlimited to degree $L = 32$, (b) Earth topography map reconstructed over Australia at bandlimit $L = 32$, using $N_{RA} \approx 15$ Slepian functions. Boundary of Australia is shown in black.	113
4-7	(a) Mars topography map, bandlimited to degree $L = 32$, (b) Mars topography map reconstructed over Tharsis at bandlimit $L = 32$, using $N_{RT} \approx 93$ Slepian functions. Boundary of Tharsis is shown in black.	114
4-8	Fractional error between the integral of the Earth (Mars) topography map (bandlimited to degree $L = 32$), evaluated over Australia (Tharsis) using the formulation in (4.7) and GL quadrature rule in (4.44), for $L \leq L_1 \leq 2048$	115
4-9	Magnitude of the first 8 Slepian functions computed for Australia at bandlimit $L = 32$. Boundary of Australia is shown in black.	116

4-10	Magnitude of the first 8 Slepian functions computed for Tharsis at bandlimit $L = 32$. Boundary of Tharsis is shown in black.	117
5-1	Earth topography map and $N_{\theta_0,0} \approx 11$ spatial-Slepian coefficients for the Earth topography map at bandlimit $L_f = 128$, using the zonal Slepian functions computed for the axisymmetric north polar cap region of angle $\theta_0 = 15^\circ$	124
5-2	Absolute mean error \mathbf{E}_{mean} , computed from the spectral coefficients of a complex-valued and random test signal $f^T(\hat{\mathbf{x}})$, and the reconstructed signal $f^R(\hat{\mathbf{x}})$, is averaged over 100 realizations of the test signal and plotted against the bandlimit $L_f = 8, 16, 32, 48, 64, 80, 96, 112, 128$. Figure shows that the error is on the order of numerical precision, which verifies the numerical stability of the inverse SST.	127
5-3	Computational complexity analysis of the spatial-Slepian transform for a complex-valued and random test signal using Slepian function at $\alpha = 1$, which is computed for a spherical ellipse $R_{(15^\circ, 20^\circ)}$. Computational time (shown in blue), which is averaged over 10 realizations of the test signal, is in agreement with the theoretical bound of $O(L_f^4)$ (shown in black).	128
5-4	Spatial variance of spatial-Slepian and scale-discretized wavelet coefficients, evaluated for the Earth topography map, bandlimited to degree $L_f = 64$. Spatial-Slepian coefficients can be seen to be better localized than the scale-discretized wavelet coefficients at most of the scales. . .	131

5-5	Fractional ratio \mathfrak{r} , for the Earth topography map, bandlimited to degree $L_f = 64$, is plotted against different number of Slepian (wavelet) scales, which are obtained by varying the polar cap angle θ_0 and the dilation parameter ϵ in such a way that the number of Slepian scales equals the number of wavelet scales. The curve shows that more number of spatial-Slepian coefficients have smaller spatial variance (and hence, better spatial localization) than scale-discretized wavelet coefficients, at every value of polar cap angle (or dilation parameter). . . .	132
5-6	Magnitude of (a) the source signal, which is a realization of a zero-mean and anisotropic Gaussian process, and (b) the first observation that contains localized variation hidden in the source signal within the elliptical region. Both signals are bandlimited to degree 32. Boundary of the elliptical region is shown in black.	135
5-7	(a) Magnitude of the first instance of localized variation, (b)–(d) sample variance of spatial-Slepian coefficients, (e)–(h) sample variance of scale-discretized wavelet coefficients. As can be seen, sample variance of spatial-Slepian coefficients quite accurately detects the region of localized hidden variations, specially at the first two Slepian scales, whereas sample variance of scale-discretized wavelet coefficients yields an over-estimate of the region of localized variations. Spherical elliptical region of localized hidden variations is unbeknownst to the framework of spatial-Slepian and scale-discretized wavelet transforms, and is drawn for reference only.	137
5-8	Spherical harmonic spectrum of the Gaussian spectral smoothing convolutive kernel at all Slepian scales for the north polar cap region of angle $\theta_0 = 5^\circ$, which gives $N_{R_5^\circ} \approx 8$	145

5-9	Output SNR plotted against input SNR, averaged over 100 realizations of a zero-mean, uncorrelated and anisotropic Gaussian noise process, for Gaussian spectral smoothing convolutive kernel and the optimal filter. Slepian scale is set by the Shannon number for a north polar cap region of angle $\theta_0 = 5^\circ$	148
5-10	(a) Mars topography map , (b) zero-mean, uncorrelated and anisotropic Gaussian noise at $\text{SNR}^f = 4.9$ dBs, (c) noise-contaminated observation, (d) Mars topography map obtained from weighted Gaussian spectral smoothing, having $\text{SNR}^{v_G} = 11.3$ dBs, and (e) Mars topography map reconstructed through optimal filtering, having $\text{SNR}^{v_o} = 24.7$ dBs.	148
6-1	Sample positions on the sphere obtained from Gauss-Legendre sampling (red dots), Driscoll-Healy sampling theorem (green dots) and McEwen-Wiaux sampling theorem (blue dots), for bandlimit $L = 12$	154
6-2	Partitioning of the sphere into different equal area pixels using HEALPix. Boundaries of the pixels in equatorial zone are shown in blue and black. Boundaries of the pixels in polar zones are shown in green and red. Pixel centers are shown as black dots.	156
6-3	Sample positions on the sphere obtained from optimal dimensionality sampling scheme (black dots), Gauss-Legendre sampling (red dots), Driscoll-Healy sampling theorem (green dots) and McEwen-Wiaux sampling theorem (blue dots), for bandlimit $L = 12$	159
6-4	Number of samples used by HEALPix and the proposed sampling scheme, along with the theoretical bound established in Lemma 1, for the accurate computation of spherical harmonic transform of a signal bandlimited to degree $2 \leq L \leq 512$. Also shown is the magnified plot, in logarithmic scale, for bandlimits $L \leq 64$	165
6-5	Visual comparison of sampling density between (a) HEALPix and (b) proposed sampling scheme, for bandlimit $L = 32$	166

6-6	Number of samples used, in units of L^2 , for the computation of spherical harmonic transform of a signal, bandlimited to degree $2 \leq L \leq 512$. For $L = 2N_{\text{side}}$, HEALPix uses $3L^2$ samples, while the proposed sampling scheme requires at most $2L^2$ samples ($\sim 1.5L^2$ samples for $L \geq 8$) to compute the SHT.	166
6-7	\mathbf{E}_{max} and \mathbf{E}_{mean} between spectral coefficients of the test and reconstructed signals, averaged over 50 realizations of the test signal, for bandlimits in the range $2 \leq L \leq 512$	167
7-1	Placement of iso-latitude rings for HEALLPix at different resolutions.	172
7-2	Placement of iso-longitude rings for HEALLPix at different resolutions.	173
7-3	Hierarchical equal area iso-latitude iso-longitude pixelization of the sphere at different resolutions.	174
7-4	HEALLPix pixel centers shown as mean of the pixel vertices in green dots. Red dots show the pixel centers which are equi-angular-distant from the pixel vertices. Pixel centers have nearly the same position on the sphere for the two methods.	176
7-5	Quaternary tree representation for HEALLPix. Each node is represented as $P(h_{\text{T}}, i_{h_{\text{T}}})$ where $0 \leq h_{\text{T}} \leq \mathfrak{H}$ is the tree level and $1 \leq i_{h_{\text{T}}} \leq 4^{h_{\text{T}}}$ is the index of the node at tree level h_{T} . \mathfrak{H} is the maximum tree level, called height of the tree.	177
7-6	Magnitude of Slepian functions for different nodes in the HEALLPix quaternary tree, constructed using (7.16) for bandlimit $L = 16$ and height $\mathfrak{H} = 4$. For each node, we show the most well-optimally concentrated and least well-optimally concentrated Slepian functions, where λ denotes the fractional energy concentration (see (2.57)). Boundary of the pixels is shown in black.	183
7-7	Angle (in degrees) between the range space of \mathfrak{D}_1 and $V_\alpha(1, 1)$ for different values of α and bandlimit $L = 16$ ($\mathfrak{H} = 4$). Thick red lines mark the integer multiples of Shannon number $N_1 = 64$	184

7-8	Mutual coherence between elements of the dictionary constructed for HEALLPix at bandlimit $L = 16$ ($\mathfrak{H} = 4$).	186
7-9	Cumulative fractional mutual coherence between dictionary elements, plotted against the range of mutual coherence values, for HEALLPix quaternary trees with height $\mathfrak{H} = 1, 2, 3, 4$, corresponding to bandlimit $L = 2, 4, 8, 16$. Arrow shows the direction in which the approximate knee of the curves is displaced with increasing values of L	187
7-10	Fraction of total number of inner products between HEALLPix dictionary elements which result in significant mutual coherence.	189
7-11	Hierarchical equal area iso-latitude pixelization of the sphere at different resolutions. Light shade of gray represents pixels at the boundary of polar and equatorial zones whereas dark and medium shades of gray represent pixels in the polar and equatorial zones respectively. Pixel boundaries are shown in black.	190
7-12	Quaternary tree representation for HEALPix scheme. Each node is represented as $P(h_T, i_{h_T})$ where $h_T \in [0, \mathfrak{H}]$ is the tree level and i_{h_T} is the index of the node at tree level h_T . \mathfrak{H} is the maximum tree level, called height of the tree.	207
7-13	Magnitude of most well-optimally concentrated Slepian functions for different nodes in the HEALPix quaternary tree, constructed for bandlimit $L = 32$ ($\mathfrak{H} = 4$). Thick green, red, black and blue lines mark the boundaries of HEALPix base-resolution pixels, where the red line also indicates the $\phi = 0$ great circle arc. Boundary of the pixels is shown in black.	215
7-14	Angle (in degrees) between the range spaces of \mathfrak{D}_1 , $V_\alpha(1, 1)$ and \mathfrak{D}_5 , $V_\alpha(1, 5)$, for different values of α at bandlimit $L = 32$ ($\mathfrak{H} = 4$). Thick red lines mark the integer multiples of Shannon number $N_1 = 85$. . .	216
7-15	Mutual coherence between elements of the dictionary constructed for HEALPix at bandlimit $L = 32$ ($\mathfrak{H} = 4$).	217

7-16 Cumulative fractional mutual coherence between dictionary elements, plotted against the range of mutual coherence values, for HEALPix quaternary trees at bandlimit $L = 4, 8, 16, 32$, having corresponding height $\mathfrak{H} = 1, 2, 3, 4$. Arrow shows the direction in which the approximate knee of the curves is displaced with increasing values of L 218

List of Tables

2.1	Associated Legendre polynomials and spherical harmonic functions for degrees $\ell = 0, 1, 2, 3$ and orders $ m \leq \ell$	21
6.1	Comparison of Gauss-Legendre, Driscoll-Healy, McEwen-Wiaux and optimal dimensionality sampling methods for the number of samples required to compute SHT of a signal bandlimited to degree $L = 12$. . .	158
7.1	Height of the HEALPix quaternary tree along with maximum HEALPix resolution parameter, for fixed N_{SF} , at different values of bandlimit L and N_{SF}	179
7.2	Height of the HEALPix quaternary tree along with maximum HEALPix resolution parameter, for varying N_{SF} , at different bandlimits L	180
7.3	Approximating the knee for each curve in Figure 7-9.	188
7.4	Height of the HEALPix quaternary tree along with maximum HEALPix resolution, for fixed N_{SF} , at different values of bandlimit L and N_{SF} . .	209
7.5	Height of the HEALPix quaternary tree along with maximum HEALPix resolution, for varying N_{SF} , at different bandlimits L	211
7.6	Approximating the knee for each curve in Figure 7-16.	218

Chapter 1

Introduction

1.1 Background and motivation

Signals are functions which convey meaningful information about the attributes of physical systems/phenomena. The objective of signal processing theories and methods is to find mathematically convenient representations of such functions in order to analyze and process them in an effective and efficient manner to extract useful information. The underlying mathematics of these methods is highly dependent on the nature of the signals under consideration. For signals defined on the 1 dimensional real line, which is usually identified with the time domain, signal processing techniques such as sampling, filtering, prediction, correlation, detection, estimation and reconstruction in the presence of noise, have been thoroughly investigated (e.g. [1, 2, 3, 4, 5, 6, 7, 8, 9, 10, 11, 12, 13, 14, 15, 16]). A natural extension of the time domain signals is the class of signals which are defined on the multidimensional Euclidean domain. There is an abundance of literature available on the processing of multidimensional Euclidean domain signals as well (e.g. [17, 18, 19, 20, 21]).

With rich literature available on the processing of Euclidean domain signals, it is only instinctive to extend these methods in a way so as to effectively process signals defined on the 2 dimensional surface of the 2-sphere¹, called spherical signals, which

¹2-sphere is defined as the set of points in the 3D Euclidean domain which are equidistant from a given point. Unit sphere, 2-sphere or simply sphere refers to the same thing.

arise whenever the underlying configuration of the problem has a spherical geometry. Hence, such signals have inherent angular dependence and are encountered in various fields of science and engineering, such as wireless communication (e.g. [22, 23, 24, 25]), 3D beamforming (e.g. [26]), computer graphics (e.g. [27, 28, 29]), medical imaging (e.g. [30, 31]), acoustics (e.g. [32, 33, 34, 35]), geodesy (e.g. [36, 37, 38]), quantum chemistry (e.g. [39, 40]), cosmology (e.g. [41, 42, 43, 44, 45, 46, 47]), astronomy (e.g. [48, 49]) and planetary sciences (e.g. [50, 51, 52, 53, 54, 55]). Examples of spherical signals include gravitational, topographic and magnetic fields of the planets, cosmic microwave background (CMB), a relic radiation from the Big Bang, pouring down on us from space, electromagnetic radiation pattern of an antenna array in spherical geometry, acoustic signal received using spherical configuration of microphones etc.

As opposed to 1D and multidimensional Euclidean domain signals, which are defined on flat Euclidean domains, spherical signals are defined on a curved domain due to which extension of Euclidean domain signal processing techniques to the spherical domain is not a trivial task. However, over the years, a lot of methods developed for Euclidean domain signals have been carefully extended to process spherical signals. Some of them include sampling and reconstruction (e.g. [56, 57, 58, 59, 60]), convolution on 2-sphere (e.g. [61, 62, 63, 64]), signal filtering (e.g. [65, 66, 67, 68, 69, 70, 71, 72]), spectrum estimation (e.g. [36, 37, 38]), Slepian spatial-spectral concentration problem (e.g. [73, 74, 75, 76, 77]) and wavelet analysis (e.g. [78, 79, 80, 81, 82, 83, 84, 85]). A brief review of the literature on some of the these methods, which are directly related to the work of this dissertation, is given below.

1.1.1 Signal filtering and estimation

Spherical observations in most of the application areas are marred with unwanted, yet unavoidable noise due to the presence of different sources of interference. Hence, many noise removal techniques, with different assumptions and constraints, have been proposed in the literature. For instance, matched filter, proposed in [67], has been used for detecting cosmic bubble collisions in [69]. Matched filter and Wiener filter

are proposed in [71] as a special case of the formulation in an abstract homogeneous space under the action of the rotation group. An isotropic Wiener filter is used for spatial averaging of the GRACE gravity-field solutions in [66]. These filtering methods process signals in either spatial or spectral domain, assuming the noise to be a realization of an isotropic process on the sphere.

To estimate signals contaminated by anisotropic noise², a minimum mean-square error filter is developed in [70]. Moreover, a zero-forcing and minimum mean-square error criterion is adopted in [72] using linear operators for equalizing linear distortions and anisotropic noise. Motivated by the idea of filtering non-stationary processes in the joint time-frequency domain proposed in [86], a spatially varying optimal filter is proposed in [87] for the estimation of spherical signals contaminated by zero-mean and anisotropic noise. The resulting filter estimates the underlying signal by performing filtering in the joint spatial-spectral domain using spatially localized spherical harmonic transform [88].

1.1.2 Localized signal analysis

Signals can be analyzed globally (over the whole sphere) or locally (over a region on the sphere). Localized signal analysis is particularly important for applications in astronomy, cosmology, geodesy and planetary sciences, where the data is either unreliable or unavailable over some region on the sphere. Localized analysis requires signal representation in terms of localized basis functions. One such basis set, referred to as Slepian basis, is obtained by solving the Slepian spatial-spectral concentration problem on the sphere [73, 36, 74, 75, 76, 77]. This problem was first studied by Slepian and his co-authors in their seminal work for the 1D time domain signals [89, 90], and was later extended to multidimensional Euclidean domain signals [91]. Spatial-spectral concentration problem on the sphere was first formulated by Albertella et al. in [73], who studied localized basis functions for the bounded region of latitudinal belt about the equator on the sphere. A rigorous mathematical treatment of the spatial-spectral concentration problem on the sphere was given by Simons et al. [74].

²See Chapter 3 for the definition of isotropic and anisotropic processes.

The resulting localized basis set on the sphere, referred to as Slepian basis, has proved very useful for accurate representation, estimation and reconstruction of signals over spatially limited spherical regions [38]. A subset of Slepian basis functions, called the zonal Slepian basis, has been used to carry out localized spectral analysis in [36]. The problem of polar gap in geodesy has been addressed in [75], where Slepian basis functions have been employed to estimate the potential fields, at the source level, from the noise-contaminated satellite data at an altitude over an incomplete portion of the sphere.

1.1.3 Sampling of signals on the sphere

In real world applications we can generate, store and process only discrete signals, i.e., signals defined at discrete points in their respective domains. For instance, gravitational, topographic and magnetic fields of a planet can only be quantified at discrete positions on its surface, cosmic microwave background radiation can only be detected at discrete angular positions on the celestial sphere³, radiation pattern of an antenna can only be measured at discrete angles in space (no matter how small the step in angular displacement is, it is still discrete), acoustic signal captured by multiple microphones placed in a spherical configuration is available only at discrete angular positions in space etc. Signal measurements at discrete points in their respective domains are called “samples”. The number and position of the samples on the sphere is an important attribute of any sampling scheme for complete characterization of the underlying signal.

Just as knowledge of the spectrum (frequency or spectral domain representation) of a Euclidean domain signal is pivotal for its perfect reconstruction [92], knowledge of the spectrum of a spherical signal is critical in exact reconstruction from its samples on the sphere. Spectral representation of a spherical signal is obtained through the spherical harmonic transform, which is the Fourier representation of the signal in terms of spherical harmonic functions [64]. Perfect reconstruction of a spherical signal depends on the ability of the sampling scheme to *exactly* compute its SHT.

³A celestial sphere is defined as an imaginary sphere with the observer at its center.

Unlike for signals in the Euclidean domain, there exists no sampling theorem on the sphere which enables exact reconstruction of a signal from an optimal number of its samples on the sphere. There exist sampling schemes which reconstruct the signal exactly but at the cost of using more than optimal number of its samples [56, 58, 59]. Khalid *et al.* proposed a sampling scheme which uses optimal number of samples but presents accurate, rather than exact, reconstruction of the signal [60]. These methods suffer from the problem of oversampling near the poles of the sphere, which can be avoided by using equal area sampling schemes that partition the sphere into equal area regions. Hierarchical equal area partitioning schemes hierarchically divide the sphere into equal area regions which can be further divided into equal area sub-regions. One such scheme that has been extensively used in cosmology to generate full sky maps, and for the analysis of cosmic microwave background, is Hierarchical Equal Area iso-Latitude Pixelization (HEALPix) [57]. However, HEALPix results in approximate reconstruction of signals from the samples.

1.1.4 Multiresolution (multiscale) analysis

Apart from global and local analysis, signals can be analyzed at different scales, i.e., over varying extents of the domain. The latter is called multiresolution or multiscale analysis and has been extensively used to study time domain signals using tools such as the wavelet transform (e.g. [93, 94, 95]), which has also been extended to study signals on the sphere [78, 51, 79, 81, 82, 83]. Wavelet transform enables a joint space-scale domain representation, which records the scale-dependent features of the signals in what are called as wavelet coefficients. Unlike in Euclidean domain, dilation on the sphere can be defined in different ways, which results in different formulations and algorithms for wavelet analysis on the sphere [80, 82, 96, 83, 85]. One of the ways to define dilation is to project wavelet functions onto a plane, which is tangent to one of the poles of the sphere. Known as dilation via stereographic projection, this method involves mapping of the wavelet functions onto the tangent plane, followed by inverse mapping of the dilated wavelet functions from the tangent plane to the sphere [80, 82, 96]. Alternatively, wavelet functions can be dilated in

the spherical harmonic degree space through the use of an infinitely differentiable Schwartz function, resulting in the wavelet transforms proposed in [83, 85].

1.2 Scope of the dissertation

The work in this dissertation is a contribution towards development of novel techniques for processing of signals defined on the sphere, and can be divided into three parts.

1. The first part is concerned with the development of novel techniques for signal filtering and estimation, using joint domain representations, in the presence of anisotropic noise.
2. The second part is related to the localized signal analysis using Slepian functions on the sphere.
3. The third part is focused on the development of a framework for multiscale (multiresolution) analysis of signals on the sphere.

1.2.1 Summary of research contributions

Highlights of the major contributions of this work, in the context of above-mentioned scope, along with the compiled research work (for ease of reference), are given below.

1. The spatially varying optimal filter, also referred to as joint spatial-spectral domain filter, proposed in [87], lacks a systematic design of the window signal required for spatial localization of signals under consideration. In this context, an optimal window design is presented to enhance the performance of the joint spatial-spectral domain filter. The utility of the filter, using the designed window signal, is illustrated on a Mars topography map. Results of this work have been published in the proceedings of IEEE International conference on acoustics, speech and signal processing, with the following details:

- (C3) **Adeem Aslam** and Zubair Khalid, “Optimal Window Design for Joint Spatial-Spectral Domain Filtering of Signals on the Sphere,” *ICASSP 2020 - 2020 IEEE International Conference on Acoustics, Speech and Signal Processing (ICASSP)*, Barcelona, Spain, 2020, pp. 5785–5789.
2. A framework for the joint $\mathbb{S}\mathbb{O}(3)$ -spectral domain filtering of spherical signals, in the presence of anisotropic noise, is presented using the directional spatially localized spherical harmonic transform, which has been demonstrated on an Earth topography map in the following publication:
- (J2) **Adeem Aslam** and Zubair Khalid, “Joint $\mathbb{S}\mathbb{O}(3)$ -Spectral Domain Filtering of Spherical Signals in the Presence of Anisotropic Noise,” in *IEEE Signal Processing Letters*, vol. 27, pp. 2109–2113, 2020.
3. Performance of the joint $\mathbb{S}\mathbb{O}(3)$ -spectral domain filter is further enhanced by designing a directional optimal window signal. Better performance of the joint $\mathbb{S}\mathbb{O}(3)$ -spectral domain filter, using the designed window signal, is demonstrated on an Earth topography map. Results of this work have been submitted to the journal of IEEE Signal Processing Letters, with the following details:
- (J6) **Adeem Aslam** and Zubair Khalid, “Optimal Window Design For Joint $\mathbb{S}\mathbb{O}(3)$ -Spectral Domain Filtering of Signals on the Sphere,” submitted to *IEEE Signal Processing Letters*.
4. Motivated by the idea of signal filtering in the joint spatial-spectral domain, an optimal filter is also formulated in the joint $\mathbb{S}\mathbb{O}(3)$ -scale domain, which is enabled by the scale-discretized wavelet transform [83, 85]. The resulting multiscale optimal filter is compared in its performance to the hard thresholding method and weighed-SPHARM based signal estimation framework. Better performance of the multiscale optimal filter is demonstrated on an Earth topography map. This work has been published with the following details:
- (J3) **Adeem Aslam**, Zubair Khalid and Jason D. McEwen, “Multiscale Optimal Filtering on the Sphere,” in *IEEE Signal Processing Letters*, vol. 28,

pp. 394–398, 2021.

5. In the context of localized signal analysis, a framework for localized signal analysis over simple spherical polygons is formulated using bandlimited Slepian functions. Specifically, analytical expressions for the (i) surface integration of signals, and (ii) computation of Slepian basis functions, over simple spherical polygons, are presented. The framework has been validated using Earth and Mars topography maps, in the following publication:

(J1) Adeem Aslam and Zubair Khalid, “Localized Analysis of Signals on the Sphere Over Polygon Regions,” in *IEEE Transactions on Signal Processing*, vol. 68, pp. 4568–4582, 2020.

6. Slepian functions are also used to formulate a novel spatial-Slepian transform on the sphere, resulting in the joint spatial-Slepian domain representation of spherical signals in the form of spatial-Slepian coefficients, which are analyzed for spatial localization on the sphere. Spatial-Slepian transform is utilized for detecting the presence of hidden and weak localized variations in the signals. Furthermore, spatial-Slepian transform is employed to construct a framework of generalized linear transformations of signals in the joint spatial-Slepian domain, which is exemplified through particular forms of the underlying spatial-Slepian transformation kernel. These works have resulted in the following research contributions:

(J4) Adeem Aslam and Zubair Khalid, “Spatial-Slepian Transform on the Sphere,” in *IEEE Transactions on Signal Processing* (accepted with minor revision for English usage, revision submitted on May 16, 2021).

(J5) Adeem Aslam and Zubair Khalid, “Linear Transformations and Signal Estimation in the Joint Spatial-Slepian Domain,” submitted to *IEEE Signal Processing Letters* (accepted for publication).

7. Slepian functions are also considered for the development of a framework of multiscale (multiresolution) analysis of spherical signals through hierarchical

partitioning of the sphere into regions, called pixels, of varying spatial extent. Different sampling (partitioning) methods on the sphere are reviewed in this respect and **H**ierarchical **E**qual **A**rea iso-**L**atitude iso-**L**ongitude **P**ixelization (HEALLPix) scheme is proposed. Employing the formulation available in the literature, an overcomplete multiscale dictionary of Slepian functions is constructed for HEALLPix. Additionally, a framework for analytical computation of Slepian functions for pixels generated using HEALPix scheme is formulated, which facilitates the construction of another overcomplete multiscale dictionary of Slepian functions on the sphere. Both dictionaries are analyzed for the range and mutual coherence of their elements. The dictionaries are shown to span the space of bandlimited signals on the sphere, with most of their respective elements exhibiting negligibly small mutual coherence. These works have resulted in the following research contributions:

- (C2) **Adeem Aslam** and Zubair Khalid, “Construction of Overcomplete Multiscale Dictionary of Slepian Functions on the Sphere,” *ICASSP 2019 - 2019 IEEE International Conference on Acoustics, Speech and Signal Processing (ICASSP)*, Brighton, United Kingdom, 2019, pp. 5137–5141.
- (J7) **Adeem Aslam** and Zubair Khalid, “Overcomplete Multiscale Dictionary of Slepian Functions for HEALPix on the Sphere,” manuscript under preparation for submission to *IEEE Transactions on Signal Processing*.

In addition, as an outcome of the review of sampling schemes, an efficient and accurate spherical harmonic transform is formulated for HEALPix, which has been published with the following details:

- (C1) **Adeem Aslam**, Zubair Khalid and Rodney A. Kennedy, “Efficient Sampling on HEALPix Grid,” *2018 IEEE International Conference on Acoustics, Speech and Signal Processing (ICASSP)*, Calgary, AB, 2018, pp. 4589–4593.

1.3 Organization

The research contributions of this dissertation are divided into five chapters. A separate chapter is dedicated to the mathematical preliminaries of signal analysis on the sphere and $\mathbb{SO}(3)$ rotation group. The overall organization of the dissertation is given below. The organization is also graphically presented through a flowchart in Figure 1-1.

- Chapter 2 presents an overview of the fundamentals of spherical signal analysis. Signal representations on the sphere, signal rotations on the sphere, signal analysis on the $\mathbb{SO}(3)$ rotation group, and convolution of signals on the sphere as well as $\mathbb{SO}(3)$ rotation group are discussed. Furthermore, a brief overview of the Slepian spatial-spectral concentration problem along with the joint domain representations, enabled by spatially localized spherical harmonic transform and scale-discretized wavelet transform, are presented.
- In Chapter 3, optimal filters in the joint $\mathbb{SO}(3)$ -spectral domain and joint $\mathbb{SO}(3)$ -scale domain, which are enabled by spatially localized spherical harmonic transform and the scale-discretized wavelet transform respectively, are presented. Moreover, optimal window signals are designed to enhance the performance of joint spatial-spectral domain filter (i.e., spatially varying filter in [87]) and the joint $\mathbb{SO}(3)$ -spectral domain filter.
- In Chapter 4, a framework for localized signal analysis over spherical polygons, using bandlimited Slepian functions, is presented.
- In Chapter 5, spatial-Slepian transform is formulated and employed for localized variation analysis to detect the presence of hidden and weak localized variations in the signals on the sphere. The resulting spatial-Slepian coefficients are also used to construct a framework for generalized linear transformations in the joint spatial-Slepian domain.
- A review of different sampling (partitioning) schemes is presented in Chapter 6

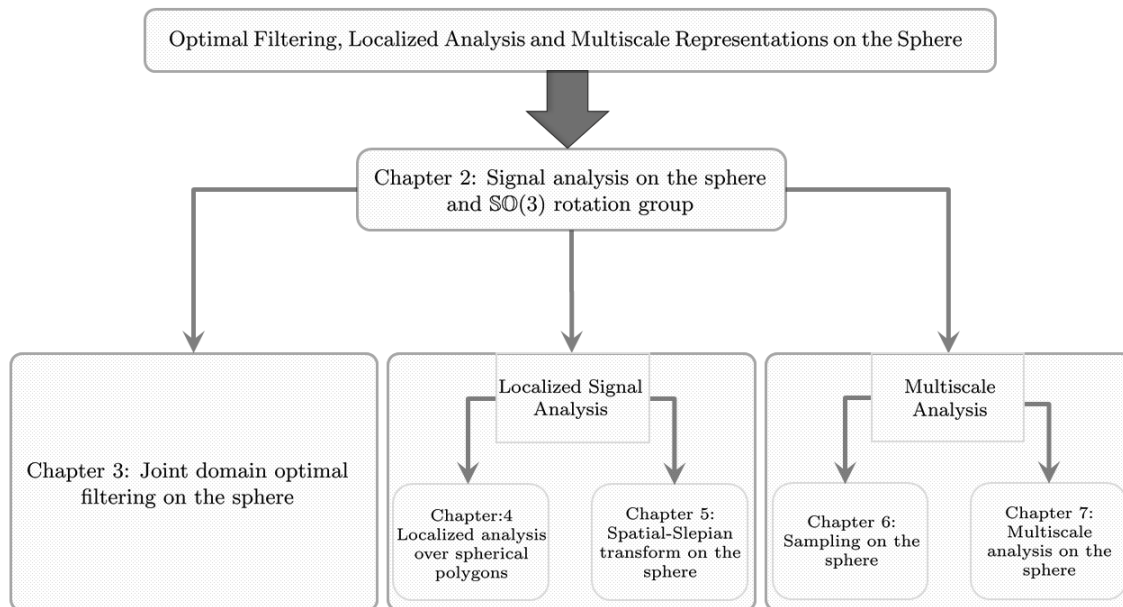


Figure 1-1: Flowchart of the organization of dissertation.

and an efficient spherical harmonic transform is presented for the HEALPix scheme.

- In Chapter 7, we formulate the HEALPix scheme for hierarchical partitioning of the sphere and employ it to develop a framework for multiscale (multiresolution) analysis of spherical signals by constructing an overcomplete multiscale dictionary of Slepian functions. Furthermore, analytical expressions for the computation of Slepian functions are presented for the HEALPix pixels, and an overcomplete multiscale dictionary of Slepian functions for HEALPix is constructed.
- In Chapter 8, we conclude by presenting a concise summary of the research contributions and discuss some potential research directions.

Chapter 2

Signal analysis on the sphere and $\mathbb{SO}(3)$ rotation group

In this chapter, we review the spherical coordinate system and necessary mathematical background for signal analysis on the sphere as well as $\mathbb{SO}(3)$ rotation group. We discuss spatial-spectral concentration problem, summarize different methods of convolution of spherical signals, and present convolution of signals on $\mathbb{SO}(3)$ rotation group. We also review mathematical formulations of joint spatial-spectral domain and joint space-scale domain representations for signals defined on the sphere.

2.1 2-sphere

Any point in the 3D Euclidean space \mathbb{R}^3 can be represented by a 3-vector as

$$\mathbf{x} \equiv (x_x, x_y, x_z)^T \in \mathbb{R}^3, \quad (2.1)$$

where $(\cdot)^T$ denotes the vector transpose. The components x_x, x_y and x_z are coordinates along the x, y and z axes respectively. Norm of the vector \mathbf{x} in the 3D Euclidean space is defined as

$$|\mathbf{x}| = \sqrt{x_x^2 + x_y^2 + x_z^2}. \quad (2.2)$$

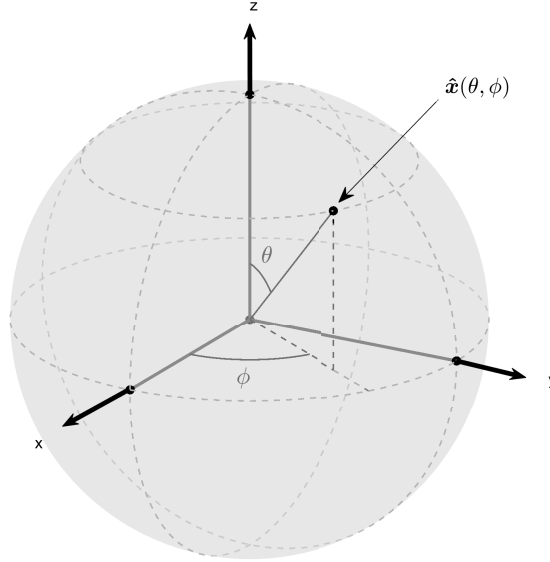


Figure 2-1: 2-sphere embedded in \mathbb{R}^3 with a point on its surface represented by a unit vector $\hat{\mathbf{x}}(\theta, \phi)$, where $\theta \in [0, \pi]$ is the colatitude and $\phi \in [0, 2\pi)$ is the longitude.

The 2-sphere, or unit sphere or just sphere, is defined as the following set

$$\mathbb{S}^2 = \{\mathbf{x} \in \mathbb{R}^3 : |\mathbf{x}| = 1\}, \quad (2.3)$$

which represents a 2D surface embedded in the 3D Euclidean space. Although the points on the sphere belong to \mathbb{R}^3 , this surface is essentially different from \mathbb{R}^3 as it is bounded and curved, having positive Gaussian curvature [97]. In contrast, Euclidean spaces have zero Gaussian curvature and are called flat.

Vectors representing points on the sphere have unit norm and hence, are called unit vectors. Unit vectors are denoted with a “hat” on top to differentiate them from non-unit vectors. Every vector \mathbf{x} has an associated unit vector $\hat{\mathbf{x}}$ which is obtained as

$$\hat{\mathbf{x}} = \frac{\mathbf{x}}{|\mathbf{x}|}. \quad (2.4)$$

Unit vector $\hat{\mathbf{x}}$ can be interpreted as the direction and $|\mathbf{x}|$ as the magnitude of the vector \mathbf{x} . Surface of the sphere can then be redefined as $\mathbb{S}^2 = \{\hat{\mathbf{x}} \in \mathbb{R}^3\}$.

2.1.1 Spherical coordinates

Each point on the surface of the sphere is parameterized by two angles, namely colatitude, denoted by $\theta \in [0, \pi]$ and measured from the positive z -axis, and longitude, denoted by $\phi \in [0, 2\pi]$ and measured from the positive x -axis in the $x - y$ plane. Any point on the surface of the sphere can then be represented by a unit vector parameterized by colatitude and longitude as

$$\hat{\mathbf{x}} \equiv \hat{\mathbf{x}}(\theta, \phi) \triangleq (\sin \theta \cos \phi, \sin \theta \sin \phi, \cos \theta)^T. \quad (2.5)$$

Conversely, given any unit vector on the sphere, one can find the colatitude and longitude as

$$\phi = \tan^{-1} \left(\frac{x_y}{x_x} \right), \quad \theta = \cos^{-1} x_z, \quad (2.6)$$

where four-quadrant definition of \tan^{-1} should be used as ϕ varies from 0 to 2π .

Angular distance between two points on the sphere, represented by the unit vectors $\hat{\mathbf{x}} = (\sin \theta_0 \cos \phi_0, \sin \theta_0 \sin \phi_0, \cos \theta_0)^T$ and $\hat{\mathbf{y}} = (\sin \theta_1 \cos \phi_1, \sin \theta_1 \sin \phi_1, \cos \theta_1)^T$, is denoted by $\Delta(\hat{\mathbf{x}}, \hat{\mathbf{y}})$ and is given by

$$\cos \Delta(\hat{\mathbf{x}}, \hat{\mathbf{y}}) = \hat{\mathbf{x}} \cdot \hat{\mathbf{y}} = \sin \theta_0 \sin \theta_1 \cos(\phi_0 - \phi_1) + \cos \theta_0 \cos \theta_1, \quad \cos \Delta(\hat{\mathbf{x}}, \hat{\mathbf{y}}) \in [-1, +1]. \quad (2.7)$$

2.1.2 Regions on the sphere

A regular region¹ on the sphere, denoted by R , has a surface area given by

$$A_R = \int_R ds(\hat{\mathbf{x}}), \quad (2.8)$$

where $ds(\hat{\mathbf{x}}) = \sin \theta d\theta d\phi$ is the differential area element on the sphere. One of the regions of particular interest is the azimuthally symmetric polar cap region centered

¹A compact set S in \mathbb{R}^n is a regular region if every neighborhood of every point on the boundary of S contains points in the interior of S .

at the north pole, also called north polar cap region, which is parameterized by the maximum colatitude θ_0 and is defined as [64]

$$R_{\theta_0} = \{(\theta, \phi) : 0 \leq \theta \leq \theta_0, 0 \leq \phi < 2\pi\}. \quad (2.9)$$

Similarly, south polar cap region is parameterized by the minimum colatitude θ_0 and is defined as

$$R_{\pi-\theta_0} = \{(\theta, \phi) : \pi - \theta_0 \leq \theta \leq \pi, 0 \leq \phi < 2\pi\}. \quad (2.10)$$

Surface area of both polar cap regions is given by $2\pi(1 - \cos \theta_0)$.

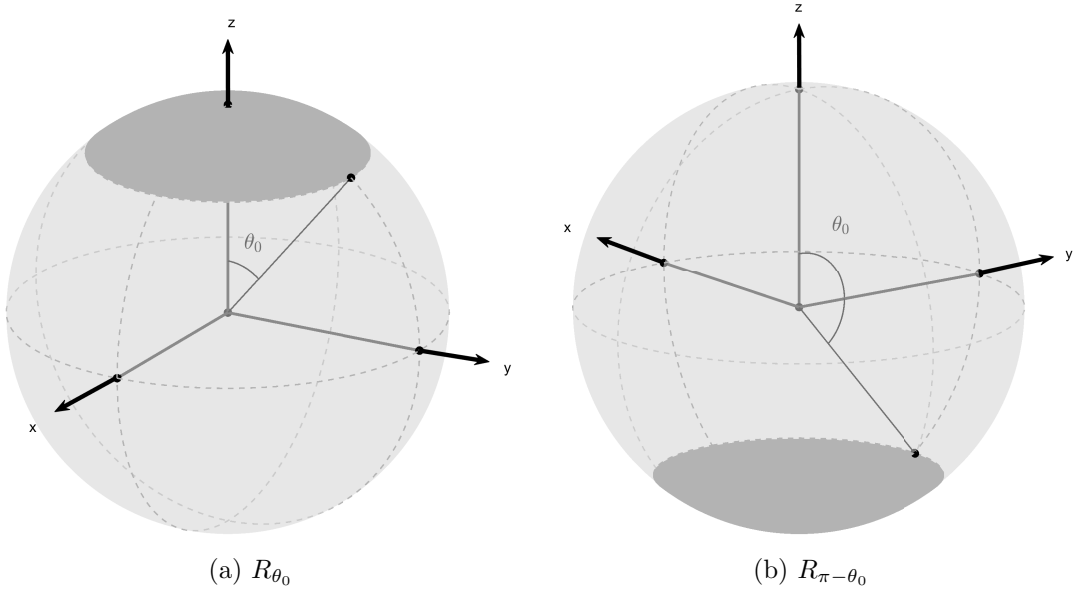


Figure 2-2: North and south polar cap regions shown as shaded areas on the surface of the sphere.

Another region of interest called the spherical ellipse, centered at the north pole and aligned with x -axis, is defined as [98]

$$R_{(\theta_0, a)} = \{(\theta, \phi) : \Delta(\hat{\mathbf{x}}_1(\theta, \phi), \hat{\mathbf{y}}_1(\theta_0, 0)) + \Delta(\hat{\mathbf{x}}_1(\theta, \phi), \hat{\mathbf{y}}_2(\theta_0, \pi)) \leq 2a\}, \quad (2.11)$$

where $\Delta(\hat{\mathbf{x}}_1, \hat{\mathbf{y}}_1)$ represents the angular distance between points $\hat{\mathbf{x}}_1$ and $\hat{\mathbf{y}}_1$, $0 \leq \theta_0 \leq a \leq \pi/2$, θ_0 is called the focus colatitude and $a \triangleq \Delta(\hat{\mathbf{x}}(0, 0), \hat{\mathbf{y}}(a, 0))$ is the semi-major

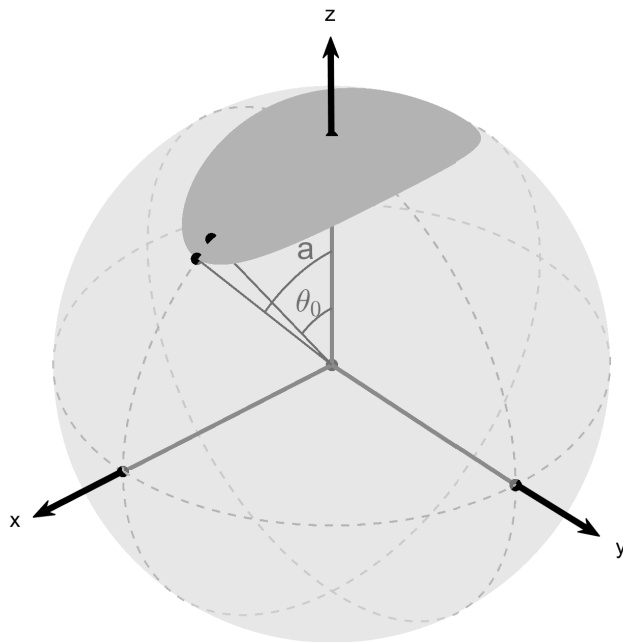


Figure 2-3: Spherical elliptical region, centered at the north pole and aligned with x -axis, with focus colatitude $\theta_0 = 35^\circ$ and semi-major axis $a = 40^\circ$.

axis of the spherical ellipse. Eccentricity of the ellipse is controlled by the difference between the focus colatitude and semi-major axis; ellipse become more eccentric, i.e., more directional along the x -axis, as a approaches θ_0 . For $a = \theta_0$, spherical ellipse becomes an arc of length $2a$, whereas for $a = \pi/2$ and $\theta_0 = 0$, it becomes a north polar cap region of polar cap angle $\pi/2$ and a respectively. Figure 2-3 shows a spherical ellipse of focus colatitude $\theta_0 = 35^\circ$ and semi-major axis $a = 40^\circ$.

2.1.3 Rotations on the sphere

There are different ways to define rotations on the sphere. In this work, we define rotations by three angles around three fixed axes. Such rotations are also called extrinsic, as opposed to intrinsic rotations which are defined by three angles around three moving axes. Since there are three independent choices for the first axis of rotation and two independent choices for each of the second and third axis of rotation, there are a total of 12 possibilities for choosing the axes for applying rotations. Also, there are right handed and left handed rules for applying rotations, which gives 24

possibilities for defining rotations. Out of these, we choose the right handed zyz convention in which a rotation is defined by three Euler angles namely, $\omega \in [0, 2\pi)$ around z -axis, $\vartheta \in [0, \pi]$ around y -axis and $\varphi \in [0, 2\pi)$ around z -axis. Rotation by each Euler angle is represented by a 3×3 orthogonal matrix. Hence, the overall rotation is given by

$$\mathbf{R} \equiv \mathbf{R}^{zyz}(\varphi, \vartheta, \omega) \triangleq \mathbf{R}^z(\varphi)\mathbf{R}^y(\vartheta)\mathbf{R}^z(\omega), \quad (2.12)$$

in the order from right to left, where $\mathbf{R}^y(\vartheta)$ and $\mathbf{R}^z(\omega)$ are 3×3 orthogonal matrices representing rotations around y and z axes by angles ϑ and ω respectively, and are given by [64]

$$\mathbf{R}^y(\vartheta) = \begin{pmatrix} \cos \vartheta & 0 & \sin \vartheta \\ 0 & 1 & 0 \\ -\sin \vartheta & 0 & \cos \vartheta \end{pmatrix}, \quad \mathbf{R}^z(\omega) = \begin{pmatrix} \cos \omega & -\sin \omega & 0 \\ \sin \omega & \cos \omega & 0 \\ 0 & 0 & 1 \end{pmatrix}. \quad (2.13)$$

2.2 Signal analysis on the sphere

We consider complex-valued functions $f(\theta, \phi) \equiv f(\hat{\mathbf{x}})$ defined on the sphere, which are square-integrable, i.e.,

$$\|f\|_{\mathbb{S}^2} = \sqrt{\int_{\mathbb{S}^2} |f(\hat{\mathbf{x}})|^2 ds(\hat{\mathbf{x}})} < \infty, \quad (2.14)$$

where, as before, $ds(\hat{\mathbf{x}}) = \sin \theta d\theta d\phi$ is the invariant measure on the sphere and integration is carried out over the whole sphere, i.e.,

$$\int_{\mathbb{S}^2} \equiv \int_{\phi=0}^{2\pi} \int_{\theta=0}^{\pi}. \quad (2.15)$$

Equipped with the following inner product between two functions $f(\hat{\mathbf{x}})$ and $h(\hat{\mathbf{x}})$

$$\langle f, h \rangle_{\mathbb{S}^2} \triangleq \int_{\mathbb{S}^2} f(\hat{\mathbf{x}}) \overline{h(\hat{\mathbf{x}})} ds(\hat{\mathbf{x}}), \quad (2.16)$$

where $\overline{(\cdot)}$ denotes the complex conjugate, the set of such functions forms a Hilbert space, denoted by $L^2(\mathbb{S}^2)$. Norm of the function in (2.14), which is induced by the inner product in (2.16), is a measure of the energy of the function, which is given by $\langle f, f \rangle_{\mathbb{S}^2}$. Finite energy functions are referred to as signals on the sphere.

2.2.1 Spherical harmonics

The Hilbert space $L^2(\mathbb{S}^2)$ is separable and contains a complete set of orthonormal basis functions, called spherical harmonic functions or spherical harmonics for short, defined as [64]

$$Y_\ell^m(\theta, \phi) \triangleq N_\ell^m P_\ell^m(\cos \theta) e^{im\phi}, \quad N_\ell^m = \sqrt{\frac{2\ell + 1}{4\pi} \frac{(\ell - m)!}{(\ell + m)!}}, \quad (2.17)$$

for integer degree $\ell \geq 0$ and integer order² $|m| \leq \ell$. $P_\ell^m(\cos \theta)$ is the associated Legendre polynomial of degree ℓ and order m , given by [64]

$$P_\ell^m(z) = \frac{(-1)^m}{2^\ell \ell!} (z^2 - 1)^{m/2} \frac{d^{\ell+m}}{dx^{\ell+m}} (z^2 - 1)^\ell, \quad z \triangleq \cos \theta, \quad 0 \leq m \leq \ell, \quad (2.18)$$

and N_ℓ^m is a normalization constant which ensures orthonormality of spherical harmonics, i.e.,

$$\langle Y_\ell^m, Y_p^q \rangle_{\mathbb{S}^2} = \int_{\mathbb{S}^2} Y_\ell^m(\hat{\mathbf{x}}) \overline{Y_p^q(\hat{\mathbf{x}})} ds(\hat{\mathbf{x}}) = \delta_{\ell,p} \delta_{m,q}, \quad (2.19)$$

where

$$\delta_{\ell,p} = \begin{cases} 1, & \ell = p, \\ 0, & \ell \neq p, \end{cases} \quad (2.20)$$

is the Kronecker delta function.

Associated Legendre polynomials for negative orders can be obtained from their

² $|m|$ denotes the absolute value (which is in fact the Euclidean norm) of the scalar m .

positive order counterparts as [64]

$$P_\ell^{-m}(z) = (-1)^m \frac{(\ell - m)!}{(\ell + m)!} P_\ell^m(z), \quad 0 \leq m \leq \ell, \quad (2.21)$$

from which we get the following conjugate symmetry property of spherical harmonics

$$Y_\ell^{-m}(\theta, \phi) = (-1)^m \overline{Y_\ell^m(\theta, \phi)}. \quad (2.22)$$

Table 2.1 tabulates associated Legendre polynomials and spherical harmonics for degrees $\ell = 0, 1, 2, 3$ and orders $|m| \leq \ell$.

As a result of completeness of spherical harmonics, any signal $f \in L^2(\mathbb{S}^2)$ can be expressed as

$$f(\hat{\mathbf{x}}) = \sum_{\ell, m} (f)_\ell^m Y_\ell^m(\hat{\mathbf{x}}), \quad \sum_{\ell, m} \equiv \sum_{\ell=0}^{\infty} \sum_{m=-\ell}^{\ell}, \quad (2.23)$$

where

$$(f)_\ell^m \triangleq \langle f, Y_\ell^m \rangle_{\mathbb{S}^2} = \int_{\mathbb{S}^2} f(\hat{\mathbf{x}}) \overline{Y_\ell^m(\hat{\mathbf{x}})} ds(\hat{\mathbf{x}}) \quad (2.24)$$

is the spherical harmonic, or spectral, coefficient of degree ℓ and order m . The transformation in (2.24) yields spectral content of the signal $f(\hat{\mathbf{x}})$ and hence, is called spherical harmonic transform (SHT). For real-valued signals, we have

$$\begin{aligned} f(\hat{\mathbf{x}}) &= \overline{f(\hat{\mathbf{x}})}, \\ \sum_{\ell, m} (f)_\ell^m Y_\ell^m(\hat{\mathbf{x}}) &= \sum_{\ell, m} \overline{(f)_\ell^m} \overline{Y_\ell^m(\hat{\mathbf{x}})}, \end{aligned} \quad (2.25)$$

which, using (2.22), results in the following symmetry for the spectral coefficients

$$(f)_\ell^m = (-1)^m \overline{(f)_\ell^{-m}}. \quad (2.26)$$

From orthonormality of spherical harmonics in (2.19) and the signal expansion in

Table 2.1: Associated Legendre polynomials and spherical harmonic functions for degrees $\ell = 0, 1, 2, 3$ and orders $|m| \leq \ell$.

Degree, ℓ	Order, m	$P_\ell^m(x)$	$Y_\ell^m(\theta, \phi)$
0	0	1	$\frac{1}{2}\sqrt{\frac{1}{\pi}}$
1	-1	$\frac{1}{2}(1-x^2)^{1/2}$	$\frac{1}{2}\sqrt{\frac{3}{2\pi}}e^{-i\phi}\sin\theta$
1	0	x	$\frac{1}{2}\sqrt{\frac{3}{\pi}}\cos\theta$
1	1	$-(1-x^2)^{1/2}$	$-\frac{1}{2}\sqrt{\frac{3}{2\pi}}e^{i\phi}\sin\theta$
2	-2	$\frac{1}{8}(1-x^2)$	$\frac{1}{4}\sqrt{\frac{15}{2\pi}}e^{-2i\phi}\sin^2\theta$
2	-1	$\frac{1}{2}x(1-x^2)^{1/2}$	$\frac{1}{2}\sqrt{\frac{15}{2\pi}}e^{-i\phi}\sin\theta\cos\theta$
2	0	$\frac{1}{2}(3x^2-1)$	$\frac{1}{4}\sqrt{\frac{5}{\pi}}(3\cos^2\theta-1)$
2	1	$-3x(1-x^2)^{1/2}$	$-\frac{1}{2}\sqrt{\frac{15}{2\pi}}e^{i\phi}\sin\theta\cos\theta$
2	2	$3(1-x^2)$	$\frac{1}{4}\sqrt{\frac{15}{2\pi}}e^{2i\phi}\sin^2\theta$
3	-3	$\frac{1}{48}(1-x^2)^{3/2}$	$\frac{1}{8}\sqrt{\frac{35}{\pi}}e^{-3i\phi}\sin^3\theta$
3	-2	$\frac{1}{8}x(1-x^2)$	$\frac{1}{4}\sqrt{\frac{105}{2\pi}}e^{-2i\phi}\sin^2\theta\cos\theta$
3	-1	$\frac{1}{8}(5x^2-1)(1-x^2)^{1/2}$	$\frac{1}{8}\sqrt{\frac{21}{\pi}}e^{-i\phi}\sin\theta(5\cos^2\theta-1)$
3	0	$\frac{1}{2}(5x^3-3x)$	$\frac{1}{4}\sqrt{\frac{7}{\pi}}(5\cos^3\theta-3\cos\theta)$
3	1	$-\frac{3}{2}(5x^2-1)(1-x^2)^{1/2}$	$-\frac{1}{8}\sqrt{\frac{21}{\pi}}e^{i\phi}\sin\theta(5\cos^2\theta-1)$
3	2	$15x(1-x^2)$	$\frac{1}{4}\sqrt{\frac{105}{2\pi}}e^{2i\phi}\sin^2\theta\cos\theta$
3	3	$-15(1-x^2)^{3/2}$	$-\frac{1}{8}\sqrt{\frac{35}{\pi}}e^{3i\phi}\sin^3\theta$

(2.23), we note that energy of the signal $f(\hat{\mathbf{x}})$ can be written as

$$\langle f, f \rangle_{\mathbb{S}^2} = \int_{\mathbb{S}^2} |f(\hat{\mathbf{x}})|^2 ds(\hat{\mathbf{x}}) = \sum_{\ell, m}^{\infty} |(f)_\ell^m|^2, \quad (2.27)$$

which is called the Parseval's relation for signals defined on the sphere.

2.2.2 Space of bandlimited signals on the sphere

A signal $f \in L^2(\mathbb{S}^2)$ is called bandlimited to degree L if $(f)_\ell^m = 0$ for $\ell \geq L, |m| \leq \ell$. Set of all such bandlimited signals on the sphere forms an L^2 dimensional subspace

of $L^2(\mathbb{S}^2)$, which is denoted by \mathcal{H}_L and defined as

$$\mathcal{H}_L \triangleq \{f \in L^2(\mathbb{S}^2) : (f)_\ell^m = 0, \forall \ell \geq L, |m| \leq \ell\}. \quad (2.28)$$

For a signal $f \in \mathcal{H}_L$, sum over degree in (2.23) is truncated at $L - 1$, i.e.,

$$f(\hat{\mathbf{x}}) = \sum_{\ell, m}^{L-1} (f)_\ell^m Y_\ell^m(\hat{\mathbf{x}}), \quad \sum_{\ell, m}^{L-1} \equiv \sum_{\ell=0}^{L-1} \sum_{m=-\ell}^{\ell}, \quad (2.29)$$

and the spectral coefficients $(f)_\ell^m$ can be represented by an $L^2 \times 1$ column vector as

$$\mathbf{f} = \left[(f)_{0,0}^0, (f)_{1,-1}^{-1}, (f)_{1,0}^0, (f)_{1,1}^1, \dots, (f)_{(L-1),-(L-1)}^{-(L-1)}, \dots, (f)_{(L-1), (L-1)}^{(L-1)} \right]^T, \quad (2.30)$$

which can be indexed by a single variable, defined as

$$n \triangleq \ell(\ell + 1) + m, \quad \ell = \lfloor \sqrt{n} \rfloor, m = n - \lfloor \sqrt{n} \rfloor (\lfloor \sqrt{n} \rfloor + 1), \quad (2.31)$$

where $\lfloor \cdot \rfloor$ is the integer floor function. Hence, $(f)_\ell^m \equiv (f)_n, n = 0, 1, \dots, L^2 - 1$. In practice, signals have vanishingly small spectral coefficients beyond a certain degree and hence, can be treated as bandlimited.

2.2.3 Space of azimuthally symmetric signals on the sphere

A signal $f \in L^2(\mathbb{S}^2)$ is called azimuthally symmetric or axisymmetric if $f(\theta, \phi) = f(\theta)$. Set of all such signals forms a subspace of $L^2(\mathbb{S}^2)$, denoted by \mathcal{H}_0 and defined as

$$\mathcal{H}_0 \triangleq \{f \in L^2(\mathbb{S}^2) : f(\theta, \phi) = f(\theta)\}. \quad (2.32)$$

It can be observed from (2.23) that for any signal $f \in \mathcal{H}_0$, $(f)_\ell^m = 0$ for $m \neq 0$. Hence,

$$f(\theta, \phi) = f(\theta) = \sum_{\ell=0}^{\infty} (f)_\ell^0 Y_\ell^0(\theta) = \sum_{\ell=0}^{\infty} \sqrt{\frac{2\ell + 1}{4\pi}} (f)_\ell^0 P_\ell(\cos \theta), \quad (2.33)$$

where $P_\ell(\cos \theta) \triangleq P_\ell^0(\cos \theta)$ is called the Legendre polynomial of integer degree ℓ , which is related to spherical harmonics through the following addition theorem [64]

$$\sum_{m=-\ell}^{\ell} Y_\ell^m(\hat{\mathbf{x}}) \overline{Y_\ell^m(\hat{\mathbf{y}})} = \left(\frac{2\ell + 1}{4\pi} \right) P_\ell(\hat{\mathbf{x}} \cdot \hat{\mathbf{y}}). \quad (2.34)$$

2.3 Signal analysis on the $\mathbb{SO}(3)$ rotation group

A group is an algebraic structure, denoted by (G, \circ) , i.e., it is a set of elements G , equipped with a binary operator, \circ , which satisfies the following axioms:

1. (Closure): $\forall x, y \in G, x \circ y \in G$,
2. (Associativity): $\forall x, y, z \in G, x \circ (y \circ z) = (x \circ y) \circ z$,
3. (Identity): $\forall x \in G$, there exists $I \in G$ such that $I \circ x = x \circ I = x$,
4. (Inverse): $\forall x \in G$, there exists $x^{-1} \in G$ such that $x \circ x^{-1} = x^{-1} \circ x = I$.

Defining ρ as the 3-tuple of Euler angles, i.e., $\rho \triangleq (\varphi, \vartheta, \omega)$, the special orthogonal rotation group, denoted by $\mathbb{SO}(3)$, is defined as the following set

$$\mathbb{SO}(3) \triangleq \{\mathbf{R}^{zyz}(\rho) : \det(\mathbf{R}^{zyz}(\rho)) = 1\}, \quad (2.35)$$

i.e., the set of all proper rotations³, which in turn are represented by orthogonal matrices having determinant +1.

Square-integrable and complex-valued functions defined on the $\mathbb{SO}(3)$ rotation group, i.e., $f(\rho)$, form a Hilbert space $L^2(\mathbb{SO}(3))$ which is equipped with the following inner product

$$\langle f, h \rangle_{\mathbb{SO}(3)} \triangleq \int_{\mathbb{SO}(3)} f(\rho) \overline{h(\rho)} d\rho, \quad f, h \in L^2(\mathbb{SO}(3)), \quad (2.36)$$

³Improper rotation are reflections about either some axis or the center of the coordinate system, and are represented by rotation matrices having determinant -1 .

where $d\rho \triangleq d\varphi \sin\vartheta d\vartheta d\omega$ is the invariant measure on the $\mathbb{SO}(3)$ rotation group and integration is carried out over all angles, i.e.

$$\int_{\mathbb{SO}(3)} \equiv \int_{\varphi=0}^{2\pi} \int_{\vartheta=0}^{\pi} \int_{\omega=0}^{2\pi} . \quad (2.37)$$

Inner product in (2.36) induces a norm of the function $f(\rho)$ as $\|f\|_{\mathbb{SO}(3)} \triangleq \sqrt{\langle f, f \rangle_{\mathbb{SO}(3)}}$, and gives its energy as $\langle f, f \rangle_{\mathbb{SO}(3)}$. Finite energy functions are referred to as signals on the $\mathbb{SO}(3)$ rotation group.

2.3.1 Wigner- D functions

The Hilbert space $L^2(\mathbb{SO}(3))$ is separable and has a complete set of orthogonal basis functions, called Wigner- D functions, which are denoted by $D_{m,m'}^\ell$ for integer degree $\ell \geq 0$ and integer orders $|m|, |m'| \leq \ell$, and are defined as [64]

$$D_{m,m'}^\ell(\rho) \triangleq e^{-im\varphi} d_{m,m'}^\ell(\vartheta) e^{-im'\omega}, \quad \rho \equiv (\varphi, \vartheta, \omega), \quad (2.38)$$

where $d_{m,m'}^\ell(\vartheta)$ are the Wigner- d functions of degree ℓ and orders m, m' . Wigner- d functions are real and obey the following orthogonality relation [64]

$$\int_0^\pi d_{m,m'}^\ell(\vartheta) d_{m,m'}^p(\vartheta) \sin\vartheta d\vartheta = \frac{2}{2\ell+1} \delta_{\ell,p}, \quad (2.39)$$

which results in the following orthogonality condition for Wigner- D functions

$$\int_{\varphi=0}^{2\pi} \int_{\vartheta=0}^{\pi} \int_{\omega=0}^{2\pi} D_{m,m'}^\ell(\varphi, \vartheta, \omega) \overline{D_{q,q'}^p(\varphi, \vartheta, \omega)} \sin\vartheta d\omega d\vartheta d\varphi = \frac{8\pi^2}{2\ell+1} \delta_{\ell,p} \delta_{m,q} \delta_{m',q'}. \quad (2.40)$$

As a result of completeness of Wigner- D functions, any signal $f \in L^2(\mathbb{SO}(3))$ can be expanded as

$$f(\rho) = \sum_{\ell,m,m'}^\infty (f)_{m,m'}^\ell D_{m,m'}^\ell(\rho), \quad \sum_{\ell,m,m'}^\infty \equiv \sum_{\ell=0}^\infty \sum_{m=-\ell}^\ell \sum_{m'=-\ell}^\ell, \quad (2.41)$$

where

$$(f)_{m,m'}^\ell \triangleq \left(\frac{2\ell + 1}{8\pi^2} \right) \langle f, D_{m,m'}^\ell \rangle_{\mathbb{SO}(3)} = \left(\frac{2\ell + 1}{8\pi^2} \right) \int_{\mathbb{SO}(3)} f(\rho) \overline{D_{m,m'}^\ell(\rho)} d\rho, \quad (2.42)$$

is the spectral coefficient of degree ℓ and orders m, m' , and constitutes the spectral domain representation of the signal $f(\rho)$.

From orthogonality of Wigner- D functions in (2.40) and the signal expansion in (2.41), we note that energy of the signal $f(\rho)$ is given by

$$\langle f, f \rangle_{\mathbb{SO}(3)} = \int_{\mathbb{SO}(3)} |f(\rho)|^2 d\rho = \sum_{\ell, m, m'}^{\infty} \left(\frac{8\pi^2}{2\ell + 1} \right) |(f)_{m,m'}^\ell|^2, \quad (2.43)$$

which is referred to as the Parseval's relation for signals defined on the $\mathbb{SO}(3)$ rotation group.

2.3.2 Space of bandlimited signals on $\mathbb{SO}(3)$ rotation group

A signal $f \in L^2(\mathbb{SO}(3))$ is considered bandlimited to degree L if $f_{m,m'}^\ell = 0, \forall \ell \geq L, |m|, |m'| \leq \ell$. For such signals, sum over degree in (2.41) is truncated at $L - 1$. Set of such bandlimited signals forms a subspace of the Hilbert space $L^2(\mathbb{SO}(3))$ whose dimension is given by $L(4L^2 - 1)/3$.

2.4 Rotation of signals on the sphere

Given the rotation matrix $\mathbf{R} \equiv \mathbf{R}^{zyz}(\rho)$ in (2.12), we associate with it the following rotation operator [64]

$$\mathcal{D}(\rho) \equiv \mathcal{D}(\varphi, \vartheta, \omega) = \mathcal{D}_z(\varphi) \circ \mathcal{D}_y(\vartheta) \circ \mathcal{D}_z(\omega), \quad (2.44)$$

where \mathcal{D}_y and \mathcal{D}_z are operators for rotation around y and z axes respectively. Action of the rotation operator $\mathcal{D}(\varphi, \vartheta, \omega)$ on a signal $f \in L^2(\mathbb{S}^2)$ is defined by the inverse

rotation of the underlying spherical coordinate system, i.e.,

$$(\mathcal{D}(\rho)f)(\hat{\mathbf{x}}) = f(\mathbf{R}^{-1}\hat{\mathbf{x}}). \quad (2.45)$$

Under the action of $\mathcal{D}(\rho)$, spectral coefficients of the rotated signal are given by [64]

$$\langle \mathcal{D}(\rho)f, Y_\ell^m \rangle_{\mathbb{S}^2} = \sum_{m'=-\ell}^{\ell} D_{m,m'}^\ell(\rho)(f)_\ell^{m'}, \quad (2.46)$$

which gives the following Fourier representation for the rotated signal

$$(\mathcal{D}(\rho)f)(\hat{\mathbf{x}}) = \sum_{\ell,m}^{\infty} \left(\sum_{m'=-\ell}^{\ell} D_{m,m'}^\ell(\rho)(f)_\ell^{m'} \right) Y_\ell^m(\hat{\mathbf{x}}). \quad (2.47)$$

Using orthonormality of spherical harmonics, the expression in (2.46) can be used to obtain a more intuitive definition of the rotation operator as

$$\left\langle \mathcal{D}(\rho)Y_\ell^{m'}, Y_\ell^m \right\rangle_{\mathbb{S}^2} = D_{m,m'}^\ell(\rho). \quad (2.48)$$

It can be observed from (2.46) that the rotation operator keeps the degrees intact but mixes the orders. From (2.38), we note that when $m' = 0$, the first rotation by ω around z -axis does not have any effect on Wigner- D function and hence, can be taken to be 0. The resulting Wigner- D function is related to spherical harmonics as [64]

$$D_{m,0}^\ell(\varphi, \vartheta, 0) = \sqrt{\frac{4\pi}{2\ell+1}} \overline{Y_\ell^m(\vartheta, \varphi)}, \quad (2.49)$$

which directly results in the following relation

$$d_{m,0}^\ell(\vartheta) = \sqrt{\frac{(\ell-m)!}{(\ell+m)!}} P_\ell^m(\cos \vartheta). \quad (2.50)$$

From the following rotation operator decomposition identity [64]

$$\mathcal{D}(\varphi, \vartheta, \omega) = \mathcal{D}\left(\varphi + \frac{\pi}{2}, \frac{\pi}{2}, \vartheta + \pi\right) \circ \mathcal{D}\left(0, \frac{\pi}{2}, \omega + \frac{\pi}{2}\right), \quad (2.51)$$

and the spectral representation of rotated signal in (2.46), we obtain the following useful expression for Wigner- d functions [64]

$$d_{m,m'}^\ell(\vartheta) = i^{m-m'} \sum_{m''=-\ell}^{\ell} \Delta_{m'',m}^\ell \Delta_{m'',m'}^\ell e^{-im''\vartheta}, \quad (2.52)$$

where $\Delta_{m'',m}^\ell \triangleq d_{m'',m}^\ell(\pi/2)$. Using the relation between spherical harmonics and Wigner- D functions in (2.49), along with the expansion for Wigner- d functions in (2.52) (with $m' = 0$), we can rewrite spherical harmonics as

$$Y_\ell^m(\theta, \phi) = \sqrt{\frac{2\ell+1}{4\pi}} (-i)^m \sum_{m'=-\ell}^{\ell} \Delta_{m',m}^\ell \Delta_{m',0}^\ell e^{im'\theta} e^{im\phi}. \quad (2.53)$$

Wigner- d functions $\Delta_{m,m'}^\ell$ can be computed using either the recursive relations given in [99] or the recursion proposed in [100], both of which are stable up to very large degrees.

2.5 Localized basis on the sphere

Spherical harmonic functions, defined in (2.17), are global basis functions, i.e., their energy is distributed over the whole sphere, due to which they are not suitable for analyzing signals over local regions $R \subset \mathbb{S}^2$. Since, real world spherical signals are bandlimited, it is desirable to find bandlimited basis functions for localized signal analysis on the sphere. Such a bandlimited basis set cannot be spatially limited to the region of analysis R [101], but can only be optimally concentrated within R , which nevertheless, provides a useful tool for accurate representation, estimation and reconstruction of signals within R . One such localized basis set is obtained by solving the Slepian spatial-spectral concentration problem, which was first studied by David Slepian and his co-authors in their seminal work on time domain signals [89, 90]. The problem was later extended to multidimensional Euclidean domain signals [91, 20], and for signals defined on the sphere [73, 36, 74, 75, 76, 77]. The problem studies temporal (or spatial) concentration of bandlimited signals (or equivalently spectral

concentration of spatially or temporally limited signals), by optimizing a quadratic energy concentration measure to obtain an orthogonal family of strictly bandlimited signals, called prolate spheroidal wavefunctions (referred to as Slepian functions in this work), which are optimally concentrated within a given time interval (or a spatial region). In the next section, we present a brief overview of the spatial concentration of bandlimited signals on the sphere.

2.5.1 Spatial concentration of bandlimited signals on the sphere

Defining local inner product between two functions $f, h \in L^2(\mathbb{S}^2)$ over a region R as

$$\langle f, h \rangle_R \triangleq \int_R f(\hat{\mathbf{x}}) \overline{h(\hat{\mathbf{x}})} ds(\hat{\mathbf{x}}), \quad R \subset \mathbb{S}^2, \quad (2.54)$$

which induces local norm of the signal f as

$$\|f\|_R = \sqrt{\langle f, f \rangle_R} = \sqrt{\int_R |f(\hat{\mathbf{x}})|^2 ds(\hat{\mathbf{x}})}, \quad (2.55)$$

the spatial energy concentration of a bandlimited signal $g \in \mathcal{H}_{L_g}$ in the region $R \subset \mathbb{S}^2$ can be maximized by optimizing the following measure of fractional energy

$$\lambda = \frac{\langle g, g \rangle_R}{\langle g, g \rangle_{\mathbb{S}^2}} = \frac{\int_R |g(\hat{\mathbf{x}})|^2 ds(\hat{\mathbf{x}})}{\int_{\mathbb{S}^2} |g(\hat{\mathbf{x}})|^2 ds(\hat{\mathbf{x}})}. \quad (2.56)$$

Using Fourier expansion of signals in (2.23), fractional energy can be rewritten as

$$\lambda = \frac{\int_R \sum_{p,q}^{L_g-1} (g)_p^q Y_p^q(\hat{\mathbf{x}}) \overline{\left(\sum_{\ell,m}^{L_g-1} (g)_\ell^m Y_\ell^m(\hat{\mathbf{x}}) \right)}}{\int_{\mathbb{S}^2} \sum_{p,q}^{L_g-1} (g)_p^q Y_p^q(\hat{\mathbf{x}}) \overline{\left(\sum_{\ell,m}^{L_g-1} (g)_\ell^m Y_\ell^m(\hat{\mathbf{x}}) \right)}} = \frac{\sum_{\ell,m}^{L_g-1} \sum_{p,q}^{L_g-1} \overline{(g)_\ell^m} (g)_p^q K_{\ell m, p q}}{\sum_{\ell,m}^{L_g-1} \overline{(g)_\ell^m} (g)_\ell^m}, \quad (2.57)$$

where

$$K_{\ell m, pq} \triangleq \int_R \overline{Y_\ell^m(\hat{\mathbf{x}})} Y_p^q(\hat{\mathbf{x}}) ds(\hat{\mathbf{x}}), \quad (2.58)$$

and we have used orthonormality of spherical harmonics on the sphere to get the final equality. Adopting the indexing introduced in (2.30), we define an $L_g^2 \times L_g^2$ matrix \mathbf{K} with elements $K_{\ell m, pq}$ for $0 \leq \ell, p \leq L_g - 1, |m| \leq \ell, |q| \leq p$, and an $L_g^2 \times 1$ column vector \mathbf{g} with elements $(g)_\ell^m$, to rewrite (2.57) in matrix form as

$$\lambda = \frac{\mathbf{g}^H \mathbf{K} \mathbf{g}}{\mathbf{g}^H \mathbf{g}}, \quad (2.59)$$

where $(\cdot)^H$ represents complex conjugate transpose. Column vectors \mathbf{g} which render λ in (2.59) stationary are solution to the following eigenvalue problem

$$\mathbf{K} \mathbf{g}_\alpha = \lambda_\alpha \mathbf{g}_\alpha, \quad 1 \leq \alpha \leq L_g^2. \quad (2.60)$$

From (2.58) and (2.57), it can be seen that the matrix \mathbf{K} is Hermitian and positive definite and hence, eigenvalues λ_α are real and eigenvectors \mathbf{g}_α are orthogonal⁴. Eigenvalues (and the associated eigenvectors) are indexed such that

$$1 > \lambda_1 \geq \lambda_2 \geq \dots \geq \lambda_{L_g^2} > 0, \quad (2.61)$$

i.e., eigenvector with highest energy concentration in region R is ranked first and eigenvector with lowest energy concentration in region R is ranked last.

For each spectral domain eigenvector \mathbf{g}_α , associated with the eigenvalue λ_α , a spatial eigenfunction $g_\alpha(\hat{\mathbf{x}})$ can be obtained from the Fourier expansion of signals in (2.23) as

$$g_\alpha(\hat{\mathbf{x}}) = \sum_{\ell, m}^{L_g-1} (g_\alpha)_\ell^m Y_\ell^m(\hat{\mathbf{x}}), \quad 1 \leq \alpha \leq L_g^2. \quad (2.62)$$

⁴We choose the eigenvectors \mathbf{g}_α to be orthonormal in this dissertation.

Set of spatial eigenfunctions, $g_\alpha(\hat{\mathbf{x}})$, $\alpha = 1, 2, \dots, L_g^2$, is orthogonal over the region R and orthonormal over the sphere \mathbb{S}^2 , i.e.,

$$\langle g_\alpha, g_\beta \rangle_R = \mathbf{g}_\alpha^H \mathbf{K} \mathbf{g}_\beta = \lambda_\alpha \delta_{\alpha,\beta}, \quad \langle g_\alpha, g_\beta \rangle_{\mathbb{S}^2} = \mathbf{g}_\alpha^H \mathbf{g}_\beta = \delta_{\alpha,\beta}. \quad (2.63)$$

These functions serve as an alternate basis for the space of bandlimited signals, i.e., \mathcal{H}_{L_g} , and are referred to as Slepian functions. Consequently, any signal $\tilde{g} \in \mathcal{H}_{L_g}$ can be represented as

$$\tilde{g}(\hat{\mathbf{x}}) = \sum_{\alpha=1}^{L_g^2} (\tilde{g})_\alpha g_\alpha(\hat{\mathbf{x}}), \quad (2.64)$$

where

$$(\tilde{g})_\alpha \triangleq \langle \tilde{g}, g_\alpha \rangle_{\mathbb{S}^2} = \int_{\mathbb{S}^2} \tilde{g}(\hat{\mathbf{x}}) \overline{g_\alpha(\hat{\mathbf{x}})} ds(\hat{\mathbf{x}}) = \mathbf{g}_\alpha^H \tilde{\mathbf{g}}, \quad 1 \leq \alpha \leq L_g^2 \quad (2.65)$$

are called the Slepian coefficients, which constitute the Slepian domain representation of the signal $\tilde{g}(\hat{\mathbf{x}})$.

As investigated in detail in [74], if most of the eigenvalues in (2.60) are either nearly 1 or nearly 0 (suggesting maximal and minimal concentration respectively for the corresponding eigenfunctions in the region R) with a sharp transition, then sum of the eigenvalues (rounded to the nearest integer), called the spherical Shannon number, is a good measure of the number of well-optimally concentrated Slepian functions within the region R . Denoted by N_R , spherical Shannon number is given by [74]

$$\begin{aligned} N_R &\triangleq \sum_{\alpha=1}^{L_g^2} \lambda_\alpha = \text{trace}(\mathbf{K}) \\ &= \sum_{\ell,m}^{L_g-1} K_{\ell m, \ell m} = \int_R \sum_{\ell=0}^{L_g-1} \sum_{m=-\ell}^{\ell} Y_p^\ell(\hat{\mathbf{x}}) \overline{Y_\ell^m(\hat{\mathbf{x}})} ds(\hat{\mathbf{x}}) \\ &= \sum_{\ell=0}^{L_g-1} \left(\frac{2\ell+1}{4\pi} \right) \int_R ds(\hat{\mathbf{x}}) = \frac{A_R}{4\pi} L_g^2, \end{aligned} \quad (2.66)$$

where $\text{trace}(\cdot)$ represents trace of a matrix, $A_R \triangleq \|1\|_R^2$ is the surface area of the spatial region R , defined in (2.8), and we have used the spherical harmonic addition theorem, given in (2.34), along with the fact that $P_\ell(1) \triangleq 1$. Hence, the set of first N_R well-optimally concentrated Slepian functions in (2.62) (rounded to the nearest integer) forms a (reduced) localized basis for the accurate reconstruction and representation of bandlimited signals in the spatial region R .

2.6 Convolution of signals on the sphere

A frequently carried out operation on signals defined on the sphere is filtering through spherical convolution. Unlike the Euclidean domain signals, there are multiple competing definitions of convolution for signals defined on the sphere [64]. These definitions primarily differ in the way rotations⁵ of the filter signal are defined on the sphere. In this section, we review different ways of convolving spherical signals, denoting the Euclidean domain convolution by $*$ and spherical convolution by \star . Spherical convolution will be called “isotropic” if the filter is an azimuthally symmetric signal.

2.6.1 Spherical convolution of type 1

For signals defined in the 2D Euclidean domain, convolution operation can be written as

$$(f * h)(\mathbf{x}) = \int_{\mathbb{R}^2} h(\mathbf{x} - \mathbf{y})f(\mathbf{o} + \mathbf{y})d\mathbf{y}, \quad \mathbf{x} \in \mathbb{R}^2, \quad (2.67)$$

where $f(\mathbf{x})$ is the signal of interest, $h(\mathbf{x})$ is the filter signal, \mathbf{o} represents the origin and \mathbf{y} represents the signal parameter in \mathbb{R}^2 . Euclidean convolution in (2.67) computes the output at point \mathbf{x} as the integral of the product of $h(-\mathbf{y})$, translated by \mathbf{x} units, and $f(\mathbf{y})$. Type 1 convolution on the sphere is defined in an analogous way by replacing

⁵Rotations can be thought of as spherical analogue of translations in the Euclidean domain.

translations with full rotations in the $\mathbb{SO}(3)$ rotation group as [64]

$$\begin{aligned} (f \star h)(\hat{\mathbf{x}}) &= \frac{1}{2\pi} \int_{\varphi=0}^{2\pi} \int_{\vartheta=0}^{\pi} \int_{\omega=0}^{2\pi} h(\mathbf{R}^{-1}\hat{\mathbf{x}}) f(\mathbf{R}\hat{\boldsymbol{\eta}}) d\omega \sin \vartheta d\vartheta d\varphi \\ &= \int_{\varphi=0}^{2\pi} \int_{\vartheta=0}^{\pi} (\mathcal{D}_z(\varphi) \circ \mathcal{D}_y(\vartheta) h_0)(\hat{\mathbf{x}}) f(\vartheta, \varphi) \sin \vartheta d\vartheta d\varphi, \end{aligned} \quad (2.68)$$

where $\boldsymbol{\eta} = [0, 0, 1]^T$ (which takes up the role of origin in \mathbb{R}^2) represents the north pole on the sphere, \mathbf{R} is the rotation matrix defined in (2.12), Euler angles $\omega, \vartheta, \varphi$ define rotations around the z, y, z axes respectively, and the second equality is obtained by observing that $\mathbf{R}\hat{\boldsymbol{\eta}} = \mathbf{R}^z(\varphi)\mathbf{R}^y(\vartheta)\mathbf{R}^z(\omega)[0, 0, 1]^T = (\vartheta, \varphi)$, and noting the following relation [64]

$$h_0(\hat{\mathbf{x}}) = \frac{1}{2\pi} \int_{\omega=0}^{2\pi} (\mathcal{D}_z(\omega)h)(\hat{\mathbf{x}}) d\omega = \sum_{\ell=0}^{\infty} (h)_{\ell}^0 Y_{\ell}^0(\hat{\mathbf{x}}). \quad (2.69)$$

From (2.68), it can be seen that spherical convolution of type 1 is isotropic and non-commutative, with the following spectral representation [64]

$$(f \star h)_{\ell}^m = \sqrt{\frac{4\pi}{2\ell+1}} (h)_{\ell}^0 (f)_{\ell}^m. \quad (2.70)$$

2.6.2 Spherical convolution of type 2

An equivalent way of defining spherical convolution of type 1 between the signal of interest $f(\hat{\mathbf{x}})$ and a filter signal $h(\hat{\mathbf{x}})$ is given by [102, 103]

$$(f \star h)(\hat{\mathbf{x}}) = \sqrt{\frac{1}{2\pi}} \int_{\mathbb{S}^2} h_0(\hat{\mathbf{x}} \cdot \hat{\boldsymbol{\gamma}}) f(\hat{\boldsymbol{\gamma}}) ds(\hat{\boldsymbol{\gamma}}), \quad (2.71)$$

where $\hat{\mathbf{x}} \cdot \hat{\boldsymbol{\gamma}}$ is the angular distance between points $\hat{\mathbf{x}}$ and $\hat{\boldsymbol{\gamma}}$, defined in (2.7), and $h_0(\cdot)$ is the azimuthally symmetric kernel whose response depends only on the angular distance between the two points and not their relative orientation. Since, spherical convolution of type 2 is equivalent to type 1, spectral coefficients of its output are given by (2.70) [64].

2.6.3 Spherical convolution of type 3

A more general definition of spherical convolution between the signal of interest $f(\hat{\mathbf{x}})$ and filter signal $h(\hat{\mathbf{x}})$ (not necessarily azimuthally symmetric) is given by [64]

$$(f \star h)(\rho) = \int_{\mathbb{S}^2} f(\hat{\mathbf{x}}) (\mathcal{D}(\rho)h)(\hat{\mathbf{x}}) ds(\hat{\mathbf{x}}), \quad (2.72)$$

where, unlike types 1 and 2, spherical convolution of type 3 maps spherical signals to the Hilbert space $L^2(\mathbb{S}\mathbb{O}(3))$. This convolution is anisotropic and non-commutative in general, with spectral representation given by [64]

$$(f \star h)_{m,m'}^\ell = (-1)^m (f)_\ell^{-m} (h)_\ell^{m'}. \quad (2.73)$$

Another closely related definition of spherical convolution is given by Wandelt *et al.* as [61]

$$(f \star h)(\rho) \triangleq \langle f, \mathcal{D}(\rho)h \rangle_{\mathbb{S}^2} = \int_{\mathbb{S}^2} f(\hat{\mathbf{x}}) \overline{(\mathcal{D}(\rho)h)(\hat{\mathbf{x}})} ds(\hat{\mathbf{x}}). \quad (2.74)$$

2.6.4 Commutative anisotropic spherical convolution

A commutative anisotropic spherical convolution, with output on the sphere, was formulated by Sadeghi *et al.* [62], which, for a signal $f(\hat{\mathbf{x}})$ and filter $h(\hat{\mathbf{x}})$ (not necessarily azimuthally symmetric), is defined as

$$(f \star h)(\vartheta, \varphi) = \int_{\mathbb{S}^2} (\mathcal{D}(\varphi, \vartheta, \pi - \varphi)h)(\hat{\mathbf{x}}) f(\hat{\mathbf{x}}) ds(\hat{\mathbf{x}}), \quad (2.75)$$

for which the spectral representation is given by [62]

$$(f \star h)_\ell^m = (-1)^m \sqrt{\pi(2\ell + 1)} \sum_{p,q}^{\infty} (f)_p^{-q} (h)_p^{q+m} \times \sum_{k,k'} (-1)^{k+k'} c_1(p, q, m, k) c_2(\ell, m, k') c_3(p, \ell, k, k'), \quad (2.76)$$

where $\max\{-p, -p-m\} \leq q \leq \min\{p, p-m\}$, $\max\{0, m\} \leq k \leq \min\{p-q, p+q+m\}$, $\max\{0, -m\} \leq k' \leq \min\{\ell, \ell-m\}$, $k+k' \leq p+\ell$ and

$$\begin{aligned} c_1(p, q, m, k) &\triangleq \frac{\sqrt{(p+q+m)!(p-q-m)!(p+q)!(p-q)!}}{(p+q+m-k)!(k)!(p-k-q)!(k-m)!}, \\ c_2(\ell, m, k') &\triangleq \frac{\sqrt{(\ell)!(\ell)!(\ell+m)!(\ell-m)!}}{(\ell-k')!(k')!(\ell-k'-m)!(k'+m)!}, \\ c_3(p, \ell, k, k') &\triangleq 2 \frac{(p+\ell-k-k')!(k+k')!}{(p+\ell+1)!}. \end{aligned} \quad (2.77)$$

2.6.5 Harmonic multiplication

Motivated by the idea of spectral representation of convolution between Euclidean domain signals, spherical convolution between two signals $f, h \in L^2(\mathbb{S}^2)$ can be defined as [87]

$$(f \star h)(\hat{\mathbf{x}}) \triangleq \sum_{\ell, m}^{\infty} (f)_{\ell}^m (h)_{\ell}^m Y_{\ell}^m(\hat{\mathbf{x}}), \quad (2.78)$$

which is commutative and, in general, anisotropic.

2.7 Convolution of signals on $\mathbb{SO}(3)$ rotation group

For two signals $f, h \in L^2(\mathbb{SO}(3))$, $\mathbb{SO}(3)$ convolution, denoted by \otimes , is given by [104, 105]

$$(f \otimes h)(\rho) = \int_{\mathbb{SO}(3)} f(\rho\rho_1^{-1}) h(\rho_1) d\rho_1, \quad (2.79)$$

where ρ, ρ_1 are the 3-tuple of Euler angles. From the spectral representation of signals in (2.42), we can write

$$\begin{aligned} (f \otimes h)_{m, m'}^{\ell} &= \left(\frac{2\ell+1}{8\pi^2} \right) \int_{\mathbb{SO}(3)} \left(\int_{\mathbb{SO}(3)} f(\rho\rho_1^{-1}) h(\rho_1) d\rho_1 \right) \overline{D_{m, m'}^{\ell}(\rho)} d\rho \\ &= \left(\frac{2\ell+1}{8\pi^2} \right) \int_{\mathbb{SO}(3)} \left(\int_{\mathbb{SO}(3)} f(\rho) \overline{D_{m, m'}^{\ell}(\rho\rho_1)} d\rho \right) h(\rho_1) d\rho_1, \end{aligned} \quad (2.80)$$

where we have used (2.79) and right invariance of the Haar measure $d\rho^6$, i.e.,

$$\int_{\mathbb{SO}(3)} f(\rho) d\rho = \int_{\mathbb{SO}(3)} f(\rho\rho_1) d\rho, \quad (2.81)$$

to obtain the second equality. Using (2.48), $D_{m,m'}^\ell(\rho\rho_1)$ can be expanded to get the addition formula for Wigner- D functions as

$$\begin{aligned} D_{m,m'}^\ell(\rho\rho_1) &= \left\langle \mathcal{D}(\rho\rho_1)Y_\ell^{m'}, Y_\ell^m \right\rangle_{\mathbb{S}^2} = \left\langle \mathcal{D}(\rho)\mathcal{D}(\rho_1)Y_\ell^{m'}, Y_\ell^m \right\rangle_{\mathbb{S}^2} \\ &= \left\langle \mathcal{D}(\rho_1)Y_\ell^{m'}, \mathcal{D}(\rho)^\dagger Y_\ell^m \right\rangle_{\mathbb{S}^2} \\ &= \sum_{p,q}^{\infty} \left\langle \mathcal{D}(\rho_1)Y_\ell^{m'}, Y_p^q \right\rangle_{\mathbb{S}^2} \overline{\left\langle \mathcal{D}(\rho)^\dagger Y_\ell^m, Y_p^q \right\rangle_{\mathbb{S}^2}} \\ &= \sum_{p,q}^{\infty} \left\langle \mathcal{D}(\rho_1)Y_\ell^{m'}, Y_p^q \right\rangle_{\mathbb{S}^2} \left\langle \mathcal{D}(\rho)Y_p^q, Y_\ell^m \right\rangle_{\mathbb{S}^2} \\ &= \sum_{p,q}^{\infty} \left(\sum_{q'=-p}^p D_{q,q'}^p(\rho_1) \left\langle Y_\ell^{m'}, Y_p^{q'} \right\rangle_{\mathbb{S}^2} \right) \left(\sum_{m'=-\ell}^{\ell} D_{m,m'}^\ell(\rho) \left\langle Y_p^q, Y_\ell^{m'} \right\rangle_{\mathbb{S}^2} \right) \\ &= \sum_{q=-\ell}^{\ell} D_{m,q}^\ell(\rho) D_{q,m'}^\ell(\rho_1), \end{aligned} \quad (2.82)$$

where $(\cdot)^\dagger$ denotes the adjoint of an operator, we have used the following definition of the adjoint \mathcal{B}^\dagger of an operator \mathcal{B} [64]

$$\langle \mathcal{B}f_1, f_2 \rangle = \langle f_1, \mathcal{B}^\dagger f_2 \rangle, \quad (2.83)$$

the following property of the inner product between two signals $f_1, f_2 \in L^2(\mathbb{S}^2)$ [64]

$$\langle f_1, f_2 \rangle_{\mathbb{S}^2} = \overline{\langle f_2, f_1 \rangle_{\mathbb{S}^2}}, \quad (2.84)$$

spectral representation of rotated signals in (2.46), and orthonormality of spherical harmonics on the sphere to get the final result, which can be used to obtain the

⁶Haar measure, which is also left invariant, is actually given by $\frac{1}{8\pi^2} d\rho = \frac{1}{8\pi^2} d\varphi \sin \vartheta d\vartheta d\omega$, but the invariance will hold for $d\rho$ as well. Here $8\pi^2$ is the normalization factor, i.e., $\int_{\mathbb{SO}(3)} \frac{1}{8\pi^2} d\rho = 1$.

spectral representation of $\mathbb{SO}(3)$ convolution as

$$\begin{aligned}
 (f \circledast h)_{m,m'}^\ell &= \sum_{q=-\ell}^{\ell} \left[\left(\frac{2\ell+1}{8\pi^2} \right) \int_{\mathbb{SO}(3)} f(\rho) \overline{D_{m,q}^\ell(\rho)} d\rho \right] \left[\int_{\mathbb{SO}(3)} h(\rho_1) \overline{D_{q,m'}^\ell(\rho_1)} d\rho_1 \right] \\
 &= \left(\frac{8\pi^2}{2\ell+1} \right) \sum_{q=-\ell}^{\ell} (f)_{m,q}^\ell (h)_{q,m'}^\ell.
 \end{aligned} \tag{2.85}$$

The output of $\mathbb{SO}(3)$ convolution can then be represented in terms of Wigner- D functions through (2.41) using (2.85).

2.8 Spatial-spectral analysis on the sphere

Spherical harmonic transform in (2.24) integrates the signal over the whole spherical domain to generate discrete frequency spectrum, in which each spherical harmonic coefficient reveals global contribution of the spherical harmonic basis functions in the signal. The concept is similar to the 1D Fourier transform for time domain signals, in which integration is carried out over all time to yield a frequency spectrum with no time localization (or information). However, a variant of the time domain Fourier transform, called the windowed Fourier transform or more commonly the short-time Fourier transform, performs frequency analysis for different segments of the time domain, resulting in the time-localized frequency content of the signal. Such a tool is specially useful when the time domain signal is non-stationary, i.e., its characteristics (e.g., the fundamental frequency) vary with time.

Motivated by the idea of short-time Fourier transform for time domain signals and driven by the need to carry out localized spectral analysis for non-stationary signals on the sphere, Khalid *et al.* proposed a windowed variant of the SHT in (2.24), called the spatially localized spherical harmonic transform (SLSHT) [88], which employs a window signal to spatially mask the signal of interest before computing its SHT, resulting in a distribution of localized spectra at every point $\hat{\mathbf{x}}(\theta, \phi)$ on the surface of the sphere. In this section, we review the mathematical details of the forward and inverse SLSHT.

2.8.1 SLSHT

For a signal $f \in \mathcal{H}_{L_f}$, directional SLSHT is defined as [98]

$$g_f(\rho; u) \triangleq \int_{\mathbb{S}^2} (\mathcal{D}(\rho)h)(\hat{\mathbf{x}}) f(\hat{\mathbf{x}}) \overline{Y_u(\hat{\mathbf{x}})} ds(\hat{\mathbf{x}}), \quad (2.86)$$

where $h \in L^2(\mathbb{S}^2)$ is a window signal, bandlimited to degree L_h , which is required to be spatially concentrated within a region on the sphere to provide spatial localization for the signal $f(\hat{\mathbf{x}})$, $\mathcal{D}(\rho)$ is the rotation operator, which rotates the window signal $h(\hat{\mathbf{x}})$ around z , y and z axes by Euler angles ω , ϑ and φ respectively, $u \triangleq v(v+1) + w$, $0 \leq v \leq L_g - 1$, $|w| \leq v$ is the spectral index, and $g_f(\rho; u)$ is called the directional SLSHT distribution of the signal $f(\hat{\mathbf{x}})$, bandlimited to degree L_g . The SLSHT distribution is called directional, for when the window signal $h(\hat{\mathbf{x}})$ (which is not azimuthally symmetric) is centered at the north pole, it is first oriented by the rotation operator by angle ω around z -axis before getting rotated to the point $\hat{\mathbf{y}}(\vartheta, \varphi)$ on the sphere. Hence, window signal $h(\hat{\mathbf{x}})$ masks the signal $f(\hat{\mathbf{x}})$ in various orientations at every point $\hat{\mathbf{y}}(\vartheta, \varphi)$ on the sphere to reveal its directional features in the form of directional SLSHT distribution, and is called directional window signal.

Using Fourier expansion of signals in (2.47) and (2.23), we can rewrite the directional SLSHT distribution as

$$\begin{aligned} g_f(\rho; u) &= \int_{\mathbb{S}^2} \sum_{p,q,q'}^{L_h-1} D_{q,q'}^p(\rho) (h)_p^{q'} Y_p^q(\hat{\mathbf{x}}) \sum_{n=0}^{L_f^2-1} (f)_n Y_n(\hat{\mathbf{x}}) \overline{Y_u(\hat{\mathbf{x}})} ds(\hat{\mathbf{x}}) \\ &= \sum_{n=0}^{L_f^2-1} (f)_n \psi_{u,n}(\rho), \end{aligned} \quad (2.87)$$

where n is the spectral index defined in (2.31),

$$\psi_{u,n}(\rho) = \sum_{p,q,q'}^{L_h-1} D_{q,q'}^p(\rho) (h)_p^{q'} T(n; p, q; u), \quad (2.88)$$

and $T(n; p, q; u) \equiv T(\ell, m; p, q; v, w)$ is the spherical harmonic triple product, defined

as [64]

$$T(n; p, q; u) \triangleq \int_{\mathbb{S}^2} Y_n(\hat{\mathbf{x}}) Y_p^q(\hat{\mathbf{x}}) \overline{Y_u(\hat{\mathbf{x}})} ds(\hat{\mathbf{x}}), \quad (2.89)$$

which is real-valued and non-zero for $0 \leq v \leq L_f + L_h - 2$. Hence, the directional SLSHT distribution is bandlimited to degree $L_g = L_f + L_h - 1$ in u . Moreover, as is apparent from (2.87) and (2.88), $g_f(\rho; u)$ is bandlimited to L_h in ρ .

Azimuthally symmetric window signal

For an azimuthally symmetric window signal, i.e., $h(\theta, \phi) = h(\theta)$, first rotation by ω around z -axis has no effect on $h(\theta)$ and can be set to 0. Therefore, $(\mathcal{D}(\varphi, \vartheta, 0)h)(\hat{\mathbf{x}})$ represents the rotationally symmetric window signal centered at the point $\hat{\mathbf{y}}(\vartheta, \varphi)$ on the sphere. The resulting SLSHT distribution of the signal $f(\hat{\mathbf{x}})$ becomes [88]

$$g_f(\hat{\mathbf{y}}; u) = \int_{\mathbb{S}^2} (\mathcal{D}(\hat{\mathbf{y}})h)(\hat{\mathbf{x}}) f(\hat{\mathbf{x}}) \overline{Y_u(\hat{\mathbf{x}})} ds(\hat{\mathbf{x}}). \quad (2.90)$$

From the representation of azimuthally symmetric signals in (2.33) and Fourier expansion of rotated signals in (2.47), we can write the rotated window signal as

$$(\mathcal{D}(\hat{\mathbf{y}})h)(\hat{\mathbf{x}}) = \sum_{p, q, q'}^{L_h-1} D_{q, q'}^p(\varphi, \vartheta, 0) (h)_p^{q'} \delta_{q', 0} Y_p^q(\hat{\mathbf{x}}) = \sum_{p, q}^{L_h-1} \sqrt{\frac{4\pi}{2p+1}} \overline{Y_p^q(\hat{\mathbf{y}})} (h)_p^0 Y_p^q(\hat{\mathbf{x}}), \quad (2.91)$$

where we have used the relation between Wigner- D functions and spherical harmonics in (2.49) to get the final result. Using Fourier expansion of signals in (2.23) along with the expression in (2.91), we can rewrite the SLSHT distribution as

$$\begin{aligned} g_f(\hat{\mathbf{y}}; u) &= \int_{\mathbb{S}^2} \sum_{p, q}^{L_h-1} \sqrt{\frac{4\pi}{2p+1}} \overline{Y_p^q(\hat{\mathbf{y}})} (h)_p^0 Y_p^q(\hat{\mathbf{x}}) \sum_{n=0}^{L_f^2-1} (f)_n Y_n(\hat{\mathbf{x}}) \overline{Y_u(\hat{\mathbf{x}})} ds(\hat{\mathbf{x}}) \\ &= \sum_{n=0}^{L_f^2-1} (f)_n \psi_{u, n}(\hat{\mathbf{y}}), \end{aligned} \quad (2.92)$$

where, unlike before, $\psi_{u,n} \in L^2(\mathbb{S}^2)$ and is given by

$$\psi_{u,n}(\hat{\mathbf{y}}) = \sum_{p,q}^{L_h-1} \sqrt{\frac{4\pi}{2p+1}} (h)_p^0 \overline{Y_p^q(\hat{\mathbf{y}})} T(n;p,q;u), \quad (2.93)$$

and $T(n;p,q;u)$ is the spherical harmonic triple product, defined in (2.89). The SLSHT distribution in (2.90) and (2.92) is non-directional, i.e., it uses rotationally symmetric window signal to spatially mask the signal $f(\hat{\mathbf{x}})$ and hence, cannot probe directional, i.e., rotationally asymmetric, features of the signal $f(\hat{\mathbf{x}})$.

2.8.2 SLSHT – Inverse transform

Spectral coefficients of the signal can be obtained from its directional spatially localized spherical harmonic transform, as has been shown in [98], by integrating the directional SLSHT distribution in (2.87) over all angles, i.e.,

$$\begin{aligned} \int_{\mathbb{S}\mathbb{O}(3)} g_f(\rho;u) d\rho &= \sum_{n=0}^{L_f^2-1} (f)_n \sum_{p,q,q'}^{L_h-1} (h)_p^{q'} T(n;p,q;u) \int_{\mathbb{S}\mathbb{O}(3)} D_{q,q'}^p(\rho) d\rho \\ &= \sum_{n=0}^{L_f^2-1} (f)_n \sum_{p,q,q'}^{L_h-1} (h)_p^{q'} T(n;p,q;u) (8\pi^2) \delta_{p,0} \delta_{q,0} \delta_{q',0} \\ &= (8\pi^2) \sum_{n=0}^{L_f^2-1} (f)_n (h)_0^0 \int_{\mathbb{S}^2} Y_n(\hat{\mathbf{x}}) Y_0^0(\hat{\mathbf{x}}) \overline{Y_u(\hat{\mathbf{x}})} ds(\hat{\mathbf{x}}) \\ &= \sqrt{16\pi^3} (f)_u (h)_0^0, \end{aligned} \quad (2.94)$$

where we have used orthogonality of complex exponential functions over $\varphi, \omega \in [0, 2\pi)$, i.e.,

$$\int_{\omega=0}^{2\pi} e^{-iq'\omega} d\omega = 2\pi \delta_{q',0}, \quad (2.95)$$

the relation in (2.50), along with the fact that

$$\int_{\vartheta=0}^{\pi} P_p(\cos \vartheta) \sin \vartheta d\vartheta = \int_{\cos \vartheta=-1}^1 P_p(\cos \vartheta) d(\cos \vartheta) = 2 \delta_{p,0}, \quad (2.96)$$

and orthonormality of spherical harmonics on the sphere to obtain the final result. Hence, spectral components of the signal $f(\hat{\mathbf{x}})$ can be recovered from its directional SLSHT distribution as

$$(f)_u = \frac{1}{\sqrt{16\pi^3}(h)_0^0} \int_{\mathbb{S}\mathbb{O}(3)} g_f(\rho; u) d\rho, \quad 0 \leq u \leq L_f^2 - 1. \quad (2.97)$$

In case of azimuthally symmetric window signal, the SLSHT distribution is integrated over the sphere, i.e., [88]

$$\begin{aligned} \int_{\mathbb{S}^2} g_f(\hat{\mathbf{y}}; u) ds(\hat{\mathbf{y}}) &= \sum_{n=0}^{L_f^2-1} (f)_n \sum_{p,q}^{L_h-1} \sqrt{\frac{4\pi}{2p+1}} (h)_p^0 T(n; p, q; u) \int_{\mathbb{S}^2} \overline{Y_p^q(\hat{\mathbf{y}})} ds(\hat{\mathbf{y}}) \\ &= \sum_{n=0}^{L_f^2-1} (f)_n \sum_{p,q}^{L_h-1} \sqrt{\frac{4\pi}{2p+1}} (h)_p^0 T(n; p, q; u) \sqrt{4\pi} \delta_{p,0} \delta_{q,0} \\ &= (4\pi) \sum_{n=0}^{L_f^2-1} (f)_n (h)_0^0 \int_{\mathbb{S}^2} Y_n(\hat{\mathbf{x}}) \sqrt{\frac{1}{4\pi}} Y_u(\hat{\mathbf{x}}) ds(\hat{\mathbf{x}}) = \sqrt{4\pi} (f)_u (h)_0^0, \end{aligned} \quad (2.98)$$

where again we have used (2.95) and (2.96), along with orthonormality of spherical harmonics, to obtain the final result, which can be used to invert the SLSHT distribution as follows

$$(f)_u = \frac{1}{\sqrt{4\pi}(h)_0^0} \int_{\mathbb{S}^2} g_f(\hat{\mathbf{y}}; u) ds(\hat{\mathbf{y}}), \quad 0 \leq u \leq L_f^2 - 1. \quad (2.99)$$

From (2.97) and (2.99), we observe that the SLSHT distribution can only be inverted when the first spectral coefficient of the window signal, i.e., $(h)_0^0$, is non-zero.

2.9 Multiscale representation for signals on the sphere

As stated earlier, spectral representation of spherical signals, obtained through spherical harmonic transform in (2.24), reveals global characteristics of the signal without

regards to the scale of those characteristics. More sophisticated signal representations are required to extract scale-dependent features from the signal. A tool that has been extensively used to represent time domain signals at different scales is the wavelet transform [93, 94, 95], which uses wavelet functions to probe scale-dependent features of the underlying signal.

The framework of wavelet transform has also been extensively investigated in the literature for signals defined on the sphere [78, 51, 79, 80, 82, 81, 83, 84, 85]. As discussed in Section 1.1.4, there are different formulations for wavelet analysis of spherical signals due to different methods of dilating spherical wavelet functions. In this section, we review the scale-discretized wavelet transform presented in [83, 85], which uses harmonic space dilation method.

2.9.1 Scale-discretized wavelet transform on the sphere

Scale-discretized wavelet transform of a signal $f \in L^2(\mathbb{S}^2)$ is defined by the convolution of the signal $f(\hat{\mathbf{x}})$ with the wavelet function, denoted by $\Psi^{(j)} \in L^2(\mathbb{S}^2)$, as

$$w_f^{\Psi^{(j)}}(\rho) \triangleq \langle f, \mathcal{D}(\rho)\Psi^{(j)} \rangle_{\mathbb{S}^2} = \int_{\mathbb{S}^2} f(\hat{\mathbf{x}}) \overline{(\mathcal{D}(\rho)\Psi^{(j)})(\hat{\mathbf{x}})} ds(\hat{\mathbf{x}}), \quad (2.100)$$

where $w_f^{\Psi^{(j)}} \in L^2(\mathbb{S}\mathbb{O}(3))$ is called the scale-discretized wavelet coefficient of the signal $f(\hat{\mathbf{x}})$, $j \in [0, j_2]$ is the discrete wavelet scale (j_2 is the largest wavelet scale) and (2.74) has been used to define convolution of spherical signals. Using the Fourier expansion of signals in (2.23), (2.47), along with orthonormality of spherical harmonics, we can write the scale-discretized wavelet coefficients as

$$\begin{aligned} w_f^{\Psi^{(j)}}(\rho) &= \sum_{\ell, m}^{\infty} (f)_{\ell}^m \sum_{p, q, q'}^{\infty} \overline{(\Psi^{(j)})_p^{q'}} \overline{D_{q, q'}^p(\rho)} \int_{\mathbb{S}^2} Y_{\ell}^m(\hat{\mathbf{x}}) \overline{Y_p^q(\hat{\mathbf{x}})} ds(\hat{\mathbf{x}}) \\ &= \sum_{\ell, m}^{\infty} (f)_{\ell}^m \sum_{m'=-\ell}^{\ell} \overline{(\Psi^{(j)})_{\ell}^{m'}} \overline{D_{m, m'}^{\ell}(\rho)}. \end{aligned} \quad (2.101)$$

Wavelet functions, centered at the north pole, are oriented by the rotation operator by an angle ω around z -axis and rotated to the point $\hat{\mathbf{y}}(\vartheta, \varphi)$ on the sphere before

projecting the signal $f(\hat{\mathbf{x}})$ onto them, hence, encoding scale-dependent directional features of the signal into wavelet coefficients. Since, wavelet functions are designed to have “band-pass” spectrum, wavelet coefficients cannot capture low frequency content of the signal $f(\hat{\mathbf{x}})$. Scaling coefficient, which is defined in terms of the axisymmetric scaling function, i.e., $\Phi \in \mathcal{H}_0$, is used to represent low frequency content of $f(\hat{\mathbf{x}})$ as

$$w_f^\Phi(\hat{\mathbf{y}}) \triangleq \langle f, \mathcal{D}(\hat{\mathbf{y}})\Phi \rangle_{\mathbb{S}^2} = \int_{\mathbb{S}^2} f(\hat{\mathbf{x}}) \overline{(\mathcal{D}(\hat{\mathbf{y}})\Phi)(\hat{\mathbf{x}})} ds(\hat{\mathbf{x}}), \quad \hat{\mathbf{y}} \equiv \hat{\mathbf{y}}(\vartheta, \varphi), \quad (2.102)$$

where $w_f^\Phi \in L^2(\mathbb{S}^2)$ denotes the scaling coefficient and we have used the fact that first rotation by ω around z -axis has no effect on $\Phi(\theta)$. Scaling function is designed to have a “low-pass” spectrum, which is the motivation behind its azimuthally symmetric profile. Using Fourier expansion of signals in (2.23), (2.47), along with the relation between Wigner- D functions and spherical harmonics in (2.49), we can rewrite the scaling coefficient as

$$\begin{aligned} w_f^\Phi(\hat{\mathbf{y}}) &= \sum_{\ell, m} (f)_\ell^m \sum_{p, q} (\Phi)_p^0 \sqrt{\frac{4\pi}{2p+1}} Y_p^q(\hat{\mathbf{y}}) \int_{\mathbb{S}^2} Y_\ell^m(\hat{\mathbf{x}}) \overline{Y_p^q(\hat{\mathbf{x}})} ds(\hat{\mathbf{x}}) \\ &= \sum_{\ell, m} \sqrt{\frac{4\pi}{2\ell+1}} (\Phi)_\ell^0 (f)_\ell^m Y_\ell^m(\hat{\mathbf{y}}), \end{aligned} \quad (2.103)$$

where we have used orthonormality of spherical harmonics to get the second equality.

Inverse transform

Scaling and wavelet coefficients encode complete information of the signal at different frequencies (scales) and hence, can be used to reconstruct the signal as

$$f(\hat{\mathbf{x}}) = \int_{\mathbb{S}^2} w_f^\Phi(\hat{\mathbf{y}}) (\mathcal{D}(\hat{\mathbf{y}})\Phi)(\hat{\mathbf{x}}) ds(\hat{\mathbf{y}}) + \sum_{j=0}^{j_2} \int_{\mathbb{SO}(3)} w_f^{\Psi^{(j)}}(\rho) (\mathcal{D}(\rho)\Psi^{(j)})(\hat{\mathbf{x}}) d\rho, \quad (2.104)$$

provided the following admissibility condition holds

$$\left[\left(\frac{4\pi}{2\ell+1} \right) |(\Phi)_\ell^0|^2 + \sum_{j=0}^{j_2} \left(\frac{8\pi^2}{2\ell+1} \right) \sum_{m'=-\ell}^{\ell} |(\Psi^{(j)})_\ell^{m'}|^2 \right] = 1, \quad \forall \ell. \quad (2.105)$$

The admissibility condition in (2.105) is obtained from (2.104) by solving the integrals as

$$\begin{aligned} \int_{\mathbb{S}^2} w_f^\Phi(\hat{\mathbf{y}})(\mathcal{D}(\hat{\mathbf{y}})\Phi)(\hat{\mathbf{x}})ds(\hat{\mathbf{x}}) &= \sum_{\ell,m} \sqrt{\frac{4\pi}{2\ell+1}} \overline{(\Phi)_\ell^0} (f)_\ell^m \sum_{p,q} \sqrt{\frac{4\pi}{2p+1}} (\Phi)_p^0 Y_p^q(\hat{\mathbf{x}}) \langle Y_\ell^m, Y_p^q \rangle_{\mathbb{S}^2} \\ &= \sum_{\ell,m} \left(\frac{4\pi}{2\ell+1} \right) |(\Phi)_\ell^0|^2 (f)_\ell^m Y_\ell^m(\hat{\mathbf{x}}), \end{aligned} \quad (2.106)$$

$$\begin{aligned} \int_{\mathbb{SO}(3)} w_f^{\Psi^{(j)}}(\rho)(\mathcal{D}(\rho)\Psi^{(j)})(\hat{\mathbf{x}})d\rho &= \sum_{\ell,m,m'} (f)_\ell^m \overline{(\Psi^{(j)})_\ell^{m'}} \sum_{p,q,q'} (\Psi^{(j)})_p^{q'} Y_p^q(\hat{\mathbf{x}}) \langle \overline{D_{m,m'}^\ell}, \overline{D_{q,q'}^p} \rangle_{\mathbb{SO}(3)} \\ &= \sum_{\ell,m,m'} \left(\frac{8\pi^2}{2\ell+1} \right) |(\Psi^{(j)})_\ell^{m'}|^2 (f)_\ell^m Y_\ell^m(\hat{\mathbf{x}}), \end{aligned} \quad (2.107)$$

and comparing the spectral representations of the left and right hand sides.

Axisymmetric wavelet functions

For axisymmetric wavelet functions $\Psi^{(j)} \in \mathcal{H}_0$, the scale-discretized wavelet coefficients are given by an expression similar to (2.102), i.e.,

$$\begin{aligned} w_f^{\Psi^{(j)}}(\hat{\mathbf{y}}) &\triangleq \langle f, \mathcal{D}(\hat{\mathbf{y}})\Psi^{(j)} \rangle_{\mathbb{S}^2} = \int_{\mathbb{S}^2} f(\hat{\mathbf{x}}) \overline{(\mathcal{D}(\hat{\mathbf{y}})\Psi^{(j)})(\hat{\mathbf{x}})} ds(\hat{\mathbf{x}}) \\ &= \sum_{\ell,m} \sqrt{\frac{4\pi}{2\ell+1}} (\Psi^{(j)})_\ell^0 (f)_\ell^m Y_\ell^m(\hat{\mathbf{y}}), \quad \hat{\mathbf{y}} \equiv \hat{\mathbf{y}}(\vartheta, \varphi), \end{aligned} \quad (2.108)$$

where the wavelet coefficients in this case are signals on the sphere, i.e., $w_f^{\Psi^{(j)}} \in L^2(\mathbb{S}^2)$. Signal $f(\hat{\mathbf{x}})$ is now reconstructed from its scaling and wavelet coefficients as

$$f(\hat{\mathbf{x}}) = \int_{\mathbb{S}^2} w_f^\Phi(\hat{\mathbf{y}})(\mathcal{D}(\hat{\mathbf{y}})\Phi)(\hat{\mathbf{x}})ds(\hat{\mathbf{y}}) + \sum_{j=0}^{j_2} \int_{\mathbb{S}^2} w_f^{\Psi^{(j)}}(\hat{\mathbf{y}})(\mathcal{D}(\hat{\mathbf{y}})\Psi^{(j)})(\hat{\mathbf{x}})ds(\hat{\mathbf{y}}), \quad (2.109)$$

if the following admissibility condition holds

$$\left(\frac{4\pi}{2\ell+1} \right) \left[|(\Phi)_\ell^0|^2 + \sum_{j=0}^{j_2} |(\Psi^{(j)})_\ell^0|^2 \right] = 1, \quad \forall \ell, \quad (2.110)$$

which can be readily obtained by employing (2.106) and the following similar expression for scale-discretized wavelet coefficients

$$\int_{\mathbb{S}^2} w_f^{\Psi^{(j)}}(\hat{\mathbf{y}}) (\mathcal{D}(\hat{\mathbf{y}})\Psi^{(j)})(\hat{\mathbf{x}}) ds(\hat{\mathbf{x}}) = \sum_{\ell, m}^{\infty} \left(\frac{4\pi}{2\ell+1} \right) \left| (\Psi^{(j)})_{\ell}^0 \right|^2 (f)_{\ell}^m Y_{\ell}^m(\hat{\mathbf{x}}), \quad (2.111)$$

to simplify the integrals in (2.109), and comparing the spectral representations of its left and right hand sides.

Construction of wavelet and scaling functions

Wavelet and scaling functions are designed to satisfy the admissibility conditions in (2.105) and (2.110), which results in the following spectral representations

$$\begin{aligned} (\Psi^{(j)})_{\ell}^m &= \sqrt{\frac{2\ell+1}{8\pi^2}} \Gamma_{\Psi}^{(j)}(\ell, \epsilon) (\xi)_{\ell}^m, \\ (\Psi^{(j)})_{\ell}^0 &= \sqrt{\frac{2\ell+1}{4\pi}} \Gamma_{\Psi}^{(j)}(\ell, \epsilon), \\ (\Phi)_{\ell}^0 &= \sqrt{\frac{2\ell+1}{4\pi}} \Gamma_{\Phi}(\ell, \epsilon), \end{aligned} \quad (2.112)$$

where $\sum_{m=-\ell}^{\ell} |(\xi)_{\ell}^m|^2 = 1$ for all values of ℓ for which $(\xi)_{\ell}^m$ is non-zero for at least one value of m . Here, $(\xi)_{\ell}^m \triangleq \langle \xi, Y_{\ell}^m \rangle_{\mathbb{S}^2}$, encodes the directional features of the wavelet functions and $\Gamma_{\Psi}^{(j)}(\ell, \epsilon)$, $\Gamma_{\Phi}(\ell, \epsilon)$ are the harmonic tiling functions, which satisfy

$$|\Gamma_{\Phi}(\ell, \epsilon)|^2 + \sum_{j=0}^{j_2} \left| \Gamma_{\Psi}^{(j)}(\ell, \epsilon) \right|^2 = 1, \quad \forall \ell, \quad (2.113)$$

and control the angular localization of the wavelet and scaling functions. $\epsilon > 1$ is the harmonic space dilation parameter, which defines dilation of the wavelet functions. It is straightforward to show that using the harmonic tiling functions constraint in (2.113), spectral coefficients of the wavelet and scaling functions in (2.112) satisfy the admissibility conditions in (2.105) and (2.110).

Harmonic tiling functions are defined as zero-order, square-integrable and positive continuous functions over the domain of non-negative real numbers, which are

constructed using the following infinitely differentiable Schwartz function⁷

$$h_\epsilon(x) \triangleq h\left(\frac{2\epsilon}{\epsilon-1}\left(x - \frac{1}{\epsilon}\right) - 1\right), \quad (2.114)$$

where

$$h(x) \triangleq \begin{cases} e^{-\frac{1}{1-x^2}}, & -1 \leq x \leq 1, \\ 0, & \text{otherwise.} \end{cases} \quad (2.115)$$

From (2.115), we note that $h_\epsilon(x)$ has compact support over the closed interval $x \in [\epsilon^{-1}, 1]$. Now considering the smoothly decreasing function, defined as

$$g_\epsilon(x) \triangleq \frac{\int_x^1 h_\epsilon^2(y) \frac{1}{y} dy}{\int_{\epsilon^{-1}}^1 h_\epsilon^2(y) \frac{1}{y} dy} = \begin{cases} 1, & x \leq \epsilon^{-1}, \\ 1 \rightarrow 0, & \epsilon^{-1} < x \leq 1, \\ 0, & x > 1, \end{cases} \quad (2.116)$$

the harmonic tiling functions are given by

$$\Gamma_\Psi^{(j)}(\ell, \epsilon) \triangleq \sqrt{g_\epsilon\left(\epsilon^{j-1} \frac{\ell}{L}\right) - g_\epsilon\left(\epsilon^j \frac{\ell}{L}\right)}. \quad (2.117)$$

From (2.116), we note that $g_\epsilon(\epsilon^{j-1} \ell L^{-1})$ has compact support over the interval $\ell \leq \epsilon^{1-j} L$ (with it being 1 for $\ell \leq \epsilon^{-j} L$) whereas $g_\epsilon(\epsilon^j \ell L^{-1})$ has compact support over the interval $\ell \leq \epsilon^{-j} L$ (with it being 1 for $\ell \leq \epsilon^{-j-1} L$). Hence, $\Gamma_\Psi^{(j)}(\ell)$ has compact support over the closed interval given by

$$\ell \in [\ell_{\min}(j) = \lfloor \epsilon^{-1-j} L \rfloor, \ell_{\max}(j) = \lceil \epsilon^{1-j} L \rceil], \quad (2.118)$$

where $\lceil \cdot \rceil$ is the integer ceiling function (integer floor and ceiling functions are used

⁷An infinitely differentiable function defined over n dimensional Euclidean domain \mathbb{R}^n , i.e., $f \in C^\infty(\mathbb{R}^n)$, is called a Schwartz function if the function and all its derivatives go to zero, as $|x| \rightarrow \infty$, faster than any inverse power of x , where $x \in \mathbb{R}^n$. [Source: <https://mathworld.wolfram.com/SchwartzFunction.html>]

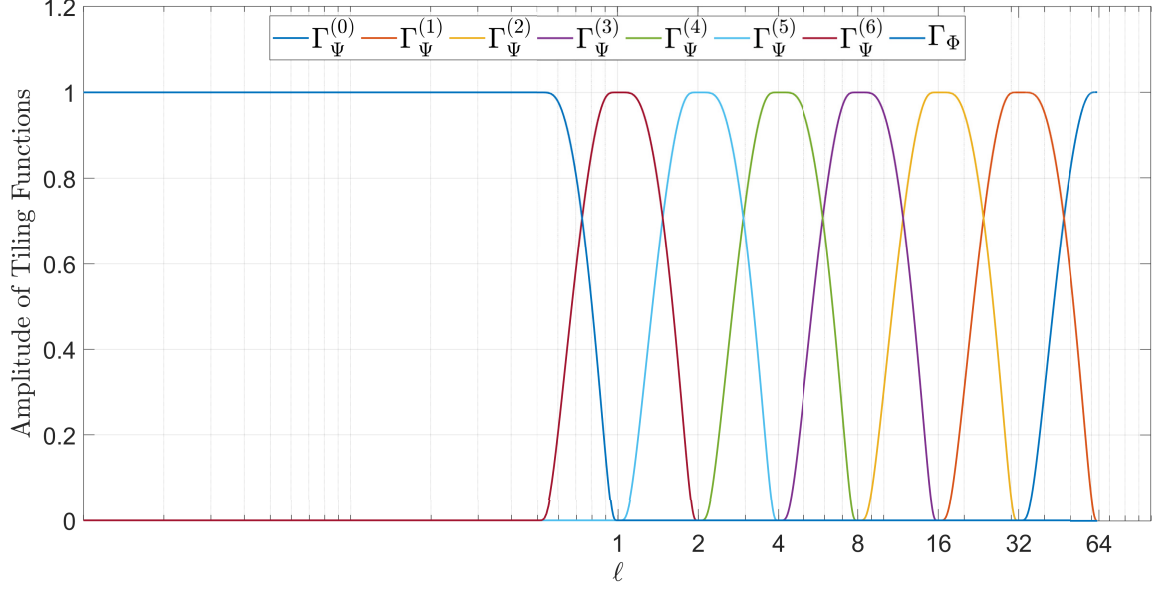


Figure 2-4: Tiling of the spherical harmonic degree space using $\Gamma_{\Psi}^{(j)}(\ell)$ and $\Gamma_{\Phi}(\ell)$ for bandlimit $L = 64$, $\epsilon = 2$ and $j_2 = J = 6$.

to end the support at integer values of ℓ), and it peaks at $\ell = \epsilon^{-j}L$.

From (2.118), we see that both ℓ_{\min} and ℓ_{\max} increase by decreasing the wavelet scale j . Hence, small scale wavelet functions probe higher frequency and large scale wavelet functions probe lower frequency content of the signal under consideration. The maximum wavelet scale, denoted by J , is defined as

$$\begin{aligned} \epsilon^{-J}L &\leq 1, \\ J &\geq \log_{\epsilon} L \Rightarrow J \triangleq \lceil \log_{\epsilon} L \rceil. \end{aligned} \quad (2.119)$$

For scales above J , we observe that

$$\begin{aligned} \ell_{\min}(J+k) &= \lfloor \epsilon^{-1-J-k}L \rfloor = \left\lfloor \epsilon^{-1-k} \frac{L}{\epsilon^J} \right\rfloor = 0, \\ \ell_{\max}(J+k) &= \lceil \epsilon^{1-J-k}L \rceil = \left\lceil \epsilon^{1-k} \frac{L}{\epsilon^J} \right\rceil = 1, \end{aligned} \quad 1 \leq k < \infty, \quad (2.120)$$

because $L/\epsilon^J \leq 1$, $\epsilon^{-1-k} < 1$ and $\epsilon^{1-k} \leq 1$. Hence, wavelet functions at scales $j = J+k$, $1 \leq k < \infty$ have compact support in the open interval $\ell \in (0, 1)$ (without considering integer flooring and ceiling) and are discarded, because they probe the

region of the spectrum that has no signal content.

Increasing the wavelet scale decreases ℓ_{\min} but in order to make $\ell_{\min} = 0$, an infinite wavelet scale is required. As a result, wavelet functions alone cannot cover the entire spherical harmonic degree space. Hence, for largest wavelet scale $0 \leq j_2 \leq J$, $\Gamma_{\Phi}(\ell)$ is defined to have compact support in the interval $\ell \in [0, \epsilon^{-j_2} L]$, i.e.,

$$\Gamma_{\Phi}(\ell) \triangleq \sqrt{g_{\epsilon} \left(\epsilon^{j_2} \frac{\ell}{L} \right)}. \quad (2.121)$$

Figure 2-4 shows tiling of the spherical harmonic degree space using harmonic tiling functions in (2.117) and (2.121) for bandlimit $L = 64$, dilation parameter $\epsilon = 2$ and largest wavelet scale set to $J = 6$. The band-pass and low-pass nature of the wavelet and scaling tiling functions can be clearly observed, which asserts the claim, made earlier, about the band-pass and low-pass nature of the spectra of wavelet and scaling functions respectively.

Design of the directionality component of the wavelet functions in (2.112), i.e., $(\xi)_{\ell}^m$, is a bit more involved and we refer the reader to the work in [83, 85] for details.

Chapter 3

Joint domain optimal filtering on the sphere

In almost all of the research areas that support signal processing, the acquired signal, called observation, is influenced by the unwanted, yet unavoidable noise due to the presence of different sources of interference, which places signal filtering and estimation from its noise-contaminated samples at the heart of signal processing techniques, resulting in abundant literature on signal estimation [66, 67, 96, 70, 71, 69, 72]. These methods assume particular settings for the signal estimation problem. For instance, the filters proposed in [66, 67, 71, 69] process signals in either spatial or spectral domain, assuming noise to be a realization of an isotropic process on the sphere¹, while the filters proposed in [70, 72] estimate signals in the presence of anisotropic noise².

Since, anisotropic processes are spherical non-stationary random processes, it is desirable to construct filters which adapt according to the statistics of noise. Using the filtering framework presented in [106], and connecting with the idea of joint time-frequency filtering of non-stationary processes in [86], a joint spatial-spectral domain filter has been designed in [87] for the estimation of signals that have been contaminated by zero-mean and anisotropic noise. The resulting filter estimates the underlying (noise-free) source signal by filtering the joint spatial-spectral domain rep-

¹Isotropic processes are counterparts of wide-sense stationary processes in the Euclidean domain.

²Anisotropic processes are spherical analogues of non-stationary processes in the Euclidean domain.

resentation of signals, which is given by the non-directional SLSHT [88]. However, as noted in Section 2.8, non-directional SLSHT employs azimuthally symmetric window signal, due to which filtering in the joint spatial-spectral domain is unable to effectively recover the directional features of the source signal.

Signal filtering and estimation, in the Euclidean domain, has also been carried out using the joint space-scale domain representation (e.g. [107, 108]), which is enabled by the wavelet transform [93, 94, 95]. Signal estimation using wavelet transform is based on the observation that noise has a distributed representation in the wavelet domain, whereas signals of interest are typically sparsely represented, which can be exploited using different thresholding methods [109, 84]. Multiscale signal estimation in the Euclidean domain has also been carried out using noise statistics through Wiener filtering [107].

In this chapter, we formulate different frameworks for filtering and estimation of spherical signals, which are assumed to be contaminated by realizations of zero-mean and anisotropic noise processes. In particular, to recover directional features in the underlying signal, we design a filter in the joint $\mathbb{SO}(3)$ -spectral domain, which is enabled by the directional SLSHT, and present a least square solution for the estimation of the underlying noise-free signal from the filtered representation. The resulting filter is optimal in the sense that the filtered representation is the minimum mean-square error estimate of the directional SLSHT distribution of the underlying noise-free signal. Since, the directional SLSHT distribution depends on the directional window signal, we also present an optimal window design to further improve the performance of the joint $\mathbb{SO}(3)$ -spectral domain filtering framework. Furthermore, we design an optimal azimuthally symmetric window signal to improve the performance of the joint spatial-spectral domain filter in [87].

We also design a filter in the joint space-scale domain using the scale-discretized wavelet transform on the sphere and show it to be optimal in the sense of mean-square error criterion. The resulting filter is shown to perform better compared to the hard thresholding method for signal denoising in the wavelet domain, and the weighted spherical harmonics (weighted-SPHARM) signal estimation framework [110].

3.1 Joint domain filtering – Problem formulation

We consider a noise-free source signal, denoted by $s \in L^2(\mathbb{S}^2)$, as a realization of an anisotropic random process on the sphere, which is contaminated by a realization of a zero-mean and anisotropic random noise process, $z \in L^2(\mathbb{S}^2)$, to give

$$f(\hat{\mathbf{x}}) = s(\hat{\mathbf{x}}) + z(\hat{\mathbf{x}}) \in L^2(\mathbb{S}^2) \quad (3.1)$$

as the noise-contaminated observation on the sphere. The objective is to determine an estimate of the source signal, denoted by $\tilde{s}(\hat{\mathbf{x}})$, which is optimal in the mean-square sense. We assume that noise is uncorrelated with the source signal, i.e.,

$$\begin{aligned} \mathbb{E} \left\{ s(\hat{\mathbf{x}}) \overline{z(\hat{\mathbf{x}})} \right\} &= \sum_{\ell, m}^{\infty} \sum_{p, q}^{\infty} \mathbb{E} \left\{ (s)_{\ell}^m \overline{(z)_p^q} \right\} Y_{\ell}^m(\hat{\mathbf{x}}) \overline{Y_p^q(\hat{\mathbf{x}})} = 0, \\ \Rightarrow \mathbb{E} \left\{ (s)_{\ell}^m \overline{(z)_p^q} \right\} &= 0, \quad \forall \ell, p, |m| \leq \ell, |q| \leq p, \end{aligned} \quad (3.2)$$

where $(s)_{\ell}^m$ and $(z)_p^q$ are the spectral representations of the source and noise signals and $\mathbb{E}\{\cdot\}$ denotes the expectation operator. We refer to this assumption by simply stating “uncorrelated noise” in the rest of this work.

Spectral covariance of a signal $d \in L^2(\mathbb{S}^2)$ is defined as

$$C_{\ell m, p q}^d = \mathbb{E} \left\{ (d)_{\ell}^m \overline{(d)_p^q} \right\}, \quad \forall \ell, p, |m| \leq \ell, |q| \leq p. \quad (3.3)$$

Hence, $C_{\ell m, p q}^s, C_{\ell m, p q}^z$ represent the elements of the spectral covariance matrices \mathbf{C}^s and \mathbf{C}^z for the source and noise signals respectively.

Performance of the filtering framework is gauged by the signal to noise ratio, which for a signal $d \in L^2(\mathbb{S}^2)$ is defined as

$$\text{SNR}^d \triangleq 10 \log \frac{\|s(\hat{\mathbf{x}})\|_{\mathbb{S}^2}^2}{\|d(\hat{\mathbf{x}}) - s(\hat{\mathbf{x}})\|_{\mathbb{S}^2}^2}. \quad (3.4)$$

Hence, the input and output SNR is given by SNR^f and SNR^s respectively.

3.1.1 Real bandlimited Gaussian noise

Assuming the noise signal $z(\hat{\mathbf{x}})$ to be bandlimited to degree L , we can represent its spectral coefficients $(z)_p^q$ by a column vector \mathbf{z} , of size $L^2 \times 1$, which can be indexed using the scheme introduced in (2.30). Spectral coefficients of the noise signal are then constructed to have Gaussian probability distribution as

$$\mathbf{z} = \mathbf{A} \mathbf{c} + \boldsymbol{\mu}, \quad (3.5)$$

where the vector \mathbf{c} contains elements $(c)_p^q$ which are drawn from the standard normal distribution, i.e., $(c)_p^q \sim \mathcal{N}(0, 1)$, $0 \leq p \leq L-1$, $|q| \leq p$, and $\boldsymbol{\mu}$ is the statistical mean of the noise vector, i.e.,

$$\mathbb{E} \{\mathbf{z}\} = \mathbf{A} \mathbb{E} \{\mathbf{c}\} + \boldsymbol{\mu} = \boldsymbol{\mu}. \quad (3.6)$$

For zero-mean noise signal, $\boldsymbol{\mu} = 0$ and hence, $\mathbf{z} = \mathbf{A} \mathbf{c}$. Matrix \mathbf{A} defines spectral covariance of the Gaussian noise process, i.e.,

$$\mathbb{E} \{\mathbf{z} \mathbf{z}^H\} = \mathbf{A} \mathbb{E} \{\mathbf{c} \mathbf{c}^H\} \mathbf{A}^H = \mathbf{A} \mathbf{I} \mathbf{A}^H = \mathbf{A} \mathbf{A}^H = \mathbf{C}^z, \quad (3.7)$$

where elements of matrix \mathbf{C}^z are given by (3.3) and \mathbf{I} denotes the identity matrix.

For the zero-mean noise signal $z(\hat{\mathbf{x}})$ to be real-valued, we observe from (2.26) that

$$\begin{aligned} (z)_p^q &= (-1)^q \overline{(z)_{p-q}^{-q}}, \\ \sum_{p', q'}^{L-1} A_{pq, p'q'} (c)_{p'}^{q'} &= (-1)^q \sum_{p', q'}^{L-1} \overline{A_{p(-q), p'q'}} \overline{(c)_{p'}^{q'}}, \end{aligned} \quad (3.8)$$

where we have used (3.5), with $\boldsymbol{\mu} = 0$, to get the last expression. As a result, we get the following constraint on the matrix \mathbf{A} and vector \mathbf{c}

$$\begin{aligned} A_{pq, p'q'} &= (-1)^q \overline{A_{p(-q), p'q'}}, & \mathbf{A} \text{ non-diagonal}, \\ (c)_{p'}^{q'} &= \overline{(c)_{p'}^{q'}}, \end{aligned} \quad (3.9)$$

$$\begin{aligned}
 A_{pq,pq} &= (-1)^q \overline{A_{p(-q),p(-q)}}, & \mathbf{A} \text{ diagonal.} \\
 (c)_p^q &= \overline{(c)_p^{-q}},
 \end{aligned} \tag{3.10}$$

Anisotropic noise

To generate real-valued, bandlimited, zero-mean and anisotropic Gaussian noise, we construct the matrix \mathbf{A} in such a way that its elements are complex, with real and imaginary parts uniformly distributed in the interval $(-1, 1)$, and obey the constraint in (3.9). Energy of the noise process is given by trace of the matrix \mathbf{C}^z , which is set by source signal energy and the specified SNR, i.e, matrix \mathbf{A} is normalized as

$$\mathbf{A}_N = \frac{\mathbf{A}}{\sqrt{\text{trace}(\mathbf{A} \mathbf{A}^H)}} \sqrt{\langle z, z \rangle_{\mathbb{S}^2}}, \quad \langle z, z \rangle_{\mathbb{S}^2} = 10^{-\frac{\text{SNR}}{10}} \langle s, s \rangle_{\mathbb{S}^2}, \tag{3.11}$$

so that

$$\text{trace}(\mathbf{C}_N^z) = \text{trace}(\mathbf{A}_N \mathbf{A}_N^H) = \frac{\text{trace}(\mathbf{A} \mathbf{A}^H)}{\text{trace}(\mathbf{A} \mathbf{A}^H)} \langle z, z \rangle_{\mathbb{S}^2} = \langle z, z \rangle_{\mathbb{S}^2}. \tag{3.12}$$

Furthermore, vector \mathbf{c} is taken to be real-valued. Hence, to summarize, the noise realization $z(\hat{\mathbf{x}})$, constructed from (3.5) using

- the matrix \mathbf{A}_N given in (3.11), where elements of matrix \mathbf{A} are uniformly distributed in the interval $(-1, 1)$ in both real and imaginary parts and obey (3.9),
- the real-valued vector \mathbf{c} with elements $(c)_p^q \sim \mathcal{N}(0, 1), 0 \leq p \leq L - 1, |q| \leq p$,
- $\boldsymbol{\mu} = 0$,

is real-valued, zero-mean, anisotropic and Gaussian, with energy given by the source signal and specified SNR.

3.1.2 Real bandlimited white Gaussian noise

For white noise, spectral covariance matrix is diagonal and is given by

$$\mathbf{C}^z = \sigma^2 \mathbf{I}, \tag{3.13}$$

where σ^2 is the white noise parameter which specifies energy of the white noise process, normalized by L^2 , and is set by energy of the source signal and the specified SNR, i.e.,

$$\sigma^2 = \frac{1}{L^2} \langle z, z \rangle_{\mathbb{S}^2} = \frac{1}{L^2} 10^{-\frac{\text{SNR}}{10}} \langle s, s \rangle_{\mathbb{S}^2}, \quad (3.14)$$

such that $\text{trace}(\mathbf{C}^z) = \langle z, z \rangle_{\mathbb{S}^2}$. Spectral coefficients of the real-valued, bandlimited, zero-mean and white Gaussian noise $(z)_p^q$ are constructed as

$$(z)_p^q = \begin{cases} \frac{\sigma}{\sqrt{2}} \left((c_1)_p^q + i(c_2)_p^q \right), & 1 \leq q \leq p, \\ \sigma(c_1)_p^q, & q = 0, \end{cases} \quad (3.15)$$

$$(z)_p^{-q} = (-1)^q \overline{(z)_p^q}, \quad 1 \leq q \leq p,$$

where $(c_1)_p^q, (c_2)_p^q$ are drawn from the standard normal distribution, i.e., $(c_1)_p^q, (c_2)_p^q \sim \mathcal{N}(0, 1)$, $0 \leq p \leq L - 1, |q| \leq p$.

3.2 Window design for joint spatial-spectral domain filter

As discussed before, in the case of contamination from realizations of spherical non-stationary, i.e., anisotropic, noise processes, it is desirable to perform spatially varying filtering of noise-contaminated signals. The SLSHT distribution, defined in (2.90), represents spatially varying spectral content of the signal and hence, presents an opportunity to construct filters for signal estimation in the joint spatial-spectral domain. Such a framework for joint spatial-spectral domain filtering has been proposed by Khalid *et al.* in [87]. In this section, we present the design of an azimuthally symmetric optimal window signal to improve the performance of the joint spatial-spectral domain filtering and signal estimation framework in [87]. Before presenting the optimal window design, we briefly review the joint spatial-spectral domain filtering framework.

3.2.1 Joint spatial-spectral domain filter

Denoting the bandlimit of the axisymmetric window signal $h(\theta)$ and noise-contaminated observation $f(\hat{\mathbf{x}})$ as L_h and L_f respectively, the SLSHT distribution, given in (2.92), for the noise-contaminated observation $f(\hat{\mathbf{x}})$ is repeated here for convenience

$$g_f(\hat{\mathbf{x}}; u) = \sum_{n=0}^{L_f^2-1} (f)_n \psi_{u,n}(\hat{\mathbf{x}}), \quad \psi_{u,n}(\hat{\mathbf{x}}) = \sum_{p',q'}^{L_h-1} \sqrt{\frac{4\pi}{2p'+1}} (h)_{p'}^0 \overline{Y_{p',q'}^{q'}(\hat{\mathbf{x}})} T(n; p', q'; u), \quad (3.16)$$

where $n = \ell(\ell + 1) + m, 0 \leq \ell \leq L_f - 1, |m| \leq \ell, u = v(v + 1) + w, 0 \leq v \leq L_g - 1, |w| \leq v$ are the spectral indices, $L_g = L_f + L_h - 1$ is the bandlimit of SLSHT distribution in u , and $T(n; p', q'; u)$ is the spherical harmonic triple product given in (2.89). Spectral representation of $g_f(\hat{\mathbf{x}}; u)$ is given by the inner product between $g_f(\hat{\mathbf{x}}; u)$ (at a particular u) and spherical harmonics, i.e.,

$$\begin{aligned} (g_f(\cdot; u))_p^q &\triangleq \langle g_f(\cdot; u), Y_p^q \rangle_{\mathbb{S}^2} \\ &= \sum_{n=0}^{L_f^2-1} (f)_n \sum_{p',q'}^{L_h-1} (-1)^{q'} \sqrt{\frac{4\pi}{2p'+1}} (h)_{p'}^0 T(n; p', q'; u) \int_{\mathbb{S}^2} Y_{p',q'}^{-q'}(\hat{\mathbf{x}}) \overline{Y_p^q(\hat{\mathbf{x}})} ds(\hat{\mathbf{x}}) \\ &= \sum_{n=0}^{L_f^2-1} (f)_n H(n; p, -q; u), \quad H(n; p, q; u) \triangleq (-1)^q \sqrt{\frac{4\pi}{2p+1}} (h)_p^0 T(n; p, q; u). \end{aligned} \quad (3.17)$$

The joint spatial-spectral domain filter is defined as the following distribution

$$\mathcal{F}(\hat{\mathbf{x}}) \triangleq [\mathcal{F}(\hat{\mathbf{x}}; 0), \mathcal{F}(\hat{\mathbf{x}}; 1), \dots, \mathcal{F}(\hat{\mathbf{x}}; L_g^2 - 1)]^T, \quad (3.18)$$

where each component $\mathcal{F}(\hat{\mathbf{x}}; u)$ is a bandlimited signal on \mathbb{S}^2 , given by

$$\mathcal{F}(\hat{\mathbf{x}}; u) = \sum_{p,q}^{L_{\mathcal{F}u}-1} (\mathcal{F}(\cdot; u))_p^q Y_p^q(\hat{\mathbf{x}}), \quad (\mathcal{F}(\cdot; u))_p^q \triangleq \langle \mathcal{F}(\cdot; u), Y_p^q \rangle_{\mathbb{S}^2}, \quad u \in [0, L_g^2 - 1]. \quad (3.19)$$

The filtered spatial-spectral representation is given by

$$\boldsymbol{\nu}(\hat{\boldsymbol{x}}) = [\nu(\hat{\boldsymbol{x}}; 0), \nu(\hat{\boldsymbol{x}}; 1), \dots, \nu(\hat{\boldsymbol{x}}; L_g^2 - 1)]^T, \quad (3.20)$$

in which each component is given by the convolution of spherical signals, defined in (2.78), as

$$\nu(\hat{\boldsymbol{x}}; u) = \sum_{p,q}^{\min\{L_h, L_{\mathcal{F}_u}\}-1} (g_f(\cdot; u))_p^q (\mathcal{F}(\cdot; u))_p^q Y_p^q(\hat{\boldsymbol{x}}) = \sum_{p,q}^{L_h-1} (g_f(\cdot; u))_p^q (\mathcal{F}(\cdot; u))_p^q Y_p^q(\hat{\boldsymbol{x}}), \quad (3.21)$$

where it has been assumed, without loss of generality, that each filter component $\mathcal{F}(\hat{\boldsymbol{x}}; u)$ is bandlimited to the bandlimit of the window signal, i.e., $L_{\mathcal{F}_u} = L_h, u = 0, 1, \dots, L_g^2 - 1$. By minimizing the joint spatial-spectral domain mean-square error, defined as

$$\mathcal{E}_{\text{mse}} = \mathbb{E} \left\{ \sum_{u=0}^{L_g^2-1} \|\nu(\hat{\boldsymbol{x}}; u) - g_s(\hat{\boldsymbol{x}}; u)\|_{\mathbb{S}^2}^2 \right\}, \quad (3.22)$$

where $g_s(\hat{\boldsymbol{x}}; u)$ is the source signal SLSHT distribution, spectral coefficients of the joint spatial-spectral domain filter are given by [87],

$$(\mathcal{F}(\cdot; u))_p^q = \frac{\sum_{n=0}^{L_f^2-1} \sum_{n'=0}^{L_f^2-1} H(n; p, -q; u) \overline{H(n'; p, -q; u)} C_{nn'}^s}{\sum_{n=0}^{L_f^2-1} \sum_{n'=0}^{L_f^2-1} H(n; p, -q; u) \overline{H(n'; p, -q; u)} (C_{nn'}^s + C_{nn'}^z)}, \quad (3.23)$$

for $\sum_{n=0}^{L_f^2-1} \sum_{n'=0}^{L_f^2-1} H(n; p, -q; u) \overline{H(n'; p, -q; u)} (C_{nn'}^s + C_{nn'}^z) \neq 0$, $(\mathcal{F}(\cdot; u))_p^q$ is zero otherwise.

Filtered spatial-spectral representation may not be an admissible SLSHT distribution, i.e., there may not exist a signal $\tilde{s} \in L^2(\mathbb{S}^2)$ such that $g_{\tilde{s}}(\hat{\boldsymbol{x}}; u) = \nu(\hat{\boldsymbol{x}}; u)$. As a result, signal estimate, in general, cannot be obtained from the inverse SLSHT given in (2.99). Therefore, a least square signal estimate has been proposed in [106] (that

has also been used to estimate the signal in [87]), which is given by

$$\begin{aligned} (\tilde{s})_n &= \underset{(\tilde{s})_n}{\operatorname{argmin}} \mathbb{E} \left\{ \sum_{u=0}^{L_g^2-1} \|\nu(\hat{\mathbf{x}}; u) - g_{\tilde{s}}(\hat{\mathbf{x}}; u)\|_{\mathbb{S}^2}^2 \right\} \\ &= \frac{1}{\langle h, h \rangle_{\mathbb{S}^2}} \sum_{u=0}^{L_g^2-1} \int_{\mathbb{S}^2} \overline{\psi_{u,n}(\hat{\mathbf{x}})} \nu(\hat{\mathbf{x}}; u) ds(\hat{\mathbf{x}}). \end{aligned} \quad (3.24)$$

3.2.2 Normalized axisymmetric optimal window design

As can be seen from (3.16), (3.21) and (3.24), the joint spatial-spectral domain filtering framework and the underlying signal estimation depend on the choice of the window signal used for spatial localization of the noise-contaminated observation. We design a normalized azimuthally symmetric optimal window signal by minimizing the mean-square error between the spectral coefficients of the source and estimated signals as

$$\mathcal{E}_{\text{mse,AW}} = \mathbb{E} \left\{ \sum_{n=0}^{L_f^2-1} |(\tilde{s})_n - (s)_n|^2 \right\}. \quad (3.25)$$

The results are presented in the following theorem.

Theorem 1. *Let $f(\hat{\mathbf{x}}) = s(\hat{\mathbf{x}}) + z(\hat{\mathbf{x}})$ be a noise-contaminated observation on the sphere, where $s(\hat{\mathbf{x}})$ is a realization of an anisotropic random process on the sphere with known spectral covariance matrix $C_{nn'}^s = \mathbb{E} \left\{ (s)_n \overline{(s)_{n'}} \right\}$, and $z(\hat{\mathbf{x}})$ is a realization of a zero-mean, uncorrelated and anisotropic noise process with known spectral covariance matrix $C_{nn'}^z = \mathbb{E} \left\{ (z)_n \overline{(z)_{n'}} \right\}$. Using the joint spatial-spectral domain filtering framework, the normalized azimuthally symmetric optimal window signal, which minimizes the mean-square error formulated in (3.25), is given by*

$$\hat{h}(\hat{\mathbf{x}}) = \sum_{p=0}^{L_h-1} \sqrt{\left(\frac{2p+1}{4\pi} \right)} x_p Y_p^0(\hat{\mathbf{x}}), \quad |(\hat{h})_p|^2 = \left(\frac{2p+1}{4\pi} \right) x_p, \quad (\hat{h})_p^0 = \frac{(h)_p^0}{\sqrt{\langle h, h \rangle_{\mathbb{S}^2}}}, \quad (3.26)$$

where x_p , for $p = 0, 1, \dots, L_h - 1$, are elements of the column vector \mathbf{x} which is

solution to the following linear system

$$\mathbf{G}\mathbf{x} = \mathbf{b}. \quad (3.27)$$

Elements of the matrix \mathbf{G} and column vector \mathbf{b} depend on the joint spatial-spectral domain filter and are given by the following expressions

$$\begin{aligned} G_{k,p} &= \sum_{n=0}^{L_f^2-1} 2 \operatorname{Re} \left\{ \mathbb{E} \left\{ F(n;p) \overline{F(n;k)} \right\} \right\}, \\ b_k &= \sum_{n=0}^{L_f^2-1} 2 \operatorname{Re} \left\{ \mathbb{E} \left\{ F(n;k) \overline{(s)_n} \right\} \right\}, \end{aligned} \quad 0 \leq k \leq L_h - 1, \quad (3.28)$$

where $\operatorname{Re}\{\cdot\}$ represents the real part and

$$F(n;p) \triangleq \sum_{n'=0}^{L_f^2-1} (f)_{n'} \sum_{q=-p}^p \sum_{u=0}^{L_g^2-1} (\mathcal{F}(\cdot; u))_p^{-q} T(n;p,q;u) T(n';p,q;u). \quad (3.29)$$

Proof. Using (3.16), (3.17) and (3.21), we can rewrite the spectral estimate of the source signal in (3.24) as

$$\begin{aligned} (\tilde{s})_n &= \frac{1}{\langle h, h \rangle} \sum_{u=0}^{L_g^2-1} \sum_{p',q'}^{L_h-1} \sqrt{\frac{4\pi}{2p'+1}} \overline{(h)_{p'}^0} T(n;p',q';u) \times \\ &\quad \sum_{p,q}^{L_h-1} \sum_{n'=0}^{L_f^2-1} (f)_{n'} (-1)^{-q} \sqrt{\frac{4\pi}{2p+1}} (h)_p^0 T(n';p,-q;u) (\mathcal{F}(\cdot; u))_p^q \left\langle Y_p^q, \overline{Y_{p'}^{q'}} \right\rangle_{\mathbb{S}^2} \\ &= \frac{1}{\langle h, h \rangle} \sum_{p',q'}^{L_h-1} \left(\frac{4\pi}{2p'+1} \right) \left| (h)_{p'}^0 \right|^2 \sum_{n'=0}^{L_f^2-1} (f)_{n'} \sum_{u=0}^{L_g^2-1} (\mathcal{F}(\cdot; u))_{p'}^{-q'} \times \\ &\quad T(n;p',q';u) T(n';p',q';u) \\ &= \sum_{p=0}^{L_h-1} \left(\frac{4\pi}{2p+1} \right) \left| (\hat{h})_p^0 \right|^2 F(n;p), \quad (\hat{h})_p^0 = \frac{(h)_p^0}{\sqrt{\langle h, h \rangle_{\mathbb{S}^2}}}, \end{aligned} \quad (3.30)$$

where we have normalized the spectral coefficients of the window signal by the norm of the window signal and $F(n;p)$ is given in (3.29). Using these formulations, mean-

square error in (3.25) can be written as

$$\begin{aligned}
 \mathcal{E}_{\text{mse,AW}} &= \sum_{n=0}^{L_f^2-1} \mathbb{E} \left\{ \left((\tilde{s})_n - (s)_n \right) \left(\overline{(\tilde{s})_n} - \overline{(s)_n} \right) \right\} \\
 &= \sum_{n=0}^{L_f^2-1} \mathbb{E} \left\{ \left(\sum_{p=0}^{L_h-1} \left(\frac{4\pi}{2p+1} \right) |(\hat{h})_p^0|^2 F(n;p) - (s)_n \right) \times \right. \\
 &\quad \left. \left(\sum_{p'=0}^{L_h-1} \left(\frac{4\pi}{2p'+1} \right) |(\hat{h})_{p'}^0|^2 \overline{F(n;p')} - \overline{(s)_n} \right) \right\} \\
 &= \sum_{n=0}^{L_f^2-1} \sum_{p=0}^{L_h-1} \sum_{p'=0}^{L_h-1} \left[\left(\frac{4\pi}{2p+1} \right) \left(\frac{4\pi}{2p'+1} \right) (\hat{h})_p^0 \overline{(\hat{h})_p^0} (\hat{h})_{p'}^0 \overline{(\hat{h})_{p'}^0} \mathbb{E} \left\{ F(n;p) \overline{F(n;p')} \right\} \right] - \\
 &\quad \sum_{n=0}^{L_f^2-1} \sum_{p=0}^{L_h-1} \left(\frac{4\pi}{2p+1} \right) (\hat{h})_p^0 \overline{(\hat{h})_p^0} \left[\mathbb{E} \left\{ F(n;p) \overline{(s)_n} \right\} + \mathbb{E} \left\{ \overline{F(n;p)} (s)_n \right\} \right] + \sum_{n=0}^{L_f^2-1} \mathbb{E} \left\{ (s)_n \overline{(s)_n} \right\}.
 \end{aligned} \tag{3.31}$$

Setting the derivative of $\mathcal{E}_{\text{mse,AW}}$ with respect to $\overline{(\hat{h})_k^0}$ equal to zero, we get

$$\begin{aligned}
 &\sum_{n=0}^{L_f^2-1} \sum_{p=0}^{L_h-1} \left(\frac{4\pi}{2p+1} \right) |(\hat{h})_p^0|^2 \left(\mathbb{E} \left\{ F(n;p) \overline{F(n;k)} \right\} + \mathbb{E} \left\{ F(n;k) \overline{F(n;p)} \right\} \right) = \\
 &\quad \sum_{n=0}^{L_f^2-1} \left(\mathbb{E} \left\{ F(n;k) \overline{(s)_n} \right\} + \mathbb{E} \left\{ \overline{F(n;k)} (s)_n \right\} \right), \quad k = 0, 1, \dots, L_h - 1.
 \end{aligned} \tag{3.32}$$

Defining a matrix \mathbf{G} and column vector \mathbf{b} with elements given in (3.28), and a column vector \mathbf{x} with elements given by

$$x_p = \left(\frac{4\pi}{2p+1} \right) |(\hat{h})_p^0|^2, \tag{3.33}$$

the expression in (3.32) can be written as

$$\sum_{p=0}^{L_h-1} G_{k,p} x_p = b_k, \quad k = 0, 1, \dots, L_h - 1, \tag{3.34}$$

which can be cast in matrix form given in (3.27). Hence, normalized azimuthally

symmetric optimal window signal with the following spectral coefficients is given by (3.26)

$$(\hat{h})_p^0 = \sqrt{\frac{2p+1}{4\pi}} \sqrt{x_p}. \quad (3.35)$$

□

It can be seen from (3.28) that matrix \mathbf{G} is real-valued, symmetric, square and therefore, invertible. The resulting window signal is called optimal because it minimizes the mean-square error between the spectral representations of the source and estimated signals. Combining (3.30) with (3.26), we get the spectral estimate as

$$(\tilde{s})_n = \sum_{p=0}^{L_h-1} x_p F(n; p). \quad (3.36)$$

Remark 1. *Spectral coefficients of the normalized azimuthally symmetric optimal window signal in (3.35) depend on the spectral covariance matrices (through the joint spatial-spectral domain filter) and hence, are specified by statistics of both the source and noise processes. Phase of the optimal window coefficients however, is completely arbitrary due to the fact that neither the signal estimate in (3.30) nor the mean-square error, defined in (3.25), is affected by it. For simplicity, we have chosen the phase to be zero³.*

Remark 2. *We note that*

$$\langle \hat{h}, \hat{h} \rangle_{\mathbb{S}^2} = \sum_{p=0}^{L_h-1} |(\hat{h})_p^0|^2 = \frac{1}{\langle h, h \rangle_{\mathbb{S}^2}} \sum_{p=0}^{L_h-1} |(h)_p^0|^2 = 1, \quad (3.37)$$

hence, the elements x_p obtained from the linear system in (3.27) have the following constraint

$$\sum_{p=0}^{L_h-1} \left(\frac{2p+1}{4\pi} \right) x_p = 1. \quad (3.38)$$

³It is the “additional” phase that has been chosen to be zero, which has allowed us to get (3.35) from (3.33), inherent phase of $(h)_p^0$ can be 90° if x_p is negative.

3.2.3 Axisymmetric optimal window design – Alternative formulation

We can rewrite the normalized axisymmetric optimal window design problem as

$$\begin{aligned} \underset{(\hat{h})_p^0}{\text{minimize}} \quad \mathcal{E}_{\text{mse,AW}} &= \mathbb{E} \left\{ \sum_{n=0}^{L_f^2-1} |(\tilde{s})_n - (s)_n|^2 \right\}, \\ \text{subject to } (\tilde{s})_n &= \sum_{p=0}^{L_h-1} \left(\frac{4\pi}{2p+1} \right) (\hat{h})_p^0 \overline{(\hat{h})_p^0} F(n; p), \end{aligned} \quad (3.39)$$

which results in the solution given by (3.26), where $F(n; p)$ is given in (3.29). This formulation results in normalized spectral coefficients of the window signal. An alternative formulation for the design of axisymmetric optimal window is given by

$$\begin{aligned} \underset{(h)_p^0}{\text{minimize}} \quad \mathcal{E}_{\text{mse,AW}} &= \mathbb{E} \left\{ \sum_{n=0}^{L_f^2-1} |\langle h, h \rangle_{\mathbb{S}^2} (\tilde{s})_n - (s)_n|^2 \right\}, \\ \text{subject to } (\tilde{s})_n &= \frac{1}{\langle h, h \rangle_{\mathbb{S}^2}} \sum_{p=0}^{L_h-1} \left(\frac{4\pi}{2p+1} \right) (h)_p^0 \overline{(h)_p^0} F(n; p), \end{aligned} \quad (3.40)$$

which gives the same form of the mean-square error as that obtained from the formulation in (3.39) and hence, results in the same expression for $(h)_p^0$, i.e.,

$$|(h)_p^0|^2 = \left(\frac{2p+1}{4\pi} \right) x_p, \quad (h)_p^0 = \sqrt{\frac{2p+1}{4\pi}} \sqrt{x_p}. \quad (3.41)$$

Moreover, the formulation in (3.40) is equivalent to the formulation in (3.39), due to the fact that

$$\langle h, h \rangle_{\mathbb{S}^2} = \sum_{p=0}^{L_h-1} |(h)_p^0|^2 = \sum_{p=0}^{L_h-1} \left(\frac{2p+1}{4\pi} \right) x_p = 1, \quad (3.42)$$

where we have used (3.41) and (3.38) to get the final result. Hence, the alternative formulation in (3.40) yields the true⁴ spectral coefficients of the axisymmetric optimal

⁴True in the sense that the spectral coefficients are not normalized. The “additional” phase (described in Footnote 3 on page 60) however, is still arbitrary and chosen to be zero.

window signal, which minimize the mean square error in (3.25), and are given by

$$h(\hat{\mathbf{x}}) = \sum_{p=0}^{L_h-1} \sqrt{\left(\frac{2p+1}{4\pi}\right)} x_p Y_p^0(\hat{\mathbf{x}}), \quad |(h)_p^0|^2 = \left(\frac{2p+1}{4\pi}\right) x_p, \quad \langle h, h \rangle_{S^2} = 1, \quad (3.43)$$

where x_p , for $p = 0, 1, \dots, L_h - 1$, is obtained by inverting the linear system in (3.27).

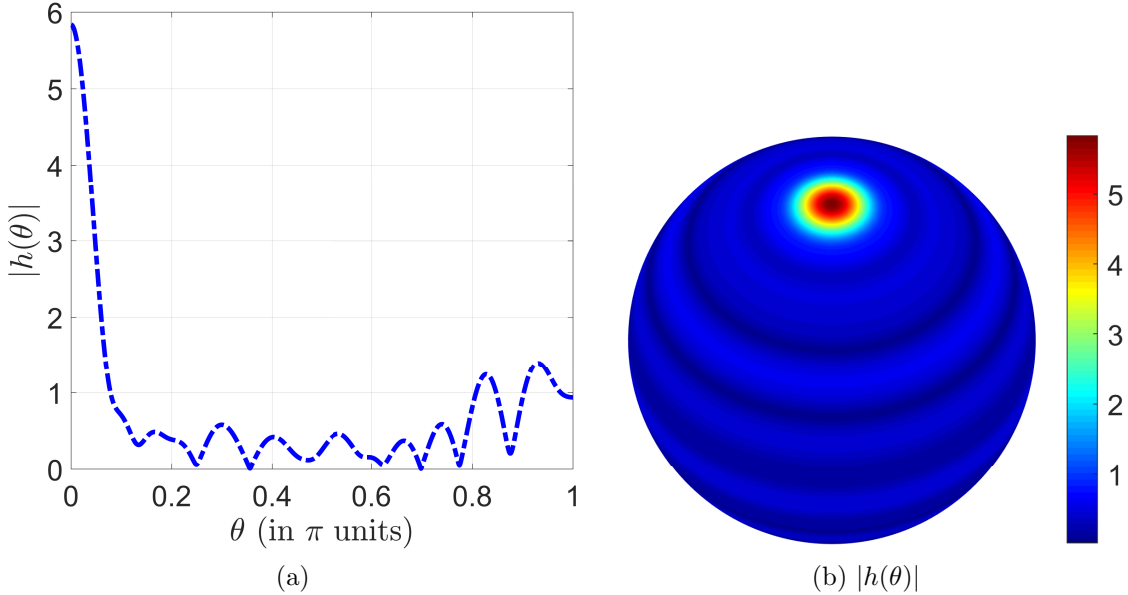


Figure 3-1: Azimuthally symmetric optimal window signal, bandlimited to degree $L_h = 16$, is constructed for the Mars topography map ($L_f = 32$) and zero-mean, uncorrelated, anisotropic Gaussian noise process at SNR = 0 dBs. (a) Magnitude of the azimuthally symmetric optimal window signal plotted against the colatitude, $\theta \in [0, \pi]$. (b) Magnitude of the axisymmetric optimal window signal on the sphere.

3.2.4 Illustrations

We employ a Mars topography map⁵ (height above the geoid and normalized to have unit norm), bandlimited to degree $L_f = 32$, as the underlying source signal $s(\hat{\mathbf{x}})$ to illustrate the capability of the joint spatial-spectral domain filtering framework using the azimuthally symmetric optimal window signal with bandlimit $L_h = 16$. Spectral covariance matrix of the source signal is constructed as $C_{\ell m, p q}^s = (s)_\ell^m \overline{(s)_p^q}$.

Figure 3-1 shows the magnitude of an optimal window signal constructed using

⁵Mars topography map was obtained from <http://geoweb.princeton.edu/people/simons/software.html>

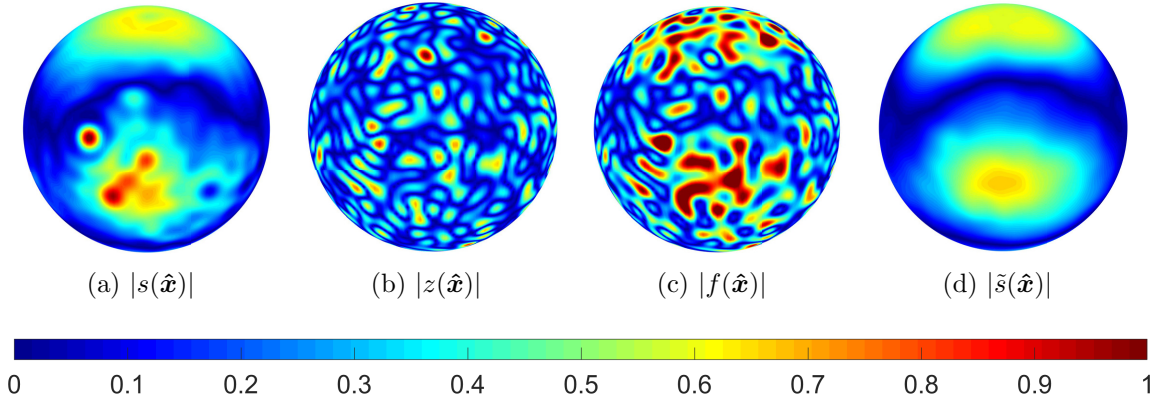


Figure 3-2: Joint spatial-spectral domain filtering using azimuthally symmetric optimal window signal ($L_h = 16$), resulting in an SNR improvement of 13 dBs. Figure shows magnitude plots of (a) the Mars topography map, $s(\hat{\mathbf{x}})$ ($L_f = 32$), (b) the zero mean, uncorrelated and anisotropic Gaussian noise signal, $z(\hat{\mathbf{x}})$, (c) the noise-contaminated observation, $f(\hat{\mathbf{x}}) = s(\hat{\mathbf{x}}) + z(\hat{\mathbf{x}})$, with $\text{SNR}^f = 0.32$ dBs, and (d) the source signal estimate, $\tilde{s}(\hat{\mathbf{x}})$, with $\text{SNR}^{\tilde{s}} = 13.33$ dBs.

(3.41) for zero mean, uncorrelated and anisotropic Gaussian noise process at $\text{SNR} = 0$ dBs. Contaminating the Mars topography map by one of the realizations of this noise process at an actual $\text{SNR}^f = 0.32$ dBs, the joint spatial-spectral domain filtering framework using this optimal window signal results in $\text{SNR}^{\tilde{s}} = 13.33$ dBs, giving an SNR improvement of 13 dBs. The results of this experiment are shown in Figure 3-2.

We also analyze the joint spatial-spectral domain filtering framework using the axisymmetric optimal window signal by contaminating the bandlimited Mars topography map at different noise levels, specified by different values of the input SNR. A similar experiment is performed using the Slepian window signal, which is most well-optimally concentrated (i.e., rank 1) in the north polar cap region of angle θ_0 (defined in (2.9)). Such a window signal is azimuthally symmetric⁶ and is given by

$$h_1(\hat{\mathbf{x}}) = \sum_{p=0}^{L_h-1} (h_1)_p^0 Y_p^0(\hat{\mathbf{x}}), \quad (3.44)$$

where the spectral coefficients $(h_1)_p^0$, $0 \leq p \leq L_h - 1$, are solution to the eigenvalue problem in (2.60). Output SNR for the joint spatial-spectral domain filtering

⁶Please see [74] for details on Slepian functions for polar cap regions.

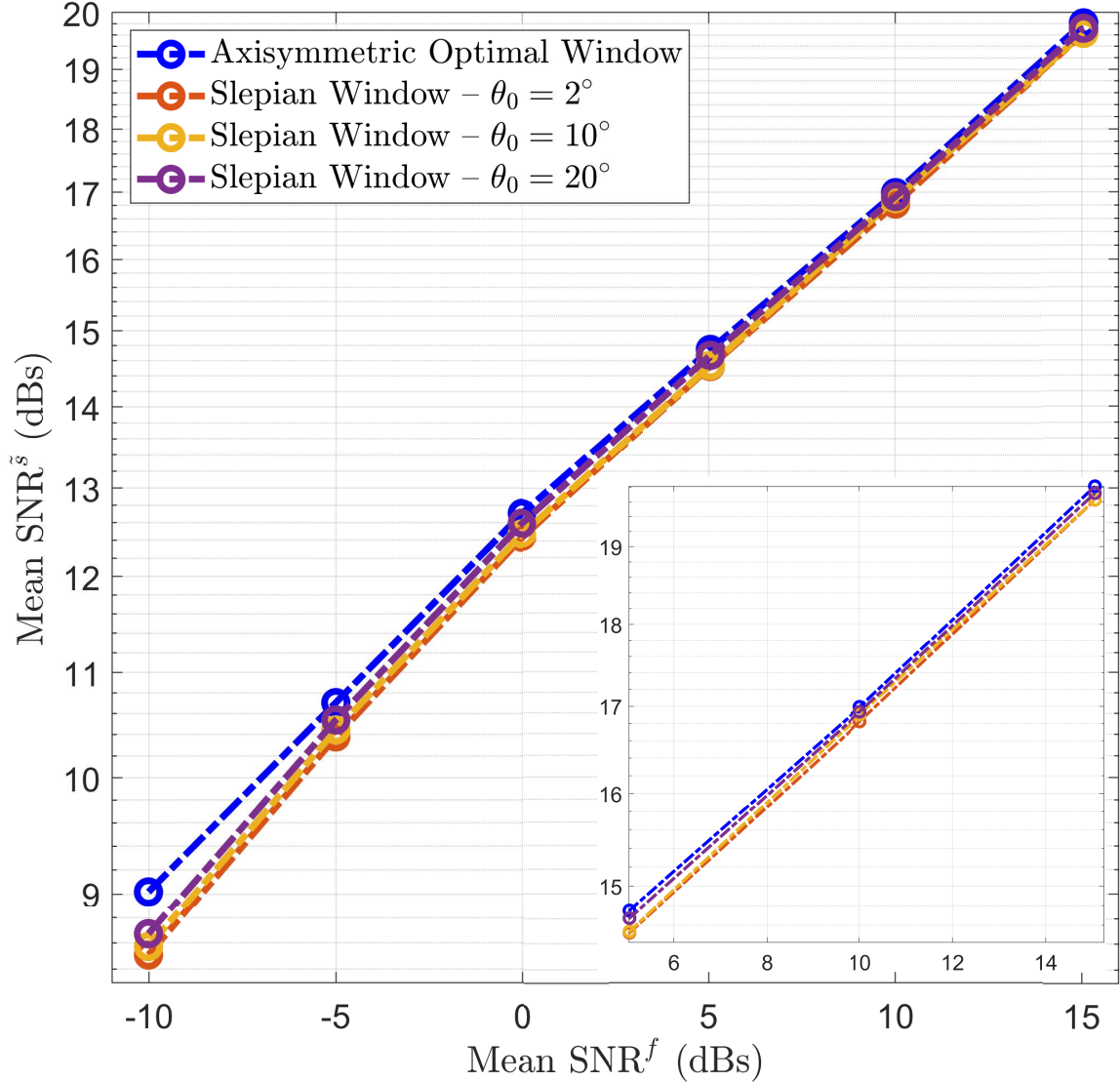


Figure 3-3: Joint spatial-spectral domain filtering of the bandlimited Mars topography map using the axisymmetric optimal window signal and rank 1 Slepian window signals for the north polar cap regions of angles $\theta_0 = 2^\circ, 10^\circ, 20^\circ$. Output SNR, $\text{SNR}^{\bar{s}}$, averaged over 100 realizations of a zero-mean, uncorrelated and anisotropic Gaussian noise process, is plotted against the average input SNR. Axisymmetric optimal window signal can be seen to perform better than the rank 1 axisymmetric Slepian window signals, specially at high noise levels. Also shown in the bottom right corner is the magnified plot at low noise levels.

framework, using the axisymmetric optimal window signal and rank 1 Slepian window signals for the north polar cap regions of angles $\theta_0 = 2^\circ, 10^\circ, 20^\circ$, is computed for 100 different realizations of the zero-mean, uncorrelated and anisotropic Gaussian noise process. The results are averaged over all realizations and plotted in Figure 3-3,

which shows the mean output SNR against the mean input SNR. As can be seen, the axisymmetric optimal window signal performs better, specially at high noise levels, compared to the rank 1 axisymmetric Slepian window signals. However, the difference in performance is not appreciable due to the fact that most of the spectral coefficients of both types of axisymmetric window signals are zero, leaving not much room for improvement.

3.3 Joint $\mathbb{SO}(3)$ -spectral domain filtering

The joint spatial-spectral domain filter processes the (non-directional) SLSHT distribution of the noise-contaminated observation, which, as noted in Section 2.8, cannot probe directional features of the signal due to the use of azimuthally symmetric window signal. Hence, the joint spatial-spectral domain filtering framework, even with the optimal window signal, is not suitable for the recovery of directional, i.e., rotationally asymmetric, features in the underlying source signal. In this section, we employ directional window signal to formulate a novel filtering and estimation framework for signals on the sphere, which is shown to be capable of recovering directional features in the presence of zero-mean, uncorrelated and anisotropic noise.

3.3.1 Joint $\mathbb{SO}(3)$ -spectral domain filter design

Directional SLSHT distribution of a signal $f(\hat{\mathbf{x}})$, bandlimited to degree L_f , is given by (2.87), which is repeated here for convenience as

$$g_f(\rho; u) = \sum_{n=0}^{L_f^2-1} (f)_n \psi_{u,n}(\rho), \quad \psi_{u,n}(\rho) = \sum_{p,q,q'}^{L_h-1} D_{q,q'}^p(\rho) (h)_p^{q'} T(n; p, q; u), \quad (3.45)$$

where again, $n = \ell(\ell + 1) + m, 0 \leq \ell \leq L_f - 1, |m| \leq \ell, u = v(v + 1) + w, 0 \leq v \leq L_g - 1, |w| \leq v$ are the spectral indices, directional window signal $h(\hat{\mathbf{x}})$ is assumed bandlimited to degree $L_h, L_g = L_f + L_h - 1$ is the bandlimit of the directional SLSHT distribution in u , and $T(n; p, q; u)$ is the spherical harmonic triple product given in

(2.89). Spectral representation of $g_f(\rho; u)$ is given by

$$\begin{aligned}
 (g_f(\cdot; u))_{q,q'}^p &= \left(\frac{2p+1}{8\pi^2} \right) \langle g_f(\cdot; u), D_{q,q'}^p \rangle_{\mathbb{SO}(3)} \\
 &= \left(\frac{2p+1}{8\pi^2} \right) \sum_{n=0}^{L_f-1} (f)_n \sum_{p',q'',q'''}^{L_h-1} (h)_{p'}^{q'''} T(n; p', q''; u) \int_{\mathbb{SO}(3)} D_{q'',q'''}^{p'}(\rho) \overline{D_{q,q'}^p(\rho)} d\rho \\
 &= (h)_p^{q'} \sum_{n=0}^{L_f-1} (f)_n T(n; p, q; u),
 \end{aligned} \tag{3.46}$$

where orthogonality of Wigner- D functions has been used.

The joint $\mathbb{SO}(3)$ -spectral domain filter distribution is defined as

$$\zeta(\rho) \triangleq [\zeta(\rho; 1), \zeta(\rho; 2), \dots, \zeta(\rho; L_g^2 - 1)]^T, \tag{3.47}$$

where each component $\zeta(\rho; u)$ is a bandlimited signal on $\mathbb{SO}(3)$, given by

$$\zeta(\rho; u) = \sum_{p,q,q'}^{L_{\zeta_u}-1} (\zeta(\cdot; u))_{q,q'}^p D_{q,q'}^p(\rho), \quad (\zeta(\cdot; u))_{q,q'}^p \triangleq \left(\frac{2p+1}{8\pi^2} \right) \langle \zeta(\cdot; u), D_{q,q'}^p \rangle_{\mathbb{SO}(3)}, \tag{3.48}$$

for $u \in [0, L_g^2 - 1]$. Action of the filter component on the directional SLSHT distribution is defined by the spectral representation of convolution of signals on the $\mathbb{SO}(3)$ rotation group, given in (2.85), i.e.,

$$\nu(\rho; u) = \sum_{p=0}^{L_h-1} \left(\frac{8\pi^2}{2p+1} \right) \sum_{q,q'=-p}^p \sum_{k=-p}^p (g_f(\cdot; u))_{k,q'}^p (\zeta(\cdot; u))_{q,k}^p D_{q,q'}^p(\rho), \tag{3.49}$$

to give the filtered $\mathbb{SO}(3)$ -spectral representation as

$$\nu(\rho) \triangleq [\nu(\rho; 1), \nu(\rho; 2), \dots, \nu(\rho; L_g^2 - 1)]^T, \tag{3.50}$$

where $\nu(\rho; u)$ is called the filtered $\mathbb{SO}(3)$ -spectral representation component and we have assumed, without loss of generality, that each filter component $\zeta(\rho; u)$ is bandlimited to L_h , i.e., $L_{\zeta_u} = L_h$, $u = 0, 1, \dots, L_g^2 - 1$. Spectral components of the filter

function in (3.48) are obtained by minimizing the following mean-square error in the joint $\mathbb{SO}(3)$ -spectral domain

$$\mathcal{E}_{\text{mse}} = \mathbb{E} \left\{ \sum_{u=0}^{L_g^2-1} \|\nu(\rho; u) - g_s(\rho; u)\|_{\mathbb{SO}(3)}^2 \right\}, \quad (3.51)$$

which makes them optimal in the mean-square sense. Here $g_s(\rho; u)$ is the source signal directional SLSHT representation. We present a linear system for the solution of spectral components of the joint $\mathbb{SO}(3)$ -spectral domain optimal filter in the following theorem.

Theorem 2. *Let $f(\hat{\mathbf{x}}) = s(\hat{\mathbf{x}}) + z(\hat{\mathbf{x}})$ be a noise-contaminated observation on the sphere, where $s(\hat{\mathbf{x}})$ is a realization of an anisotropic random process of interest, called the source signal, and $z(\hat{\mathbf{x}})$ is a realization of a zero-mean and anisotropic random process, representing the noise signal. Assuming that the source and noise signals are uncorrelated with known spectral covariance matrices, denoted by \mathbf{C}^s and \mathbf{C}^z respectively, spectral components of the joint $\mathbb{SO}(3)$ -spectral domain filter, which minimize the mean-square error defined in (3.51), are obtained by inverting the following linear system*

$$\mathbf{G}(p, u) \mathbf{x}(p, q, u) = \mathbf{b}(p, q, u), \quad (3.52)$$

for $0 \leq p \leq L_h - 1$, $|q| \leq p$, $0 \leq u \leq L_g^2 - 1$, where $\mathbf{x}(p, q, u)$ is a column vector of size $(2p + 1)$, with elements $x_k = (\zeta(\cdot; u))_{q,k}^p$, $|k| \leq p$. Elements of the matrix \mathbf{G} and column vector \mathbf{b} are given by

$$\begin{aligned} G_{k',k} &= \left(\frac{8\pi^2}{2p+1} \right) \sum_{n=0}^{L_f^2-1} \sum_{n'=0}^{L_f^2-1} T(n; p, k; u) T(n'; p, k'; u) (C_{nn'}^s + C_{nn'}^z), \\ & \quad |k'| \leq p, \quad (3.53) \\ b_{k'} &= \sum_{n=0}^{L_f^2-1} \sum_{n'=0}^{L_f^2-1} T(n; p, q; u) T(n'; p, k'; u) C_{nn'}^s, \end{aligned}$$

where $C_{nn'}^s = \mathbb{E} \left\{ (s)_n \overline{(s)_{n'}} \right\}$ and $C_{nn'}^z = \mathbb{E} \left\{ (z)_n \overline{(z)_{n'}} \right\}$ are the elements of \mathbf{C}^s and \mathbf{C}^z

respectively.

Proof. Using (3.49) and (3.46) (for the directional SLSHT distribution of the source signal), mean-square error in (3.51) can be written as

$$\begin{aligned}
 \mathcal{E}_{\text{mse}} &= \mathbb{E} \left\{ \sum_{u=0}^{L_g^2-1} \left\langle \sum_{p,q,q'}^{L_h-1} \left(\frac{8\pi^2}{2p+1} \sum_{k=-p}^p (g_f(\cdot; u))_{k,q'}^p (\zeta(\cdot; u))_{q,k}^p - (g_s(\cdot; u))_{q,q'}^p \right) D_{q,q'}^p, \right. \right. \\
 &\quad \left. \left. \sum_{p',q'',q'''}^{L_h-1} \left(\frac{8\pi^2}{2p'+1} \sum_{k'=-p'}^{p'} (g_f(\cdot; u))_{k',q'''}^{p'} (\zeta(\cdot; u))_{q'',k'}^{p'} - (g_s(\cdot; u))_{q'',q'''}^{p'} \right) D_{q'',q'''}^{p'} \right\rangle_{\mathbb{SO}(3)} \right\} \\
 &= \sum_{u=0}^{L_g^2-1} \sum_{p,q,q'}^{L_h-1} \left(\frac{8\pi^2}{2p+1} \right) \times \\
 &\quad \mathbb{E} \left\{ \left(\frac{8\pi^2}{2p+1} \sum_{k=-p}^p (h)_p^{q'} \sum_{n=0}^{L_f^2-1} (f)_n T(n; p, k; u) (\zeta(\cdot; u))_{q,k}^p - (h)_p^{q'} \sum_{n=0}^{L_f^2-1} (s)_n T(n; p, q; u) \right) \times \right. \\
 &\quad \left. \frac{\left(\frac{8\pi^2}{2p+1} \sum_{k'=-p}^p (h)_p^{q'} \sum_{n'=0}^{L_f^2-1} (f)_{n'} T(n'; p, k'; u) (\zeta(\cdot; u))_{q,k'}^p - (h)_p^{q'} \sum_{n'=0}^{L_f^2-1} (s)_{n'} T(n'; p, q; u) \right)}{\left(\frac{8\pi^2}{2p+1} \sum_{k'=-p}^p (h)_p^{q'} \sum_{n'=0}^{L_f^2-1} (f)_{n'} T(n'; p, k'; u) (\zeta(\cdot; u))_{q,k'}^p - (h)_p^{q'} \sum_{n'=0}^{L_f^2-1} (s)_{n'} T(n'; p, q; u) \right)} \right\}, \tag{3.54}
 \end{aligned}$$

where orthogonality of Wigner- D functions has been used. Setting the derivative of \mathcal{E}_{mse} with respect to $\overline{(\zeta(\cdot; u))_{q,k'}^p}$ equal to zero, we get

$$\begin{aligned}
 \left(\frac{8\pi^2}{2p+1} \right) \sum_{q'=-p}^p \left| (h)_p^{q'} \right|^2 \sum_{k=-p}^p \sum_{n,n'=0}^{L_f^2-1} \mathbb{E} \left\{ (f)_n \overline{(f)_{n'}} \right\} T(n; p, k; u) T(n'; p, k'; u) \times \\
 (\zeta(\cdot; u))_{q,k}^p = \sum_{q'=-p}^p \left| (h)_p^{q'} \right|^2 \sum_{n,n'=0}^{L_f^2-1} \mathbb{E} \left\{ (s)_n \overline{(f)_{n'}} \right\} T(n; p, q; u) T(n'; p, k'; u), \tag{3.55}
 \end{aligned}$$

for $|q|, |k'| \leq p$. Noting the fact that signal and noise are uncorrelated, i.e.,

$$\begin{aligned}
 \mathbb{E} \left\{ (f)_n \overline{(f)_{n'}} \right\} &= \mathbb{E} \left\{ (s)_n \overline{(s)_{n'}} + (s)_n \overline{(z)_{n'}} + (z)_n \overline{(s)_{n'}} + (z)_n \overline{(z)_{n'}} \right\} = C_{nn'}^s + C_{nn'}^z, \\
 \mathbb{E} \left\{ (s)_n \overline{(f)_{n'}} \right\} &= \mathbb{E} \left\{ (s)_n \overline{(s)_{n'}} + (s)_n \overline{(z)_{n'}} \right\} = C_{nn'}^s, \tag{3.56}
 \end{aligned}$$

the linear system of equations in (3.55) can be cast in matrix form in (3.52) using the

definitions in (3.53)⁷. □

3.3.2 Signal estimation

The filtered $\mathbb{SO}(3)$ -spectral representation $\nu(\rho; u)$ may not be an admissible directional SLSHT distribution, i.e., there may not exist a signal $\tilde{s} \in L^2(\mathbb{S}^2)$ such that $g_{\tilde{s}}(\rho; u) = \nu(\rho; u)$. As a result, inverse directional SLSHT given in (2.97) cannot be used, in general, to obtain the source signal estimate from $\nu(\rho; u)$. However, a least square solution of the spectral estimate of the source signal can be obtained, as shown in the following theorem.

Theorem 3. *Let $g_f(\rho; u)$ be the directional SLSHT distribution of the noise contaminated random signal on the sphere, which is filtered in the joint $\mathbb{SO}(3)$ -spectral domain using the filter coefficients obtained from (3.52), resulting in a filtered $\mathbb{SO}(3)$ -spectral representation $\nu(\rho)$, whose components are given in (3.49). Then, a least square spectral estimate of the source signal can be obtained from the filtered $\mathbb{SO}(3)$ -spectral representation as*

$$(\tilde{s})_n = \underset{(\tilde{s})_n}{\operatorname{argmin}} \left\{ \sum_{u=0}^{L_g^2-1} \|\nu(\rho; u) - g_{\tilde{s}}(\rho; u)\|_{\mathbb{SO}(3)}^2 \right\} = \sum_{n'=0}^{L_f^2-1} \Upsilon_{n,n'}(f)_{n'}, \quad (3.57)$$

for $0 \leq n \leq L_f^2 - 1$, where $L_g = L_f + L_h - 1$, $(f)_n$ is the spectral representation of the noise-contaminated observation, indexed by single variable n , and

$$\Upsilon_{n,n'} = \frac{32\pi^3}{\langle h, h \rangle_{\mathbb{S}^2}} \sum_{u=0}^{L_g^2-1} \sum_{p,q,q'}^{L_h-1} \frac{1}{(2p+1)^2} \left| (h)_p^{q'} \right|^2 \sum_{k=-p}^p (\zeta(\cdot; u))_{q,k}^p T(n; p, q; u) T(n'; p, k; u). \quad (3.58)$$

Proof. Denoting the squared error in (3.57) by \mathcal{E}_{se} , we rewrite it, using the expression

⁷We note that the linear system formulated in (3.52) becomes ill-conditioned for certain values of p, q and u , in which case we use the Moore-Penrose pseudo-inverse to obtain the filter coefficients $(\zeta(\cdot; u))_{q,k}^p$.

for directional SLSHT distribution in (3.45), as

$$\begin{aligned}
 \mathcal{E}_{\text{se}} &= \sum_{u=0}^{L_g^2-1} \|\nu(\rho; u) - g_{\tilde{s}}(\rho; u)\|_{\mathbb{S}\mathbb{O}(3)}^2 = \sum_{u=0}^{L_g^2-1} \int_{\mathbb{S}\mathbb{O}(3)} \left| \nu(\rho; u) - \sum_{n=0}^{L_f^2-1} \psi_{u,n}(\rho)(\tilde{s})_n \right|^2 d\rho \\
 &= \sum_{u=0}^{L_g^2-1} \int_{\mathbb{S}\mathbb{O}(3)} \left(\nu(\rho; u) - \sum_{n=0}^{L_f^2-1} \psi_{u,n}(\rho)(\tilde{s})_n \right) \overline{\left(\nu(\rho; u) - \sum_{n'=0}^{L_f^2-1} \psi_{u,n'}(\rho)(\tilde{s})_{n'} \right)} d\rho \\
 &= \sum_{u=0}^{L_g^2-1} \int_{\mathbb{S}\mathbb{O}(3)} \left(\nu(\rho; u) \overline{\nu(\rho; u)} - \nu(\rho; u) \sum_{n'=0}^{L_f^2-1} \overline{\psi_{u,n'}(\rho)(\tilde{s})_{n'}} - \right. \\
 &\quad \left. \sum_{n=0}^{L_f^2-1} \psi_{u,n}(\rho)(\tilde{s})_n \overline{\nu(\rho; u)} + \sum_{n=0}^{L_f^2-1} \sum_{n'=0}^{L_f^2-1} \psi_{u,n}(\rho) \overline{\psi_{u,n'}(\rho)(\tilde{s})_{n'}} \right). \quad (3.59)
 \end{aligned}$$

Differentiating \mathcal{E}_{se} with respect to $\overline{(\tilde{s})_{n'}}$ and setting the result equal to zero, we get the following relation

$$\sum_{n=0}^{L_f^2-1} \sum_{u=0}^{L_g^2-1} \int_{\mathbb{S}\mathbb{O}(3)} \psi_{u,n}(\rho) \overline{\psi_{u,n'}(\rho)} d\rho(\tilde{s})_n = \sum_{u=0}^{L_g^2-1} \int_{\mathbb{S}\mathbb{O}(3)} \nu(\rho; u) \overline{\psi_{u,n'}(\rho)} d\rho, \quad (3.60)$$

for $n' \in [0, L_f^2 - 1]$. From the definition of $\psi_{u,n}$ in (3.45), we can write

$$\sum_{u=0}^{L_g^2-1} \int_{\mathbb{S}\mathbb{O}(3)} \psi_{u,n'}(\rho) \overline{\psi_{u,n}(\rho)} d\rho = \sum_{u=0}^{L_g^2-1} \sum_{p,q,q'}^{L_h-1} \left(\frac{8\pi^2}{2p+1} \right) \left| (h)_p^{q'} \right|^2 T(n'; p, q; u) \overline{T(n; p, q; u)}, \quad (3.61)$$

where orthogonality of Wigner- D functions has been used. Spherical harmonic triple product can be written, using the conjugate symmetry property of spherical harmonics, as

$$\begin{aligned}
 T(\ell, m; p, q; v, w) &= \int_{\mathbb{S}^2} Y_\ell^m(\hat{\mathbf{x}}) Y_p^q(\hat{\mathbf{x}}) \overline{Y_v^w(\hat{\mathbf{x}})} ds(\hat{\mathbf{x}}) = (-1)^w \int_{\mathbb{S}^2} Y_\ell^m(\hat{\mathbf{x}}) Y_p^q(\hat{\mathbf{x}}) Y_v^{-w}(\hat{\mathbf{x}}) ds(\hat{\mathbf{x}}) \\
 &= (-1)^w \sqrt{\frac{(2\ell+1)(2p+1)(2v+1)}{4\pi}} \begin{pmatrix} \ell & p & v \\ 0 & 0 & 0 \end{pmatrix} \begin{pmatrix} \ell & p & v \\ m & q & -w \end{pmatrix}, \quad (3.62)
 \end{aligned}$$

where $\begin{pmatrix} \ell & p & v \\ m & q & w \end{pmatrix}$ is called the Wigner-3j symbol [64]. Using (3.62) and noting that

$$\sum_{w=-v}^v \sum_{q=-p}^p \begin{pmatrix} \ell & p & v \\ m & q & -w \end{pmatrix} \begin{pmatrix} \ell' & p & v \\ m' & q & -w \end{pmatrix} = \frac{1}{(2\ell+1)} \delta_{\ell,\ell'} \delta_{m,m'}, \quad (3.63)$$

left hand side of (3.60) can be simplified through (3.61) as

$$\begin{aligned} \sum_{n=0}^{L_f^2-1} \sum_{u=0}^{L_g^2-1} \int_{\mathbb{S}\mathbb{O}(3)} \psi_{u,n}(\rho) \overline{\psi_{u,n'}(\rho)} d\rho(\tilde{s})_n &= 2\pi \sum_{p,q}^{L_h-1} \left| (h)_p^{q'} \right|^2 \sum_{v=0}^{L_g-1} (2v+1) \begin{pmatrix} \ell & p & v \\ 0 & 0 & 0 \end{pmatrix}^2 \delta_{n,n'} \\ &= 2\pi \sum_{p,q}^{L_h-1} \left| (h)_p^{q'} \right|^2 \delta_{n,n'} = 2\pi \langle h, h \rangle_{\mathbb{S}^2} \delta_{n,n'}, \end{aligned} \quad (3.64)$$

where we have used the following property of Wigner-3j symbols to get the penultimate equality

$$\sum_{v=0}^{L_g-1} (2v+1) \begin{pmatrix} \ell & p & v \\ 0 & 0 & 0 \end{pmatrix}^2 = 1. \quad (3.65)$$

Hence, (3.60) gives the spectral estimate as

$$\begin{aligned} (\tilde{s})_n &= \frac{1}{2\pi \langle h, h \rangle_{\mathbb{S}^2}} \sum_{u=0}^{L_g^2-1} \int_{\mathbb{S}\mathbb{O}(3)} \nu(\rho; u) \overline{\psi_{u,n}(\rho)} d\rho \\ &= \frac{1}{2\pi \langle h, h \rangle_{\mathbb{S}^2}} \sum_{u=0}^{L_g^2-1} \sum_{p,q,q'}^{L_h-1} \left(\frac{8\pi^2}{2p+1} \right) \sum_{k=-p}^p (g_f(\cdot; u))_{k,q'}^p (\zeta(\cdot; u))_{q,k}^p \times \\ &\quad \sum_{p',q'',q'''}^{L_h-1} \overline{(h)_{p'}^{q'''} T(n; p', q''; u)} \int_{\mathbb{S}\mathbb{O}(3)} D_{q,q'}^p(\rho) \overline{D_{q'',q'''}^{p'}(\rho)} d\rho \\ &= \frac{32\pi^3}{\langle h, h \rangle_{\mathbb{S}^2}} \sum_{u=0}^{L_g^2-1} \sum_{p,q,q'}^{L_h-1} \frac{1}{(2p+1)^2} \left| (h)_p^{q'} \right|^2 \sum_{k=-p}^p \sum_{n'=0}^{L_f-1} (f)_{n'} T(n'; p, k; u) (\zeta(\cdot; u))_{q,k}^p T(n; p, q; u), \end{aligned} \quad (3.66)$$

where we have used the definition of filtered $\mathbb{S}\mathbb{O}(3)$ -spectral representation in (3.49),

the expression for $\psi_{u,n}(\rho)$ in (3.45), the expression in (3.46) and orthogonality of Wigner- D functions to get the final result, which can be written as the linear system given in (3.57) through (3.58). \square

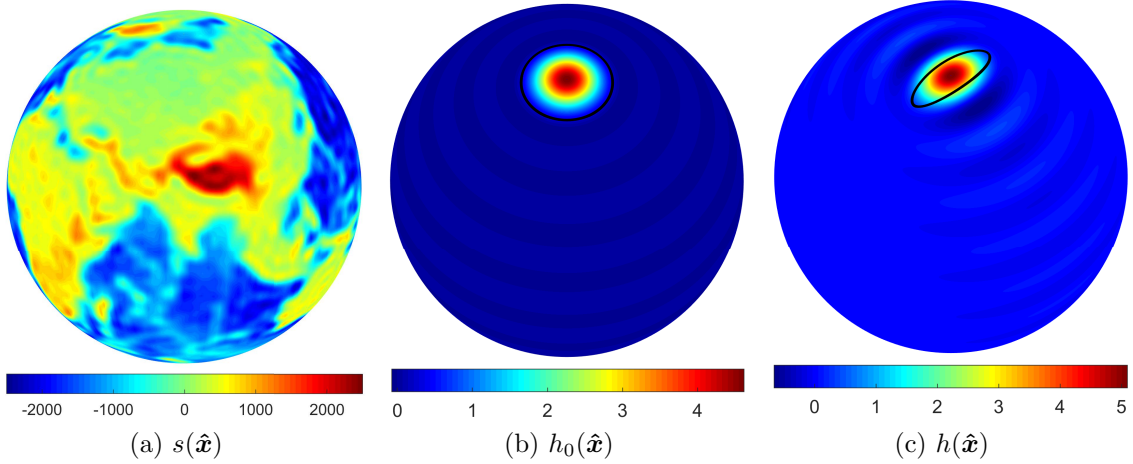


Figure 3-4: (a) Earth topography map, bandlimited to degree $L_f = 64$, used as the source signal $s(\hat{\mathbf{x}})$, (b) most well-optimally concentrated azimuthally symmetric Slepian window signal, bandlimited to degree $L_{h_0} = 20$, computed for the north polar cap region R_{15° , and (c) most well-optimally concentrated directional Slepian window signal, bandlimited to degree $L_h = 20$, computed for the spherical ellipse $R_{(15^\circ, 16^\circ)}$. Boundary of the north polar cap region and spherical ellipse is shown in black.

3.3.3 Analysis

To demonstrate the effectiveness of the joint $\mathbb{S}\mathbb{O}(3)$ -spectral domain filtering framework, we use an Earth topography map⁸, bandlimited to degree $L_f = 64$, as the source signal $s(\hat{\mathbf{x}})$ and gauge the performance using SNR, defined in (3.4). As before, spectral covariance matrix of the source signal is constructed as $C_{\ell m, p q}^s = (s)_\ell^m \overline{(s)_p^q}$. We employ the (directional) Slepian function, which is most well-optimally concentrated (i.e., has rank 1) in a spherical ellipse (defined in (2.11)) of focus colatitude $\theta_0 = 15^\circ$ and semi-major axis $a = 16^\circ$, as the window signal $h(\hat{\mathbf{x}})$, bandlimited to degree $L_h = 20$, for computing the source signal estimate $\tilde{s}(\hat{\mathbf{x}})$. For comparison, we also employ the rank 1 Slepian function for a north polar cap region of angle $\theta_0 = 15^\circ$,

⁸Earth topography map was obtained from <http://geoweb.princeton.edu/people/simons/software.html>

as the azimuthally symmetric window signal $h_0(\hat{\mathbf{x}})$, bandlimited to degree $L_{h_0} = 20$, and obtain the signal estimate, through joint spatial-spectral domain filter (reviewed in Section 3.2.1), as $\tilde{s}_0(\hat{\mathbf{x}})$. Figure 3-4 shows the bandlimited Earth topography map and the window signals used to obtain the joint $\mathbb{SO}(3)$ -spectral domain and the joint spatial-spectral domain signal estimates.

As an illustration, we use a realization of a zero-mean, uncorrelated and anisotropic Gaussian noise process, $z(\hat{\mathbf{x}})$, to obtain the noise-contaminated observation $f(\hat{\mathbf{x}}) = s(\hat{\mathbf{x}}) + z(\hat{\mathbf{x}})$ such that $\text{SNR}^f = 0.001$ dBs. Output SNR using the joint $\mathbb{SO}(3)$ -spectral

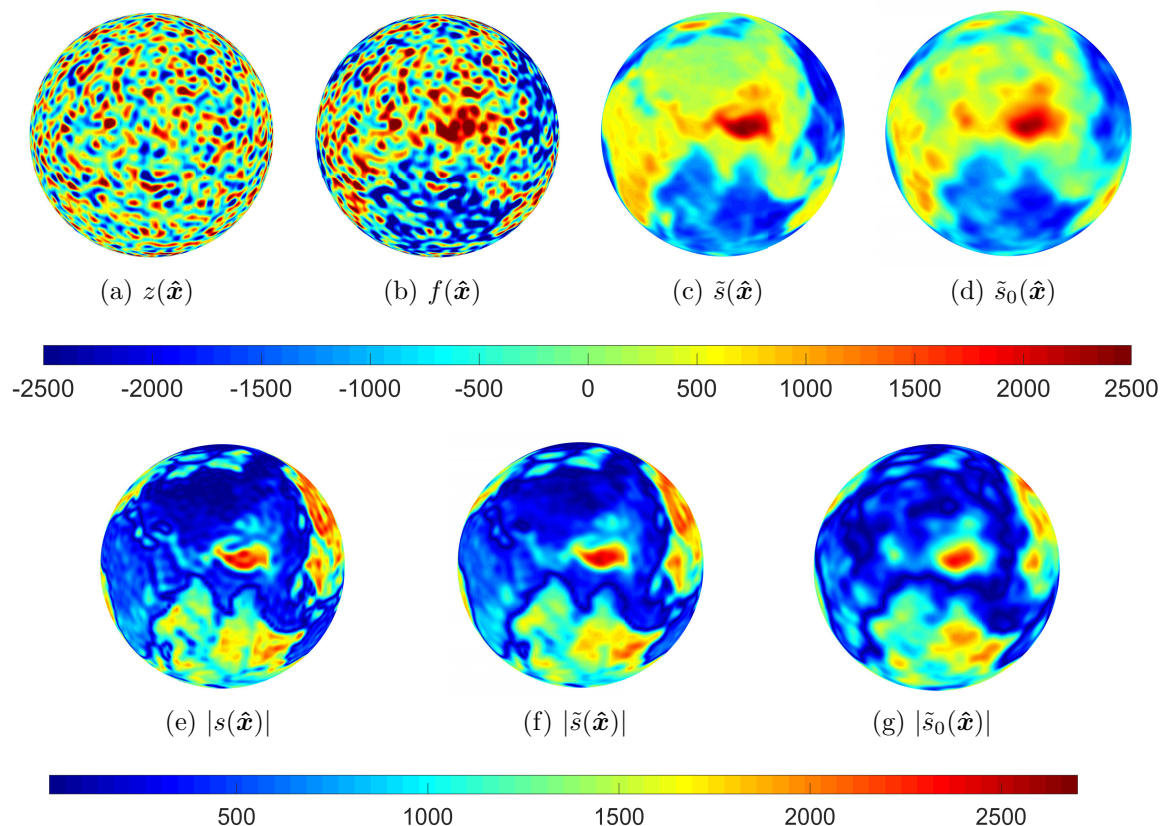


Figure 3-5: (a) Zero-mean, uncorrelated and anisotropic Gaussian noise $z(\hat{\mathbf{x}})$, (b) noise-contaminated observation $f(\hat{\mathbf{x}})$ with $\text{SNR}^f = 0.001$ dBs, (c) signal estimate obtained from the joint $\mathbb{SO}(3)$ -spectral domain filtering framework $\tilde{s}(\hat{\mathbf{x}})$, (d) signal estimate obtained from the joint spatial-spectral domain filtering framework $\tilde{s}_0(\hat{\mathbf{x}})$. Figures (e)–(g) show the magnitude plots of $s(\hat{\mathbf{x}})$, $\tilde{s}(\hat{\mathbf{x}})$ and $\tilde{s}_0(\hat{\mathbf{x}})$. Joint $\mathbb{SO}(3)$ -spectral domain filtering, with $\text{SNR}^{\tilde{s}} = 18.33$ dBs, outperforms the joint spatial-spectral domain filtering by 8 dBs. Moreover, magnitude plots show much better reconstruction of the directional features, such as the dark blue contours marking the boundary between land and water, using the joint $\mathbb{SO}(3)$ -spectral domain filter.

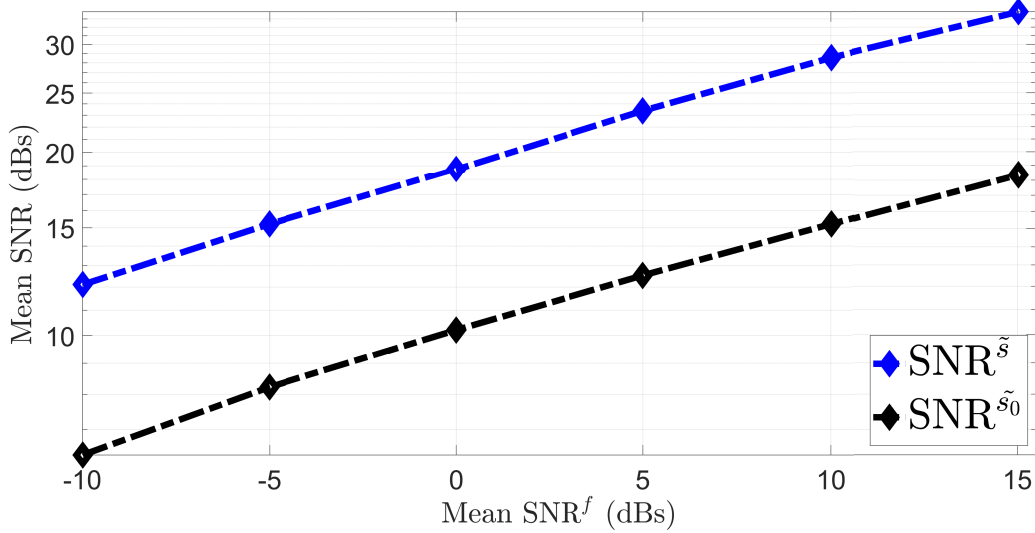


Figure 3-6: Mean output SNR plotted against mean input SNR for 100 realizations of a zero-mean, uncorrelated and anisotropic Gaussian noise process. Blue and black curves show the results for the estimation of Earth topography map, bandlimited to degree $L_f = 64$, using the joint $\mathbb{SO}(3)$ -spectral domain and the joint spatial-spectral domain filtering frameworks respectively.

domain filter, i.e., SNR^s , is measured to be 18.33 dBs, indicating a significant gain in SNR, compared to the joint spatial-spectral domain filtered estimate which results in $\text{SNR}^{s_0} = 10.36$ dBs. As expected, the joint $\mathbb{SO}(3)$ -spectral domain filtering framework outperforms the joint spatial-spectral domain filtering framework (by 8 dBs) due to its ability to better detect the underlying directional features of the data. The results are shown in Figure 3-5, where in addition to better reconstruction using the proposed framework, better estimate of the directional features of the Earth topography map can be observed, e.g., in the dark blue contours marking the boundary between land and water, as depicted in the magnitude plots.

To test the robustness of the proposed framework, we contaminate the Earth topography map with 100 realizations of zero-mean, uncorrelated and anisotropic Gaussian noise process, at different noise levels, and compute the output SNR, i.e., SNR^s . A similar experiment is conducted for the joint spatial-spectral domain filtering framework and SNR^{s_0} is computed. The results are averaged over all realizations and plotted in Figure 3-6, which shows the mean output SNR against the mean input SNR. As can be seen, the joint $\mathbb{SO}(3)$ -spectral domain filter performs much better

compared to the joint spatial-spectral domain filter, even at high noise levels.

3.4 Optimal window design for joint $\mathbb{SO}(3)$ -spectral domain filter

Signal estimation using the joint $\mathbb{SO}(3)$ -spectral domain filtering framework depends on the choice of the directional window signal used for spatial localization of the observation $f(\hat{\mathbf{x}})$. By minimizing the following mean-square error

$$\mathcal{E}_{\text{mse,DW}} = \mathbb{E} \left\{ \sum_{n=0}^{L_f^2-1} |(\tilde{s})_n - (s)_n|^2 \right\}, \quad (3.67)$$

energy per degree of the normalized directional optimal (in the mean-square sense) window signal can be obtained. We present such mathematical formulation in the following theorem.

Theorem 4. *Let $s(\hat{\mathbf{x}})$ be a realization of a random process on the sphere with known spectral covariance matrix $C_{nn'}^s = \mathbb{E} \left\{ (s)_n \overline{(s)_{n'}} \right\}$, which is assumed to be contaminated by a realization of a zero-mean, uncorrelated and anisotropic noise process $z(\hat{\mathbf{x}})$, with known spectral covariance matrix $C_{nn'}^z = \mathbb{E} \left\{ (z)_n \overline{(z)_{n'}} \right\}$, to get the noise-contaminated observation $f(\hat{\mathbf{x}}) = s(\hat{\mathbf{x}}) + z(\hat{\mathbf{x}})$ on the sphere. Using the joint $\mathbb{SO}(3)$ -spectral domain filtering framework, presented in Section 3.3, energy per degree of the normalized directional optimal window signal, which minimizes the mean-square error formulated in (3.67), is given by*

$$\sum_{q'=-p}^p \left| (\hat{h})_p^{q'} \right|^2 = \frac{(2p+1)^2}{32\pi^3} x_p, \quad (\hat{h})_p^{q'} = \frac{(h)_p^{q'}}{\sqrt{\langle h, h \rangle_{\mathbb{S}^2}}}, \quad (3.68)$$

where x_p , for $p = 0, 1, \dots, L_h - 1$, are elements of the column vector \mathbf{x} which is solution to the following linear system

$$\mathbf{G}\mathbf{x} = \mathbf{b}. \quad (3.69)$$

Elements of the matrix \mathbf{G} and column vector \mathbf{b} are given by

$$\begin{aligned} G_{p',p} &= \sum_{n=0}^{L_f^2-1} 2 \operatorname{Re} \left\{ \mathbb{E} \left\{ F(n; p') \overline{F(n; p)} \right\} \right\}, \\ b_{p'} &= \sum_{n=0}^{L_f^2-1} 2 \operatorname{Re} \left\{ \mathbb{E} \left\{ F(n; p') \overline{(s)_n} \right\} \right\}, \end{aligned} \quad 0 \leq p, p' \leq L_h - 1, \quad (3.70)$$

where

$$F(n; p) = \sum_{u=0}^{L_g-1} \sum_{q=-p}^p T(n; p, q; u) \sum_{k=-p}^p (\zeta(\cdot; u))_{q,k}^p \sum_{n'=0}^{L_f-1} (f)_{n'} T(n'; p, k; u), \quad (3.71)$$

and $L_g = L_f + L_h - 1$.

Proof. Using (3.71), source spectral estimate in (3.66) can be rewritten as

$$(\tilde{s})_n = 32\pi^3 \sum_{p=0}^{L_h-1} \frac{1}{(2p+1)^2} \sum_{q'=-p}^p (\hat{h})_p^{q'} \overline{(\hat{h})_p^{q'}} F(n; p), \quad (\hat{h})_p^{q'} \triangleq \frac{(h)_p^{q'}}{\sqrt{\langle h, h \rangle_{\mathbb{S}^2}}}, \quad (3.72)$$

where we have normalized the spectral coefficients of the directional window signal by the norm of the window signal. Using this formulation, the mean-square error in (3.67) can be written as

$$\begin{aligned} \mathcal{E}_{\text{mse,DW}} &= \sum_{n=0}^{L_f^2-1} \mathbb{E} \left\{ \left(\sum_{p=0}^{L_h-1} \frac{32\pi^3}{(2p+1)^2} \sum_{q'=-p}^p \overline{(\hat{h})_p^{q'}} (\hat{h})_p^{q'} F(n; p) - (s)_n \right) \times \right. \\ &\quad \left. \overline{\left(\sum_{p'=0}^{L_h-1} \frac{32\pi^3}{(2p'+1)^2} \sum_{q''=-p'}^{p'} \overline{(\hat{h})_{p'}^{q''}} (\hat{h})_{p'}^{q''} F(n; p') - (s)_n \right)} \right\} \\ &= \sum_{n=0}^{L_f^2-1} \sum_{p,p'=0}^{L_h-1} \frac{32\pi^3}{(2p+1)^2} \frac{32\pi^3}{(2p'+1)^2} \sum_{q'=-p}^p \overline{(\hat{h})_p^{q'}} (\hat{h})_p^{q'} \sum_{q''=-p'}^{p'} \overline{(\hat{h})_{p'}^{q''}} (\hat{h})_{p'}^{q''} \left(\mathbb{E} \{ F(n; p) \overline{F(n; p')} \} \right) - \\ &\quad \sum_{n=0}^{L_f^2-1} \sum_{p=0}^{L_h-1} \frac{32\pi^3}{(2p+1)^2} \sum_{q'=-p}^p \overline{(\hat{h})_p^{q'}} (\hat{h})_p^{q'} \left[\mathbb{E} \{ F(n; p) \overline{(s)_n} \} + \mathbb{E} \{ \overline{F(n; p)} (s)_n \} \right] + \sum_{n=0}^{L_f^2-1} \mathbb{E} \{ (s)_n \overline{(s)_n} \}. \end{aligned} \quad (3.73)$$

Setting the derivative of $\mathcal{E}_{\text{mse,DW}}$ in (3.73) with respect to $\overline{(\hat{h})_{p_1}^{q_1}}$ equal to zero, we get

the following expression

$$\begin{aligned}
 \frac{\partial \mathcal{E}_{\text{mse,DW}}}{\partial (\hat{h})_{p_1}^{q_1}} &= \sum_{n=0}^{L_f^2-1} \frac{32\pi^3}{(2p_1+1)^2} (\hat{h})_{p_1}^{q_1} \sum_{p'=0}^{L_h-1} \frac{32\pi^3}{(2p'+1)^2} \sum_{q''=-p'}^{p'} (\hat{h})_{p'}^{q''} (\hat{h})_{p'}^{q''} \left(\mathbb{E}\{F(n;p_1)\overline{F(n;p')}\} \right) \\
 &+ \sum_{n=0}^{L_f^2-1} \frac{32\pi^3}{(2p_1+1)^2} (\hat{h})_{p_1}^{q_1} \sum_{p=0}^{L_h-1} \frac{32\pi^3}{(2p+1)^2} \sum_{q'=-p}^p (\hat{h})_p^{q'} (\hat{h})_p^{q'} \left(\mathbb{E}\{F(n;p)\overline{F(n;p_1)}\} \right) - \\
 &\quad \sum_{n=0}^{L_f^2-1} \frac{32\pi^3}{(2p_1+1)^2} (\hat{h})_{p_1}^{q_1} \left(\mathbb{E}\{F(n;p_1)\overline{(s)_n}\} + \mathbb{E}\{\overline{F(n;p_1)}(s)_n\} \right) + 0 = 0, \\
 &\sum_{n=0}^{L_f^2-1} \sum_{p=0}^{L_h-1} \frac{32\pi^3}{(2p+1)^2} \sum_{q'=-p}^p (\hat{h})_p^{q'} (\hat{h})_p^{q'} \left[\mathbb{E}\{F(n;p')\overline{F(n;p)}\} + \mathbb{E}\{F(n;p)\overline{F(n;p')}\} \right] \\
 &= \sum_{n=0}^{L_f^2-1} \left[\mathbb{E}\{F(n;p')\overline{(s)_n} + \overline{F(n;p')}(s)_n\} \right], \quad 0 \leq p' \leq L_h - 1.
 \end{aligned} \tag{3.74}$$

By defining x_p as

$$x_p \triangleq \frac{32\pi^3}{(2p+1)^2} \sum_{q'=-p}^p \left| (\hat{h})_p^{q'} \right|^2, \tag{3.75}$$

the set of equations in (3.74) can be cast in the matrix form given in (3.69) using the definitions in (3.70). Therefore, inverting (3.75) results in the energy per degree of the normalized directional optimal window signal given in (3.68). \square

Remark 3. *Energy per degree (and hence, the spectral coefficients) of the normalized directional optimal window signal in (3.68) is specified by the spectral covariance (through the joint $\mathbb{SO}(3)$ -spectral domain filter) and hence, by statistics of both the source and noise processes. The linear system in (3.68) is under-determined and there are multiple solutions (avoiding those which result in azimuthally symmetric window signal) for the spectral coefficients of the normalized directional optimal window signal. However, every solution yields the same result, because the spectral estimate in (3.72) and the mean-square error in (3.67) only depend on the energy per degree of the window signal.*

3.4.1 Directional optimal window design – Alternative formulation

We can rewrite the normalized directional optimal window design problem as

$$\begin{aligned} \underset{(\hat{h})_p^{q'}}{\text{minimize}} \mathcal{E}_{\text{mse,DW}} &= \mathbb{E} \left\{ \sum_{n=0}^{L_f^2-1} |(\tilde{s})_n - (s)_n|^2 \right\}, \\ \text{subject to } (\tilde{s})_n &= \sum_{p=0}^{L_h-1} \frac{32\pi^3}{(2p+1)^2} \sum_{q'=-p}^p (\hat{h})_p^{q'} \overline{(\hat{h})_p^{q'}} F(n; p), \end{aligned} \quad (3.76)$$

which results in the solution given by (3.68), where $F(n; p)$ is given in (3.71). This formulation results in energy per degree of the normalized directional window signal. An alternative formulation for the design of directional optimal window is given by

$$\begin{aligned} \underset{(h)_p^{q'}}{\text{minimize}} \mathcal{E}_{\text{mse,DW}} &= \mathbb{E} \left\{ \sum_{n=0}^{L_f^2-1} |\langle h, h \rangle_{\mathbb{S}^2} (\tilde{s})_n - (s)_n|^2 \right\}, \\ \text{subject to } (\tilde{s})_n &= \frac{1}{\langle h, h \rangle_{\mathbb{S}^2}} \sum_{p=0}^{L_h-1} \frac{32\pi^3}{(2p+1)^2} \sum_{q'=-p}^p (h)_p^{q'} \overline{(h)_p^{q'}} F(n; p), \end{aligned} \quad (3.77)$$

which gives the same form of the mean-square error as that obtained from (3.76) and hence, results in the same expression for energy per degree of the window signal, i.e.,

$$\sum_{q'=-p}^p \left| (h)_p^{q'} \right|^2 = \frac{(2p+1)^2}{32\pi^3} x_p. \quad (3.78)$$

Moreover, the formulation in (3.77) is equivalent to that in (3.76) because

$$\left\langle \hat{h}, \hat{h} \right\rangle_{\mathbb{S}^2} = \sum_{p,q'}^{L_h-1} \frac{\left| (h)_p^{q'} \right|^2}{\langle h, h \rangle_{\mathbb{S}^2}} = 1 \Rightarrow \sum_{p=0}^{L_h-1} \frac{(2p+1)^2}{32\pi^3} x_p = 1 \Rightarrow \sum_{p,q'}^{L_h-1} \left| (h)_p^{q'} \right|^2 = \langle h, h \rangle_{\mathbb{S}^2} = 1, \quad (3.79)$$

where we have used (3.68) and (3.78) to get the final result. Hence, the formulation in (3.77) (in which x_p , $0 \leq p \leq L_h - 1$, is given by the solution of (3.69)) yields energy per degree of the directional optimal window signal without any normalization.

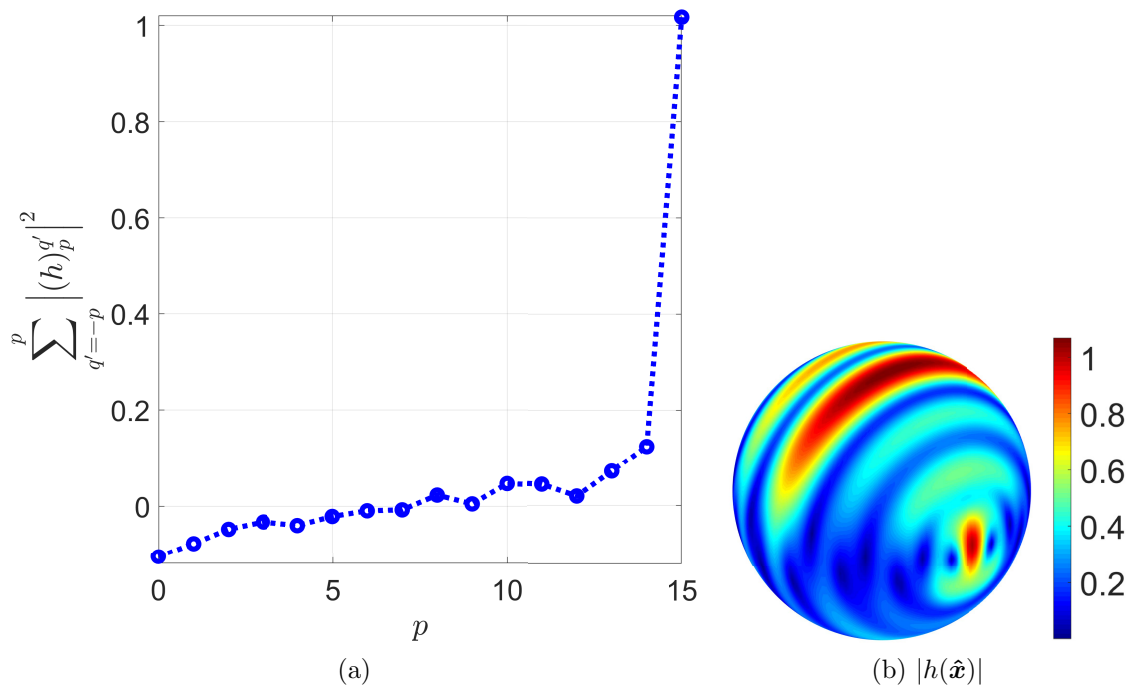


Figure 3-7: (a) Energy per degree plot of the directional optimal window signal for the Earth topography map, bandlimited to degree $L_f = 32$, constructed for a zero-mean, uncorrelated and anisotropic Gaussian noise process at $\text{SNR} = 0$ dBs. (b) Magnitude of the directional optimal window signal on the sphere. Directional optimal window signal is bandlimited to degree $L_h = 16$.

3.4.2 Illustrations

We compute energy per degree of the directional optimal window signal, at bandlimit $L_h = 16$ using (3.78), for the Earth topography map $s(\hat{\mathbf{x}})$, bandlimited to degree $L_f = 32$, and zero-mean, uncorrelated, anisotropic Gaussian noise process at $\text{SNR} = 0$ dBs⁹. We choose the spectral coefficients of the directional optimal window signal to satisfy (3.78) as

$$|(h)_p^q| = (h)_p^q = \sqrt{\frac{(2p+1)x_p}{32\pi^3}}, \quad 0 \leq p \leq L_h - 1, |q| \leq p. \quad (3.80)$$

Figure 3-7 shows the energy per degree plot and magnitude of the directional optimal window signal on the sphere. Using this energy per degree for the directional optimal window signal, we estimate the bandlimited Earth topography map contaminated by

⁹For the spectral covariance matrix of the Earth topography map, please see Section 3.3.3.

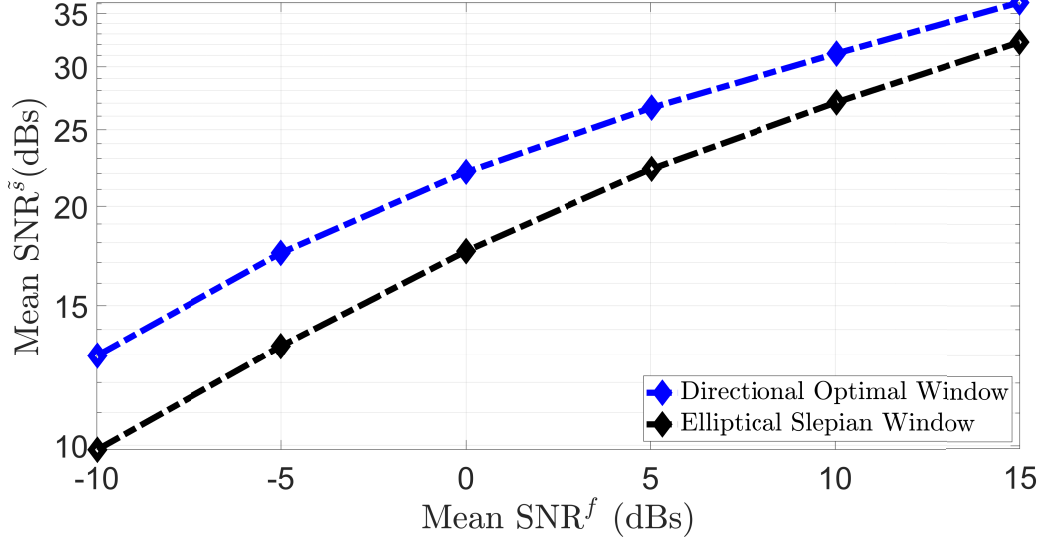


Figure 3-8: Mean output SNR plotted against mean input SNR for 100 realizations of zero-mean, uncorrelated and anisotropic Gaussian noise process. Blue and black curves quantify the performance of the joint $\mathbb{S}\mathbb{O}(3)$ -spectral domain filter using directional optimal window signal and rank 1 Slepian window signal (computed for the spherical ellipse $R_{(15^\circ, 16^\circ)}$) respectively, on the Earth topography map, bandlimited to degree $L_f = 32$.

100 realizations of zero-mean, uncorrelated and anisotropic Gaussian noise process at different noise levels. For comparison, we use the most well-optimally concentrated Slepian function within the elliptical region $R_{(15^\circ, 16^\circ)}$, as another window signal at bandlimit $L_h = 16$, to estimate the Earth topography map for the same realizations of the noise process, and denote the signal estimate by $\tilde{s}_1(\hat{\mathbf{x}})$. Output SNR of the joint $\mathbb{S}\mathbb{O}(3)$ -spectral domain filtering and signal estimation framework, for both directional window signals, is averaged over all realizations and plotted against the mean input SNR in Figure 3-8, which shows significant improvement in the performance of joint $\mathbb{S}\mathbb{O}(3)$ -spectral domain signal estimation using directional optimal window signal.

Reconstructed Earth topography map, for a realization of the zero-mean, uncorrelated and anisotropic Gaussian process at $\text{SNR}^f = -0.15$ dBs, using the directional optimal window signal, is shown in Figure 3-9. For comparison, we also show the reconstructed map using the most well-optimally concentrated elliptical Slepian function within $R_{(15^\circ, 16^\circ)}$, along with the original Earth topography map, noise realization and noise-contaminated observation. Output SNR measured from the spectral esti-

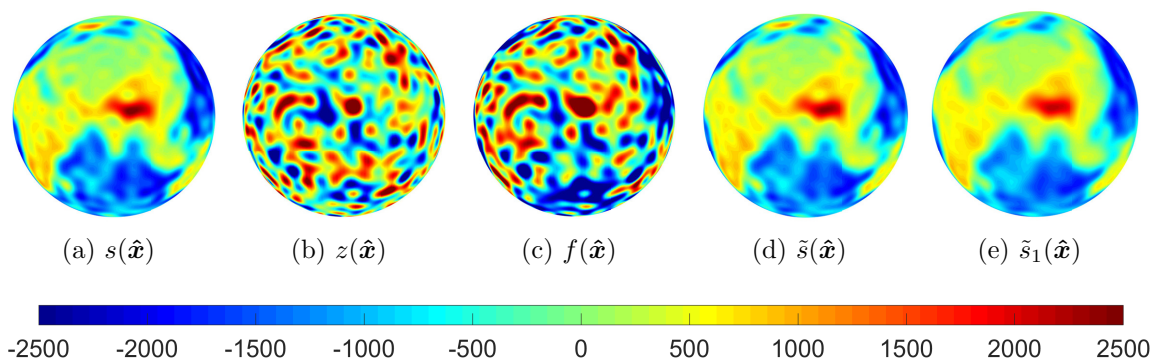


Figure 3-9: Joint $\mathbb{SO}(3)$ -spectral domain filtering of the Earth topography map $s(\hat{\mathbf{x}})$, bandlimited to degree $L_f = 32$, contaminated by a realization of a zero-mean, uncorrelated and anisotropic Gaussian noise process $z(\hat{\mathbf{x}})$ at $\text{SNR}^f = -0.15$ dBs, resulting in an SNR gain of 20.37 dBs for the signal estimate $\tilde{s}(\hat{\mathbf{x}})$, compared to an SNR gain of 16.39 dBs for $\tilde{s}_1(\hat{\mathbf{x}})$.

mates $\tilde{s}(\hat{\mathbf{x}})$ and $\tilde{s}_1(\hat{\mathbf{x}})$ is 20.22 dBs and 16.24 dBs respectively. Higher output SNR is reflected in better reconstruction of $\tilde{s}(\hat{\mathbf{x}})$ compared to $\tilde{s}_1(\hat{\mathbf{x}})$.

3.5 Multiscale optimal filter

Wavelet transforms offer another joint domain representation by projecting the signal content onto wavelet functions. In particular, scale-discretized wavelet transform, reviewed in Section 2.9, projects the signal onto rotated wavelet functions, which in turn form a tight frame on the sphere [85]. The transformed signal is represented by wavelet coefficients, which are defined on the $\mathbb{SO}(3)$ rotation group (or the sphere for axisymmetric wavelet functions) at different wavelet scales and hence, constitute joint $\mathbb{SO}(3)$ -scale domain representation of signals on the sphere.

Following the philosophy of the framework of joint $\mathbb{SO}(3)$ -spectral domain filter, presented in Section 3.3, we employ the scale-discretized wavelet transform to define a joint $\mathbb{SO}(3)$ -scale domain (or multiscale) filter distribution as

$$\Xi(\rho) \triangleq [\Xi(\rho; 0), \Xi(\rho; 1), \dots, \Xi(\rho; j_2)]^T, \quad (3.81)$$

where j_2 is the largest wavelet scale, and each joint $\mathbb{SO}(3)$ -scale domain filter distri-

bution component $\Xi(\rho; j)$ is a bandlimited signal on the $\mathbb{SO}(3)$ rotation group, given by

$$\begin{aligned} \Xi(\rho; j) &= \sum_{\ell, m, m'}^{L_{\Xi_j} - 1} (\Xi(\cdot; j))_{m, m'}^\ell \overline{D_{m, m'}^\ell(\rho)}, \\ (\Xi(\cdot; j))_{m, m'}^\ell &\triangleq \left(\frac{2\ell + 1}{8\pi^2} \right) \left\langle \Xi(\cdot; j), \overline{D_{m, m'}^\ell} \right\rangle_{\mathbb{SO}(3)}, \end{aligned} \quad (3.82)$$

for the wavelet scale $j \in [0, j_2]$, where L_{Ξ_j} is the bandlimit of the filter component at wavelet scale j . Action of the filter component on scale-discretized wavelet coefficients of the noise-contaminated observation $f(\hat{\mathbf{x}})$ is defined by the spectral representation of convolution of signals on the $\mathbb{SO}(3)$ rotation group, given in (2.85), i.e.,

$$w_s^{\Psi^{(j)}}(\rho) = \sum_{\ell=0}^{L_f - 1} \left(\frac{8\pi^2}{2\ell + 1} \right) \sum_{m, m' = -\ell}^{\ell} \sum_{k=-\ell}^{\ell} (f)_\ell^k (\Xi(\cdot; j))_{m, k}^\ell \overline{(\Psi^{(j)})_\ell^{m'} D_{m, m'}^\ell(\rho)}, \quad (3.83)$$

to define the filtered $\mathbb{SO}(3)$ -scale representation as

$$\mathbf{w}_s^\Psi(\rho) \triangleq \left[w_s^{\Psi^{(0)}}(\rho), w_s^{\Psi^{(1)}}(\rho), \dots, w_s^{\Psi^{(j_2)}}(\rho) \right]^\top, \quad (3.84)$$

where $w_s^{\Psi^{(j)}}(\rho)$ is the scale-discretized wavelet coefficient of the estimate of the source signal $s(\hat{\mathbf{x}})$ and we have assumed, without loss of generality, that bandlimit of the filter component at each wavelet scale is equal to the signal bandlimit, i.e., $L_{\Xi_j} = L_f$, $j \in [0, j_2]$. Spectral components of the filter function in (3.82) are obtained by minimizing the following mean-square error in the joint $\mathbb{SO}(3)$ -scale domain

$$\mathcal{E}_{\text{mse}} = \mathbb{E} \left\{ \sum_{j=0}^{j_2} \left\| w_s^{\Psi^{(j)}}(\rho) - w_s^{\Psi^{(j)}}(\rho) \right\|_{\mathbb{SO}(3)}^2 \right\}, \quad (3.85)$$

which makes the multiscale filter optimal in the mean-square sense. Here $w_s^{\Psi^{(j)}}(\rho)$ is the scale-discretized wavelet coefficient of source signal $s(\hat{\mathbf{x}})$ at wavelet scale j . We present the mathematical formulation for the spectral components of the multiscale optimal filter in the following theorem.

Theorem 5. *Let the source signal $s(\hat{\mathbf{x}})$ be a realization of an anisotropic random process which is contaminated by a realization of a zero-mean and anisotropic noise process $z(\hat{\mathbf{x}})$, to obtain the noise-contaminated observation $f(\hat{\mathbf{x}}) = s(\hat{\mathbf{x}}) + z(\hat{\mathbf{x}})$ on the sphere, where the source and noise signals are uncorrelated with known spectral covariance, defined by matrices $C_{\ell m, pq}^s = \mathbb{E} \left\{ (s)_\ell^m \overline{(s)_p^q} \right\}$ and $C_{\ell m, pq}^z = \mathbb{E} \left\{ (z)_\ell^m \overline{(z)_p^q} \right\}$ respectively. Then, spectral coefficients of the joint $\mathbb{SO}(3)$ -scale domain filter function in (3.82), which minimize the joint $\mathbb{SO}(3)$ -scale domain mean-square error in (3.85), are obtained by inverting the following linear system*

$$\mathbf{G}(\ell) \mathbf{x}(j, \ell, m) = \mathbf{b}(\ell, m), \quad (3.86)$$

for $0 \leq \ell \leq L_f - 1$, $|m| \leq \ell$, $0 \leq j \leq j_2$, where elements of the column vector $\mathbf{x}(j, \ell, m)$ are given by $x_k = (\Xi(\cdot; j))_{m, k}^\ell$, $|k| \leq \ell$, and elements of the matrix \mathbf{G} and column vector \mathbf{b} are given by

$$G_{k', k} = \left(\frac{8\pi^2}{2\ell + 1} \right) (C_{\ell k, \ell k'}^s + C_{\ell k, \ell k'}^z), \quad b_{k'} = C_{\ell m, \ell k'}^s, \quad |k'| \leq \ell. \quad (3.87)$$

Proof. Using the expression for wavelet coefficients in (2.101) and (3.83), the joint $\mathbb{SO}(3)$ -scale domain mean-square error in (3.85) can be written as

$$\begin{aligned} \mathcal{E}_{\text{mse}} &= \mathbb{E} \left\{ \sum_{j=0}^{j_2} \left\langle \sum_{\ell, m, m'}^{L_f-1} \left(\frac{8\pi^2}{2\ell + 1} \sum_{k=-\ell}^{\ell} (f)_\ell^k \overline{(\Psi^{(j)})_\ell^{m'}} (\Xi(\cdot; j))_{m, k}^\ell - (s)_\ell^m \overline{(\Psi^{(j)})_\ell^{m'}} \right) \times \right. \right. \\ &\quad \left. \left. \overline{D_{m, m'}^\ell}, \sum_{p, q, q'}^{L_f-1} \left(\frac{8\pi^2}{2p + 1} \sum_{k'=-p}^p (f)_p^{k'} \overline{(\Psi^{(j)})_p^{q'}} (\Xi(\cdot; j))_{q, k'}^p - (s)_p^q \overline{(\Psi^{(j)})_p^{q'}} \right) \overline{D_{q, q'}^p} \right\rangle_{\mathbb{SO}(3)} \right\} \\ &= \sum_{j=0}^{j_2} \sum_{\ell, m, m'}^{L_f-1} \left(\frac{8\pi^2}{2\ell + 1} \right) \mathbb{E} \left\{ \left(\frac{8\pi^2}{2\ell + 1} \sum_{k=-\ell}^{\ell} (f)_\ell^k \overline{(\Psi^{(j)})_\ell^{m'}} (\Xi(\cdot; j))_{m, k}^\ell - (s)_\ell^m \overline{(\Psi^{(j)})_\ell^{m'}} \right) \times \right. \\ &\quad \left. \overline{\left(\frac{8\pi^2}{2\ell + 1} \sum_{k'=-\ell}^{\ell} (f)_\ell^{k'} \overline{(\Psi^{(j)})_\ell^{m'}} (\Xi(\cdot; j))_{m, k'}^\ell - (s)_\ell^m \overline{(\Psi^{(j)})_\ell^{m'}} \right)} \right\}, \end{aligned} \quad (3.88)$$

where we have used orthogonality of Wigner- D functions on the $\mathbb{SO}(3)$ rotation group.

Setting the derivative of \mathcal{E}_{mse} in (3.88) with respect to $\overline{(\Xi(\cdot; j))_{m,k}^\ell}$ equal to zero and noting the fact that the source and noise signals are uncorrelated, i.e., (3.56), we get the following linear system

$$\sum_{k=-\ell}^{\ell} \left(\frac{8\pi^2}{2\ell+1} \right) (C_{\ell k, \ell k'}^s + C_{\ell k, \ell k'}^z) (\Xi(\cdot; j))_{m,k}^\ell = C_{\ell m, \ell k'}^s, \quad |m|, |k'| \leq \ell, \quad (3.89)$$

which can be cast in the matrix form given in (3.86) using the expressions in (3.87)¹⁰. \square

Having found the spectral representation of the joint $\mathbb{SO}(3)$ -scale domain filter, signal estimate $\tilde{s}(\hat{\mathbf{x}})$ is obtained from the wavelet coefficients in (3.83), using (2.104), as

$$\begin{aligned} \tilde{s}(\hat{\mathbf{x}}) &= \int_{\mathbb{S}^2} w_f^\Phi(\hat{\mathbf{y}}) (\mathcal{D}(\hat{\mathbf{y}})\Phi)(\hat{\mathbf{x}}) ds(\hat{\mathbf{y}}) + \sum_{j=0}^{j_2} \int_{\mathbb{SO}(3)} w_s^{\Psi^{(j)}}(\rho) (\mathcal{D}(\rho)\Psi^{(j)})(\hat{\mathbf{x}}) d\rho \\ &= \sum_{\ell, m}^{L_f-1} \frac{4\pi}{2\ell+1} \left[|(\Phi)_\ell^0|^2 (f)_\ell^m + 2\pi \sum_{m'=-\ell}^{\ell} \sum_{j=0}^{j_2} \left| (\Psi^{(j)})_\ell^{m'} \right|^2 \sum_{k=-\ell}^{\ell} (f)_\ell^k (\Xi(\cdot; j))_{m,k}^\ell \right] Y_\ell^m(\hat{\mathbf{x}}), \end{aligned} \quad (3.90)$$

where we have used the scaling coefficient in (2.106) and the expression in (2.107) to obtain the final result.

Remark 4. For wavelet functions which are axisymmetric, i.e., $(\Psi^{(j)})_\ell^m = (\Psi^{(j)})_\ell^0 \delta_{m,0}$, scale-discretized wavelet coefficients, given by (2.108), are functions defined on the sphere. Hence, instead of the joint $\mathbb{SO}(3)$ -scale domain filter, we design a joint space-scale domain filter as

$$\Xi(\hat{\mathbf{x}}; j) = \sum_{\ell, m}^{L_{\Xi_j}-1} (\Xi(\cdot; j))_\ell^m Y_\ell^m(\hat{\mathbf{x}}), \quad L_{\Xi_j} = L_f, \quad j \in [0, j_2], \quad (3.91)$$

whose action on the noise-contaminated observation $f(\hat{\mathbf{x}})$ is defined by the convolution

¹⁰It must be noted that the linear system formulated in (3.86) may become ill-conditioned at severely low noise levels, in which case Moore-Penrose pseudo-inverse can be used to obtain the filter coefficients $(\Xi(\cdot; j))_{m,k}^\ell$.

of spherical signals, given by (2.78), i.e.,

$$w_s^{\Psi^{(j)}}(\hat{\mathbf{x}}) = \sum_{\ell, m}^{L_f-1} \left(\sqrt{\frac{4\pi}{2\ell+1}} (f)_\ell^m \overline{(\Psi^{(j)})_\ell^0} \right) (\Xi(\cdot; j))_\ell^m Y_\ell^m(\hat{\mathbf{x}}), \quad (3.92)$$

which necessitates the minimization of the following joint space-scale domain mean-square error for finding the spectral coefficients of the filter function in (3.91)

$$\mathcal{E}_{\text{mse}} = \mathbb{E} \left\{ \sum_{j=0}^{j_2} \left\| w_s^{\Psi^{(j)}}(\hat{\mathbf{x}}) - w_s^{\Psi^{(j)}}(\hat{\mathbf{x}}) \right\|_{\mathbb{S}^2}^2 \right\}. \quad (3.93)$$

From the relation between Wigner-D functions and spherical harmonics in (2.49), it can be seen that (3.92) can be obtained from (3.83) by setting $m' = 0$ and $(\Xi(\cdot; j))_{m, k}^\ell = \left(\frac{2\ell+1}{8\pi^2}\right) (\Xi(\cdot; j))_\ell^m \delta_{m, k}$. Hence, by setting $k = k' = m$ in (3.87), spectral coefficients of the filter in (3.91) can be directly obtained from (3.86) and (3.87) as

$$(\Xi(\cdot; j))_\ell^m = \frac{C_{\ell m, \ell m}^s}{(C_{\ell m, \ell m}^s + C_{\ell m, \ell m}^z)}. \quad (3.94)$$

Solving (2.109) using (2.106), (2.111) and (3.92), signal estimate is obtained as

$$\tilde{s}(\hat{\mathbf{x}}) = \sum_{\ell, m}^{L_f-1} \left(\frac{4\pi}{2\ell+1} \right) \left[|(\Phi)_\ell^0|^2 + \sum_{j=0}^{j_2} |(\Psi^{(j)})_\ell^0|^2 (\Xi(\cdot; j))_\ell^m \right] (f)_\ell^m Y_\ell^m(\hat{\mathbf{x}}). \quad (3.95)$$

3.5.1 Analysis

Performance of the multiscale optimal filter is analyzed by using the Earth topography, bandlimited to degree $L_f = 64$, as the source signal $s(\hat{\mathbf{x}})$, for which the spectral covariance matrix is given by $C_{\ell m, p q}^s = (s)_\ell^m \overline{(s)_p^q}$. We use azimuthally symmetric wavelet and scaling functions for filtering and estimation of the Earth topography map, by setting the dilation parameter ϵ to 2. Largest wavelet scale is set to J , which from (2.119) becomes 6 at bandlimit $L_f = 64$, resulting in a total of 7 wavelet scales. Figure 3-10 shows an illustration of the multiscale optimal filtering framework in which the Earth topography map is contaminated by zero-mean, uncorrelated and

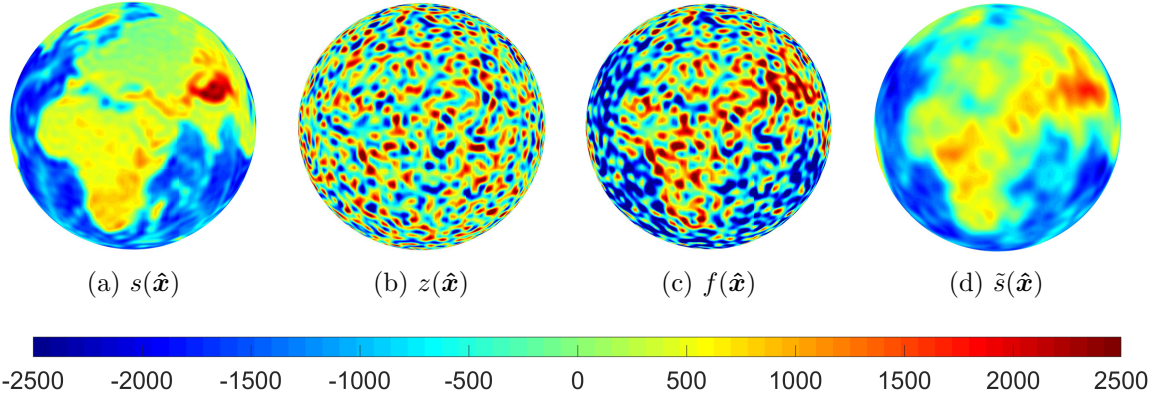


Figure 3-10: Multiscale optimal filtering of the Earth topography map $s(\hat{\mathbf{x}})$, bandlimited to degree $L_f = 64$, which is contaminated by zero-mean, uncorrelated and white Gaussian noise $z(\hat{\mathbf{x}})$ at $\text{SNR}^f = -0.057$ dBs. Output SNR obtained from the source signal estimate $\tilde{s}(\hat{\mathbf{x}})$ is 9.68 dBs, resulting in SNR improvement of 9.7 dBs.

white Gaussian noise¹¹ at $\text{SNR}^f = -0.057$ dBs. The output SNR is measured to be 9.68 dBs, giving an SNR gain of 9.7 dBs.

Comparison with hard thresholding and weighted-SPHARM methods

Performance of the multiscale optimal filtering framework is compared with the hard thresholding method for signal denoising [84], in which the filtered wavelet coefficient, at wavelet scale j , is given by the following hard thresholding scheme

$$w_{\tilde{s}}^{\Psi^{(j)}}(\hat{\mathbf{x}}) = \begin{cases} 0, & |w_f^{\Psi^{(j)}}(\hat{\mathbf{x}})| < 3\sigma_j, \\ w_f^{\Psi^{(j)}}(\hat{\mathbf{x}}), & \text{otherwise,} \end{cases} \quad (3.96)$$

where $3\sigma_j$ is the threshold and σ_j^2 is the noise variance in the wavelet domain, i.e., [84]

$$\begin{aligned} \sigma_j^2 &\triangleq \mathbb{E} \left\{ \left| w_z^{\Psi^{(j)}}(\hat{\mathbf{x}}) \right|^2 \right\} = \sum_{\ell, m}^{L_f-1} \sqrt{\frac{4\pi}{2\ell+1}} (\Psi^{(j)})_{\ell}^0 Y_{\ell}^m(\hat{\mathbf{x}}) \sum_{p, q}^{L_f-1} \sqrt{\frac{4\pi}{2p+1}} (\Psi^{(j)})_p^0 \overline{Y_p^q(\hat{\mathbf{x}})} \times \\ &\mathbb{E} \left\{ (z_{\ell}^m \overline{(z_p^q)}) \right\} = \sigma^2 \sum_{\ell=0}^{L_f-1} \left(\frac{4\pi}{2\ell+1} \right) \left| (\Psi^{(j)})_{\ell}^0 \right|^2 \left(\frac{2\ell+1}{4\pi} \right) P_{\ell}(\hat{\mathbf{x}} \cdot \hat{\mathbf{x}}) = \sigma^2 \sum_{\ell=0}^{L_f-1} \left| (\Psi^{(j)})_{\ell}^0 \right|^2, \end{aligned} \quad (3.97)$$

¹¹White noise parameter σ^2 in (3.14) is specified by $\text{SNR} = 0$ dBs for this illustration.

where we have used the expression for wavelet coefficients in (2.108), the definition of white noise spectral covariance matrix in (3.13), spherical harmonic addition theorem in (2.34), and the fact that $P_\ell(1) = 1$, to get the final result.

Multiscale optimal filter is also compared with the weighted spherical harmonic (weighted-SPHARM) framework presented in [110], which uses Gauss-Weierstrass kernel smoothing (GWKS) to obtain the signal estimate by minimizing the following weighted squared error¹²

$$\begin{aligned} \mathcal{E}_{\text{KS}} &\triangleq \int_{\mathbb{S}^2} \int_{\mathbb{S}^2} \overline{K_{\text{GW}}(\hat{\mathbf{x}}, \hat{\mathbf{y}})} |f(\hat{\mathbf{y}}) - \tilde{s}_{\text{GW}}(\hat{\mathbf{x}})|^2 ds(\hat{\mathbf{y}}) ds(\hat{\mathbf{x}}) \\ &= \int_{\mathbb{S}^2} \int_{\mathbb{S}^2} \overline{K_{\text{GW}}(\hat{\mathbf{x}}, \hat{\mathbf{y}})} \left(f(\hat{\mathbf{y}}) - \sum_{\ell, m}^{L_f-1} (\tilde{s}_{\text{GW}})_\ell^m Y_\ell^m(\hat{\mathbf{x}}) \right) \\ &\quad \overline{\left(f(\hat{\mathbf{y}}) - \sum_{p, q}^{L_f-1} (\tilde{s}_{\text{GW}})_p^q Y_p^q(\hat{\mathbf{x}}) \right)} ds(\hat{\mathbf{y}}) ds(\hat{\mathbf{x}}), \end{aligned} \quad (3.98)$$

where $\tilde{s}_{\text{GW}}(\hat{\mathbf{x}})$ denotes the estimate of the source signal $s(\hat{\mathbf{x}})$, obtained from Gauss-Weierstrass kernel smoothing, and $K_{\text{GW}}(\hat{\mathbf{x}}, \hat{\mathbf{y}})$ is the self-adjoint Gauss-Weierstrass (GW) kernel given by [111]

$$K_{\text{GW}}(\hat{\mathbf{x}}, \hat{\mathbf{y}}) = \sum_{\ell, m}^{L_f-1} e^{-\ell(\ell+1)\kappa} Y_\ell^m(\hat{\mathbf{x}}) \overline{Y_\ell^m(\hat{\mathbf{y}})}, \quad \kappa \in [0, 1], \quad (3.99)$$

which satisfies the following

$$\int_{\mathbb{S}^2} K_{\text{GW}}(\hat{\mathbf{x}}, \hat{\mathbf{y}}) ds(\hat{\mathbf{y}}) = \sum_{\ell, m}^{L_f-1} e^{-\ell(\ell+1)\kappa} Y_\ell^m(\hat{\mathbf{x}}) \int_{\mathbb{S}^2} \overline{Y_\ell^m(\hat{\mathbf{y}})} ds(\hat{\mathbf{y}}) = 1, \quad (3.100)$$

where we have used the expressions in (2.95) and (2.96) to solve the integral.

Differentiating \mathcal{E}_{KS} with respect to $(\tilde{s}_{\text{GW}})_\ell^m$ and putting the result equal to zero

¹²Signal estimate obtained from weighted-SPHARM method will remain unchanged if Gauss-Weierstrass kernel K_{GW} is used without complex conjugation in (3.98) and the error is optimized with respect to $(\tilde{s}_{\text{GW}})_p^q$. We use complex conjugate of K_{GW} to reproduce the results of weighted-SPHARM using complex spherical harmonics in exactly the same manner as in [110], i.e., optimizing with respect to $(\tilde{s}_{\text{GW}})_\ell^m$ (and not with its complex conjugate).

gives the spectral estimate of the source signal as

$$\begin{aligned}
 (\tilde{s}_{\text{GW}})_\ell^m &= \int_{\mathbb{S}^2} \overline{Y_\ell^m(\hat{\mathbf{x}})} \int_{\mathbb{S}^2} f(\hat{\mathbf{y}}) K(\hat{\mathbf{x}}, \hat{\mathbf{y}}) ds(\hat{\mathbf{y}}) ds(\hat{\mathbf{x}}) \\
 &= \int_{\mathbb{S}^2} \overline{Y_\ell^m(\hat{\mathbf{x}})} \int_{\mathbb{S}^2} f(\hat{\mathbf{y}}) \sum_{p,q}^{L_f-1} e^{-p(p+1)\kappa} Y_p^q(\hat{\mathbf{x}}) \overline{Y_p^q(\hat{\mathbf{y}})} ds(\hat{\mathbf{y}}) ds(\hat{\mathbf{x}}) \\
 &= \sum_{p,q}^{L_f-1} (f)_p^q e^{-p(p+1)\kappa} \int_{\mathbb{S}^2} Y_p^q(\hat{\mathbf{x}}) \overline{Y_\ell^m(\hat{\mathbf{x}})} ds(\hat{\mathbf{x}}) = (f)_\ell^m e^{-\ell(\ell+1)\kappa}, \quad (3.101)
 \end{aligned}$$

where we have used (3.100) and orthonormality of spherical harmonics to get the final result¹³. Hence, signal estimate using weighted-SPHARM framework is given by

$$\tilde{s}_{\text{GW}}(\hat{\mathbf{x}}) = \sum_{\ell,m}^{L_f-1} e^{-\ell(\ell+1)\kappa} (f)_\ell^m Y_\ell^m(\hat{\mathbf{x}}). \quad (3.102)$$

For $\kappa = 0$, GW kernel becomes bandlimited Dirac delta kernel, i.e.,

$$K_{\text{GW}}(\hat{\mathbf{x}}, \hat{\mathbf{y}}) = \sum_{\ell,m}^{L_f-1} Y_\ell^m(\hat{\mathbf{x}}) \overline{Y_\ell^m(\hat{\mathbf{y}})} \triangleq \delta(\hat{\mathbf{x}} - \hat{\mathbf{y}}), \quad (3.103)$$

which reduces the weighted-SPHARM framework to traditional SPHARM, resulting in the following signal estimate

$$\tilde{s}_{\text{GW}_0}(\hat{\mathbf{x}}) = \sum_{\ell,m}^{L_f-1} (f)_\ell^m Y_\ell^m(\hat{\mathbf{x}}). \quad (3.104)$$

We contaminate the Earth topography map, bandlimited to degree $L_f = 64$, with 100 realizations of a zero-mean, uncorrelated and white Gaussian noise process at different values of SNR^f , and compute the output SNR for multiscale optimal filter, hard thresholding method and weighted-SPHARM based GWKS. Figure 3-11 shows the output SNR versus input SNR, averaged over all realizations¹⁴, in which

¹³Spectral estimate in (3.101) justifies our assumption about the bandlimit of K_{GW} and \tilde{s}_{GW} being equal to L_f in (3.99) and (3.98) respectively.

¹⁴Average output SNR becomes negative in Figure 3-11 (and hence, is not shown on the logarithmic scale) at some values of the average input SNR for hard thresholding and weighted-SPHARM methods.

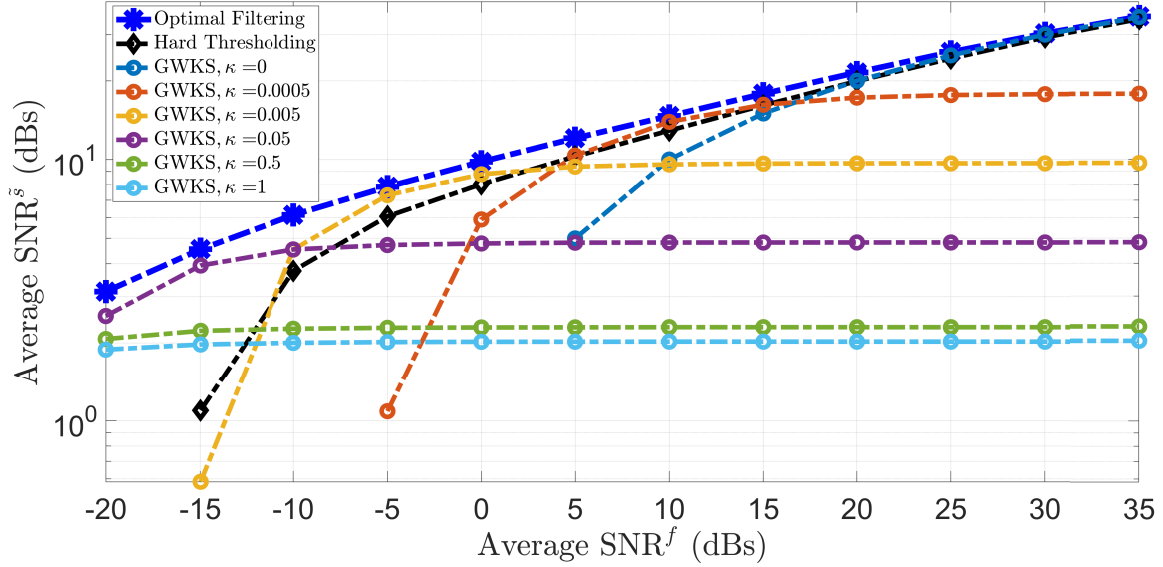


Figure 3-11: Output SNR, averaged over 100 realizations of a zero-mean, uncorrelated and white Gaussian noise process, is plotted versus average input SNR for the estimation of Earth topography map, bandlimited to degree $L_f = 64$, through multiscale optimal filtering framework (blue curve), hard thresholding method (black curve), and weighted-SPHARM based GWKS at different values of κ .

multiscale optimal filter can be seen to perform better than the hard thresholding method, particularly in the low SNR regime. Since there is no systematic way of choosing the GW kernel parameter κ for weighted-SPHARM framework, we estimate the Earth topography map at various values of κ in the interval $[0, 1]$ and show in Figure 3-11 that multiscale optimal filter outperforms the weighted-SPHARM based GWKS at all values of κ .

3.6 Performance comparison of joint domain optimal filters

The filtering methods presented in Section 3.3, Section 3.5 and the optimal window designs presented in Section 3.2, Section 3.4 optimize the mean-square error criterion for joint domain filtering and estimation of signals on the sphere. In this section, we compare the performance of the proposed filtering frameworks and their variants employing optimal window signals, using the Earth topography map, bandlimited to

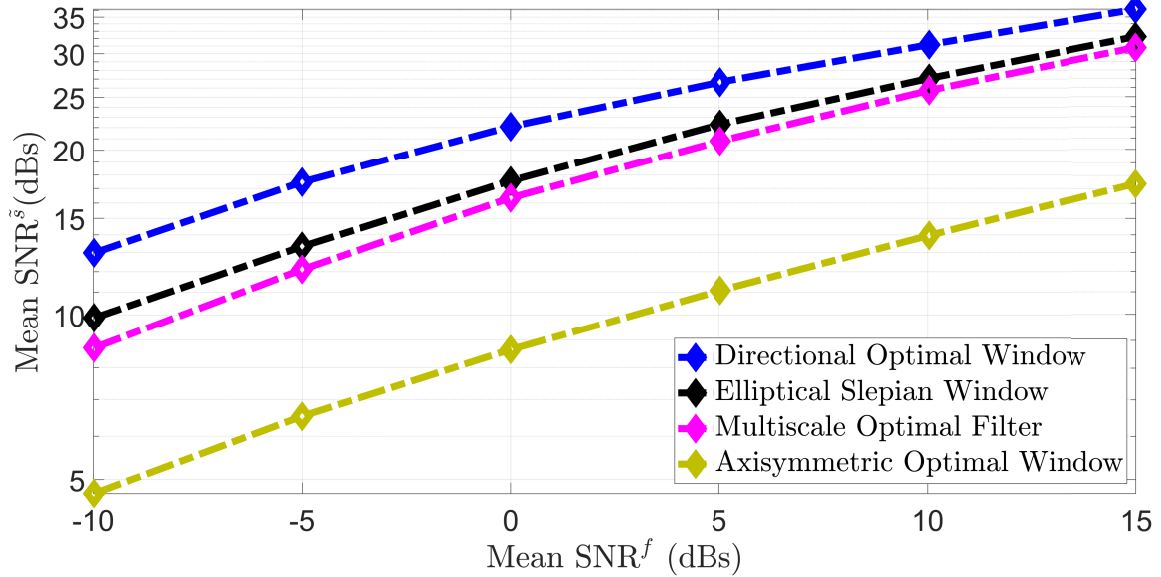


Figure 3-12: Output SNR, averaged over 100 realizations of a zero-mean, uncorrelated and anisotropic Gaussian noise process, is plotted against average input SNR for filtering and estimation of the Earth topography map, bandlimited to degree $L_f = 32$. Signal estimate is computed using joint spatial-spectral domain filter with axisymmetric optimal window signal, joint $\mathbb{SO}(3)$ -spectral domain filter with rank 1 Slepian window signal for the spherical ellipse $R_{(15^\circ, 16^\circ)}$, joint $\mathbb{SO}(3)$ -spectral domain filter with directional optimal window signal and multiscale optimal filter employing directional wavelet functions with dilation parameter $\epsilon = 2$ and largest wavelet scale set to $J = 5$. All the window signals are bandlimited to degree $L_h = 16$.

degree $L_f = 32$. We contaminate the map with 100 different realizations of a zero-mean, uncorrelated and anisotropic Gaussian noise process, and obtain the spectral estimate using joint spatial-spectral domain filter with axisymmetric optimal window signal (bandlimited to degree $L_h = 16$), joint $\mathbb{SO}(3)$ -spectral domain filter with rank 1 (i.e., most well-optimally concentrated) Slepian window signal for the spherical ellipse $R_{(15^\circ, 16^\circ)}$ (bandlimited to degree $L_h = 16$), joint $\mathbb{SO}(3)$ -spectral domain filter with directional optimal window signal (bandlimited to degree $L_h = 16$) and multiscale optimal filter employing directional wavelet functions with dilation parameter $\epsilon = 2$ and largest wavelet scale set to $J = 5$ ¹⁵. Output SNR obtained from the signal estimates using each of these methods is averaged over all realizations. The results

¹⁵Directional wavelet functions are constructed for an azimuthal bandlimit of $L_\phi = 5$. As before, we refer the reader to [83, 85] for details on the construction of directionality component of wavelet functions.

are shown in Figure 3-12, which plots the average output SNR against average input SNR.

Due to its ability to better reconstruct the directional features of the underlying signal, along with the performance boost provided by the directional optimal window signal, it is not unexpected for the joint $\mathbb{SO}(3)$ -spectral domain filter with directional optimal window signal to outperform the other methods. Although directional wavelet functions have the ability to record scale-dependent directional features of the signal, the resulting multiscale optimal filter is independent of the wavelet scale due to the scale-independent statistics of the signal and noise, which makes it low-performance in comparison to the joint $\mathbb{SO}(3)$ -spectral domain filter.

Chapter 4

Localized analysis over spherical polygons

Analysis of spherical signals is aimed at extracting useful information from the underlying data distributed over the sphere, and drawing inferences on the physical variable/process represented by the data. Signal analysis can be performed globally (over \mathbb{S}^2) or locally (over a region $R \subset \mathbb{S}^2$). Localized signal analysis finds applications in fields like astronomy, cosmology, geodesy and planetary sciences, where the data is either unreliable or unavailable over some region on the sphere. For example, measurements for the Earth gravitational or magnetic field are either unavailable or are unreliable around the North/South pole. In cosmology, CMB, which contains information about the early stage of the universe, is obscured over considerable portion of the sky by galactic emissions in the foreground. To support signal analysis in these application areas, there is a need to perform localized analysis such as determining the average value of a signal over some spatial region on the sphere, or finding localized basis functions for accurate representation of spatially limited signals. As discussed in Section 2.5, a localized basis set can be obtained by solving Slepian spatial-spectral concentration problem on the sphere [73, 36, 74, 75, 38, 76, 77]. However, computation of Slepian basis functions requires evaluation of an integral over the given spatial region on the sphere. Since integration over a spatially limited spherical region depends on its boundary, localized signal analysis is often complicated by the shape

of the underlying spatial region due to which, Slepian spatial-spectral concentration problem has been studied for regions given by mathematically simple boundaries. For instance, axisymmetric polar cap region, a pair of axisymmetric antipodal polar cap regions with the same radius and a latitudinal belt region about the equator have been considered in the formulation of Slepian problem in [36, 74, 75, 38]. In [76], Slepian basis functions have been obtained over regions bounded by rings of constant colatitude and longitude. Arbitrary-shaped regions have been considered in [77], but the integrals are computed numerically.

In this chapter, a framework for the analytic evaluation of the integral of spherical signals, and for the analytic solution of the Slepian spatial-spectral concentration problem, over simple spherical polygons is developed to support localized signal analysis on the sphere. A polygon right-angled triangulation method for the division of a simple spherical polygon into spherical right-angled triangles is proposed, which allows to decompose the problem of integrating signals, or solving the spatial-spectral concentration problem, over polygon region into sub-problems that require evaluation of an integral of complex exponential functions over spherical right-angled triangles of arbitrary orientation and position. We derive closed-form expressions for the evaluation of such integrals by finding appropriate rotation angles and using Wigner- D functions. We also present convergence criterion for the infinite series expansions involved in the evaluation of the integral of complex exponential functions, and establish the validity of the proposed developments by evaluating the integral and computing the Slepian basis functions over the geographical region of Australia and the volcanic plateau of Tharsis, using the Earth and Mars topography maps respectively.

4.1 Spherical polygon

We consider a non-self-intersecting, and in general non-convex, polygon on the surface of sphere, denoted by $R_P \subset \mathbb{S}^2$, such that

$$\mathbf{int}\{R_P\} \cup \mathbf{bd}\{R_P\} = R_P, \quad (4.1)$$

i.e., without any holes in it ($\mathbf{int}\{R_P\}$ and $\mathbf{bd}\{R_P\}$ denote the interior and boundary of the polygon respectively). We refer to such simple spherical polygon as spherical polygon (or just polygon) for short. An n -sided spherical polygon is specified by n points on the surface of the sphere, called vertices, and n great circle arcs between pairs of adjacent vertices, which define the boundary of the polygon and are referred to as boundary edges¹. We define *diagonals* as permissible edges, i.e., non-intersecting edges between non-adjacent vertices which lie completely inside the polygon. Due to the bounded nature of the spherical domain, there is ambiguity about the interior of the polygon. To resolve this ambiguity, definition of the polygon is augmented with the information of its centroid (mean of the vertices) as either being inside or outside the polygon.

4.1.1 Polygon right-angled triangulation

Polygon triangulation problem has been studied for decades in the field of computational geometry. Over the years, many different schemes have been proposed for triangulating polygons (e.g. [112, 113, 114, 115, 116, 117, 118]). However, most of the triangulation schemes are applicable to planar polygons. An important triangulation scheme which can triangulate polygons in k -dimensions (where $k \geq 2$) is Delaunay triangulation [112], which triangulates the convex hull of a given set of points, \mathcal{P} , in such a way that the interior of the circumscribed circles (or circumscribed spheres for higher dimensions) does not contain any point from \mathcal{P} . There exist extensions of Delaunay triangulation for a set of points distributed on the surface of the sphere (e.g. [119, 120]) but these extensions also triangulate the convex hull of the set of points and hence, are not applicable to non-convex spherical polygons. To the best of our knowledge, there exists no triangulation scheme which uses great circle arcs to triangulate simple non-convex polygons on the sphere.

We propose a triangulation scheme which seeks to find all possible diagonals for an n -sided simple, non-convex spherical polygon. Once the polygon has been triangulated, it is divided into spherical right-angled triangles by dividing each non-right-

¹An edge is defined as the great circle arc between any two vertices of the spherical polygon.

angled triangle into two right-angled triangles. Due to the periodic nature of the spherical domain, polygon triangulation is performed quadrant-wise along the longitude, i.e., the whole spherical domain is divided into sub-domains, called quadrants, where the k -th quadrant is specified by $\phi = [(k-1)\pi/2, k\pi/2], \theta = [0, \pi], k = 1, 2, 3, 4$. A summary of the polygon right-angled triangulation method is given below.

1. If the north pole ($\theta = 0$) and/or the south pole ($\theta = \pi$) are inside the polygon and do not represent vertex of the polygon, then place vertex at their respective positions.
2. Bisect the boundary edges (by placing a vertex midway between the vertices of the respective edges) which have arc-length greater than $\pi/2$. This ensures that maximum great circle arc-length of a spherical right-angled triangle is either less than or equal to $\pi/2$.
3. Limit the edges to within their respective quadrants by placing vertices at the intersection of the quadrant boundaries and those edges which cross them. Construct edges along the quadrant boundaries, between the newly created vertices, only if these edges lie inside the polygon.
4. Identify those vertices which lie within the quadrant under consideration and construct all possible non-intersecting edges among them. Identify diagonals as those non-intersecting edges which lie completely inside the polygon.
5. Bisect the diagonals (by placing a vertex midway between the vertices of the respective diagonals) which have arc-length greater than $\pi/2$.
6. Finding the diagonals results in the triangulation of the region of the polygon within the quadrant under consideration. Repeat steps 3 to 5 for all longitudinal quadrants to triangulate the whole polygon.
7. Traverse through all triangles and identify those which are not right-angled (by finding the interior angles). For each non-right-angled triangle, find the vertex with the maximum interior angle. By constructing a perpendicular great circle

Procedure 1 Point-in-Spherical Polygon Algorithm**Require:** p_{inside}

```

1: procedure POINT-IN-SPHERICAL POLYGON( $B, \hat{\mathbf{u}}, \hat{\mathbf{c}}$ )
2:    $e \leftarrow$  great circle arc between points  $\hat{\mathbf{u}}$  and  $\hat{\mathbf{c}}$ 
3:   Find number of intersections between  $e$  and boundary edges  $\in B$ 
4:   if  $\hat{\mathbf{c}} \in$  interior of Polygon then
5:     if number of intersections is even then
6:        $p_{\text{inside}} = 1$ 
7:     else
8:        $p_{\text{inside}} = 0$ 
9:     end if
10:  else
11:    if number of intersections is odd then
12:       $p_{\text{inside}} = 1$ 
13:    else
14:       $p_{\text{inside}} = 0$ 
15:    end if
16:  end if
17:  return  $p_{\text{inside}}$ 
18: end procedure

```

arc from this vertex to the great circle arc formed by the other two vertices, divide each non-right-angled triangle into two right-angled triangles.

Following these steps, a spherical polygon region R_P can be divided into disjoint spherical right-angled triangles as

$$R_P = \bigcup_{t=1}^{N_\Delta} \tilde{R}_t, \quad (4.2)$$

where \tilde{R}_t is the region bounded by the t -th spherical right-angled triangle and N_Δ is the number of spherical right-angled triangles. We further elaborate on the proposed triangulation method by presenting algorithms to carry out steps 1, 3 and 4.

Step 1: North/south pole in spherical polygon

Finding whether north/south pole lies inside a spherical polygon is essentially a point-in-polygon problem for which the ray casting algorithm is employed, using centroid

Procedure 2 Finding Diagonals Algorithm

Require: D

```

1: procedure FINDING DIAGONALS( $B, v_D, \hat{c}$ )
2:   for  $\hat{v}_k \in v_D$  do
3:     for  $\hat{v}_p \in v_D, \hat{v}_p \neq \hat{v}_k$  do
4:        $e \leftarrow$  great circle arc between vertices  $\hat{v}_k$  and  $\hat{v}_p$ 
5:        $n \leftarrow$  Number of intersections between  $e$  and boundary edges  $\in B$ 
           and diagonals  $\in D$ 
6:       if  $n = 0$  then
7:          $\hat{m} \leftarrow \text{GreatCircleMidPoint}(e)$ 
8:          $p_{\text{inside}} = \text{Point-in-Spherical Polygon}(B, \hat{m}, \hat{c})$ 
9:         if  $p_{\text{inside}} = 1$  then
10:             $D \leftarrow e$ 
11:        end if
12:      end if
13:    end for
14:  end for
15:  return  $D$ 
16: end procedure
    
```

of the polygon as the emanating point and north/south pole as the ending point of the ray². In the algorithm presented in Procedure 1, the point to be tested (e.g., north/south pole in this case) is denoted by \hat{u} , \hat{c} is the centroid, B represents the set of boundary edges of the polygon and p_{inside} is a flag which is either 0 or 1, indicating that the point under test is either outside or inside the polygon respectively.

Step 3: Identifying permissible edges along quadrant boundaries

Edges along the quadrant boundaries lie either completely inside or completely outside the polygon. Hence, the point-in-spherical polygon algorithm, in Procedure 1, can be used again by setting \hat{u} equal to the mid-point of the edge under consideration.

Step 4: Finding diagonals

Let v_D denote the subset of vertices v which participate in the creation of diagonals and D be the set of diagonals, then the algorithm to identify diagonals is given in

²A ray on the sphere is a great circle arc.

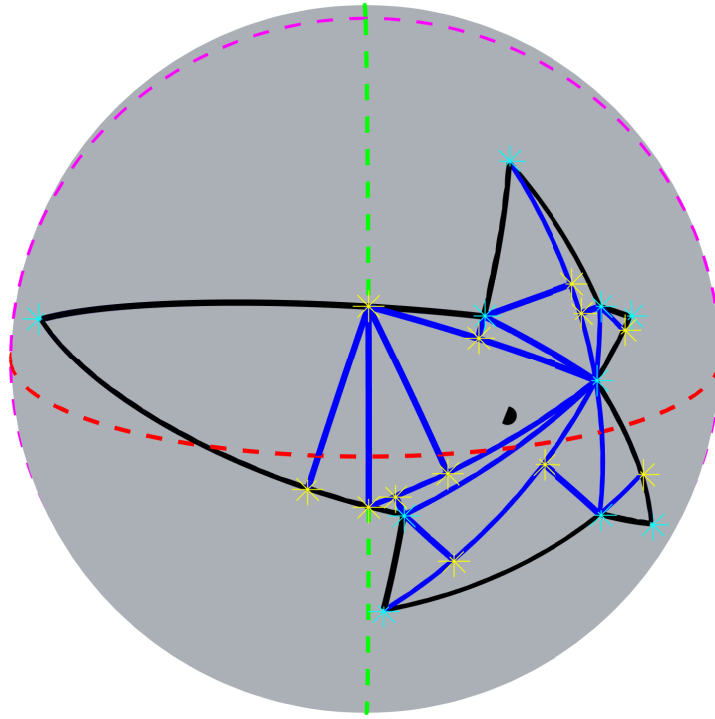


Figure 4-1: Right-angled triangulation of a spherical polygon which is located in the longitudinal quadrants 2 and 3. Vertices shown in yellow are created as a result of either limiting the edges to respective quadrants or dividing the spherical triangles into spherical right-angled triangles. Thick black dot marks the centroid of the polygon.

Procedure 2. Please note that $GreatCircleMidPoint(e)$ returns the mid-point of the edge e .

As an illustration of the polygon right-angled triangulation algorithm, an arbitrary-shaped spherical polygon and its right-angled triangulation are shown in Figure 4-1.

4.2 Localized signal analysis over simple polygons on the sphere

Polygon right-angled triangulation method, presented in Section 4.1.1, facilitates the problem of localized signal analysis by reducing the computational framework to spherical right-angled triangles. In this section, we present formulations for:

- i. analytical evaluation of the integral of a signal,

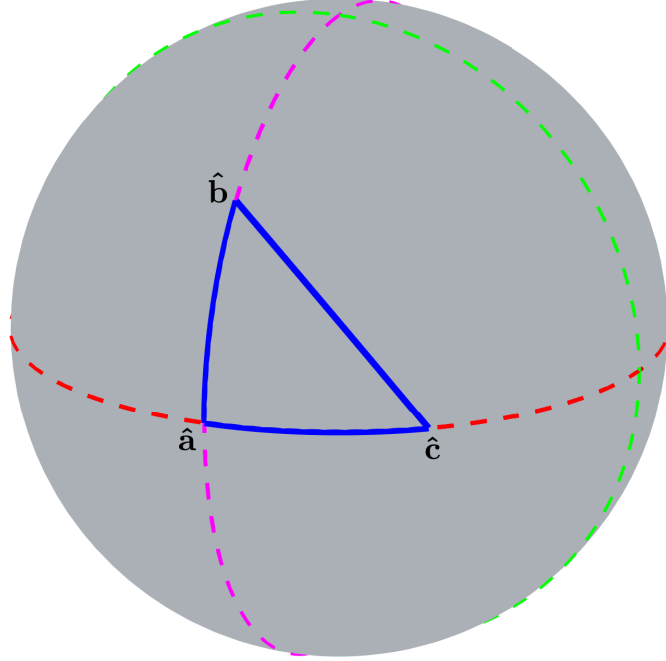


Figure 4-2: Spherical right-angled triangle in standard orientation with vertices $\hat{\mathbf{a}}(\pi/2, 0)$, $\hat{\mathbf{b}}(\theta_{b,t}, 0)$ and $\hat{\mathbf{c}}(\pi/2, \phi_{c,t})$, where $\theta_{b,t} = 5\pi/18$ and $\phi_{c,t} = 2\pi/9$.

- ii. analytical solution of Slepian spatial-spectral concentration problem of finding bandlimited signals with optimal spatial energy concentration,

over spherical right-angled triangles. By finding appropriate rotation angles and employing Wigner- D functions, the results for spherical right-angled triangles are mapped to simple polygons on the sphere.

4.2.1 Integration of signals over a spherical polygon

We consider the integral of a signal $f \in L^2(\mathbb{S}^2)$ over a simple spherical polygon region R_P as

$$I_{R_P} = \int_{R_P} f(\hat{\mathbf{x}}) ds(\hat{\mathbf{x}}) = \sum_{t=1}^{N_\Delta} \int_{\tilde{R}_t} f(\hat{\mathbf{x}}) ds(\hat{\mathbf{x}}), \quad (4.3)$$

where the expression in (4.2) has been used to obtain the second equality. To evaluate the integral of the signal $f(\hat{\mathbf{x}})$ over the t -th spherical right-angled triangular region \tilde{R}_t , we rotate the t -th spherical right-angled triangle, using the rotation ma-

trix $\mathbf{R}^{zyz}(\varphi_t, \vartheta_t, \omega_t)$ defined in (2.12), such that

$$\mathbf{R}^{zyz}(\varphi_t, \vartheta_t, \omega_t)\hat{\mathbf{u}} \in R(\theta_{b,t}, \phi_{c,t}), \quad \forall \hat{\mathbf{u}} \in \tilde{R}_t, \quad (4.4)$$

where the Euler angles $(\varphi_t, \vartheta_t, \omega_t)$ depend on the position and orientation of the t -th spherical right-angled triangle \tilde{R}_t and $R(\theta_{b,t}, \phi_{c,t}) \equiv R_t$ is the spherical right-angled triangle with vertices $\hat{\mathbf{a}}(\pi/2, 0)$, $\hat{\mathbf{b}}(\theta_{b,t}, 0)$ and $\hat{\mathbf{c}}(\pi/2, \phi_{c,t})$ for $0 < \phi_{c,t} \leq \pi/2$, $0 \leq \theta_{b,t} < \pi/2$, for instance, as shown in Figure 4-2. We refer to the spherical right-angled triangle R_t , having sides aligned with $\theta = \pi/2$ and $\phi = 0$ great circles, as the spherical right-angled triangle in “standard” orientation.

Integral of the signal $f(\hat{\mathbf{x}})$ over the t -th arbitrarily oriented spherical right-angled triangular region \tilde{R}_t can then be determined by rotating the signal through the rotation operator $\mathcal{D}(\varphi_t, \vartheta_t, \omega_t)$, which corresponds to the rotation matrix in (4.4), and evaluating the integral of the rotated signal $(\mathcal{D}(\varphi_t, \vartheta_t, \omega_t)f)(\hat{\mathbf{x}})$ over the spherical right-angled triangular region R_t , i.e.,

$$\begin{aligned} \int_{\tilde{R}_t} f(\hat{\mathbf{x}}) ds(\hat{\mathbf{x}}) &= \int_{R_t} (\mathcal{D}(\varphi_t, \vartheta_t, \omega_t)f)(\hat{\mathbf{x}}) ds(\hat{\mathbf{x}}) \\ &= \sum_{\ell, m}^{\infty} (f)_{\ell}^m \int_{R_t} (\mathcal{D}(\varphi_t, \vartheta_t, \omega_t)Y_{\ell}^m)(\hat{\mathbf{x}}) ds(\hat{\mathbf{x}}), \end{aligned} \quad (4.5)$$

where Fourier expansion of signals in (2.23) has been used. Using the spectral representation of rotated signals in (2.46) along with orthonormality of spherical harmonics on the sphere, we can evaluate the rotated spherical harmonic function $(\mathcal{D}(\varphi_t, \vartheta_t, \omega_t)Y_{\ell}^m)(\hat{\mathbf{x}})$ as

$$\begin{aligned} (\mathcal{D}(\varphi_t, \vartheta_t, \omega_t)Y_{\ell}^m)(\hat{\mathbf{x}}) &= \sum_{p, q}^{\infty} \langle \mathcal{D}(\varphi_t, \vartheta_t, \omega_t)Y_{\ell}^m, Y_p^q \rangle_{\mathbb{S}^2} Y_p^q(\hat{\mathbf{x}}) \\ &= \sum_{p, q}^{\infty} \left(\sum_{q'=-p}^p D_{q, q'}^p(\varphi_t, \vartheta_t, \omega_t) \langle Y_{\ell}^m, Y_p^{q'} \rangle_{\mathbb{S}^2} \right) Y_p^q(\hat{\mathbf{x}}) \\ &= \sum_{q=-\ell}^{\ell} D_{q, m}^{\ell}(\varphi_t, \vartheta_t, \omega_t) Y_{\ell}^q(\hat{\mathbf{x}}), \end{aligned} \quad (4.6)$$

which enables us to write the integral in (4.3) as

$$\begin{aligned}
 I_{R_P} &= \sum_{\ell, m}^{\infty} (f)_{\ell}^m \sum_{t=1}^{N_{\Delta}} \sum_{q=-\ell}^{\ell} D_{q, m}^{\ell}(\varphi_t, \vartheta_t, \omega_t) \int_{R_t} Y_{\ell}^q(\hat{\mathbf{x}}) ds(\hat{\mathbf{x}}) \\
 &= \sum_{\ell, m}^{\infty} (f)_{\ell}^m \sum_{t=1}^{N_{\Delta}} \sum_{q=-\ell}^{\ell} D_{q, m}^{\ell}(\varphi_t, \vartheta_t, \omega_t) \sum_{m'=-\ell}^{\ell} \frac{F_{m', q}^{\ell}}{2i} \times \\
 &\quad \left(\mathbb{I}(q, m' + 1, \theta_{b, t}, \phi_{c, t}) - \mathbb{I}(q, m' - 1, \theta_{b, t}, \phi_{c, t}) \right), \quad (4.7)
 \end{aligned}$$

where

$$F_{m', q}^{\ell} = (-i)^q \sqrt{\frac{2\ell + 1}{4\pi}} \Delta_{m', q}^{\ell} \Delta_{m', 0}^{\ell}, \quad \Delta_{m', q}^{\ell} \triangleq d_{m', q}^{\ell}(\pi/2), \quad (4.8)$$

and (2.53) has been used to get the final result. Here,

$$\mathbb{I}(\mathbf{q}, \mathbf{m}, \theta_{b, t}, \phi_{c, t}) = \int_{R_t} e^{iq\phi} e^{im\theta} d\theta d\phi \quad (4.9)$$

represents the integral of product of complex exponential functions over the spherical right-angled triangle in standard orientation. An analytical expression to evaluate $\mathbb{I}(\mathbf{q}, \mathbf{m}, \theta_{b, t}, \phi_{c, t})$ is given in Section 4.2.3.

4.2.2 Slepian functions over a spherical polygon

Bandlimited and spatially optimally concentrated Slepian functions are obtained as solution to the eigenvalue problem given in (2.60), which is repeated here for ease of reference

$$\mathbf{K} \mathbf{g}_{\alpha} = \lambda_{\alpha} \mathbf{g}_{\alpha}, \quad \alpha = 1, 2, \dots, L_g^2, \quad (4.10)$$

where L_g is the bandlimit of the Slepian function $g_{\alpha}(\hat{\mathbf{x}})$, \mathbf{g}_{α} is a column vector representing the spectral components of $g_{\alpha}(\hat{\mathbf{x}})$ according to the indexing scheme introduced in (2.30), and λ_{α} is the fractional energy concentration of $g_{\alpha}(\hat{\mathbf{x}})$ within the spatial region under consideration. Slepian functions for the spherical polygon R_P can be

computed by constructing the matrix \mathbf{K} from its elements $K_{\ell m, pq}$ as

$$\begin{aligned}
 K_{\ell m, pq} &= \int_{R_P} \overline{Y_\ell^m(\hat{\mathbf{x}})} Y_p^q(\hat{\mathbf{x}}) ds(\hat{\mathbf{x}}) \\
 &= \sum_{t=1}^{N_\Delta} \int_{\tilde{R}_t} \overline{Y_\ell^m(\hat{\mathbf{x}})} Y_p^q(\hat{\mathbf{x}}) ds(\hat{\mathbf{x}}) \\
 &= \sum_{t=1}^{N_\Delta} \int_{R_t} (\mathcal{D}(\varphi_t, \vartheta_t, \omega_t) \overline{Y_\ell^m} Y_p^q)(\hat{\mathbf{x}}) ds(\hat{\mathbf{x}}) \\
 &= \sum_{t=1}^{N_\Delta} \sum_{m'=-\ell}^{\ell} \sum_{q'=-p}^p \overline{D_{m', m}^\ell(\varphi_t, \vartheta_t, \omega_t)} D_{q', q}^p(\varphi_t, \vartheta_t, \omega_t) \int_{R_t} \overline{Y_\ell^{m'}(\hat{\mathbf{x}})} Y_p^{q'}(\hat{\mathbf{x}}) ds(\hat{\mathbf{x}}) \\
 &= \sum_{t=1}^{N_\Delta} \sum_{m'=-\ell}^{\ell} \sum_{q'=-p}^p \overline{D_{m', m}^\ell(\varphi_t, \vartheta_t, \omega_t)} D_{q', q}^p(\varphi_t, \vartheta_t, \omega_t) \times \\
 &\quad \sum_{m''=-\ell}^{\ell} F_{m'', m'}^\ell \sum_{q''=-p}^p F_{q'', q'}^p G_{m'q', m''q''}, \tag{4.11}
 \end{aligned}$$

where $F_{m'', m'}^\ell$ is given in (4.8),

$$\begin{aligned}
 G_{mq, m'q'} &= \int_{R_t} e^{i(q-m)\phi} e^{i(m'+q')\theta} \sin \theta d\theta d\phi \\
 &= \frac{1}{2i} \left(\mathbb{I}(q-m, m'+q'+1, \theta_{b,t}, \phi_{c,t}) - \mathbb{I}(q-m, m'+q'-1, \theta_{b,t}, \phi_{c,t}) \right), \tag{4.12}
 \end{aligned}$$

\mathbb{I} represents the integral of product of complex exponential functions given in (4.9), and we have used (4.6) and (2.53) to obtain the penultimate and final expressions respectively.

4.2.3 Evaluation of the integral of complex exponential functions

Evaluation of the integral of spherical signals and computation of Slepian functions, over polygon region R_P , depends on the integral $\mathbb{I}(\mathbf{q}, \mathbf{m}, \theta_{b,t}, \phi_{c,t})$ given in (4.9). We first define the spatial region bounded by the t -th spherical right-angled triangle R_t (in standard orientation), which in turn requires the parameterization of great circles.

Parameterization of great circles

A great circle on the sphere can be parameterized with a unit outward normal vector, denoted by $\hat{\mathbf{n}}(\Theta, \Omega)$, having colatitude $\Theta \in [0, \pi]$ and longitude $\Omega \in [0, 2\pi)$ ³, such that

$$\mathbf{R}^{zyz}(0, -\Theta, -\Omega) \hat{\mathbf{n}} = (0, 0, 1)^T, \quad (4.13)$$

where $\mathbf{R}^{zyz}(0, -\Theta, -\Omega)$ is the rotation matrix defined in (2.12) and $(0, 0, 1)^T \equiv \hat{\boldsymbol{\eta}}$ represent the north pole on the sphere. Denoting a point on the great circle by $\hat{\mathbf{x}}(\theta, \phi)$, we note that rotating the great circle by $-\Omega$ around z -axis transforms $\hat{\mathbf{x}}(\theta, \phi)$ to $\hat{\mathbf{x}}(\theta, \phi - \Omega)$. Second rotation by $-\Theta$ around y -axis transforms $\hat{\mathbf{x}}(\theta, \phi - \Omega)$ to a point on the equator, given by $\hat{\mathbf{x}}(\pi/2, \phi - \Omega + \Delta\phi)$, where $\Delta\phi$ is the change in longitude due to the rotation around y -axis. Third rotation around z -axis should bring $\phi - \Omega + \Delta\phi$ to some reference longitude. We choose the reference longitude to be 0, which gives the third angle as

$$\Lambda(\theta, \phi) = \Omega - \phi - \Delta\phi. \quad (4.14)$$

Hence, we can express the rotation of great circle in the following compact form

$$\mathbf{R}^{zyz}(\Lambda, -\Theta, -\Omega) \hat{\mathbf{x}} = (1, 0, 0)^T, \quad (4.15)$$

which results in the following set of equations

$$\begin{aligned} \sin \theta \left[\sin(\Lambda) \sin(\Omega - \phi) + \cos \Theta \cos(\Lambda) \cos(\Omega - \phi) \right] - \cos \theta \sin \Theta \cos(\Lambda) &= 1, \\ \sin \theta \left[\cos \Theta \sin(\Lambda) \cos(\Omega - \phi) - \cos(\Lambda) \sin(\Omega - \phi) \right] - \sin \Theta \cos \theta \sin(\Lambda) &= 0, \\ \sin \theta \sin \Theta \cos(\Omega - \phi) + \cos \Theta \cos \theta &= 0, \end{aligned} \quad (4.16)$$

³Since outward normal vector to the great circle passes through the center of the spherical coordinate system, it can equivalently be parameterized by $\hat{\mathbf{n}}(\pi - \Theta, \pi + \Omega)$, which is antipodal to the point $\hat{\mathbf{n}}(\Theta, \Omega)$ on the sphere.

where we have dropped the dependence of Λ on (θ, ϕ) for convenience and have used the definition of $\hat{\mathbf{x}}(\theta, \phi)$ in (2.5). From the second expression in (4.16), we find Λ as

$$\Lambda(\theta, \phi) = \text{atan2}\left(\frac{\sin \theta \sin(\Omega - \phi)}{\cos \Theta \sin \theta \cos(\phi - \Omega) - \sin \Theta \cos \theta}\right), \quad (4.17)$$

where $\text{atan2}(\cdot)$ is the four-quadrant inverse tangent function. Equation of the great circle parameterized by the unit outward normal vector $\hat{\mathbf{n}}(\Theta, \Omega)$ is obtained, by solving the third expression in (4.16), as

$$\tan \theta = -\frac{\cot \Theta}{\cos(\Omega - \phi)}. \quad (4.18)$$

Now referring to Figure 4-2, let the side of the spherical right-angled triangle joining the vertices $\hat{\mathbf{b}}$ and $\hat{\mathbf{c}}$ be a part of the great circle with unit outward normal vector given by $\hat{\mathbf{n}}(\Theta_o, \Omega_o)$. Solving (4.18) for vertices $\hat{\mathbf{b}}$ and $\hat{\mathbf{c}}$, we get

$$\Omega_o = \phi_{c,t} + \frac{\pi}{2}, \quad \Theta_o = \cot^{-1}\left(\tan \theta_{b,t} \sin \phi_{c,t}\right). \quad (4.19)$$

Since $0 < \phi_{c,t} \leq \pi/2$ and $0 \leq \theta_{b,t} < \pi/2$, unit outward normal vector $\hat{\mathbf{n}}(\Theta_o, \Omega_o)$ is a point in the $(-, +, +)$ octant on the sphere which implies $\Omega_o \in (\pi/2, \pi]$ and $\Theta_o \in (0, \pi/2]$. Using (4.19), the great circle arc between vertices $\hat{\mathbf{b}}$ and $\hat{\mathbf{c}}$ is given by the following equation

$$\tan \theta = \frac{\mathbf{k}_t(\theta_{b,t}, \phi_{c,t})}{\sin(\phi_{c,t} - \phi)}, \quad \mathbf{k}_t(\theta_{b,t}, \phi_{c,t}) = \tan \theta_{b,t} \sin \phi_{c,t}. \quad (4.20)$$

For notational convenience, the dependence of \mathbf{k}_t on $\theta_{b,t}$ and $\phi_{c,t}$ is dropped, i.e., $\mathbf{k}_t \equiv \mathbf{k}_t(\theta_{b,t}, \phi_{c,t})$ for the remainder of this work. Having parameterized the great circle arc between vertices $\hat{\mathbf{b}}$ and $\hat{\mathbf{c}}$ of the spherical right-angled triangle in standard orientation, we present analytical expressions for the evaluation of the integral $\mathbb{I}(\mathbf{q}, \mathbf{m}, \theta_{b,t}, \phi_{c,t})$ in the following theorem.

Theorem 6. *Integral of the form given in (4.9), where $R_t \equiv R(\theta_{b,t}, \phi_{c,t})$ represents the spatial region bounded by the spherical right-angled triangle in standard orientation,*

is given by

$$\mathbb{I}(\mathbf{q}, \mathbf{m}, \theta_{b,t}, \phi_{c,t}) = \begin{cases} \mathbb{I}(0, 0, \theta_{b,t}, \phi_{c,t}), & \mathbf{q} = 0, \mathbf{m} = 0, \\ \frac{i^{\mathbf{m}} \phi_{c,t}}{i\mathbf{m}} - \frac{1}{i\mathbf{m}} S(0, \mathbf{m}, \theta_{b,t}, \phi_{c,t}), & \mathbf{q} = 0, \mathbf{m} \neq 0, \\ \frac{\pi(e^{i\mathbf{q}\phi_{c,t}} - 1)}{2i\mathbf{q}} - Q(\mathbf{q}, \theta_{b,t}, \phi_{c,t}), & \mathbf{q} \neq 0, \mathbf{m} = 0, \\ \frac{-i^{\mathbf{m}}(e^{i\mathbf{q}\phi_{c,t}} - 1)}{\mathbf{m}\phi} - \frac{1}{i\mathbf{m}} S(\mathbf{q}, \mathbf{m}, \theta_{b,t}, \phi_{c,t}), & \mathbf{q} \neq 0, \mathbf{m} \neq 0, \end{cases} \quad (4.21)$$

where

$$\mathbb{I}(0, 0, \theta_{b,t}, \phi_{c,t}) = \begin{cases} \frac{\pi}{2} \phi_1 + \sum_{n_1=0}^{\infty} \frac{\mathbf{k}_t (-1)^{n_1}}{(2n_1+1)} W_1(\theta_{b,t}, \phi_{c,t}, \phi_1, n_1) + \\ \sum_{n_2=0}^{\infty} \frac{\mathbf{k}_t (-1)^{n_2}}{(2n_2+1)} W_2(\theta_{b,t}, \phi_{c,t}, \phi_{c,t} - \phi_1, n_2), & 0 \leq \theta_{b,t} < \frac{\pi}{4}, \\ \sum_{n_3=0}^{\infty} \frac{\mathbf{k}_t (-1)^{n_3}}{(2n_3+1)} W_2(\theta_{b,t}, \phi_{c,t}, \phi_{c,t}, n_3), & \frac{\pi}{4} \leq \theta_{b,t} < \frac{\pi}{2}, \end{cases} \quad (4.22)$$

$$Q(\mathbf{q}, \theta_{b,t}, \phi_{c,t}) = -\frac{e^{i\mathbf{q}\phi_{c,t}}}{i\mathbf{q}} \left(e^{-i\mathbf{q}\phi_{c,t}} \tan^{-1} \left(\frac{\mathbf{k}_t}{\sin \phi_{c,t}} \right) - \frac{\pi}{2} \right) - \frac{e^{i\mathbf{q}\phi_{c,t}} \mathbf{k}_t}{i\mathbf{q}} \sum_{n_0=0}^{|\mathbf{q}|} \binom{|\mathbf{q}|}{n_0} A(\mathbf{q}, n_0) W_3(n_0, \mathbf{q}, \theta_{b,t}, \phi_{c,t}), \quad (4.23)$$

$$S(\mathbf{q}, \mathbf{m}, \theta_{b,t}, \phi_{c,t}) = e^{i\mathbf{q}\phi_{c,t}} \sum_{n_0=0}^{|\mathbf{q}|} \binom{|\mathbf{q}|}{n_0} A(\mathbf{q}, n_0) \sum_{r=0}^{|\mathbf{m}|} (-1)^r \binom{|\mathbf{m}|}{r} \times A(\mathbf{m}, r) \mathbf{k}_t^{|\mathbf{m}|-r} W_4(n_0, r, \mathbf{q}, \mathbf{m}, \theta_{b,t}, \phi_{c,t}), \quad (4.24)$$

$$\phi_1 = \phi_{c,t} - \sin^{-1}(\mathbf{k}_t), \quad (4.25)$$

$$A(\mathbf{q}, n_0) = \begin{cases} i^{|\mathbf{q}|-n_0}, & \mathbf{q} \geq 0, \\ (-i)^{|\mathbf{q}|-n_0}, & \mathbf{q} < 0, \end{cases} \quad (4.26)$$

$$W_1(\theta_{b,t}, \phi_{c,t}, \phi_1, n_1) = \sum_{J_1=0}^{\infty} \binom{-1/2}{J_1} (-1)^{J_1} \times \begin{cases} \left[\frac{(\mathbf{k}_t / \sin \phi)^{2n_1} \sin^{2J_1} \phi}{(2n_1 - 2J_1)} \right]_{\phi_{c,t} - \phi_1}^{\phi_{c,t}}, & n_1 \neq J_1, \\ \left[\mathbf{k}_t^{2J_1} \log(1 / \sin \phi) \right]_{\phi_{c,t} - \phi_1}^{\phi_{c,t}}, & n_1 = J_1, \end{cases} \quad (4.27)$$

$$W_2(\theta_{b,t}, \phi_{c,t}, \phi_u, n_2) = \sum_{J_2=0}^{\infty} \binom{-1/2}{J_2} (-1)^{J_2} \times \left[\frac{(\sin \phi / \mathbf{k}_t)^{2n_2+2} \sin^{2J_2} \phi}{(2n_2 + 2 + 2J_2)} \right]_0^{\phi_u}, \quad (4.28)$$

$$W_3(n_0, \mathbf{q}, \theta_{b,t}, \phi_{c,t}) = \frac{(-\sin \phi_{c,t})^{(1+|\mathbf{q}|-n_0)}}{\mathbf{k}_t^2 (n_0 - |\mathbf{q}| - 1)} \times F_1 \left(\frac{(1 + |\mathbf{q}| - n_0)}{2}, \frac{-n_0}{2}, 1, \frac{(3 + |\mathbf{q}| - n_0)}{2}, \sin^2 \phi_{c,t}, -\frac{\sin^2 \phi_{c,t}}{\mathbf{k}_t^2} \right), \quad (4.29)$$

$$W_4(n_0, r, \mathbf{q}, \mathbf{m}, \theta_{b,t}, \phi_{c,t}) = \frac{(-\sin \phi_{c,t})^{1+|\mathbf{q}|-n_0+r}}{\mathbf{k}_t^{|\mathbf{m}|} (n_0 - r - |\mathbf{q}| - 1)} \times F_1 \left(\frac{(1 + |\mathbf{q}| - n_0 + r)}{2}, \frac{1 - n_0}{2}, \frac{|\mathbf{m}|}{2}, \frac{(3 + |\mathbf{q}| - n_0 + r)}{2}, \sin^2 \phi_{c,t}, -\frac{\sin^2 \phi_{c,t}}{\mathbf{k}_t^2} \right). \quad (4.30)$$

F_1 is the Appell F_1 hypergeometric function.

Proof. See Appendix A for the proof of Theorem 6 and Section 4.2.5 for the convergence criteria of infinite series expansions. \square

4.2.4 Rotation of spherical right-angled triangles

It remains to determine the rotation angles in (4.4) for the rotation of a spherical right-angled triangle in arbitrary orientation such that the rotated triangle is in standard orientation. A t -th arbitrarily oriented spherical right-angled triangle, with vertices $\hat{\mathbf{v}}_{1,t}(\theta_{v_1}, \phi_{v_1})$, $\hat{\mathbf{v}}_{2,t}(\theta_{v_2}, \phi_{v_2})$, $\hat{\mathbf{v}}_{3,t}(\theta_{v_3}, \phi_{v_3})$, bounding spatial region \tilde{R}_t , can be transformed into standard orientation through a sequential rotation by ω around z -

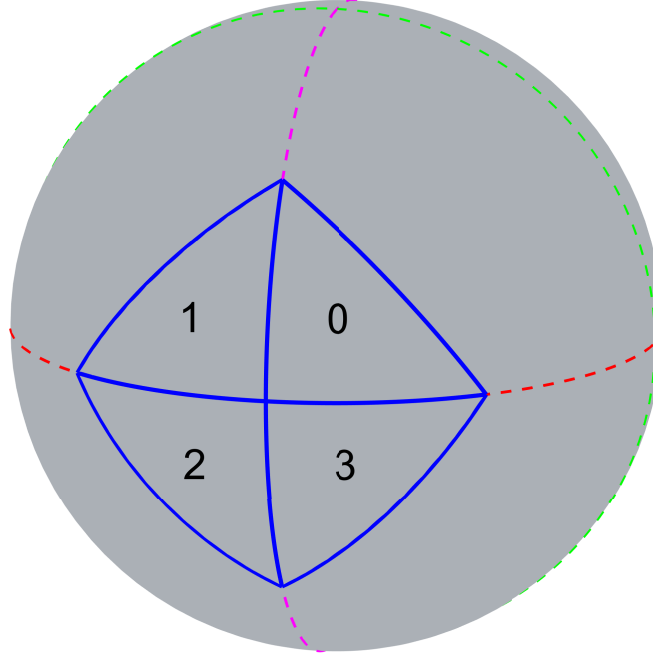


Figure 4-3: Possible orientations of a randomly oriented spherical right-angled triangle after first pass of zyz rotation by angles $\varphi_1 \vartheta_1 \omega_1$ (in the order from right to left in zyz -convention).

axis, ϑ around y -axis and φ around z -axis in the zyz convention. Assuming $\hat{v}_{1,t}$ to be the “right” vertex (which has an interior angle of 90°), angles φ , ϑ , ω can be found by rotating one of the arcs out of $\hat{v}_{1,t} - \hat{v}_{2,t}$ and $\hat{v}_{1,t} - \hat{v}_{3,t}$ onto the equator, which brings the arbitrarily oriented spherical right-angled triangle into one of four possible orientations shown in Figure 4-3. Hence, rotation of an arbitrarily oriented spherical right-angled triangle into the standard orientation is a two phase process.

In the first rotation phase, we choose to rotate the longer of the two arcs ($\hat{v}_{1,t} - \hat{v}_{2,t}$, $\hat{v}_{1,t} - \hat{v}_{3,t}$) onto the equator if this choice results in the rotation of arbitrarily oriented spherical right-angled triangle into the orientation 0 or 2, we choose to rotate the shorter arc onto the equator otherwise. Angles obtained in this way for the first rotation phase are given by

$$\omega_1 = -\Omega, \quad \vartheta_1 = -\Theta, \quad \varphi_1 = \begin{cases} \Lambda(\theta_{v_1}, \phi_{v_1}) - \Omega, & \theta_{v_1} = 0, \pi, \\ \Lambda(\theta_{v_1}, \phi_{v_1}), & \text{otherwise,} \end{cases} \quad (4.31)$$

where $\hat{\mathbf{n}}(\Theta, \Omega)$ is the unit outward normal vector of the great circle containing the chosen arc (out of $\hat{\mathbf{v}}_{1,t} - \hat{\mathbf{v}}_{2,t}$ and $\hat{\mathbf{v}}_{1,t} - \hat{\mathbf{v}}_{3,t}$) for rotation onto the equator, and $\Lambda(\theta, \phi)$ is given in (4.17). Note that $\omega_1 = \vartheta_1 = \varphi_1 = 0$ if the arbitrarily oriented spherical right-angled triangle is already in one of the orientations 0 – 3. Angles for the second rotation phase are given by

$$\text{orientation 0 : } \omega_2 = \vartheta_2 = \varphi_2 = 0, \quad (4.32)$$

$$\text{orientation 1 : } \omega_2 = -\frac{\pi}{2}, \vartheta_2 = \frac{\pi}{2}, \varphi_2 = \frac{\pi}{2}, \quad (4.33)$$

$$\text{orientation 2 : } \omega_2 = \pi, \vartheta_2 = \pi, \varphi_2 = 0, \quad (4.34)$$

$$\text{orientation 3 : } \omega_2 = -\frac{\pi}{2}, \vartheta_2 = -\frac{\pi}{2}, \varphi_2 = \frac{\pi}{2}. \quad (4.35)$$

Hence, a t -th arbitrarily oriented spherical right-angled triangle can be rotated into standard orientation using (4.4), in which

$$\mathbf{R}^{zyz}(\varphi_t, \vartheta_t, \omega_t) = \begin{cases} \mathbf{R}^{zyz}(\varphi_1, \vartheta_1, \omega_1), & \text{single phase rotation,} \\ \mathbf{R}^{zyz}(\varphi_2, \vartheta_2, \omega_2)\mathbf{R}^{zyz}(\varphi_1, \vartheta_1, \omega_1), & \text{two phase rotation.} \end{cases} \quad (4.36)$$

4.2.5 Computational considerations

For evaluation of the integral $\mathbb{I}(\mathbf{q}, \mathbf{m}, \theta_{b,t}, \phi_{c,t})$ using the results presented in Theorem 6, Wigner- d functions $\Delta_{m,n}^\ell$ must be known and infinite series expansions in equations (4.22), (4.27) and (4.28) must be truncated in such a way that the truncation error is insignificant. $\Delta_{m,n}^\ell$ are computed using the recursions in [99, 100], as commented at the end of Section 2.4, and the infinite series expansions are truncated according to the criteria given below.

Taylor series expansion of tangent inverse

Taylor series expansion of $\tan^{-1}(\cdot)$ in (A.6) results in an alternating series⁴. If S_N denotes the partial sum of $N + 1$ terms in the series and S denotes the limit point of

⁴An alternating series is given by $\sum_{k=0}^{\infty} (-1)^k a_k$, $a_k > 0 \forall k$.

the series, then from the alternating series estimation theorem [121],

$$|S_N - S| \leq a_{N+1}, \quad (4.37)$$

where a_{N+1} is the $(N + 2)^{\text{th}}$ term in the alternating series and marks the residual error. Hence, the two alternating series, indexed by n_1 and n_2 in (A.6) and (A.7), can be truncated at N_1 and N_2 respectively, if

$$a_{N_1+1} = \frac{1}{2(N_1 + 1) + 1} \left(\frac{\mathbf{k}_t}{\sin(\phi_{c,t} - (\phi_1 - \delta_{N_1}))} \right)^{2(N_1+1)+1} \leq \text{tol}, \quad (4.38)$$

$$a_{N_2+1} = \frac{1}{2(N_2 + 1) + 1} \left(\frac{\sin(\phi_{c,t} - (\phi_1 + \delta_{N_2}))}{\mathbf{k}_t} \right)^{2(N_2+1)+1} \leq \text{tol}, \quad (4.39)$$

where tol is the preset tolerance. To ensure that the residual error of the partial sum of the series in (A.6) is below a certain threshold for all values of $\phi \in [0, \phi_1]$, a_{N_1+1} in (4.38) must be evaluated at $\phi = \phi_1$, because the residual error will be smaller at all other values of ϕ (for fixed N_1). However, this proposed choice requires an unnecessarily large number of terms to reduce a_{N_1+1} as $\mathbf{k}_t / \sin(\phi_{c,t} - \phi_1) = 1$. Consequently, the residual error is minimized at $\phi = \phi_1 - \delta_{N_1}$, where δ_{N_1} is a small deviation from ϕ_1 . Similarly, for the residual error of the partial sum of the series in (A.7) to be below a certain threshold for all values of $\phi \in [\phi_1, \phi_{c,t}]$, a_{N_2+1} should be minimized at $\phi = \phi_1$ but since $\sin(\phi_{c,t} - \phi_1) / \mathbf{k}_t = 1$, it will take an unnecessarily large number of terms to reduce a_{N_2+1} . Hence, a_{N_2+1} is minimized instead at $\phi = \phi_1 + \delta_{N_2}$, where δ_{N_2} is a small deviation from ϕ_1 .

Following a similar argument, the alternating series indexed by n_3 in (4.22) can be truncated at N_3 if

$$a_{N_3+1} = \frac{1}{2(N_3 + 1) + 1} \left(\frac{\sin(\phi_{c,t} - \delta_{N_3})}{\mathbf{k}_t} \right)^{2(N_3+1)+1} \leq \text{tol}, \quad (4.40)$$

where δ_{N_3} is a small increment if $\theta_{b,t} = \pi/4$ and is zero otherwise.

Generalized binomial expansion

We propose to truncate the generalized binomial expansion in (A.9) and (A.10) at $J_1 = T_{J_1}$ and $J_2 = T_{J_2}$ respectively, such that

$$\left| \sec \phi_{c,t} - \sum_{J_1=0}^{T_{J_1}} \binom{-1/2}{J_1} (-1)^{J_1} \sin^{2J_1} \phi_{c,t} \right| \leq \text{tol}, \quad (4.41)$$

$$\left| \sec(\phi_{c,t} - \phi_1) - \sum_{J_2=0}^{T_{J_2}} \binom{-1/2}{J_2} (-1)^{J_2} \sin^{2J_2}(\phi_{c,t} - \phi_1) \right| \leq \text{tol}, \quad (4.42)$$

where tol denotes the preset tolerance and slowest rate of convergence has been considered in the truncation criterion.

4.3 Numerical validation and illustrations

We establish the validity of the integrals formulated in Section 4.2.1 and Section 4.2.2 using the Earth and Mars topography maps⁵. The geographical region of Australia is used for illustration on the Earth topography map. The Australian coastlines data is extracted from the worldmap data, available in MATLAB, to obtain a spherical polygon with 299 vertices. To speed up computation, the Australian polygon is manually down-sampled to 124 vertices and triangulated to obtain 244 spherical right-angled triangles. Geographical region of Australia and its down-sampled version are shown in Figure 4-4, from which it can be seen that the down-sampled Australian polygon is not much different from the original Australian polygon. We evaluate the integral of the Earth topography map and compute bandlimited Slepian functions over the down-sampled Australian region, which from now on is referred to as Australia, and is denoted by R_A .

For illustration on the Mars topography map, which is processed to have zero

⁵Please refer to Footnote 5 (on page 62) and Footnote 8 (on page 72) for the source of Earth and Mars topography maps respectively.

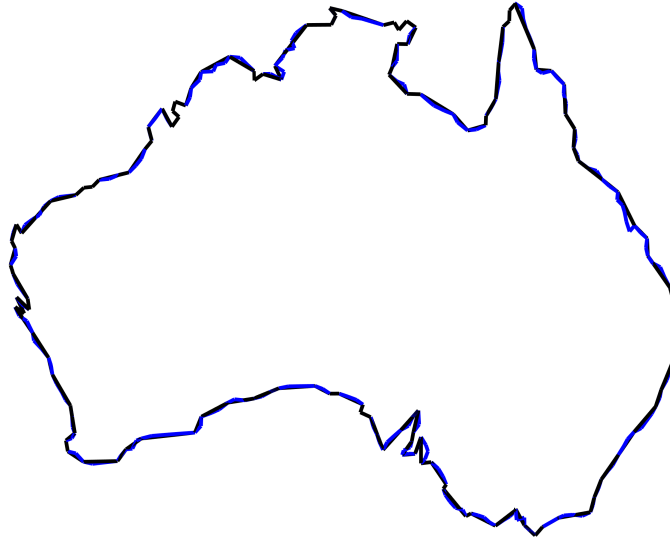


Figure 4-4: Geographical region of Australia (shown in blue) and its down-sampled version (shown in black), excluding Tasmania and neighboring islands.

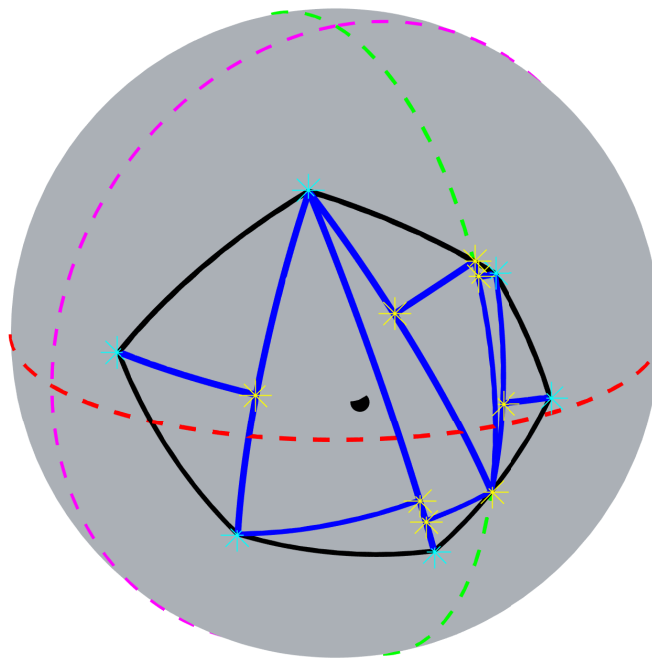


Figure 4-5: Simple polygon, which encloses the volcanic plateau of Tharsis on the Mars topography map, and its right-angled triangulation. Boundary of the polygon is shown in black. Thick black dot marks the centroid of the polygon.

average value and unit norm, a simple polygon is constructed on the sphere with 6 vertices at positions $(\theta, \phi) = (45^\circ, 54^\circ), (63^\circ, 94^\circ), (87^\circ, 102^\circ), (114^\circ, 80^\circ), (110^\circ, 42^\circ),$

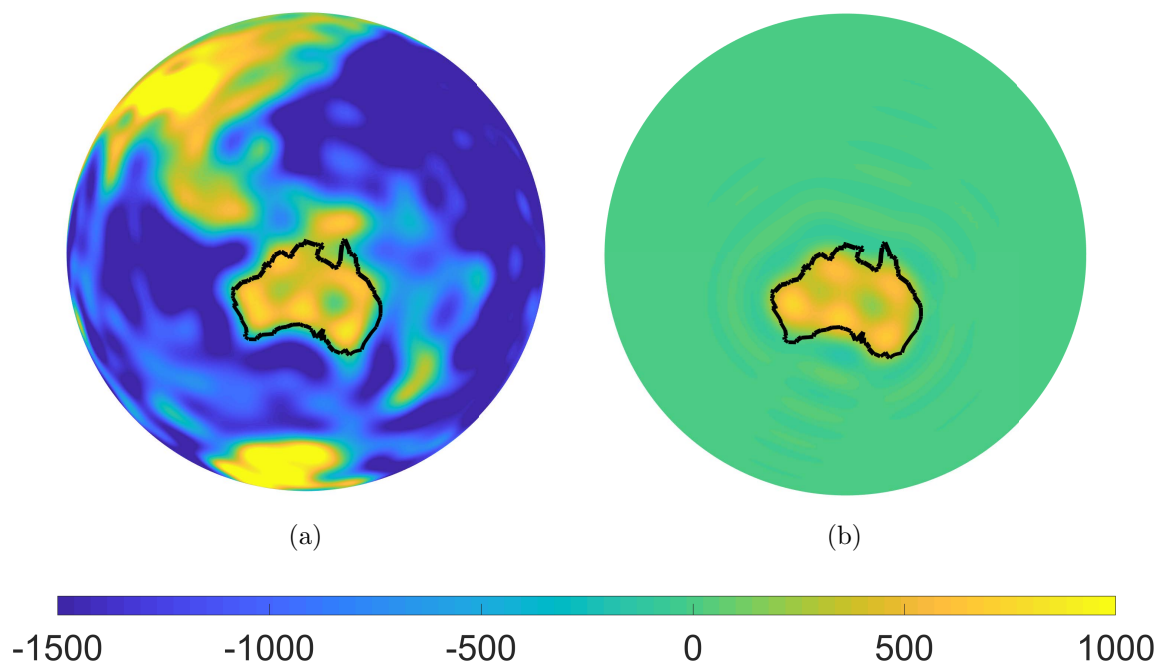


Figure 4-6: (a) Earth topography map, bandlimited to degree $L = 32$, (b) Earth topography map reconstructed over Australia at bandlimit $L = 32$, using $N_{R_A} \approx 15$ Slepian functions. Boundary of Australia is shown in black.

($79^\circ, 18^\circ$), such that the polygon encloses the volcanic plateau of Tharsis on Mars. For simplicity, we refer to the region of the Mars topography map enclosed by the polygon as Tharsis and denote it by R_T . The polygon is triangulated to obtain 12 spherical right-angled triangles, which are shown in Figure 4-5.

Preset tolerance in (4.38), (4.39), (4.40), (4.41) and (4.42), for both illustrations, is set to 10^{-16} (double floating point numerical precision).

Integrating Earth and Mars topography maps over Australia and Tharsis respectively

We consider the Earth and Mars topography maps as the test signals, bandlimited to degree $L = 32$ and shown in Figure 4-6 and Figure 4-7, for integration over Australia and Tharsis respectively. We verify the integration using the Gauss-Legendre (GL) quadrature rule [58] applied to the samples within the polygons enclosing Australia and Tharsis respectively. GL sampling scheme, parameterized by L_1 , places L_1 iso-

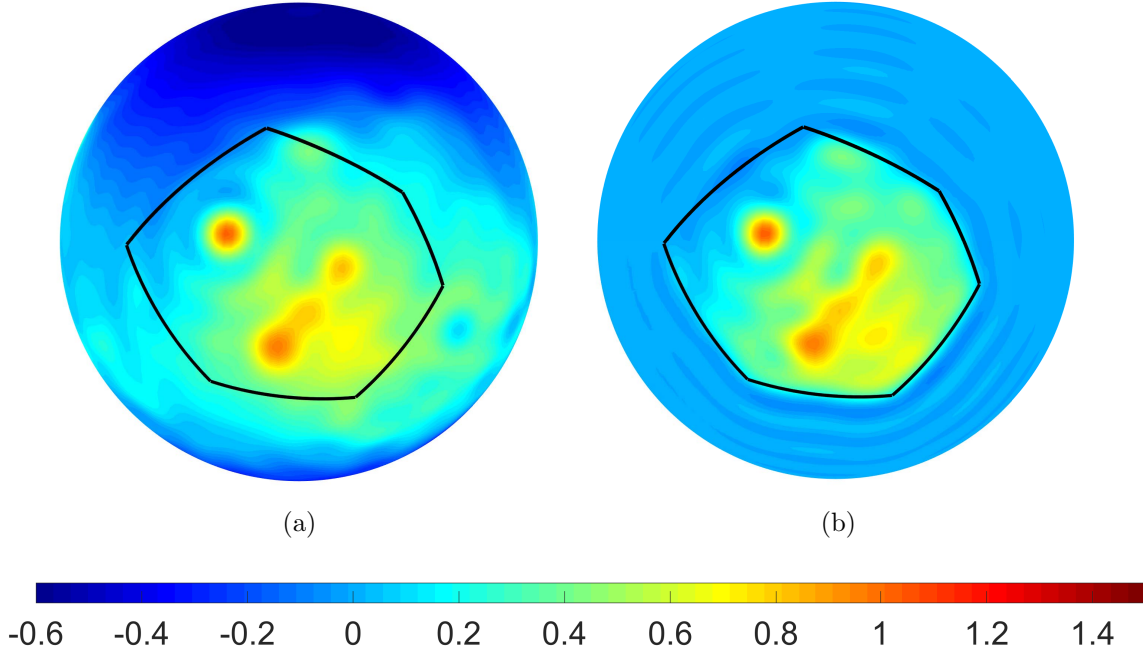


Figure 4-7: (a) Mars topography map, bandlimited to degree $L = 32$, (b) Mars topography map reconstructed over Tharsis at bandlimit $L = 32$, using $N_{RT} \approx 93$ Slepian functions. Boundary of Tharsis is shown in black.

latitude rings (rings of constant colatitude) of samples on the sphere at locations given by the roots of the Legendre polynomial of degree L_1 , with each ring having $2L_1 - 1$ uniformly placed samples along longitude. For the test signal $f(\hat{\mathbf{x}})$, GL quadrature on the sphere, utilizing these samples, is computed as

$$I_{GL,L_1,S^2} = \int_{S^2} f(\theta, \phi) \sin \theta d\theta d\phi = \frac{2\pi}{2L_1 - 1} \sum_{j=0}^{L_1-1} \sum_{k=0}^{2L_1-1} w_j(\theta_j) f(\theta_j, \phi_k), \quad (4.43)$$

where $w_j(\theta_j)$ is the GL quadrature weight for the iso-latitude ring located at $\theta = \theta_j$ [58]. We use the GL quadrature in (4.43) (which is exact for bandlimit $L \leq L_1$) to approximate the integration of the test signal $f(\hat{\mathbf{x}})$ over a spherical polygon bounding spatial region R_P , as

$$I_{GL,L_1,R_P} = \int_{R_P} f(\theta, \phi) \sin \theta d\theta d\phi \approx \frac{2\pi}{2L_1 - 1} \sum_{j=0}^{L_1-1} \sum_{k=0}^{2L_1-1} w_j(\theta_j) f(\theta_j, \phi_k) m(\theta_j, \phi_k), \quad (4.44)$$

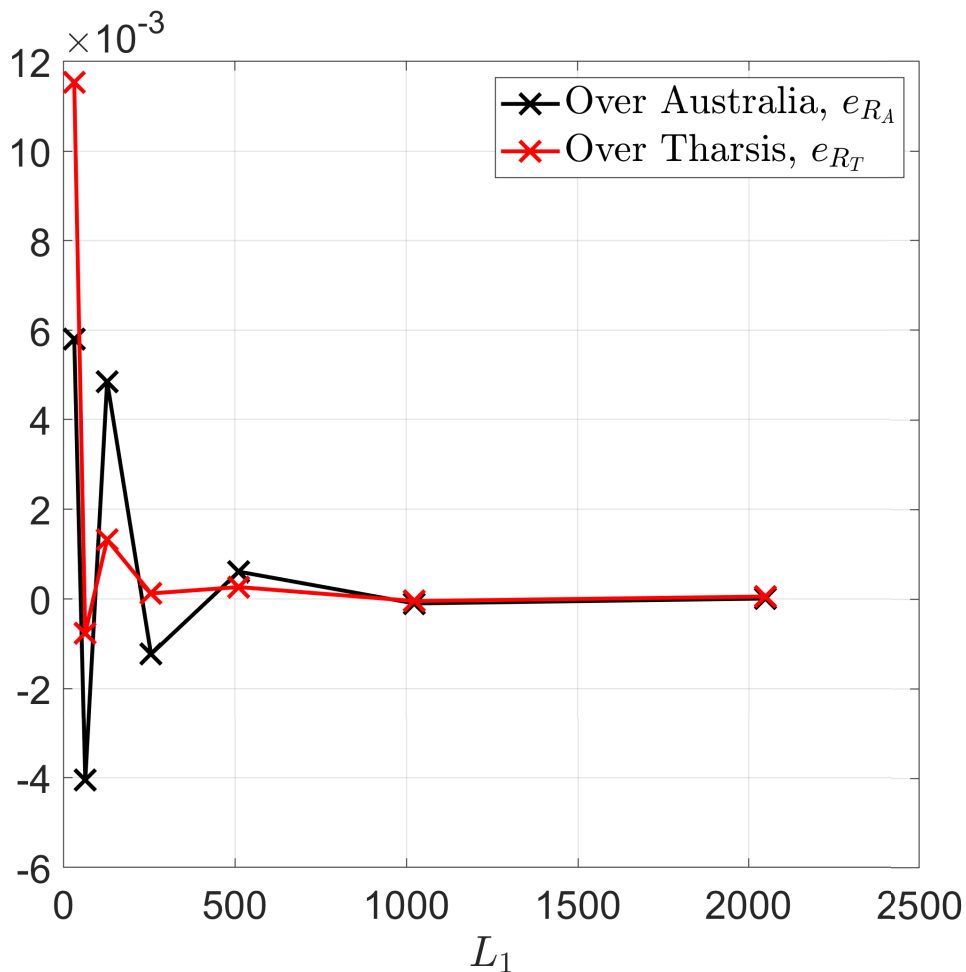


Figure 4-8: Fractional error between the integral of the Earth (Mars) topography map (bandlimited to degree $L = 32$), evaluated over Australia (Tharsis) using the formulation in (4.7) and GL quadrature rule in (4.44), for $L \leq L_1 \leq 2048$.

where

$$m(\theta_j, \phi_k) = \begin{cases} 1, & (\theta_j, \phi_k) \in R_P, \\ 0, & \text{otherwise} \end{cases} \quad (4.45)$$

limits the spatial extent of the bandlimited test signal $f(\hat{\mathbf{x}})$ to within the polygon and hence, essentially makes $f(\hat{\mathbf{x}})$ a band-unlimited signal. As a result, approximation in (4.44) approaches equality as $L_1 \rightarrow \infty$.

We evaluate I_{R_P} using the proposed analytic formulation in (4.7), compute I_{GL, L_1, R_P}

for different values of L_1 , and obtain the fractional error, given by

$$e_{R_P}(L_1) = \frac{I_{R_P} - I_{GL,L_1,R_P}}{I_{R_P}}. \quad (4.46)$$

Figure 4-8 shows the fractional error curves e_{R_A} and e_{R_T} , for the Australian and Tharsis regions on the Earth and Mars topography maps respectively, versus the GL sampling scheme parameter L_1 . It is evident that the integral of the Earth and Mars topography maps, over the spherical polygons representing the regions of Australia and Tharsis respectively, obtained using GL quadrature rule approaches the analytical expression given in (4.7) as the number of GL samples are increased.

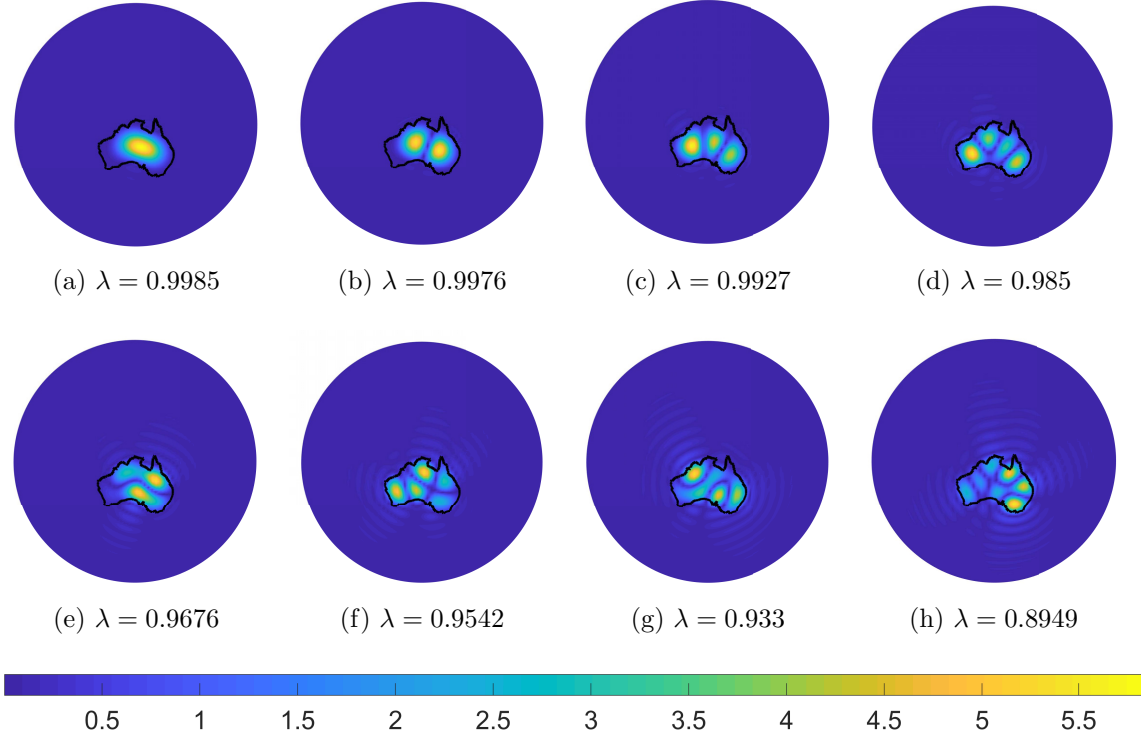


Figure 4-9: Magnitude of the first 8 Slepian functions computed for Australia at bandlimit $L = 32$. Boundary of Australia is shown in black.

Computation of Slepian functions over Australia and Tharsis

For the computation of Slepian functions over the regions of Australia, i.e., R_A , and Tharsis, i.e., R_T , the respective matrices in (4.10), for bandlimit $L = 32$, are

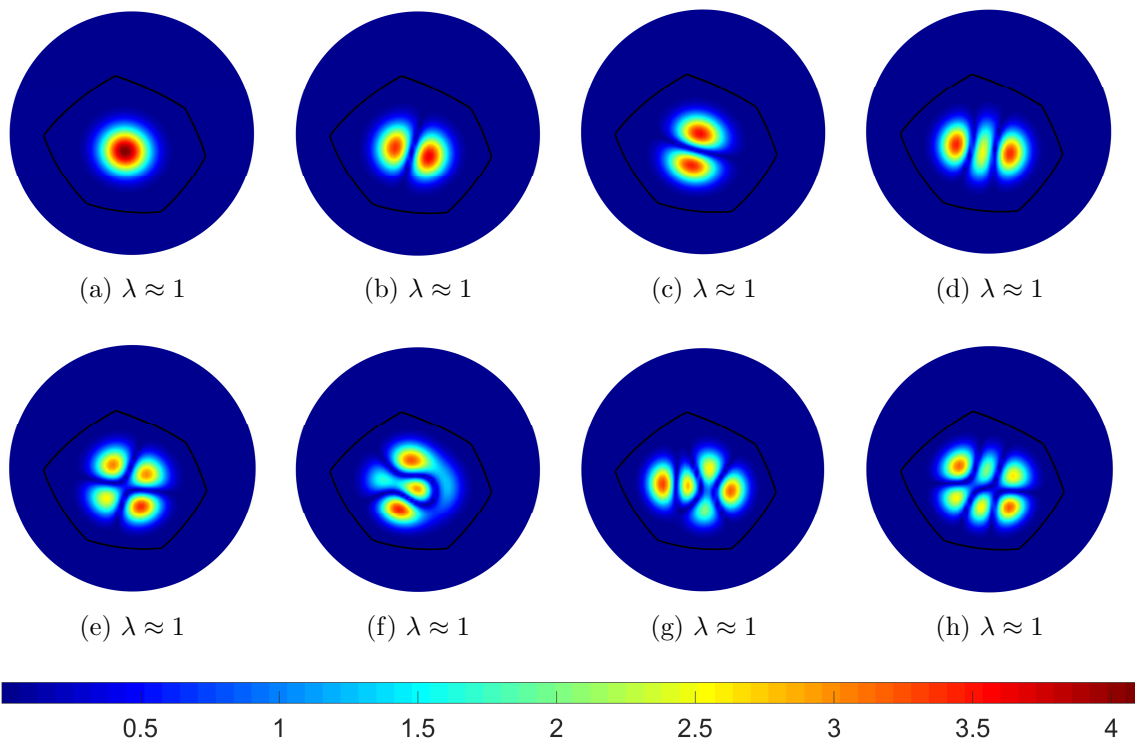


Figure 4-10: Magnitude of the first 8 Slepian functions computed for Tharsis at bandlimit $L = 32$. Boundary of Tharsis is shown in black.

constructed by computing the elements in (4.11) and eigenvalue decomposition is performed to obtain the Slepian functions in the spectral domain. Using the spherical Shannon number defined in (2.66), which is rounded to the nearest integer, number of well-optimally concentrated Slepian functions for Australia and Tharsis is given by $N_{R_A} \approx 15$ and $N_{R_T} \approx 93$ respectively. The magnitude of the first 8 Slepian functions for Australia is shown in Figure 4-9, whereas Figure 4-10 shows the magnitude of the first 8 Slepian functions for Tharsis. By projecting the respective maps onto the N_{R_A} and N_{R_T} well-optimally concentrated Slepian functions, the Earth topography map is reconstructed over Australia and shown in Figure 4-6, whereas the Mars topography map is reconstructed over Tharsis and shown in Figure 4-7.

Chapter 5

Spatial-Slepian transform on the sphere

Motivated by the idea of wavelet transform, where the signal content is essentially spread out in the joint space-scale domain, we seek to find a representation of signals to analyze their local characteristics in an effort to detect localized hidden features. Naturally, we revert to Slepian spatial-spectral concentration problem on the sphere, which results in optimally localized Slepian basis functions that can be used for accurate representation and reconstruction of signals in a given region on the sphere. Using well-optimally localized Slepian functions, with varying fractional energy concentration within a region on the sphere, we propose a transform, referred to as spatial-Slepian transform (SST), which is similar in mathematical formulation to the scale-discretized wavelet transform but uses bandlimited and spatially well-optimally concentrated Slepian functions, instead of wavelet functions. The proposed transform records “Slepian scale”-dependent information of the underlying signal in spatial-Slepian coefficients, which constitute a novel joint spatial-Slepian domain representation for signals on the sphere. We also propose an inverse transform to recover the spectral representation of the signal from its spatial-Slepian coefficients, and formulate an algorithm for efficient numerical computation of SST.

Depending on the shape of the underlying region for Slepian functions, spatial-Slepian coefficients are either spherical signals or signals defined on the $\text{SO}(3)$ rotation

group. The number of spatial-Slepian coefficients is shown to be determined by the fractional area of the region chosen to solve the Slepian spatial-spectral concentration problem. By analyzing spatial variance of spatial-Slepian coefficients, we show them to exhibit much better spatial localization than scale-discretized wavelet coefficients, thus highlighting their ability to probe local contents of the signal.

To demonstrate the utility of spatial-Slepian transform, we formulate a framework for detecting the presence of hidden (weak) localized variations in the signal, by statistically analyzing the spatial-Slepian coefficients. Furthermore, we present a novel framework for generalized linear transformations in the joint spatial-Slepian domain and exemplify through particular forms of the underlying spatial-Slepian transformation kernel.

5.1 Spatial-Slepian transform (SST)

We consider a region R on the sphere and solve the eigenvalue problem in (2.60) to obtain the Slepian functions $g_\alpha(\hat{\mathbf{x}})$, bandlimited to degree L_g and having spectral representations given by the eigenvectors \mathbf{g}_α , where $\alpha = 1, 2, \dots, L_g^2$ enables indexing of the Slepian functions according to (2.61). The framework of spatial-Slepian transform is formulated by using the well-optimally concentrated Slepian functions, i.e., $g_\alpha(\hat{\mathbf{x}})$, $\alpha \in [1, N_R]$, where N_R is the spherical Shannon number, defined in (2.66), rounded to the nearest integer.

5.1.1 SST formulation

For a signal $f \in \mathcal{H}_{L_f}$, spatial-Slepian transform is defined as

$$F_{g_\alpha}(\rho) \triangleq \langle f, \mathcal{D}(\rho)g_\alpha \rangle_{\mathbb{S}^2} = \int_{\mathbb{S}^2} f(\hat{\mathbf{x}}) \overline{(\mathcal{D}(\rho)g_\alpha)(\hat{\mathbf{x}})} ds(\hat{\mathbf{x}}), \quad (5.1)$$

where $\mathcal{D}(\rho) \equiv \mathcal{D}(\varphi, \vartheta, \omega)$ is the rotation operator, which rotates the Slepian function $g_\alpha(\hat{\mathbf{x}})$ around z , y , z axes by angles ω , ϑ , φ respectively, $F_{g_\alpha} \in L^2(\mathbb{SO}(3))$ is called the α^{th} spatial-Slepian coefficient of the signal $f(\hat{\mathbf{x}})$, and we have used the definition

of convolution of spherical signals given in (2.74). Spatial-Slepian transform in (5.1) probes the signal content by projecting it onto all possible rotated orientations of the well-optimally concentrated Slepian functions on the sphere, essentially spreading out the signal in the so called joint spatial-Slepian domain. The extent of the spread of the signal in the joint spatial-Slepian domain, which is quantified by the number of spatial-Slepian coefficients, is specified by the rounded spherical Shannon number, and therefore, depends on the fractional surface area of the region R on the sphere and the bandlimit L_g of Slepian functions. In this context, we refer to α as the Slepian scale and $F_{g_\alpha}(\rho)$ as the spatial-Slepian coefficient at the Slepian scale α .

Using the expansion of signals in (2.23) and (2.47), we can rewrite (5.1) as

$$\begin{aligned} F_{g_\alpha}(\rho) &= \sum_{\ell, m}^{L_f-1} (f)_\ell^m \sum_{p, q, m'}^{L_g-1} \overline{(g_\alpha)_p^{m'}} \overline{D_{q, m'}^p(\rho)} \int_{\mathbb{S}^2} Y_\ell^m(\hat{\mathbf{x}}) \overline{Y_p^q(\hat{\mathbf{x}})} ds(\hat{\mathbf{x}}) \\ &= \sum_{\ell, m, m'}^{\min\{L_f, L_g\}-1} (f)_\ell^m \overline{(g_\alpha)_\ell^{m'}} \overline{D_{m, m'}^\ell(\rho)}, \end{aligned} \quad (5.2)$$

where we have used orthonormality of spherical harmonics on the sphere to obtain the final expression, which expands the spatial-Slepian coefficient in terms of complex conjugate of Wigner- D functions. As a result, we define the spectral representation of spatial-Slepian coefficients as

$$(F_{g_\alpha})_{m, m'}^\ell \triangleq \left(\frac{2\ell + 1}{8\pi^2} \right) \left\langle F_{g_\alpha}, \overline{D_{m, m'}^\ell} \right\rangle_{\mathbb{S}\mathbb{O}(3)} = (f)_\ell^m \overline{(g_\alpha)_\ell^{m'}}, \quad (5.3)$$

for $0 \leq \ell \leq \min\{L_f, L_g\} - 1$, $|m|, |m'| \leq \ell$.

Remark 5. *Spatial-Slepian transform, formulated in (5.1), employs the definition of spherical convolution given in (2.74), which has also been adopted to define the scale-discretized wavelet transform on the sphere (reviewed in Section 2.9). Hence, spatial-Slepian transform in (5.1) appears similar in its mathematical formulation to the scale-discretized wavelet transform. However, the proposed transform uses bandlimited and spatially well-optimally localized Slepian functions rather than wavelet functions and results in a joint spatial-Slepian domain representation, which is not only different*

from the multiscale wavelet representation, but serves as an important tool for probing contents of any signal, which is localized within a region on the sphere.

5.1.2 Inverse SST

From the spectral representation of spatial-Slepian coefficients in (5.3), we can recover the spectral coefficients of the original signal $f(\hat{\mathbf{x}})$ as

$$\begin{aligned} (f)_\ell^m &= \left(\frac{2\ell + 1}{8\pi^2} \right) \frac{\left\langle F_{g_\alpha}, \overline{D_{m,m'}^\ell} \right\rangle_{\mathbb{SO}(3)}}{(g_\alpha)_\ell^{m'}} \\ &= \left(\frac{2\ell + 1}{8\pi^2} \right) \frac{\int_{\mathbb{SO}(3)} F_{g_\alpha}(\rho) D_{m,m'}^\ell(\rho) d\rho}{(g_\alpha)_\ell^{m'}}, \end{aligned} \quad (5.4)$$

provided the spherical harmonic coefficients of the Slepian functions, i.e., $(g_\alpha)_\ell^{m'}$, are non-zero for all degrees $0 \leq \ell \leq \min\{L_f, L_g\} - 1$ and at least one order $|m'| \leq \ell$.

Remark 6. For the case where $L_f > L_g$, inverse SST cannot recover all of the spectral coefficients of the signal $f(\hat{\mathbf{x}})$. On the other hand if $L_f < L_g$, then Slepian functions are under-utilized in obtaining the spatial-Slepian coefficients for the signal $f(\hat{\mathbf{x}})$. Hence, we assume that $L_f = L_g$, so that not only the Slepian functions are fully utilized, signal $f(\hat{\mathbf{x}})$ is also perfectly recovered from its spatial-Slepian coefficients.

5.1.3 Fast computation of spatial-Slepian transform

Since we define the spatial-Slepian transform through the definition of convolution given in (2.74), and originally presented in [61], we adopt the framework for fast computation of convolution of spherical signals, developed in [61], to efficiently compute the spatial-Slepian coefficients. This fast algorithm has become a standard tool for efficient computation of transforms, which are defined through the inner product between signals on the sphere, such as the directional spatially localized spherical harmonic transform [98] and the scale-discretized wavelet transform on the sphere [122].

From the definition of Wigner- D functions in (2.38), we note that the spatial-

Slepian coefficient in (5.2) can be written as

$$\begin{aligned}
 F_{g_\alpha}(\varphi, \vartheta, \omega) &= \sum_{\ell, m, m'}^{L_f-1} (f)_\ell^m \overline{(g_\alpha)_\ell^{m'}} e^{im\varphi} d_{m, m'}^\ell(\vartheta) e^{im'\omega} \\
 &= \sum_{\ell, m}^{L_f-1} (f)_\ell^m e^{im\varphi} \sum_{m'=-\ell}^{\ell} \overline{(g_\alpha)_\ell^{m'}} i^{m'-m} e^{im'\omega} \sum_{m''=-\ell}^{\ell} \Delta_{m'', m}^\ell \Delta_{m'', m'}^\ell e^{im''\vartheta}, \quad (5.5)
 \end{aligned}$$

where $\Delta_{m, m'}^\ell \triangleq d_{m, m'}^\ell(\pi/2)$ and we have used the expansion for Wigner- d functions in (2.52). By rearranging the summations in (5.5), we can rewrite the spatial-Slepian coefficient as

$$F_{g_\alpha}(\rho) = \sum_{m, m', m''=-(L_f-1)}^{L_f-1} C_{m, m', m''}^\alpha e^{i(m\varphi + m''\vartheta + m'\omega)}, \quad (5.6)$$

where

$$C_{m, m', m''}^\alpha = i^{m'-m} \sum_{\ell=\max\{|m|, |m'|, |m''|\}}^{L_f-1} (f)_\ell^m \overline{(g_\alpha)_\ell^{m'}} \Delta_{m'', m}^\ell \Delta_{m'', m'}^\ell. \quad (5.7)$$

The expression in (5.6) is a simple rearrangement of the initial expression in (5.2) and hence, is not more efficient. However, the presence of complex exponential functions in (5.6) facilitates the use of the fast Fourier transform (FFT) algorithm to compute the spatial-Slepian coefficients efficiently.

5.1.4 SST using zonal Slepian functions

Slepian spatial-spectral concentration problem for polar cap regions has been analytically solved in [74]. In this section, we employ the zero-order Slepian functions, optimally localized in the north polar cap region of angle θ_0 , to compute the spatial-Slepian transform. Such Slepian functions are axisymmetric by definition and are called zonal Slepian functions, for which the spherical Shannon number is given by [36]

$$N_{\theta_0, 0} = L \frac{\theta_0}{\pi}. \quad (5.8)$$

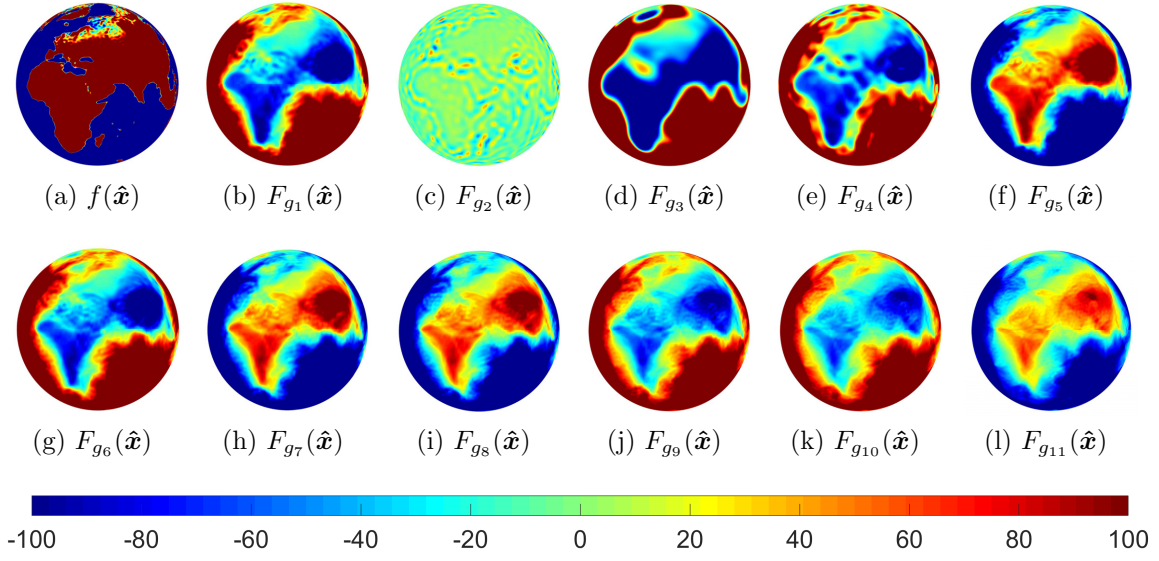


Figure 5-1: Earth topography map and $N_{\theta_0,0} \approx 11$ spatial-Slepian coefficients for the Earth topography map at bandlimit $L_f = 128$, using the zonal Slepian functions computed for the axisymmetric north polar cap region of angle $\theta_0 = 15^\circ$.

Using the following spectral representation for zonal Slepian functions

$$(g_\alpha)_\ell^m = (g_\alpha)_\ell^0 \delta_{m,0}, \quad (5.9)$$

we can write the rotated signal $(\mathcal{D}(\rho)g_\alpha)$ in (5.1) as

$$\begin{aligned}
 (\mathcal{D}(\rho)g_\alpha)(\hat{\mathbf{x}}) &= \sum_{\ell,m}^{L-1} \left(\sum_{m'=-\ell}^{\ell} D_{m,m'}^\ell(\rho) (g_\alpha)_{\ell}^{m'} \right) Y_\ell^m(\hat{\mathbf{x}}) = \sum_{\ell,m}^{L-1} D_{m,0}^\ell(\vartheta, \varphi, \omega) (g_\alpha)_\ell^0 Y_\ell^m(\hat{\mathbf{x}}) \\
 &= \sum_{\ell,m}^{L-1} \sqrt{\frac{4\pi}{2\ell+1}} \overline{Y_\ell^m(\vartheta, \varphi)} (g_\alpha)_\ell^0 Y_\ell^m(\hat{\mathbf{x}}), \quad (5.10)
 \end{aligned}$$

where we have used the relation between Wigner- D functions and spherical harmonics in (2.49) to obtain the final result. Therefore, spatial-Slepian coefficients in (5.1), for zonal Slepian functions, can be written as

$$\begin{aligned}
 F_{g_\alpha}(\rho) &= \langle f, \mathcal{D}(\rho)g_\alpha \rangle_{\mathbb{S}^2} = \sum_{\ell,m}^{L-1} \sqrt{\frac{4\pi}{2\ell+1}} (f)_\ell^m \overline{(g_\alpha)_\ell^0} Y_\ell^m(\vartheta, \varphi) \\
 &= F_{g_\alpha}(\hat{\mathbf{x}}), \quad \hat{\mathbf{x}} \equiv \hat{\mathbf{x}}(\vartheta, \varphi), \quad \alpha \in [1, N_{\theta_0,0}], \quad (5.11)
 \end{aligned}$$

where orthonormality of spherical harmonics has been used. We note that spatial-Slepian coefficients, in this case, are signals on the sphere with spherical harmonic coefficients given by

$$(F_{g_\alpha})_\ell^m = \langle F_{g_\alpha}, Y_\ell^m \rangle_{\mathbb{S}^2} = \sqrt{\frac{4\pi}{2\ell+1}} (f)_\ell^m \overline{(g_\alpha)_\ell^0}. \quad (5.12)$$

As a result, signal $f(\hat{\mathbf{x}})$ can be reconstructed perfectly from its spatial-Slepian coefficients as

$$f(\hat{\mathbf{x}}) = \sum_{\ell, m}^{L-1} \left[\sqrt{\frac{2\ell+1}{4\pi}} \frac{\langle F_{g_\alpha}, Y_\ell^m \rangle_{\mathbb{S}^2}}{\overline{(g_\alpha)_\ell^0}} \right] Y_\ell^m(\hat{\mathbf{x}}), \quad \overline{(g_\alpha)_\ell^0} \neq 0, \quad 0 \leq \ell \leq L_f - 1. \quad (5.13)$$

We use the Earth topography map¹, bandlimited to degree $L_f = 128$, for the computation of spatial-Slepian transform using zonal Slepian functions for the north polar cap region of angle $\theta_0 = 15^\circ$. Figure 5-1 shows the spatial-Slepian coefficients for the first $N_{\theta_0,0} \approx 11$ Slepian scales, along with the Earth topography map.

5.2 Analysis

In this section, we validate the inverse spatial-Slepian transform in (5.4) using different realizations of a random test signal at various bandlimits and perform computational complexity analysis of the fast algorithm presented in Section 5.1.3. Furthermore, we quantify spatial variance of spatial-Slepian coefficients and conduct different experiments to show that spatial-Slepian coefficients have better spatial localization than scale-discretized wavelet coefficients.

5.2.1 Inverse SST validation

We analyze the accuracy of the inverse SST using different realizations of a complex-valued and random test signal $f^T(\hat{\mathbf{x}})$, whose spectral coefficients are uniformly distributed in the interval $(-1, 1)$ in both real and imaginary parts. We compute

¹Please refer to Footnote 8 (on page 72) for the source of Earth topography map.

the spectral components of the spatial-Slepian coefficients of the test signal, i.e., $(F_{g_\alpha}^T)_{m,m'}^\ell$, from (5.3) using Slepian functions that are well-optimally concentrated in the north polar cap region of angle $\theta_0 = 15^\circ$. Spectral components of the reconstructed signal, denoted by $(f^R)_\ell^m$, are computed from the inverse SST in (5.4) using the Slepian function at Slepian scale $\alpha = 1$, i.e.,

$$(f^R)_\ell^m = \frac{(F_{g_1}^T)_{m,m'}^\ell}{(g_1)_\ell^{m'}}, \quad 0 \leq \ell \leq L_f - 1, |m| \leq \ell, \quad (5.14)$$

where L_f is the bandlimit of the test signal. Numerical accuracy of the inverse SST is evaluated by defining the absolute mean error as

$$\mathbf{E}_{\text{mean}} = \frac{1}{L_f^2} \sum_{\ell,m}^{L_f-1} |(f^T)_\ell^m - (f^R)_\ell^m|, \quad (5.15)$$

which is averaged over 100 realizations of the test signal. The results of this experiment are shown in Figure 5-2 at different values of the bandlimit L_f . As expected, average absolute mean error is on the order of numerical precision, which establishes the numerical stability of the inverse SST.

5.2.2 Computational complexity analysis

Spatial-Slepian coefficients in (5.6) require computation of coefficients $\mathcal{C}_{m,m',m''}^\alpha$ over the three dimensional space of orders m , m' and m'' . Coefficients $\mathcal{C}_{m,m',m''}^\alpha$ in turn require a single summation over the degree ℓ for each m , m' , m'' . As a result, the complexity of computing $\mathcal{C}_{m,m',m''}^\alpha$ scales as $O(L_f^4)$ with bandlimit L_f . We note that Wigner- d functions $\Delta_{m,m'}^\ell$ do not depend on either the signal or Slepian functions and hence, can be independently computed, in time which scales as $O(L_f^3)$, using the recursion in [100]. However, we compute $\Delta_{m,m'}^\ell$ on-the-fly to minimize storage requirements and note that this does not change the computational complexity of $O(L_f^4)$ for the coefficients $\mathcal{C}_{m,m',m''}^\alpha$. Computational complexity of the three dimensional fast Fourier transform scales as $O(L_f^3 \log_2 L_f)$ with bandlimit L_f . Hence, the

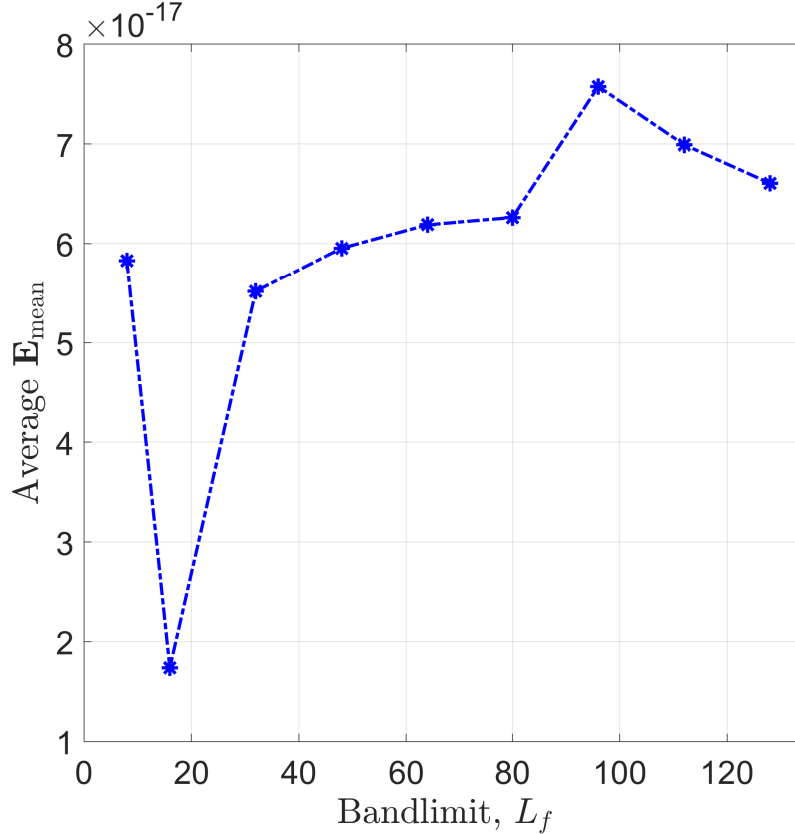


Figure 5-2: Absolute mean error \mathbf{E}_{mean} , computed from the spectral coefficients of a complex-valued and random test signal $f^T(\hat{\mathbf{x}})$, and the reconstructed signal $f^R(\hat{\mathbf{x}})$, is averaged over 100 realizations of the test signal and plotted against the bandlimit $L_f = 8, 16, 32, 48, 64, 80, 96, 112, 128$. Figure shows that the error is on the order of numerical precision, which verifies the numerical stability of the inverse SST.

overall complexity for computing the spatial-Slepian coefficient in (5.6) is governed by the coefficients $\mathcal{C}_{m,m',m''}^\alpha$, and is given by $O(L_f^4)$ for a fixed Slepian scale α , and $O(N_R L_f^4)$ for all Slepian scales, i.e., $\alpha = 1, 2, \dots, N_R$.

We validate the computational complexity of the spatial-Slepian transform using one of the Slepian functions (at Slepian scale $\alpha = 1$), computed for a spherical ellipse, defined in (2.11), having focus colatitude $\theta_0 = 15^\circ$ and semi-major axis $a = 20^\circ$. Spatial-Slepian coefficient is computed for a test signal, which is generated in the spectral domain such that the spectral coefficients are complex, with real and imaginary parts uniformly distributed in the interval $(0, 1)$. The experiment is performed in MATLAB, running on a 2.2 GHz Intel Core i7 processor with 16 GB RAM, for 10 realizations of the test signal. We record the mean time (averaged over

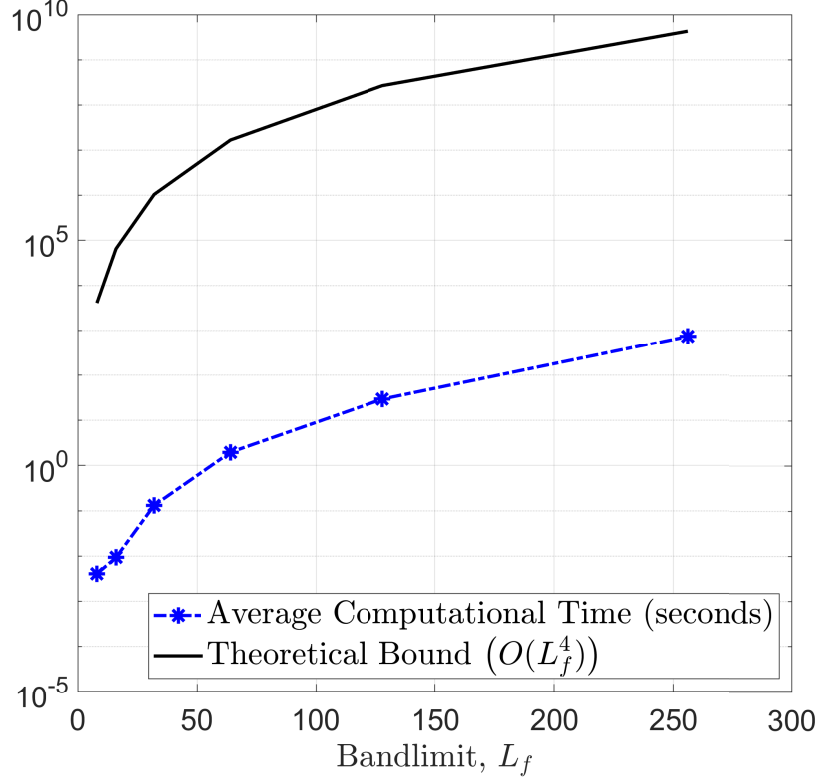


Figure 5-3: Computational complexity analysis of the spatial-Slepian transform for a complex-valued and random test signal using Slepian function at $\alpha = 1$, which is computed for a spherical ellipse $R_{(15^\circ, 20^\circ)}$. Computational time (shown in blue), which is averaged over 10 realizations of the test signal, is in agreement with the theoretical bound of $O(L_f^4)$ (shown in black).

10 realizations) at different values of the bandlimit L_f and plot it in Figure 5-3, where we also show the theoretical bound which scales as $O(L_f^4)$. As expected, the results in Figure 5-3 corroborate the theoretically established bound on the computational complexity of the spatial-Slepian transform.

5.2.3 Localization of spatial-Slepian coefficients

We adopt the mathematical formulation, used to evaluate the spatial variance of wavelet coefficients, presented in [123], to quantify the localization of spatial-Slepian coefficients on the $\mathbb{SO}(3)$ rotation group as

$$\text{var}_{F_{g_\alpha}(\rho)} = \mu_{|F_{g_\alpha}(\rho)|^2} - |\mu_{F_{g_\alpha}(\rho)}|^2, \quad (5.16)$$

where $\mu_{f(\rho)}$ is the spatial mean of a signal $f \in L^2(\mathbb{SO}(3))$ over all Euler angles, and is defined as

$$\mu_{f(\rho)} \triangleq \frac{1}{8\pi^2} \int_{\mathbb{SO}(3)} f(\rho) d\rho. \quad (5.17)$$

Hence, spatial mean of the spatial-Slepian coefficients is obtained as

$$\begin{aligned} \mu_{F_{g_\alpha}(\rho)} &= \sum_{\ell, m, m'}^{L_f-1} (f)_\ell^m \overline{(g_\alpha)_\ell^{m'}} \overline{\mu_{D_{m, m'}^\ell(\rho)}} = \sum_{\ell, m, m'}^{L_f-1} (f)_\ell^m (g_\alpha)_\ell^{m'} \frac{1}{8\pi^2} \int_{\mathbb{SO}(3)} \overline{D_{m, m'}^\ell(\rho)} d\rho \\ &= \sum_{\ell, m, m'}^{L_f-1} (f)_\ell^m \overline{(g_\alpha)_\ell^{m'}} \frac{1}{8\pi^2} \int_{\varphi=0}^{2\pi} e^{im\varphi} d\varphi \int_{\vartheta=0}^{\pi} \sin \vartheta d_{m, m'}^\ell(\vartheta) d\vartheta \int_{\omega=0}^{2\pi} e^{im'\omega} d\omega \\ &= \sum_{\ell, m, m'}^{L_f-1} (f)_\ell^m \overline{(g_\alpha)_\ell^{m'}} \frac{1}{8\pi^2} (4\pi^2) \delta_{m,0} \delta_{m',0} (2) \delta_{\ell,0} = (f)_0^0 \overline{(g_\alpha)_0^0}, \end{aligned} \quad (5.18)$$

where we have used the expression for Wigner- D functions in (2.38), the relation between Wigner- d functions and Legendre polynomials in (2.50) and the results in (2.95), (2.96) to obtain the final expression. The result in (5.18) is then used to compute spatial variance of the spatial-Slepian coefficient, at Slepian scale α , as

$$\begin{aligned} \text{var}_{F_{g_\alpha}(\rho)} &= \mu_{|F_{g_\alpha}(\rho)|^2} - |(f)_0^0|^2 |(g_\alpha)_0^0|^2 \\ &= \sum_{\ell, m, m'}^{L_f-1} (f)_\ell^m \overline{(g_\alpha)_\ell^{m'}} \sum_{p, q, q'}^{L_f-1} \overline{(f)_p^q} (g_\alpha)_p^{q'} \frac{1}{8\pi^2} \left(\frac{8\pi^2}{2\ell+1} \right) \delta_{\ell, p} \delta_{m, q} \delta_{m', q'} - |(f)_0^0|^2 |(g_\alpha)_0^0|^2 \\ &= \sum_{\ell, m, m'}^{L_f-1} \left(\frac{1}{2\ell+1} \right) |(f)_\ell^m|^2 |(g_\alpha)_\ell^{m'}|^2 - |(f)_0^0|^2 |(g_\alpha)_0^0|^2, \end{aligned} \quad (5.19)$$

where we have used orthogonality of Wigner- D functions over $\mathbb{SO}(3)$ rotation group to get the final result. As is evident from the expression in (5.19), spatial variance of the spatial-Slepian coefficient depends on the signal under consideration in addition to Slepian function.

We compute spatial variance of spatial-Slepian coefficients for the Earth topography map, bandlimited to degree $L_f = 64$, using Slepian functions which are well-optimally concentrated in the north polar cap region. For comparison, we also evalu-

ate spatial variance of scale-discretized wavelet coefficients of the bandlimited Earth topography map, which is given by [123]

$$\text{var}_{w_f^{\Psi^{(j)}}(\rho)} = \sum_{\ell, m, m'}^{L_f-1} \left(\frac{1}{2\ell+1} \right) |(f)_\ell^m|^2 |(\Psi^{(j)})_\ell^{m'}|^2, \quad (5.20)$$

where $\Psi^{(j)} \in L^2(\mathbb{S}^2)$ is the wavelet function at wavelet scale j , $w_f^{\Psi^{(j)}}(\rho)$ is the scale-discretized wavelet coefficient defined in (2.100), and we have used the fact that $(\Psi^{(j)})_0^0 = 0$, which can be seen from the harmonic tiling functions in Figure 2-4. We relate the angle of the north polar cap region, i.e., θ_0 to the dilation parameter ϵ in such a way that the number of wavelet scales is equal to the number of Slepian scales, i.e.,

$$N_{R_{\theta_0}} = \frac{2\pi(1 - \cos \theta_0)}{4\pi} L_f^2 = J + 1 = \lceil \log_\epsilon L_f \rceil + 1, \quad (5.21)$$

where we have chosen the largest wavelet scale to be J (the smallest wavelet scale is 0)². By setting the dilation parameter ϵ to 2, maximum wavelet scale J becomes 6 and $N_{R_{\theta_0}} = 7$, from which the polar cap angle θ_0 is found to be 4.7°. Spatial variance of spatial-Slepian and scale-discretized wavelet coefficients, for the bandlimited Earth topography map, is computed at each Slepian and wavelet scale, and plotted in Figure 5-4. Spatial-Slepian coefficients can be seen to exhibit smaller spatial variance compared to scale-discretized wavelet coefficients at most of the scales, which is evidence of better spatial localization of spatial-Slepian coefficients compared to the scale-discretized wavelet coefficients.

We also vary the dilation parameter ϵ while keeping bandlimit the same, i.e., $L_f = 64$, to obtain different number of wavelet scales for the scale-discretized wavelet transform of the Earth topography map. We compute spatial-Slepian coefficients of the Earth topography map using Slepian functions, which are well-optimally concentrated in the north polar cap regions of different polar cap angles, such that the

²We use directional wavelet functions and compute the directionality component $(\xi)_\ell^m$ for azimuthal bandlimit $L_\phi = 5$. As mentioned at the end of Section 2.9, we refer the reader to [83, 85] for details on the construction of $(\xi)_\ell^m$.

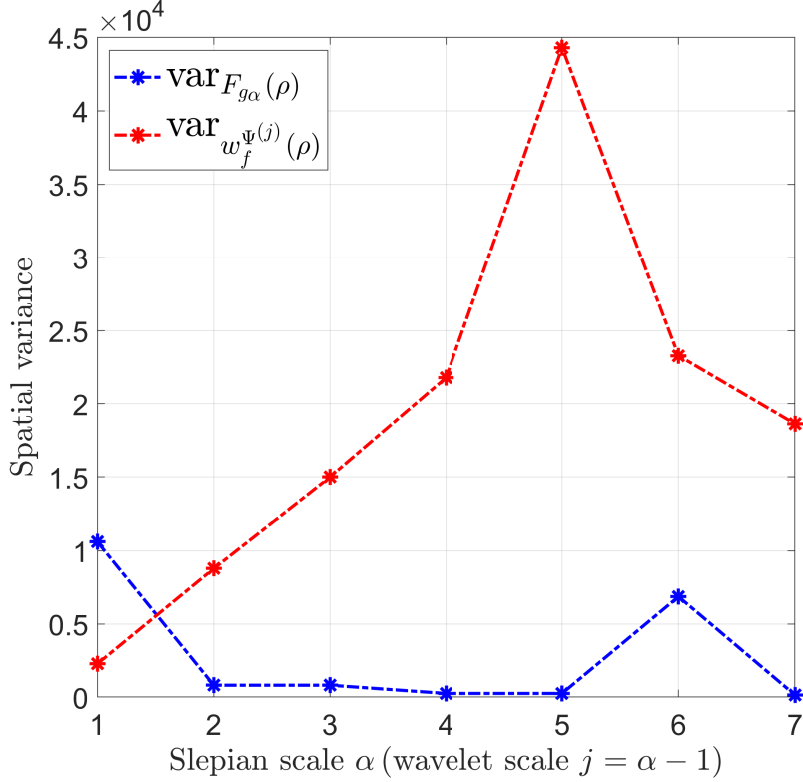


Figure 5-4: Spatial variance of spatial-Slepian and scale-discretized wavelet coefficients, evaluated for the Earth topography map, bandlimited to degree $L_f = 64$. Spatial-Slepian coefficients can be seen to be better localized than the scale-discretized wavelet coefficients at most of the scales.

number of Slepian scales equals the number of wavelet scales, according to (5.21). The fractional ratio of the number of spatial-Slepian coefficients (at each polar cap angle θ_0) having smaller spatial variance than scale-discretized wavelet coefficients (at each dilation parameter ϵ corresponding to θ_0), denoted by \mathbf{r} , is quantified as

$$\mathbf{r}(\theta_0) \triangleq \frac{\# \left\{ \text{var}_{F_{g\alpha}}(\rho) \leq \text{var}_{w_f^{\Psi(j)}(\rho)} \right\}}{N_{R_{\theta_0}}}, \quad (5.22)$$

where $\# \{ \cdot \}$ computes the number of elements satisfying the logical condition inside the braces. For dilation parameter $\epsilon = 1.5, 1.8, 2, 2.5, 3, 4$, we obtain polar cap angles, from (5.21), as $\theta_0 = 6.2^\circ, 5.4^\circ, 4.7^\circ, 4.4^\circ, 4^\circ, 3.6^\circ$, such that the number of corresponding Slepian (or wavelet) scales are 12, 9, 7, 6, 5, 4. The resulting fractional ratio \mathbf{r} is plotted against the number of Slepian (wavelet) scales in Figure 5-5, which shows a

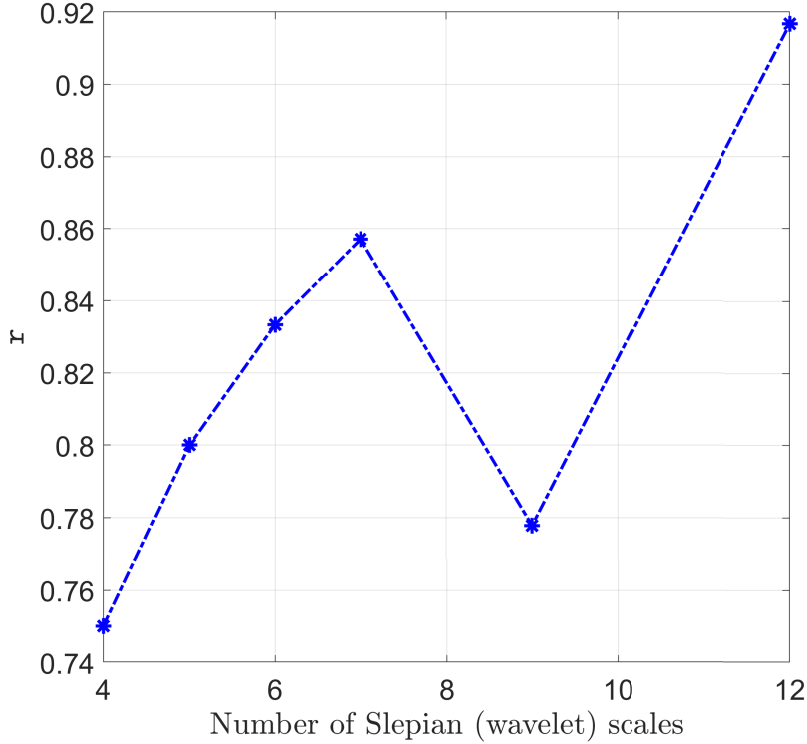


Figure 5-5: Fractional ratio r , for the Earth topography map, bandlimited to degree $L_f = 64$, is plotted against different number of Slepian (wavelet) scales, which are obtained by varying the polar cap angle θ_0 and the dilation parameter ϵ in such a way that the number of Slepian scales equals the number of wavelet scales. The curve shows that more number of spatial-Slepian coefficients have smaller spatial variance (and hence, better spatial localization) than scale-discretized wavelet coefficients, at every value of polar cap angle (or dilation parameter).

higher percentage of spatial-Slepian coefficients having smaller spatial variance than scale-discretized wavelet coefficients.

5.3 Localized variation analysis

As discussed in Section 2.5, bandlimited Slepian functions form an alternative basis for the representation of bandlimited signals on the sphere, and the well-optimally concentrated bandlimited Slepian functions form a (reduced) localized basis set for the accurate representation and reconstruction of bandlimited signals over a region on the sphere. Hence, this reduced basis can prove to be a useful tool for probing contents of any signal which is localized within a region on the sphere. In this con-

text, we present localized variation analysis as an application of the spatial-Slepian transform. The objective is to use spatial-Slepian coefficients of a signal to detect the presence of extremely weak localized spatial variations, hidden in the signal, along with an estimate of the underlying region that the spatial variations are localized within. In the following, we elaborate on the need for localized variation analysis to establish sufficient motivation, formulate its mathematical framework using spatial-Slepian transform, and use synthetic data to provide illustrations. Furthermore, we compare the results obtained from the spatial-Slepian transform with those obtained from the scale-discretized wavelet transform, and show that spatial-Slepian transform performs better by achieving a better estimate of the underlying region of localized variations.

5.3.1 Motivation

The problem of localized variation analysis is motivated by an application in the field of medical imaging, in which images of a human organ, e.g. the brain, are analyzed across different patients to diagnose the growth of a hidden anomaly, e.g., a tumor, which is not readily apparent in the images. The tumor can be effectively modeled as a localized variation which is hidden in the spherical image of the brain. We refer to the scan of the healthy brain, i.e., without the anomaly, as the source signal $s(\hat{\mathbf{x}})$, which is unknown. The anomaly is modeled as an extremely weak localized variation $c(\hat{\mathbf{x}})$, which is hidden in the source signal $s(\hat{\mathbf{x}})$ to give the scan of the brain as the spherical observation $f(\hat{\mathbf{x}}) = s(\hat{\mathbf{x}}) + c(\hat{\mathbf{x}})$, $\|c\|_{\mathbb{S}^2} \ll \|s\|_{\mathbb{S}^2}$. We assume that N_c different patients take part in this medical study, resulting in N_c different instances (realizations) of such a localized variation, which gives us an ensemble of observations on the sphere as

$$f^k(\hat{\mathbf{x}}) = s(\hat{\mathbf{x}}) + c^k(\hat{\mathbf{x}}), \quad \|c^k\|_{\mathbb{S}^2} \ll \|s\|_{\mathbb{S}^2}, \quad \forall k \in [1, N_c]. \quad (5.23)$$

The objective of localized variation analysis is to statistically identify the portion of the brain which has been affected by the tumor.

5.3.2 Mathematical framework

We compute spatial-Slepian coefficients of the observations using Slepian functions, which are well-optimally concentrated in a region R on the sphere. From linearity of the spatial-Slepian transform, we can write the spatial-Slepian coefficient of k^{th} observation as

$$F_{g_\alpha}^k(\rho) = S_{g_\alpha}(\rho) + C_{g_\alpha}^k(\rho), \quad \alpha \in [1, N_R], k = 1, 2, \dots, N_c, \quad (5.24)$$

with statistical mean and variance given by

$$\mathbb{E}\{F_{g_\alpha}(\rho)\} = S_{g_\alpha}(\rho) + \mathbb{E}\{C_{g_\alpha}(\rho)\}, \quad \alpha \in [1, N_R] \quad (5.25)$$

and

$$\begin{aligned} \sigma_{F_{g_\alpha}}^2(\rho) &= \mathbb{E}\{|F_{g_\alpha}(\rho) - \mathbb{E}\{F_{g_\alpha}(\rho)\}|^2\} \\ &= \mathbb{E}\{|C_{g_\alpha}(\rho)|^2\} - |\mathbb{E}\{C_{g_\alpha}(\rho)\}|^2 = \sigma_{C_{g_\alpha}}^2(\rho), \quad \alpha \in [1, N_R] \end{aligned} \quad (5.26)$$

respectively. We observe that spatial-Slepian coefficients of the observation have same variance as the spatial-Slepian coefficients of the localized variations, which enables us to use sample variance across different instances, denoted by $\Sigma_{F_{g_\alpha}}^2$ and given by,

$$\Sigma_{F_{g_\alpha}}^2(\rho) = \frac{1}{N_c} \sum_{k=1}^{N_c} \left| F_{g_\alpha}^k(\rho) - \frac{1}{N_c} \sum_{k=1}^{N_c} F_{g_\alpha}^k(\rho) \right|^2, \quad \alpha \in [1, N_R], \quad (5.27)$$

as a statistical measure for detecting the presence of hidden localized variations in the signal at different Slepian scales α .

5.3.3 Illustration

As an illustration, we consider a realization of a zero-mean and anisotropic Gaussian process as the source signal $s(\hat{\mathbf{x}})$, with bandlimit $L_s = 32$. We generate localized variations within the region $\tilde{R} = \mathbf{R}^{zyz}(60^\circ, 90^\circ, 45^\circ)R_{(20^\circ, 25^\circ)}$, which defines a spherical

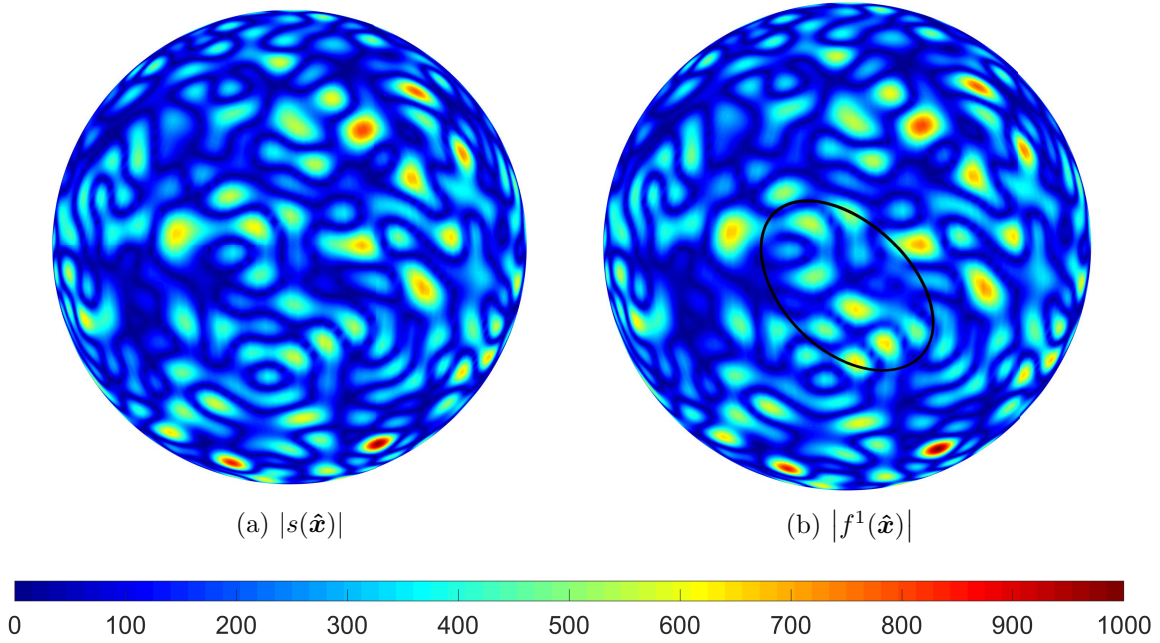


Figure 5-6: Magnitude of (a) the source signal, which is a realization of a zero-mean and anisotropic Gaussian process, and (b) the first observation that contains localized variation hidden in the source signal within the elliptical region. Both signals are bandlimited to degree 32. Boundary of the elliptical region is shown in black.

ellipse $R_{(20^\circ, 25^\circ)}$, given in (2.11), that is rotated by the Euler angles $\rho = (60^\circ, 90^\circ, 45^\circ)$.

The localized variations are given by

$$c^k(\hat{\mathbf{x}}) = \sum_{\beta=1}^{30} a_\beta^k \tilde{g}_\beta(\hat{\mathbf{x}}), \quad k = 1, 2, \dots, N_c, \quad (5.28)$$

where $\tilde{g}_\beta(\hat{\mathbf{x}})$ are the well-optimally concentrated Slepian functions for the elliptical region \tilde{R} , bandlimited to degree $L_{\tilde{g}} = 32$, a_β^k are random scalars drawn from the standard normal distribution, i.e., $a_\beta^k \sim \mathcal{N}(0, 1)$, and $N_{\tilde{R}} \approx 30$ is the spherical Shannon number (rounded to the nearest integer) for the region \tilde{R} . The strength of these variations is specified by signal to variation ratio (SVR), defined for the k^{th} instance as

$$\text{SVR}^k = 10 \log \frac{\|s(\hat{\mathbf{x}})\|_{\mathbb{S}^2}^2}{\|c^k(\hat{\mathbf{x}})\|_{\mathbb{S}^2}^2}. \quad (5.29)$$

We generate $N_c = 10$ instances of the localized variation such that SVR is 20 dBs for each variation, yielding $N_c = 10$ different observations on the sphere as

$$f^k(\hat{\mathbf{x}}) = s(\hat{\mathbf{x}}) + \sum_{\beta=1}^{30} a_{\beta}^k \tilde{g}_{\beta}(\hat{\mathbf{x}}), \quad k = 1, 2, \dots, N_c = 10, \quad (5.30)$$

where each observation is bandlimited to degree $L_f = 32$. Magnitude of the source signal $s(\hat{\mathbf{x}})$ and the observation, which contains the first instance of the localized variation, i.e., $f^1(\hat{\mathbf{x}})$, are shown in Figure 5-6. As can be seen, the localized variation in the highlighted elliptical region is hidden in the source signal. It must be noted that the source signal, localized variations and the spherical elliptical region \tilde{R} are unbeknownst to the framework of spatial-Slepian transform.

The presence of hidden variations is detected by obtaining spatial-Slepian coefficients of the observations using the zonal Slepian functions for a north polar cap region R of angle $\theta_0 = 15^\circ$, bandlimited to degree $L_g = 32$, and finding the sample variance across $N_c = 10$ instances at each Slepian scale $\alpha = 1, \dots, N_{\theta_0,0} \approx 3$. The results are shown in Figure 5-7, in which the unknown spherical elliptical region \tilde{R} is drawn for reference only. For comparison, we also plot the sample variance of scale-discretized wavelet coefficients, which are obtained from the axisymmetric wavelet functions through (2.108) (bandlimited to degree 32) by setting the dilation parameter ϵ to 2 and largest wavelet scale to $J = 5$, for a total of 6 wavelet scales. However, we choose to show the sample variance for the first 4 wavelet scales as there is negligibly small sample variance at wavelet scales $j = 4, 5$.

As can be seen from Figure 5-7, sample variance computed using the spatial-Slepian transform yields much more accurate detection of the hidden localized variations, specially at the first two Slepian scales, compared to the scale-discretized wavelet transform, which yields an over-estimate of the underlying region of localized variations. Superior performance of the spatial-Slepian transform is due to the fact that well-optimally concentrated Slepian functions are better suited to probe local content of the signal than wavelet functions. Although, wavelet functions have been shown to exhibit good spatial localization [85], unlike Slepian functions, their char-

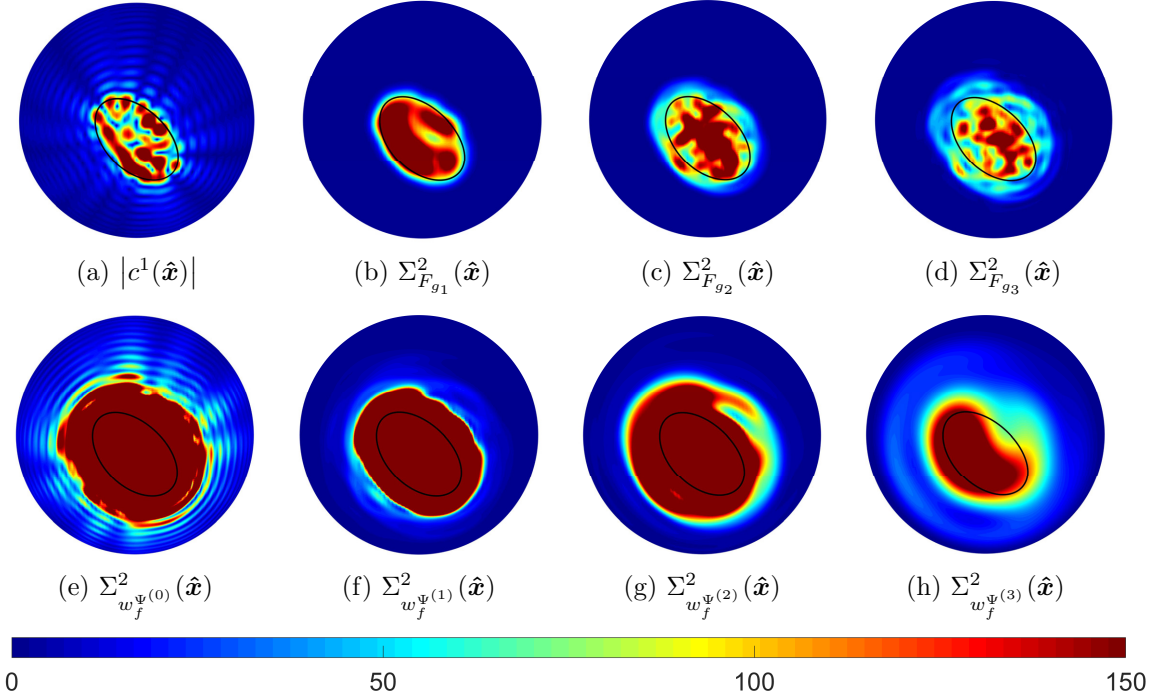


Figure 5-7: (a) Magnitude of the first instance of localized variation, (b)–(d) sample variance of spatial-Slepian coefficients, (e)–(h) sample variance of scale-discretized wavelet coefficients. As can be seen, sample variance of spatial-Slepian coefficients quite accurately detects the region of localized hidden variations, specially at the first two Slepian scales, whereas sample variance of scale-discretized wavelet coefficients yields an over-estimate of the region of localized variations. Spherical elliptical region of localized hidden variations is unbeknownst to the framework of spatial-Slepian and scale-discretized wavelet transforms, and is drawn for reference only.

acteristics are not defined by the shape of the underlying region, which makes them ill-suited for localized signal analysis on the sphere.

5.4 Generalized linear transformations in the joint spatial-Slepian domain

We define a general linear transformation of the spatial-Slepian coefficient of a signal $f \in \mathcal{H}_{L_f}$, at Slepian scale α , as

$$\nu_{g_\alpha}(\rho) = \sum_{\beta=1}^{N_R} (\mathfrak{S}F_{g_\beta})(\rho) \triangleq \sum_{\beta=1}^{N_R} \int_{\mathbb{SO}(3)} \zeta_{\alpha,\beta}(\rho, \rho_1) F_{g_\beta}(\rho_1) d\rho_1, \quad (5.31)$$

where $\zeta_{\alpha,\beta}(\rho, \rho_1)$ is the spatial-Slepian transformation kernel, $g_\beta(\hat{\mathbf{x}})$ are the bandlimited Slepian functions computed for the spherical region R , N_R is the spherical Shannon number and \mathfrak{S} is the spatial-Slepian transformation operator, which results in the modified spatial-Slepian representation, $\nu_{g_\alpha} \in L^2(\mathbb{SO}(3))$, of the signal $f(\hat{\mathbf{x}})$. From the definition of spatial-Slepian coefficients in (5.2), we note that

$$\begin{aligned} (\mathfrak{S}F_{g_\beta})(\rho) &= \mathfrak{S} \left(\sum_{\ell,m,m'}^{L_f-1} (F_{g_\beta})_{m,m'}^\ell \overline{D_{m,m'}^\ell(\rho)} \right) = \sum_{\ell,m,m'}^{L_f-1} (F_{g_\beta})_{m,m'}^\ell (\mathfrak{S} \overline{D_{m,m'}^\ell}(\rho)) \\ &= \sum_{\ell,m,m'}^{L_f-1} (F_{g_\beta})_{m,m'}^\ell \left(\sum_{p,q,q'}^{L_v-1} \left(\frac{2p+1}{8\pi^2} \right) \left\langle \mathfrak{S} \overline{D_{m,m'}^\ell}, \overline{D_{q,q'}^p} \right\rangle_{\mathbb{SO}(3)} \overline{D_{q,q'}^p(\rho)} \right) \\ &= \sum_{\ell,m,m'}^{L_f-1} (F_{g_\beta})_{m,m'}^\ell \left(\sum_{p,q,q'}^{L_v-1} \left(\frac{2p+1}{8\pi^2} \right) \mathfrak{s}_{\alpha,\beta}^{pq q', \ell m m'} \overline{D_{q,q'}^p(\rho)} \right), \end{aligned} \quad (5.32)$$

where L_v is the bandlimit of the modified representation $\nu_{g_\alpha}(\rho)$ (see (5.36)) and

$$\mathfrak{s}_{\alpha,\beta}^{pq q', \ell m m'} \triangleq \left\langle \mathfrak{S} \overline{D_{m,m'}^\ell}, \overline{D_{q,q'}^p} \right\rangle_{\mathbb{SO}(3)} = \int_{\mathbb{SO}(3)} \int_{\mathbb{SO}(3)} \zeta_{\alpha,\beta}(\rho, \rho_1) \overline{D_{m,m'}^\ell(\rho_1)} d\rho_1 D_{q,q'}^p(\rho) d\rho \quad (5.33)$$

are called the spatial-Slepian transformation operator matrix elements, which quantify the projection of $\overline{D_{m,m'}^\ell(\rho)}$ onto $\overline{D_{q,q'}^p(\rho)}$ ³. Using the definition of spectral representation of spatial-Slepian coefficients in (5.3), we can rewrite (5.32) as

$$\begin{aligned} (\mathfrak{S}F_{g_\beta})(\rho) &= \sum_{\ell,m,m'}^{L_f-1} \left(\frac{2\ell+1}{8\pi^2} \right) \int_{\mathbb{SO}(3)} F_{g_\beta}(\rho_1) D_{m,m'}^\ell(\rho_1) d\rho_1 \sum_{p,q,q'}^{L_v-1} \left(\frac{2p+1}{8\pi^2} \right) \mathfrak{s}_{\alpha,\beta}^{pq q', \ell m m'} \overline{D_{q,q'}^p(\rho)} \\ &= \int_{\mathbb{SO}(3)} \left(\sum_{p,q,q'}^{L_v-1} \sum_{\ell,m,m'}^{L_f-1} \left(\frac{2p+1}{8\pi^2} \right) \left(\frac{2\ell+1}{8\pi^2} \right) \mathfrak{s}_{\alpha,\beta}^{pq q', \ell m m'} \overline{D_{q,q'}^p(\rho)} D_{m,m'}^\ell(\rho_1) \right) F_{g_\beta}(\rho_1) d\rho_1. \end{aligned} \quad (5.34)$$

Comparing (5.34) with (5.31) yields an expression for the spatial-Slepian transformation kernel in terms of Wigner- D functions as

$$\zeta_{\alpha,\beta}(\rho, \rho_1) = \sum_{p,q,q'}^{L_v-1} \sum_{\ell,m,m'}^{L_f-1} \left(\frac{2\ell+1}{8\pi^2} \right) \left(\frac{2p+1}{8\pi^2} \right) \mathfrak{s}_{\alpha,\beta}^{pq q', \ell m m'} \overline{D_{q,q'}^p(\rho)} D_{m,m'}^\ell(\rho_1). \quad (5.35)$$

³We have used Fourier expansion of signals in terms of complex conjugate of Wigner- D functions.

Putting it back in (5.31), using (5.3) and employing orthogonality of Wigner- D functions on the $\mathbb{S}\mathbb{O}(3)$ rotation group, we can write the modified spatial-Slepian representation as the following Fourier expansion

$$\nu_{g_\alpha}(\rho) = \sum_{p,q,q'}^{L_v-1} \left(\frac{2p+1}{8\pi^2} \right) \left(\sum_{\beta=1}^{N_R} \sum_{\ell,m,m'}^{L_f-1} \mathfrak{s}_{\alpha,\beta}^{pqq',\ell mm'} (f)_\ell^m \overline{(g_\beta)_\ell^{m'}} \right) \overline{D_{q,q'}^p(\rho)}, \quad (5.36)$$

which shows that the modified spatial-Slepian representation is bandlimited to degree L_v , as mentioned above, and gives the spectral coefficients as

$$(\nu_{g_\alpha})_{q,q'}^p = \left(\frac{2p+1}{8\pi^2} \right) \left(\sum_{\beta=1}^{N_R} \sum_{\ell,m,m'}^{L_f-1} \mathfrak{s}_{\alpha,\beta}^{pqq',\ell mm'} (f)_\ell^m \overline{(g_\beta)_\ell^{m'}} \right). \quad (5.37)$$

5.4.1 Admissibility condition

For $\nu_{g_\alpha}(\rho)$ to be an admissible spatial-Slepian representation, there must exist a signal $v \in L^2(\mathbb{S}^2)$, bandlimited to degree L_v , such that

$$\nu_{g_\alpha}(\rho) = \sum_{p,q}^{L_v-1} \psi_{\alpha,pq}(\rho) (v)_p^q, \quad \psi_{\alpha,pq}(\rho) = \sum_{q'=-p}^p \overline{(g_\alpha)_p^{q'}} \overline{D_{q,q'}^p(\rho)}, \quad (5.38)$$

where

$$(v)_p^q = \frac{(\nu_{g_\beta})_{q,q'}^p}{(g_\beta)_p^{q'}} = \left(\frac{2p+1}{8\pi^2} \right) \frac{1}{(g_\beta)_p^{q'}} \int_{\mathbb{S}\mathbb{O}(3)} \nu_{g_\beta}(\rho) D_{q,q'}^p(\rho) d\rho. \quad (5.39)$$

Combining (5.38) with (5.39), we get the following condition for $\nu_{g_\alpha}(\rho)$ to be an admissible spatial-Slepian representation

$$\begin{aligned} \overline{(g_\beta)_p^{q'}} \nu_{g_\alpha}(\rho) &= \sum_{p,q}^{L_v-1} \left(\frac{2p+1}{8\pi^2} \right) \psi_{\alpha,pq}(\rho) \int_{\mathbb{S}\mathbb{O}(3)} \nu_{g_\beta}(\rho) D_{q,q'}^p(\rho) d\rho \\ &= \sum_{p,q}^{L_v-1} \left(\frac{2p+1}{8\pi^2} \right) \psi_{\alpha,pq}(\rho) \left(\sum_{\beta'=1}^{N_R} \sum_{\ell,m,m'}^{L_f-1} \mathfrak{s}_{\beta,\beta'}^{pqq',\ell mm'} (f)_\ell^m \overline{(g_{\beta'})_\ell^{m'}} \right), \end{aligned} \quad (5.40)$$

where we have used (5.37) to get the second equality.

5.4.2 Least square signal estimation

The modified spatial-Slepian representation $\nu_{g_\alpha}(\rho)$ can be inverted, using (5.4), to obtain the spectral coefficients of the corresponding modified spherical signal $v \in L^2(\mathbb{S}^2)$ (assumed bandlimited to degree L_v), only if $\nu_{g_\alpha}(\rho)$ is an admissible representation. If $\nu_{g_\alpha}(\rho)$ does not satisfy the admissibility condition in (5.40), then a least square estimate for the modified spherical signal $v(\hat{\mathbf{x}})$ is obtained by minimizing the following squared error in the joint spatial-Slepian domain

$$\mathcal{E}_{\text{se}} = \sum_{\alpha=1}^{N_R} \left\| \nu_{g_\alpha}(\rho) - \sum_{p,q}^{L_v-1} \psi_{\alpha,pq}(\rho) (v)_p^q \right\|_{\mathbb{SO}(3)}^2. \quad (5.41)$$

We present the least square estimate in the following theorem.

Theorem 7. *Let a spatial-Slepian transformation kernel $\zeta_{\alpha,\beta}(\rho, \rho_1)$ modify the spatial-Slepian coefficient of a signal $f \in \mathcal{H}_{L_f}$ according to the linear transformation defined in (5.31), to give $\nu_{g_\alpha}(\rho)$ as an inadmissible modified spatial-Slepian representation. Then, a spectral estimate of the modified spherical signal, which minimizes the joint spatial-Slepian domain squared error, defined in (5.41), is given by the following linear system*

$$(v)_p^q = \sum_{\ell,m}^{L_f-1} \Upsilon_{pq,\ell m} (f)_\ell^m, \quad 0 \leq p \leq L_v - 1, |q| \leq p, \quad (5.42)$$

where L_v is the bandlimit of the estimated signal $v(\hat{\mathbf{x}})$ and the coefficients $\Upsilon_{pq,\ell m}$ are given by the following expression

$$\begin{aligned} \Upsilon_{pq,\ell m} = & \frac{1}{\left(\frac{8\pi^2}{2p+1}\right) \sum_{\alpha=1}^{N_R} \sum_{q'=p}^p |(g_\alpha)^{q'}|^2} \sum_{\alpha,\beta=1}^{N_R} \sum_{q'=-p}^p (g_\alpha)^{q'} \sum_{m'=-\ell}^{\ell} \overline{(g_\beta)^{m'}} \times \\ & \int_{\mathbb{SO}(3)} D_{q,q'}^p(\rho) \int_{\mathbb{SO}(3)} \zeta_{\alpha,\beta}(\rho, \rho_1) \overline{D_{m,m'}^\ell(\rho_1)} d\rho_1 d\rho. \end{aligned} \quad (5.43)$$

Proof. Expanding the joint spatial-Slepian domain squared error in (5.41) using (5.38)

and setting its derivative with respect to $(v)_p^q$ equal to zero, we get

$$\begin{aligned}
 \frac{\partial \mathcal{E}_{se}}{\partial (v)_p^q} &= \sum_{\alpha=1}^{N_R} \int_{\mathbb{SO}(3)} \frac{\partial}{\partial (v)_p^q} \left(\nu_{g_\alpha}(\rho) - \sum_{p,q}^{L_v-1} \psi_{\alpha,pq}(\rho) (v)_p^q \right) \overline{\left(\nu_{g_\alpha}(\rho) - \sum_{p',q'}^{L_v-1} \psi_{\alpha,p'q'}(\rho) (v)_{p'}^{q'} \right)} d\rho \\
 &= \sum_{\alpha=1}^{N_R} \int_{\mathbb{SO}(3)} \frac{\partial}{\partial (v)_p^q} \left[\nu_{g_\alpha}(\rho) \overline{\nu_{g_\alpha}(\rho)} - \nu_{g_\alpha}(\rho) \sum_{p',q'}^{L_v-1} \overline{\psi_{\alpha,p'q'}(\rho)} \overline{(v)_{p'}^{q'}} - \right. \\
 &\quad \left. \sum_{p,q}^{L_v-1} \psi_{\alpha,pq}(\rho) (v)_p^q \overline{\nu_{g_\alpha}(\rho)} + \sum_{p,q}^{L_v-1} \psi_{\alpha,pq}(\rho) (v)_p^q \sum_{p',q'}^{L_v-1} \overline{\psi_{\alpha,p'q'}(\rho)} \overline{(v)_{p'}^{q'}} \right] d\rho = 0, \\
 \sum_{\alpha=1}^{N_R} \sum_{p',q'}^{L_v-1} \int_{\mathbb{SO}(3)} \psi_{\alpha,pq}(\rho) \overline{\psi_{\alpha,p'q'}(\rho)} \overline{(v)_{p'}^{q'}} d\rho &= \sum_{\alpha=1}^{N_R} \int_{\mathbb{SO}(3)} \psi_{\alpha,pq}(\rho) \overline{\nu_{g_\alpha}(\rho)} d\rho, \\
 \sum_{\alpha=1}^{N_R} \sum_{p',q'}^{L_v-1} \int_{\mathbb{SO}(3)} \overline{\psi_{\alpha,pq}(\rho)} \psi_{\alpha,p'q'}(\rho) d\rho (v)_{p'}^{q'} &= \sum_{\alpha=1}^{N_R} \int_{\mathbb{SO}(3)} \overline{\psi_{\alpha,pq}(\rho)} \nu_{g_\alpha}(\rho) d\rho, \quad (5.44)
 \end{aligned}$$

for $0 \leq p \leq L_v - 1$, $|q| \leq p$, where, using orthogonality of Wigner- D functions, we can write

$$\begin{aligned}
 \int_{\mathbb{SO}(3)} \overline{\psi_{\alpha,pq}(\rho)} \psi_{\alpha,p'q'}(\rho) d\rho &= \int_{\mathbb{SO}(3)} \sum_{q''=-p}^p (g_\alpha)_{p'}^{q''} D_{q,q''}^p(\rho) \sum_{q'''=-p}^p \overline{(g_\alpha)_{p'}^{q'''}} \overline{D_{q',q'''}^{p'}(\rho)} d\rho \\
 &= \left(\frac{8\pi^2}{2p+1} \right) \sum_{q''=-p}^p \left| (g_\alpha)_{p'}^{q''} \right|^2 \delta_{p,p'} \delta_{q,q'}, \quad (5.45)
 \end{aligned}$$

which results in spectral coefficients of the signal $v(\hat{\mathbf{x}})$ as

$$\begin{aligned}
 (v)_p^q &= \frac{1}{\left(\frac{8\pi^2}{2p+1} \right) \sum_{\alpha=1}^{N_R} \sum_{q'=-p}^p \left| (g_\alpha)_{p'}^{q'} \right|^2} \sum_{\alpha=1}^{N_R} \int_{\mathbb{SO}(3)} \overline{\psi_{\alpha,pq}(\rho)} \nu_{g_\alpha}(\rho) d\rho \\
 &= \frac{1}{\left(\frac{8\pi^2}{2p+1} \right) \sum_{\alpha=1}^{N_R} \sum_{q'=-p}^p \left| (g_\alpha)_{p'}^{q'} \right|^2} \sum_{\alpha=1}^{N_R} \sum_{q'=-p}^p (g_\alpha)_{p'}^{q'} \sum_{\beta=1}^{N_R} \sum_{\ell,m,m'}^{L_f-1} (f)_\ell^m \overline{(g_\beta)_{\ell'}^{m'}} \times \\
 &\quad \int_{\mathbb{SO}(3)} D_{q,q'}^p(\rho) \int_{\mathbb{SO}(3)} \zeta_{\alpha,\beta}(\rho, \rho_1) \overline{D_{m,m'}^\ell(\rho_1)} d\rho_1 d\rho, \quad 0 \leq p \leq L_v - 1, |q| \leq p. \quad (5.46)
 \end{aligned}$$

The above expression can be compactly written as (5.42) using (5.43). \square

Admissible Transformation

The simplest linear transformation, resulting in an admissible spatial-Slepian representation, is obtained by choosing the spatial-Slepian transformation kernel as⁴

$$\zeta_{\alpha,\beta}(\rho, \rho_1) = C_1 \delta_{\alpha,\beta} \delta(\rho - \rho_1), \quad (5.47)$$

where C_1 is some complex number, $\delta_{\alpha,\beta}$ is the Kronecker delta function and

$$\delta(\rho - \rho_1) \triangleq (\sin \vartheta)^{-1} \delta(\varphi - \varphi_1) \delta(\vartheta - \vartheta_1) \delta(\omega - \omega_1), \quad (5.48)$$

is the $\mathbb{SO}(3)$ Dirac delta function. The estimated signal in this case simply becomes

$$(v)_p^q = \sum_{\ell,m}^{L-1} \Upsilon_{pq,\ell m} (f)_\ell^m = \sum_{\ell,m}^{L_f-1} \delta_{\ell,p} \delta_{m,q} (f)_\ell^m = (f)_p^q. \quad (5.49)$$

Inadmissible Transformations

Let the transformation kernel be defined as

$$\zeta_{\alpha,\beta}^M(\rho, \rho_1) \triangleq \zeta_\alpha^M(\rho) \delta_{\alpha,\beta} \delta(\rho - \rho_1), \quad (5.50)$$

then the modified spatial-Slepian representation, given by

$$\nu_{g_\alpha}^M(\rho) = \zeta_\alpha^M(\rho) F_{g_\alpha}(\rho), \quad (5.51)$$

is called multiplicative transformation, for which the signal estimate is given by (5.42)

through the following $\Upsilon_{pq,\ell m}$

$$\Upsilon_{pq,\ell m} = \frac{\sum_{\alpha=1}^{N_R} \sum_{q'=-p}^p (g_\alpha)^{q'} \sum_{m'=-\ell}^{\ell} \overline{(g_\alpha)^{m'}} \int_{\mathbb{SO}(3)} \zeta_\alpha^M(\rho) D_{q,q'}^p(\rho) \overline{D_{m,m'}^\ell(\rho)} d\rho}{\left(\frac{8\pi^2}{2p+1}\right) \sum_{\alpha=1}^{N_R} \sum_{q'=-p}^p |(g_\alpha)^{q'}|^2}. \quad (5.52)$$

⁴It is trivial to show that modified spatial-Slepian representation corresponding to the spatial-Slepian transformation kernel in (5.47) satisfies the admissibility condition in (5.40).

Alternatively, defining the spatial-Slepian transformation kernel as

$$\zeta_{\alpha,\beta}^{\otimes}(\rho, \rho_1) \triangleq \zeta_{\alpha}^{\otimes}(\rho\rho_1^{-1})\delta_{\alpha,\beta}, \quad (5.53)$$

we get the following convolutive transformation in the joint spatial-Slepian domain

$$\nu_{g_{\alpha}}^{\otimes}(\rho) = \int_{\mathbb{SO}(3)} \zeta_{\alpha}^{\otimes}(\rho\rho_1^{-1})F_{g_{\alpha}}(\rho_1)d\rho_1 = (\zeta_{\alpha}^{\otimes} \otimes F_{g_{\alpha}})(\rho), \quad (5.54)$$

where we have used the definition of convolution of signals defined on the $\mathbb{SO}(3)$ rotation group, given in (2.79). Using the spectral representation of convolution of $\mathbb{SO}(3)$ signals in (2.85), i.e.,⁵

$$(\nu_{g_{\alpha}}^{\otimes})_{q,q'}^p = \left\langle \nu_{g_{\alpha}}^{\otimes}, \overline{D_{q,q'}^p} \right\rangle_{\mathbb{SO}(3)} = \left(\frac{8\pi^2}{2p+1} \right) \sum_{k=-p}^p (\zeta_{\alpha}^{\otimes})_{q,k}^p (F_{g_{\alpha}})_{k,q'}^p, \quad (5.55)$$

in which $(\zeta_{\alpha}^{\otimes})_{q,k}^p$ denotes the spectral representation of the convolutive transformation kernel, and employing orthogonality of Wigner- D functions, modified signal is obtained from the linear system in (5.42) as

$$\begin{aligned} (v)_p^q &= \frac{1}{\left(\frac{8\pi^2}{2p+1} \right) \sum_{\alpha=1}^{N_R} \sum_{q'=-p}^p \left| (g_{\alpha})_p^{q'} \right|^2} \sum_{\ell,m}^{L_f-1} (f)_{\ell}^m \sum_{\alpha=1}^{N_R} \sum_{q'=-p}^p (g_{\alpha})_p^{q'} \sum_{m'=-\ell}^{\ell} \overline{(g_{\alpha})_{\ell}^{m'}} \times \\ &\quad \int_{\mathbb{SO}(3)} D_{q,q'}^p(\rho) \int_{\mathbb{SO}(3)} \zeta_{\alpha}^{\otimes}(\rho\rho_1^{-1}) \overline{D_{m,m'}^{\ell}(\rho_1)} d\rho_1 d\rho \\ &= \frac{1}{\left(\frac{8\pi^2}{2p+1} \right) \sum_{\alpha=1}^{N_R} \sum_{q'=-p}^p \left| (g_{\alpha})_p^{q'} \right|^2} \sum_{\ell,m}^{L_f-1} (f)_{\ell}^m \sum_{\alpha=1}^{N_R} \sum_{q'=-p}^p (g_{\alpha})_p^{q'} \sum_{m'=-\ell}^{\ell} \overline{(g_{\alpha})_{\ell}^{m'}} \left(\frac{8\pi^2}{2p+1} \right) \times \\ &\quad \left(\int_{\mathbb{SO}(3)} \zeta_{\alpha}^{\otimes}(\rho\rho_1^{-1}) \overline{D_{m,m'}^{\ell}(\rho_1)} d\rho_1 \right)_{q,q'}^p \\ &= \frac{\left(\frac{8\pi^2}{2p+1} \right)}{\sum_{\alpha=1}^{N_R} \sum_{q'=-p}^p \left| (g_{\alpha})_p^{q'} \right|^2} \sum_{\alpha=1}^{N_R} \sum_{q'=-p}^p \left| (g_{\alpha})_p^{q'} \right|^2 \sum_{m=-p}^p (\zeta_{\alpha}^{\otimes})_{q,m}^p (f)_p^m, \quad 0 \leq |q| \leq p \leq L_v - 1. \end{aligned} \quad (5.56)$$

⁵(2.85) remains same for signals represented in terms of complex conjugate of Wigner- D functions.

It can be observed that modified representations in (5.51) and (5.54) do not satisfy (5.40) in general and hence, may not be admissible spatial-Slepian representations.

5.4.3 Filters in the joint spatial-Slepian domain

The convolutive transformation in (5.54) represents filtering of the spatial-Slepian coefficient $F_{g_\alpha}(\rho)$ with the joint spatial-Slepian domain filter function $\zeta_\alpha^\otimes(\rho)$, which, from (5.55), can be assumed bandlimited to degree L_f . This, in turn, makes the modified spatial-Slepian representation $\nu_{g_\alpha}^\otimes(\rho)$, and the resulting signal estimate in (5.56), bandlimited to degree L_f . In this context, as a simple application of the framework of generalized linear transformations in the joint spatial-Slepian domain, we consider $f(\hat{\mathbf{x}})$ to be a noise-contaminated observation of a source signal $s \in L^2(\mathbb{S}^2)$, i.e., $f(\hat{\mathbf{x}}) = s(\hat{\mathbf{x}}) + z(\hat{\mathbf{x}})$, where $z \in L^2(\mathbb{S}^2)$ is a realization of a zero-mean and anisotropic noise process on the sphere. The source and noise signals are assumed to be uncorrelated, i.e., $\mathbb{E} \left\{ (s)_\ell^m \overline{(z)_{\ell'}^{m'}} \right\} = 0, \forall \ell, \ell', |m| \leq \ell, |m'| \leq \ell'$. We further assume that spectral covariance of the source and noise signals is known and is given by matrices \mathbf{C}^s and \mathbf{C}^z with elements $C_{\ell m, \ell' m'}^s = \mathbb{E} \left\{ (s)_\ell^m \overline{(s)_{\ell'}^{m'}} \right\}$ and $C_{\ell m, \ell' m'}^z = \mathbb{E} \left\{ (z)_\ell^m \overline{(z)_{\ell'}^{m'}} \right\}$ respectively. Then, we use the convolutive transformation kernel in (5.53) to obtain $(v)_p^q$ in (5.56) as the spectral estimate of the source signal $s(\hat{\mathbf{x}})$, and gauge the quality of signal estimation through the signal to noise ratio (SNR), defined in (3.4).

Gaussian spectral smoothing

We compute the signal estimate by smoothing the noise-contaminated observation $f(\hat{\mathbf{x}})$ in the spectral domain through a Gaussian kernel at each Slepian scale, i.e., we define the convolutive transformation kernel as

$$(\zeta_\alpha^\otimes)_{q,m}^p \triangleq \left(\frac{2p+1}{8\pi^2} \right) (\zeta_\alpha^\otimes)_p^q \delta_{q,m}, \quad (\zeta_\alpha^\otimes)_p^q = e^{-\frac{[p(p+1)+q]^2 \alpha^2}{L_f^4}}, \quad (5.57)$$

to obtain the spectral estimate, denoted by $(v_G)_p^q$, as

$$(v_G)_p^q = \left(\sum_{\alpha=1}^{N_R} \sum_{q'=-p}^p \left| (g_\alpha)_{p'}^{q'} \right|^2 \right)^{-1} \sum_{\alpha=1}^{N_R} \sum_{q'=-p}^p \left| (g_\alpha)_{p'}^{q'} \right|^2 (\zeta_\alpha^\otimes)_p^q (f)_{p'}^q. \quad (5.58)$$

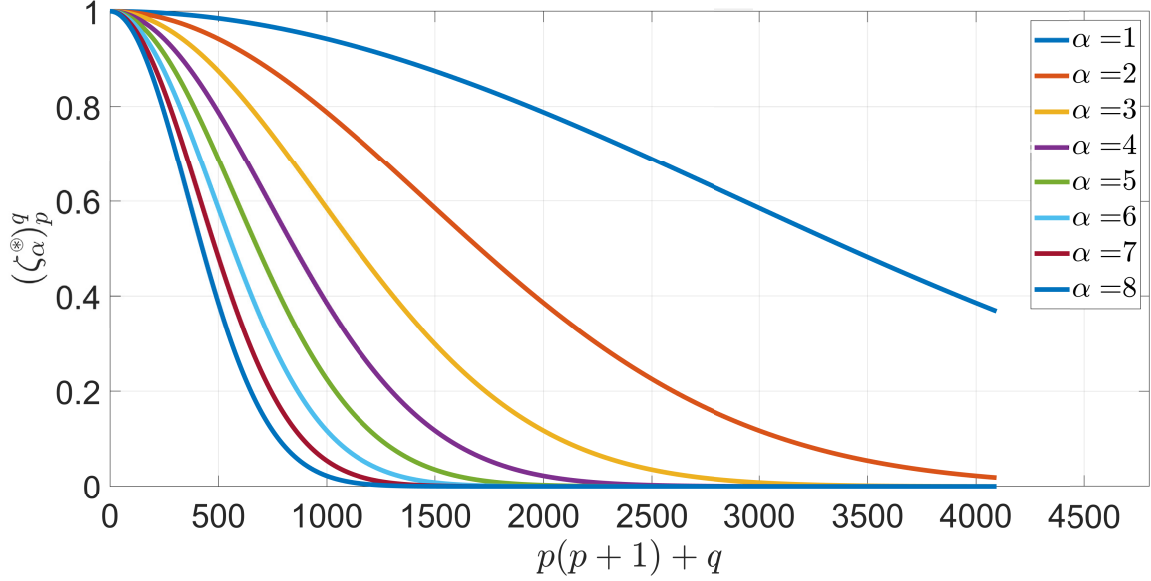


Figure 5-8: Spherical harmonic spectrum of the Gaussian spectral smoothing convolutive kernel at all Slepian scales for the north polar cap region of angle $\theta_0 = 5^\circ$, which gives $N_{R_{5^\circ}} \approx 8$.

We use the north polar cap region of angle $\theta_0 = 5^\circ$, for which the number of Slepian scales is given by $N_{R_{5^\circ}} \approx 8$. Figure 5-8 shows the spherical harmonic spectrum of the Gaussian spectral smoothing convolutive kernel at all Slepian scales, for bandlimit $L_f = 64$.

Optimal filter in the joint spatial-Slepian domain

Alternatively, a more sophisticated convolutive transformation kernel can be defined by minimizing the following mean-square error

$$\begin{aligned}
 \mathcal{E}_{\text{mse}} &= \sum_{p,q}^{L_f-1} \mathbb{E} \left\{ |(v)_p^q - (s)_p^q|^2 \right\} \\
 &= \sum_{p,q}^{L_f-1} \mathbb{E} \left\{ \left(\left(\sum_{\alpha=1}^{N_R} E_{p,\alpha} \right)^{-1} \left(\frac{8\pi^2}{2p+1} \right) \sum_{\alpha=1}^{N_R} E_{p,\alpha} \sum_{m=-p}^p (\zeta_\alpha^\circ)_{q,m}^p (f)_p^m - (s)_p^q \right) \times \right. \\
 &\quad \left. \frac{\left(\left(\sum_{\alpha=1}^{N_R} E_{p,\alpha} \right)^{-1} \left(\frac{8\pi^2}{2p+1} \right) \sum_{\alpha'=1}^{N_R} E_{p,\alpha'} \sum_{m'=-p}^p (\zeta_{\alpha'}^\circ)_{q,m'}^p (f)_p^{m'} - (s)_p^q \right)}{\left(\left(\sum_{\alpha=1}^{N_R} E_{p,\alpha} \right)^{-1} \left(\frac{8\pi^2}{2p+1} \right) \sum_{\alpha'=1}^{N_R} E_{p,\alpha'} \sum_{m'=-p}^p (\zeta_{\alpha'}^\circ)_{q,m'}^p (f)_p^{m'} - (s)_p^q \right)} \right\}, \tag{5.59}
 \end{aligned}$$

where we have used (5.56) in which energy per degree of the Slepian function $g_\alpha(\hat{\mathbf{x}})$ has been denoted by $E_{p,\alpha}$, i.e.,

$$E_{p,\alpha} \triangleq \sum_{q'=-p}^p \left| (g_\alpha)_{p}^{q'} \right|^2. \quad (5.60)$$

Noting the fact that source and noise signals are uncorrelated, i.e., equation (3.56), mean-square error in (5.59) can be simplified to get the following expression

$$\begin{aligned} \mathcal{E}_{\text{mse}} = & \sum_{p,q}^{L_f-1} \left[\left(\frac{8\pi^2}{2p+1} \right)^2 \frac{1}{\sum_{\alpha=1}^{N_R} E_{p,\alpha}} \frac{1}{\sum_{\alpha=1}^{N_R} E_{p,\alpha}} \sum_{\alpha=1}^{N_R} E_{p,\alpha} \sum_{\alpha'=1}^{N_R} E_{p,\alpha'} \times \right. \\ & \sum_{m=-p}^p \sum_{m'=-p}^p (\zeta_\alpha^*)_{q,m}^p \overline{(\zeta_{\alpha'}^*)_{q,m'}}^p (C_{pm,pm'}^s + C_{pm,pm'}^z) - \left. \left(\frac{8\pi^2}{2p+1} \right) \times \right. \\ & \left. \left(\sum_{\alpha=1}^{N_R} E_{p,\alpha} \right)^{-1} \sum_{\alpha=1}^{N_R} E_{p,\alpha} \sum_{m=-p}^p \left[(\zeta_\alpha^*)_{q,m}^p C_{pm,pq}^s + \overline{(\zeta_\alpha^*)_{q,m}}^p C_{pq,pm}^s \right] + C_{pq,pq}^s \right], \quad (5.61) \end{aligned}$$

which, when differentiated with respect to $\overline{(\zeta_{\alpha_1}^*)_{q_1,m_1}^{p_1}}$ and put equal to 0, results in the following linear system

$$\mathbf{G}(p) \mathbf{x}(p, q) = \mathbf{b}(p, q), \quad |q| \leq p, \quad 0 \leq p \leq L_f - 1, \quad \alpha \in [1, N_R], \quad (5.62)$$

where elements of the matrix \mathbf{G} and column vectors \mathbf{b} , \mathbf{x} are given by

$$\begin{aligned} G_{m',m} &= \left(\frac{8\pi^2}{2p+1} \right) (C_{pm,pm'}^s + C_{pm,pm'}^z), \quad b_{m'} = C_{pq,pm'}^s, \quad |m'| \leq p, \\ x_m &= \left(\sum_{\alpha=1}^{N_R} E_{p,\alpha} \right)^{-1} \sum_{\alpha=1}^{N_R} E_{p,\alpha} (\zeta_\alpha^*)_{q,m}^p, \quad |m| \leq p. \end{aligned} \quad (5.63)$$

The expression for x_m in (5.63) represents an under-determined system which results in infinitely many solutions for $(\zeta_\alpha^*)_{q,m}^p$ (for $\alpha > 1$). We choose $(\zeta_\alpha^*)_{q,m}^p$ to be independent of the Slepian scale as

$$(\zeta_\alpha^*)_{q,m}^p = x_m \equiv (\zeta^*)_{q,m}^p, \quad \forall \alpha \in [1, N_R], \quad (5.64)$$

which can be seen to satisfy the under-determined system in (5.63) and is directly given by the solution of (5.62), i.e.,

$$\mathbf{G}(p) \boldsymbol{\zeta}^{\otimes}(p, q) = \mathbf{b}(p, q), \quad |q| \leq p, 0 \leq p \leq L_f - 1, \quad (5.65)$$

where $\boldsymbol{\zeta}^{\otimes}(p, q)$ represents a column vector with elements $(\zeta^{\otimes})_{q,m}^p$, $|m| \leq p$. The spectral representation of the resulting signal estimate, which is denoted by $v_{\text{O}}(\hat{\mathbf{x}})$, is obtained from (5.56) as

$$(v_{\text{O}})_p^q = \left(\frac{8\pi^2}{2p+1} \right) \sum_{m=-p}^p (\zeta^{\otimes})_{q,m}^p (f)_p^m, \quad 0 \leq |q| \leq p \leq L_f - 1. \quad (5.66)$$

We refer to $\boldsymbol{\zeta}^{\otimes}(p, q)$ in (5.65) as an optimal filter because it optimizes the mean-square error in (5.59).

Remark 7. *As there is a close similarity in the mathematical formulation of the spatial-Slepian transform and the scale discretized wavelet transform (SDWT), a similar framework of linear transformations can be formulated for SDWT as well. We further note that the optimal filter in (5.65) has the same formulation as the multiscale optimal filter designed in Section 3.5.*

5.4.4 Illustrations

We consider a Mars topography map⁶ (processed to have zero average value and unit norm), bandlimited to degree $L_f = 64$, as the source signal $s(\hat{\mathbf{x}})$ and contaminate it with different realizations of zero-mean, uncorrelated and anisotropic Gaussian noise process to get the noise-contaminated observation $f(\hat{\mathbf{x}})$. We compute the spectral estimate in (5.58) using the Gaussian spectral smoothing convolutive kernel in (5.57) for $\alpha \in [1, N_{R_{5^\circ}}]$, where $N_{R_{5^\circ}} \approx 8$ represents the spherical Shannon number (rounded to the nearest integer) for a north polar cap region of angle $\theta_0 = 5^\circ$. We generate 100 realizations of the zero-mean, uncorrelated and anisotropic Gaussian noise process

⁶Please refer to Footnote 5 (on page 62) for the source of Mars topography map.

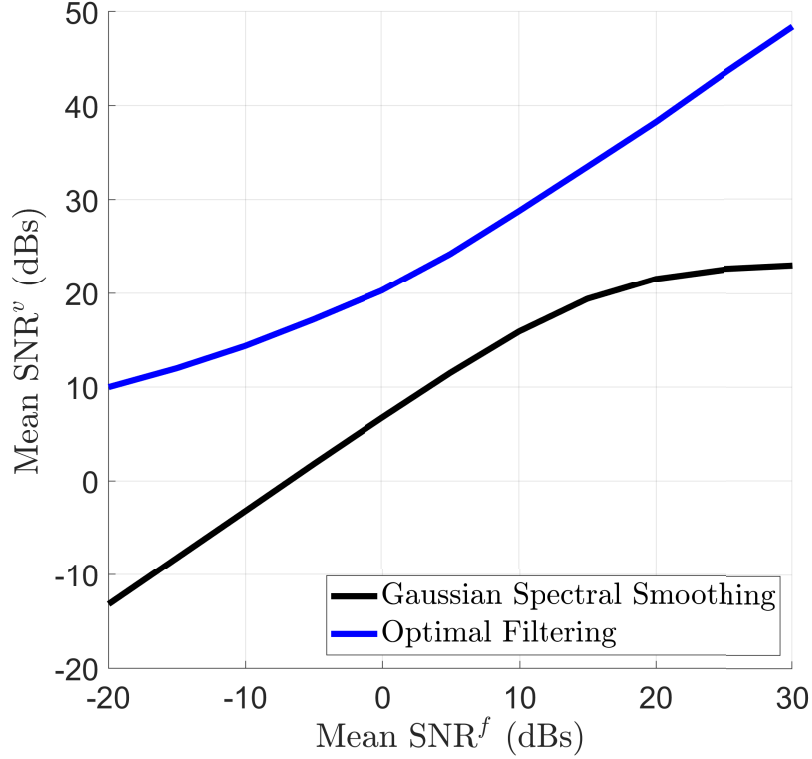


Figure 5-9: Output SNR plotted against input SNR, averaged over 100 realizations of a zero-mean, uncorrelated and anisotropic Gaussian noise process, for Gaussian spectral smoothing convolutive kernel and the optimal filter. Slepian scale is set by the Shannon number for a north polar cap region of angle $\theta_0 = 5^\circ$.

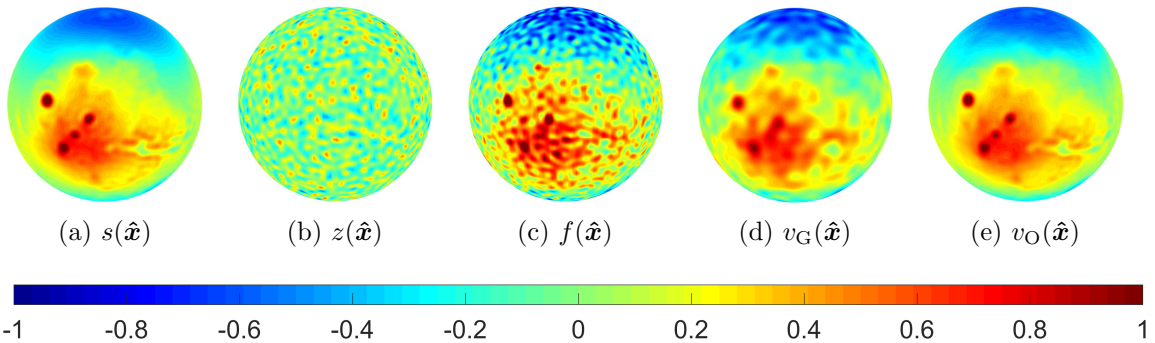


Figure 5-10: (a) Mars topography map , (b) zero-mean, uncorrelated and anisotropic Gaussian noise at $\text{SNR}^f = 4.9$ dBs, (c) noise-contaminated observation, (d) Mars topography map obtained from weighted Gaussian spectral smoothing, having $\text{SNR}^{v_G} = 11.3$ dBs, and (e) Mars topography map reconstructed through optimal filtering, having $\text{SNR}^{v_O} = 24.7$ dBs.

at different values of SNR^f and compute SNR^{v_G} . Figure 5-9 shows the output SNR against input SNR, averaged over all realizations. Also, shown is the SNR curve ob-

tained for the signal estimate in (5.66) using the optimal filter in (5.65)⁷. As expected, optimal filtering performs better than weighted Gaussian spectral smoothing.

Figure 5-10 shows an illustration, for a realization of zero-mean, uncorrelated and anisotropic Gaussian noise process, at $\text{SNR}^f = 4.9$ dBs. Output SNRs for the signal estimates obtained from weighted Gaussian spectral smoothing and optimal filtering are $\text{SNR}^{v_G} = 11.3$ dBs and $\text{SNR}^{v_o} = 24.7$ dBs respectively.

⁷As before, $C_{\ell m, \ell' m'}^s = (s)_\ell^m \overline{(s)_{\ell'}^{m'}}$ and we refer the reader to Section 3.1.1 for the spectral covariance of a zero-mean and anisotropic Gaussian noise process.

Chapter 6

Sampling on the sphere

Sampling schemes determine the number and position of samples for bandlimited signals defined on the sphere in such a way that the resulting samples completely characterize the underlying signal. Referring to (2.23) and (2.24), both of which are repeated here for convenience as

$$\begin{aligned} f(\theta, \phi) &= \sum_{\ell, m}^{L-1} (f)_{\ell}^m Y_{\ell}^m(\theta, \phi), \\ (f)_{\ell}^m &= \langle f, Y_{\ell}^m \rangle_{\mathbb{S}^2} = \int_{\mathbb{S}^2} f(\theta, \phi) \overline{Y_{\ell}^m(\theta, \phi)} \sin \theta d\theta d\phi, \end{aligned} \tag{6.1}$$

the signal $f \in \mathcal{H}_L$ is completely characterized by its spherical harmonic (spectral) coefficients $(f)_{\ell}^m$ and hence, can be reconstructed at any point on the sphere, provided the spectral coefficients are known. The chief objective of any sampling scheme is the exact computation of the spherical harmonic transform (SHT) in (6.1) from samples of the bandlimited signal on the sphere.

Number of samples required to compute the SHT of a bandlimited signal is a fundamental property of a sampling scheme and depends on the bandlimit of the signal. Different sampling schemes, using different number of samples, have been proposed for the computation of SHT in (6.1). We restrict ourselves to iso-latitude sampling schemes, which place samples on rings of constant colatitude, called iso-latitude rings. Such schemes facilitate separation of variables in (6.1), by allowing

independent processing of the samples in a given iso-latitude ring, as

$$\begin{aligned}
 (f)_\ell^m &= \int_{\theta=0}^{\pi} \int_{\phi=0}^{2\pi} f(\theta_k, \phi) N_\ell^m P_\ell^m(\cos \theta) e^{-im\phi} \sin \theta d\theta d\phi \\
 &= N_\ell^m \int_{z=-1}^1 \int_{\phi=0}^{2\pi} f(\theta_k, \phi) P_\ell^m(z) e^{-im\phi} dz d\phi, \quad z = \cos \theta \\
 &= N_\ell^m \int_{z=-1}^1 P_\ell^m(z) G_m(\theta_k) dz,
 \end{aligned} \tag{6.2}$$

where $f(\theta_k, \phi)$ is the signal $f(\theta, \phi)$ evaluated at the iso-latitude ring $\theta = \theta_k$, $G_m(\theta_k)$ is the Fourier transform of $f(\theta_k, \phi)$, i.e.,

$$G_m(\theta_k) \triangleq \int_{\phi=0}^{2\pi} f(\theta_k, \phi) e^{-im\phi} d\phi, \tag{6.3}$$

and $(f)_\ell^m$ in (6.2) is evaluated as the associated Legendre transform of $G_m(\theta_k)$. Fourier transform $G_m(\theta_k)$ can be efficiently computed using FFT algorithm. As a result, computational complexity of SHT in (6.2) is dominated by the associated Legendre transform, which still results in a low computational cost compared to the evaluation of SHT in (6.1). Iso-latitude sampling schemes can further be classified into *Equiangular* and *Equal Area* sampling schemes.

6.1 Equiangular sampling

Equiangular sampling schemes enable exact computation of SHT in (6.2) by placing samples on rings of constant colatitude (iso-latitude rings) and constant longitude (called iso-longitude rings). For a signal bandlimited to degree L , an exact computation of the integral in (6.2) is possible through the Gauss-Legendre (GL) quadrature using $N_{\text{GL}} = L(2L - 1) \sim 2L^2$ samples, where sample locations along the colatitude are chosen as roots of the Legendre polynomial of degree L and $2L - 1$ equiangular samples are placed in each iso-latitude ring. GL quadrature has also been used by Shukowsky to develop an equiangular sampling theorem, which utilizes $(2L - 1)^2$ samples on the sphere for exact numerical evaluation of the SHT in (6.2) [124]. **Gauss-LEgendre Sky Pixelization (GLESP)** [58] is another sampling

scheme which is constructed using GL quadrature, however, it uses twice as many samples along colatitude for a total of $\sim 4L^2$ samples on the sphere to compute the SHT of the signal.

Driscoll and Healy presented a sampling theorem on the sphere which employs equiangular samples placed on $2L$ iso-latitude and $2L$ iso-longitude rings, for a total of $4L^2$ samples on the sphere, to exactly compute the SHT of a signal with bandlimit L [56]. More recently, a sampling theorem for the exact computation of SHT of a bandlimited signal has been developed by McEwen and Wiaux, which requires $2L - 1$ samples in each of the $L - 1$ iso-latitude rings and one sample on the south pole, for a total of $(L - 1)(2L - 1) + 1 \sim 2L^2$ equiangular samples on the sphere [59].

Although equiangular sampling schemes enable exact computation of SHT of a bandlimited signal, they suffer from massive oversampling of the signal near the poles, which renders them sub-optimal for certain applications. In Figure 6-1, we plot the sample positions on the sphere for Gauss-Legendre sampling, Driscoll-Healy sampling theorem and McEwen-Wiaux sampling theorem, which shows a clear increase in the density of samples near the poles.

6.2 Equal area and hierarchical sampling

Equal area sampling schemes partition the sphere into equal area regions and place samples within these regions. Equal area schemes with samples placed on iso-latitude rings are desirable because not only do they avoid the problem of oversampling near the poles, they enable separation of variables and hence, support faster computation of SHT. Furthermore, the quadrature rule associated with equal area sampling schemes applies the same statistical weight (area of the partitioned region) to all the samples on the sphere.

Hierarchical sampling schemes partition the sphere into different regions in a nested fashion, i.e., these schemes facilitate the partitioning of each region into multiple sub-regions. One such scheme that has found considerable application in cosmology, particularly in the analysis of CMB, is HEALPix.

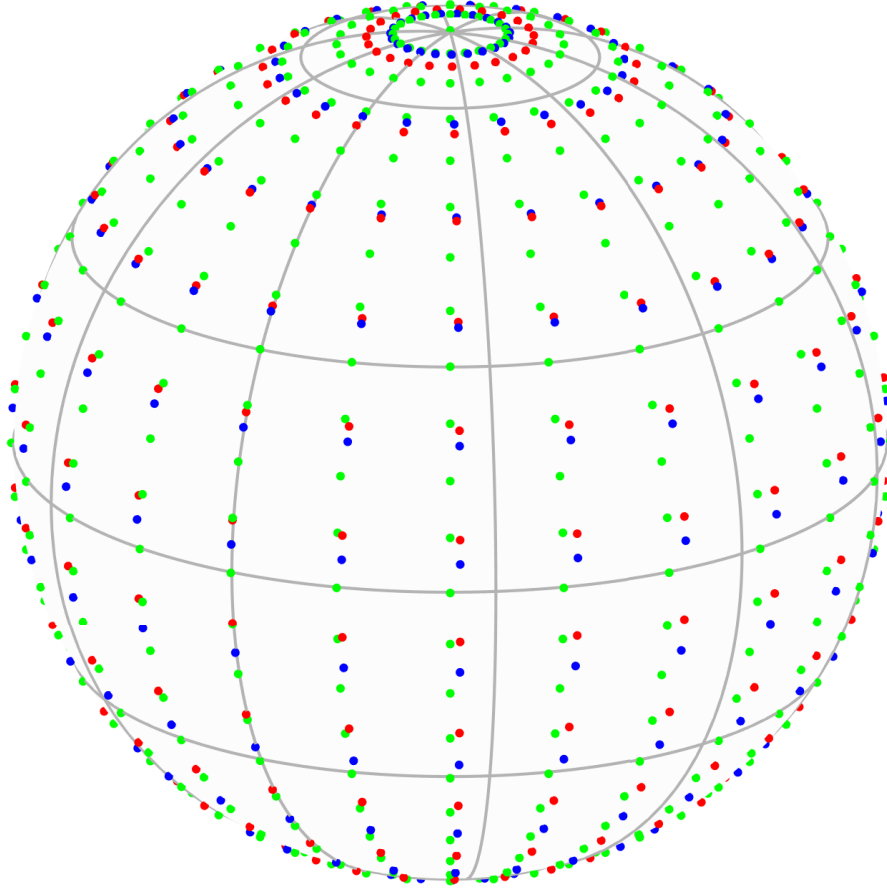


Figure 6-1: Sample positions on the sphere obtained from Gauss-Legendre sampling (red dots), Driscoll-Healy sampling theorem (green dots) and McEwen-Wiaux sampling theorem (blue dots), for bandlimit $L = 12$.

6.2.1 HEALPix

Hierarchical Equal Area iso-Latitude Pixelization (HEALPix) facilitates hierarchical partitioning of the sphere into equal area regions, called pixels [57]. In addition to having quaternary tree structure, it supports hierarchical tree structure for the database of samples, which facilitates various topological methods of analysis and enables fast computation through fast look-up of neighboring data elements.

HEALPix places three iso-latitude rings of samples, with four samples in each ring, dividing the sphere into 12 equal area pixels at the base-resolution. Sampling grid density is parameterized by $N_{\text{side}} = 2^k, k = 0, 1, 2, \dots$, which is defined as the number of divisions along the side of a base-resolution pixel needed to reach a desired

high-resolution pixelization. An increase in resolution level by one step divides each of the equal area pixels on the sphere into four sub-pixels. Total number of pixels on the HEALPix grid is given by $N_{\text{pix}} = 12N_{\text{side}}^2 = 12(2^{2k})$ and are placed into three zones: Equatorial ($-2/3 < z < 2/3$), North polar ($z \geq 2/3$) and South polar ($z \leq -2/3$), where $z = \cos(\theta)$. Total number of iso-latitude rings on the sampling grid is $4N_{\text{side}} - 1$ out of which $2N_{\text{side}} - 1$ are located in the equatorial zone and N_{side} are located in each polar zone. All equatorial rings contain maximum number of samples per ring, equal to $4N_{\text{side}}$, whereas rings in the polar zone contain varying number of samples. Figure 6-2 shows the partitioning of the sphere using HEALPix for different values of the resolution parameter N_{side} .

HEALPix supports ring as well as nested indexing scheme. Ring scheme numbers pixels in anticlockwise direction along longitude (starting at $\phi = 0$) and from north to south along colatitude, whereas nested scheme follows the indexing of the associated hierarchical tree structure [57]. Defining k_θ and k_ϕ as the iso-latitude ring and pixel-in-iso-latitude-ring indices, pixel centers $(\theta_{k_\theta}, \phi_{k_\phi})$, which also represent the sample positions, are given by the following set of equations [57]

$$\begin{aligned} \cos \theta_{k_\theta} &= 1 - \frac{k_\theta^2}{3N_{\text{side}}^2}, & \phi_{k_\phi} &= \frac{\pi}{2k_\theta} \left(k_\phi - \frac{1}{2} \right), \\ \text{North polar : } 1 \leq k_\theta &= \left\lfloor \sqrt{\left(\frac{\mathbf{p} + 1}{2} \right)} - \sqrt{\left\lfloor \left(\frac{\mathbf{p} + 1}{2} \right) \right\rfloor} \right\rfloor + 1 < N_{\text{side}}, & (6.4) \\ 1 \leq k_\phi &= \mathbf{p} + 1 - 2k_\theta(k_\theta - 1) \leq 4k_\theta, \end{aligned}$$

$$\begin{aligned} \cos \theta_{k_\theta} &= \frac{4}{3} - \frac{2k_\theta}{3N_{\text{side}}}, \\ \text{Northern equatorial : } \phi_{k_\phi} &= \frac{\pi}{2N_{\text{side}}} \left(k_\phi - \frac{(k_\theta - N_{\text{side}} + 1) \bmod 2}{2} \right), \\ N_{\text{side}} \leq k_\theta &= \left\lfloor \frac{\mathbf{p} - 2N_{\text{side}}(N_{\text{side}} - 1)}{4N_{\text{side}}} \right\rfloor + N_{\text{side}} \leq 2N_{\text{side}}, \\ 1 \leq k_\phi &= (\mathbf{p} - 2N_{\text{side}}(N_{\text{side}} - 1) \bmod 4N_{\text{side}}) + 1 \leq 4N_{\text{side}}, & (6.5) \end{aligned}$$

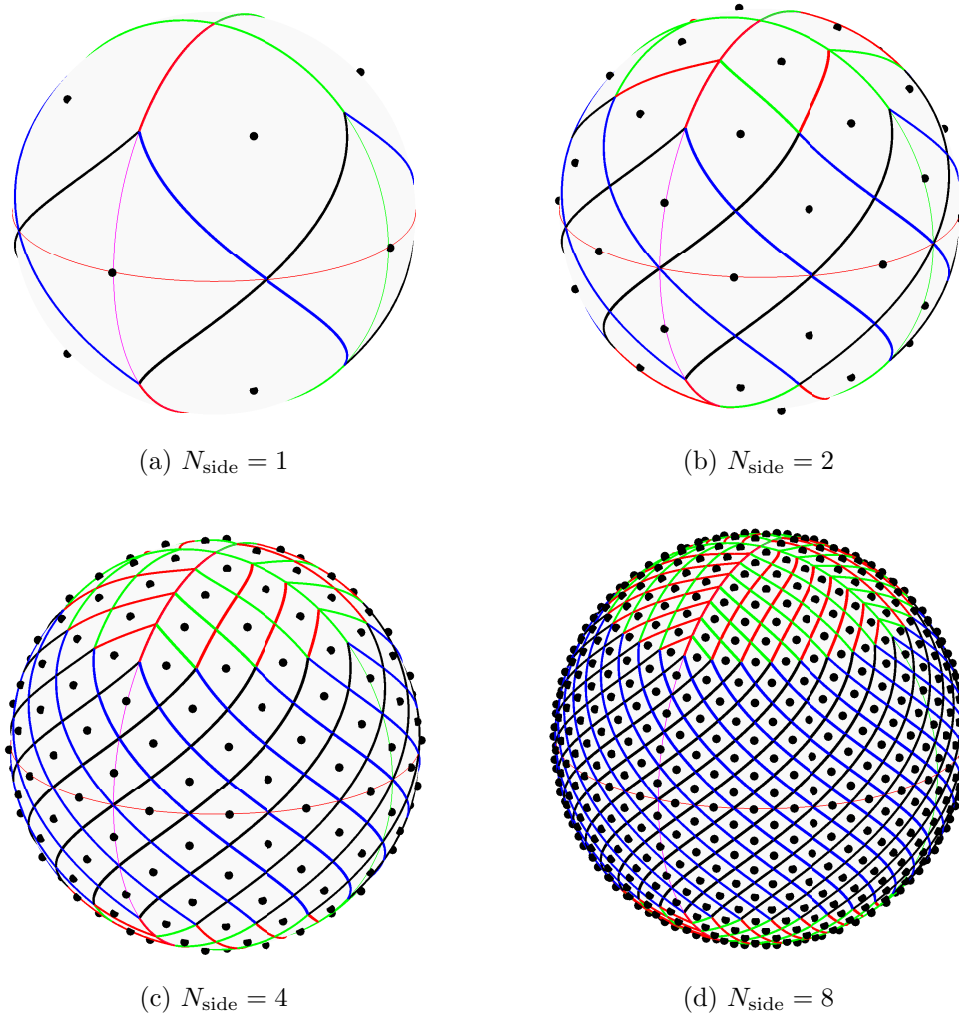


Figure 6-2: Partitioning of the sphere into different equal area pixels using HEALPix. Boundaries of the pixels in equatorial zone are shown in blue and black. Boundaries of the pixels in polar zones are shown in green and red. Pixel centers are shown as black dots.

where \mathbf{p} is the ring-scheme index of the pixel. Sample positions for the equatorial pixels in the southern hemisphere and south polar pixels are obtained by mirroring the samples in the northern hemisphere about the equator.

HEALPix quadrature

There is no quadrature rule for the exact computation of spherical harmonic transform of a bandlimited signal from its samples on the HEALPix grid. For a signal $f(\theta, \phi)$,

SHT is computed through the following approximate quadrature rule¹

$$(\hat{f})_\ell^m = \frac{4\pi}{N_{\text{pix}}} \sum_{\mathbf{p}=0}^{N_{\text{pix}}-1} f(\theta_{k_\theta}, \phi_{k_\phi}) \overline{Y_\ell^m(\theta_{k_\theta}, \phi_{k_\phi})}, \quad (6.6)$$

where $(\theta_{k_\theta}, \phi_{k_\phi})$ denote the position of HEALPix samples on the sphere. Since the approximate quadrature in (6.6) is a zero-order estimate, following Jacobi iterative method is applied on it to improve its accuracy

$$\mathbf{f}^{(k)} = \mathbf{f}^{(k-1)} + \mathbf{S} \cdot (\mathbf{f}_s - \mathbf{I} \cdot \mathbf{f}^{(k-1)}), \quad (6.7)$$

in which $\mathbf{f}^{(k)}$ is the column vector (indexed according to (2.30)) containing the estimate of the spectral coefficients at iteration k , \mathbf{f}_s is the column vector containing signal samples on the sphere, \mathbf{S} is the operator that computes SHT using (6.6) and \mathbf{I} is the inverse SHT operator, which evaluates the signal from its spectral coefficients through (6.1). The iterative method in (6.7) is terminated when the error between current and previous iteration becomes sufficiently small. Although HEALPix quadrature in (6.6) is approximate, it is accurate enough for all practical purposes.

6.3 Optimal dimensionality sampling scheme

This sampling scheme is neither exact, nor equiangular nor equal area nor hierarchical, but it has one other important feature: it achieves theoretically minimum possible number of samples on the sphere to accurately compute the SHT of a bandlimited signal, i.e., for a signal bandlimited to degree L , it employs $N_{\text{OD}} = L^2$ samples to accurately compute its SHT [60]. The samples are placed on iso-latitude rings at colatitude $\theta_k, k = 0, 1, \dots, L - 1$, such that there are $2k + 1$ equally spaced samples along longitude, on the iso-latitude ring at $\theta = \theta_k$, with positions given by

$$\boldsymbol{\phi}_k = [0, \Delta_k, 2\Delta_k, \dots, 2k\Delta_k]^\text{T}, \quad \Delta_k = \frac{2\pi}{2k + 1}. \quad (6.8)$$

¹<http://healpix.sourceforge.net/documentation.php>

Table 6.1: Comparison of Gauss-Legendre, Driscoll-Healy, McEwen-Wiaux and optimal dimensionality sampling methods for the number of samples required to compute SHT of a signal bandlimited to degree $L = 12$.

Sampling method	Computation of SHT	Number of samples
Gauss-Legendre	Exact	276
Driscoll-Healy	Exact	576
McEwen-Wiaux	Exact	254
Optimal dimensionality	Approximate (accurate)	144

The iso-latitude rings are equiangular and their positions are defined by the following set

$$\theta_k \in \left\{ \frac{\pi(2t+1)}{2L-1}, t = 0, 1, \dots, L-1 \right\}, \quad k = 0, 1, \dots, L-1. \quad (6.9)$$

The actual positions of iso-latitude rings is determined by the formulation of the proposed spherical harmonic transform [60]. Figure 6-3 shows the placement of L^2 samples using the optimal dimensionality sampling scheme for bandlimit $L = 12$. For comparison, samples obtained from Gauss-Legendre sampling, Driscoll-Healy sampling theorem and McEwen-Wiaux sampling theorem are also shown. Table 6.1 lists the number of samples required to compute the SHT of a signal bandlimited to degree $L = 12$ for Gauss-Legendre, Driscoll-Healy, McEwen-Wiaux and optimal dimensionality sampling schemes.

6.4 Efficient sampling on HEALPix grid

HEALPix quadrature requires all samples on the grid to evaluate the spherical harmonic transform of a signal. Although HEALPix supports accurate computation of SHT, it is a high-resolution sampling grid which renders the quadrature rule in (6.7) computationally expensive, specially at large bandlimits. In this section, we propose a method to reduce the number of HEALPix samples for accurate computation of spherical harmonic transform of a signal, bandlimited to degree L , by adopting the formulation of spherical harmonic transform, presented in optimal dimensionality sampling scheme [60], which is reviewed next.

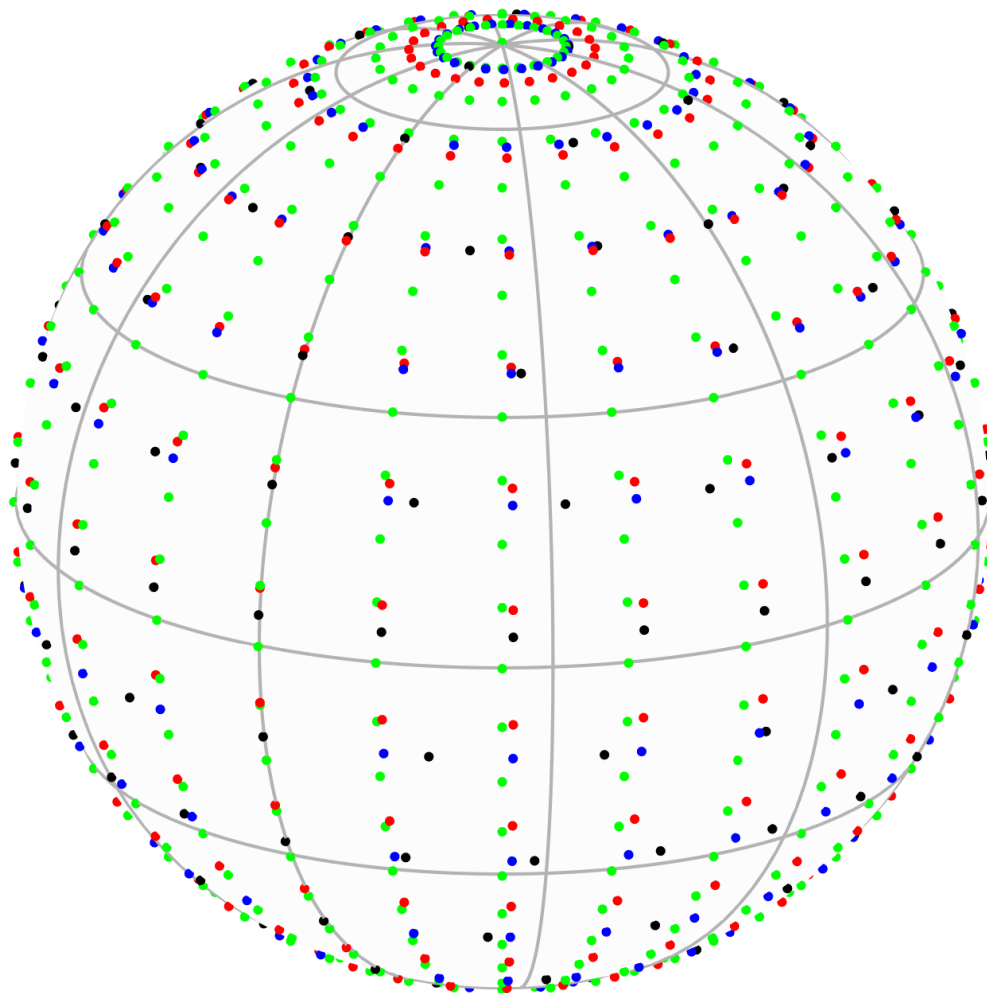


Figure 6-3: Sample positions on the sphere obtained from optimal dimensionality sampling scheme (black dots), Gauss-Legendre sampling (red dots), Driscoll-Healy sampling theorem (green dots) and McEwen-Wiaux sampling theorem (blue dots), for bandlimit $L = 12$.

6.4.1 Spherical harmonic transform for optimal dimensionality sampling scheme – A quick review

Since HEALPix, like the optimal dimensionality sampling, is an iso-latitude sampling scheme, we can adopt the formulation presented in [60] to compute the spherical harmonic transform of a bandlimited signal using HEALPix samples. For a signal $f \in \mathcal{H}_L$, the order m spherical harmonic coefficients can be expressed, through Fourier

transform in (6.3), as

$$G_m(\theta_k) \triangleq \int_{\phi=0}^{2\pi} f(\theta_k, \phi) e^{-im\phi} d\phi = 2\pi \sum_{\ell=|m|}^{L-1} (f)_{\ell}^m \tilde{P}_{\ell}^m(\theta_k), \quad |m| \leq L-1, \quad (6.10)$$

where

$$\tilde{P}_{\ell}^m(\theta_k) \triangleq Y_{\ell}^m(\theta_k, 0) = N_{\ell}^m P_{\ell}^m(\cos \theta_k) \quad (6.11)$$

is the scaled associated Legendre polynomial and we have used the Fourier expansion of signals in (6.1) along with (2.95). By defining a column vector \mathbf{g}_m as a vector of Fourier transform of the signal at $L - |m|$ different iso-latitude rings, given by

$$\mathbf{g}_m \triangleq [G_m(\theta_{|m|}), G_m(\theta_{|m|+1}), \dots, G_m(\theta_{L-1})]^T, \quad (6.12)$$

and a column vector \mathbf{f}_m containing spherical harmonic coefficients of order m as

$$\mathbf{f}_m \equiv [f_{|m|}^m, f_{|m|+1}^m, \dots, f_{|L-1|}^m]^T, \quad (6.13)$$

we can compactly express $L - |m|$ equations of the form given in (6.10) as

$$\mathbf{g}_m = 2\pi \mathbf{P}_m \mathbf{f}_m, \quad |m| \leq L-1, \quad (6.14)$$

where

$$\mathbf{P}_m \triangleq \begin{bmatrix} \tilde{P}_{|m|}^m(\theta_{|m|}) & \tilde{P}_{|m|+1}^m(\theta_{|m|}) & \cdots & \tilde{P}_{L-1}^m(\theta_{|m|}) \\ \tilde{P}_{|m|}^m(\theta_{|m|+1}) & \tilde{P}_{|m|+1}^m(\theta_{|m|+1}) & \cdots & \tilde{P}_{L-1}^m(\theta_{|m|+1}) \\ \vdots & \vdots & \ddots & \vdots \\ \tilde{P}_{|m|}^m(\theta_{L-1}) & \tilde{P}_{|m|+1}^m(\theta_{L-1}) & \cdots & \tilde{P}_{L-1}^m(\theta_{L-1}) \end{bmatrix}. \quad (6.15)$$

It becomes clear from (6.15) that in order for \mathbf{P}_0 to be invertible, Fourier transform in (6.10) must be evaluated along ϕ for at least L different iso-latitude rings. By computing $G_m(\theta_k)$ at different iso-latitude rings placed at $\theta_k, k = |m|, |m|+1, \dots, L-1$

and inverting \mathbf{P}_m in (6.15), we can use (6.14) to compute the spherical harmonic coefficients of order m and degrees $|m| \leq \ell \leq L - 1$.

Accurate computation of spherical harmonic coefficients of order m , contained in the vector \mathbf{f}_m , through (6.14) is only possible if \mathbf{g}_m is computed correctly and \mathbf{P}_m is well-conditioned to be invertible. Consequently, accuracy of the formulated SHT is dictated by the computation of $G_m(\theta_k)$ and condition number of \mathbf{P}_m . Accurate computation of $G_m(\theta_k)$ depends on the number of samples along longitude in the iso-latitude ring at $\theta = \theta_k$, and condition number of \mathbf{P}_m depends on the locations $\theta_{|m|}, \theta_{|m|+1}, \dots, \theta_{L-1}$ of the iso-latitude rings.

Avoiding aliasing in $G_m(\theta_k)$

Using (6.10) and changing the order of summation in (6.1), a signal $f(\theta, \phi)$, bandlimited to degree L and evaluated at samples in an iso-latitude ring at $\theta = \theta_k$, can be written as

$$f(\theta_k, \phi) = \frac{1}{2\pi} \sum_{m=-(L-1)}^{L-1} G_m(\theta_k) e^{im\phi}, \quad (6.16)$$

which can be observed to have contributions from $2L - 1$ complex exponential functions $e^{im\phi}$, $|m| \leq L - 1$. Therefore, to avoid the effects of aliasing on $G_m(\theta_k)$, signal $f(\theta_k, \phi)$ should have samples on at least $2L - 1$ positions along the longitude, regardless of the choice of the iso-latitude ring. However, if the spherical harmonic coefficients of orders $|m| \leq m' \leq L - 1$ are known, the contribution of these $2L - 2|m|$ spectral coefficients can be subtracted from the signal samples in the iso-latitude ring placed at $\theta_{|m|-1}$, if this ring does not have $2L - 1$ samples. The modified signal is then left with contribution from $2L - 1 - (2L - 2|m|) = 2|m| - 1 = 2(|m| - 1) + 1$ complex exponential functions and hence, is required to have only at least $2(|m| - 1) + 1$ samples for $G_{|m|-1}(\theta_{|m|-1})$ to be free of any aliasing errors. We further elaborate on this concept.

Equation (6.14) can be used to solve for $(f)_{L-1}^{L-1}$ by computing $G_{L-1}(\theta_{L-1})$ at a ring placed at θ_{L-1} , which is required to have at least $2L - 1$ samples. If the next

ring at $\theta = \theta_{L-2}$ has at least $2L - 1$ samples, we can compute $G_{L-2}(\theta_{L-2})$ without aliasing. However, if the number of samples is less than $2L - 1$, but at least $2L - 3$, then we have to subtract the contribution of $(f)_{L-1}^{L-1}$ and $(f)_{L-1}^{-(L-1)}$ from the samples $f(\theta_{L-2}, \phi)$ and update it as

$$f(\theta_{L-2}, \phi) \leftarrow f(\theta_{L-2}, \phi) - \tilde{f}_{L-1}(\theta_{L-2}, \phi), \quad (6.17)$$

where

$$\begin{aligned} \tilde{f}_{|m|}(\theta_k, \phi) &= \sum_{\ell=|m|}^{L-1} \{(f)_{\ell}^m \tilde{P}_{\ell}^m(\theta_k) e^{im\phi} + (f)_{\ell}^{-m} \tilde{P}_{\ell}^{-m}(\theta_k) e^{-im\phi}\} \\ &= \frac{1}{2\pi} (G_m(\theta_k) e^{im\phi} + G_{-m}(\theta_k) e^{-im\phi}), \quad 0 < m < L - 1 \end{aligned} \quad (6.18)$$

is the contribution of spectral coefficients of order $\pm m$, for all degrees $|m| \leq \ell \leq L - 1$. Hence, the iso-latitude ring at $\theta = \theta_{L-1}$ is required to have at least $2L - 1$ samples, the iso-latitude ring at $\theta = \theta_{L-2}$ is required to have at least $2L - 3$ samples and so on, for (aliasing-free) accurate computation of $G_m(\theta_k)$.

6.4.2 Proposed sampling scheme – Requirements

Using the formulation in (6.14), SHT of a signal, bandlimited to degree L , can be accurately computed by sampling it on L iso-latitude rings, located at θ_k , $k = 0, 1, \dots, L - 1$, provided the following requirements are fulfilled:

- (R1) The iso-latitude ring at $\theta = \theta_k$ has at least $2k + 1$ samples along longitude.
- (R2) Ring locations, θ_k , $k = 0, 1, \dots, L - 1$, are chosen such that the matrix \mathbf{P}_m , given in (6.15), is well-conditioned for each $m = 0, 1, \dots, L - 1$ ².

SHT can be computed accurately if the sampling scheme design takes into account these requirements as (R1) and (R2) ensure accurate computation of \mathbf{g}_m and accurate inversion of (6.15) (for each $|m| \leq L - 1$) respectively.

²We only need to ensure that \mathbf{P}_m is well-conditioned for non-negative orders as $\mathbf{P}_{-m} = (-1)^m \mathbf{P}_m$, which follows from the conjugate symmetry of spherical harmonics in (2.22).

6.4.3 Proposed sampling scheme – Design

We devise an algorithm to design a sampling scheme which is comprised of a subset of HEALPix samples. Before we present an algorithm that selects the iso-latitude rings of samples from the HEALPix grid, taking into account the sampling requirements given in Section 6.4.2, we establish a relation between the HEALPix resolution parameter N_{side} and signal bandlimit L .

Since the number of samples required in the first ring, i.e., at colatitude θ_{L-1} , is $2L - 1$, and all the rings in equatorial zone on the HEALPix grid contain maximum number of samples per ring, i.e., $4N_{\text{side}}$, first ring must be chosen from the equatorial zone. This puts an upper bound on the bandlimit of the signal as,

$$2L - 1 \leq 4N_{\text{side}} \Rightarrow L \leq 2N_{\text{side}}. \quad (6.19)$$

Hence, for a sampling grid with resolution parameter N_{side} , we can compute the spherical harmonic transform of a signal for a maximum bandlimit of $2N_{\text{side}}$.

To select iso-latitude rings of samples from the HEALPix grid with resolution parameter N_{side} , we propose the following iso-latitude ring selection algorithm, taking into account **(R1)** and **(R2)**. We use θ_{k_θ} and n_{k_θ} to denote the location of an iso-latitude ring and the number of samples along longitude in it, where $k_\theta = 1, 2, \dots, 4N_{\text{side}} - 1$.

Procedure 3 Ring Selection Algorithm

Require: $\theta_k, k = 0, 1, \dots, L - 1$

- 1: **procedure** RING SELECTION($\theta_{k_\theta}, N_{\text{side}}$)
 - 2: $\Theta = \{\theta_{k_\theta}\}_{k_\theta=1}^{4N_{\text{side}}-1}$
 - 3: $\theta_{L-1} = \pi/2$ (first ring)
 - 4: **for** $m = L - 2, L - 3, \dots, 0$ **do**
 - 5: $\Theta_m = \{\theta_{k_\theta} \in \Theta : n_{k_\theta} \geq 2m + 1\}$
 - 6: Choose $\theta_m \in \Theta_m$ which minimizes the condition number of \mathbf{P}_m
 - 7: **end for**
 - 8: **return** $\theta_k, k = 0, 1, \dots, L - 1$.
 - 9: **end procedure**
-

The proposed algorithm identifies the iso-latitude rings from the HEALPix grid in such a way that each \mathbf{P}_m matrix is well-conditioned and the ring located at θ_k has at least $2k + 1$ samples along longitude, thus serving both sampling design requirements and ensuring accurate computation of SHT.

6.4.4 Multipass SHT

Like the HEALPix quadrature rule in (6.7), we also employ a similar iterative method to further improve the accuracy of spherical harmonic transform. After computing the spectral coefficients in the first pass, we reconstruct the signal in spatial domain using (6.1). Spherical harmonic coefficients of the difference between original and reconstructed spatial signals are computed and added to the previously computed spectral coefficients, obtaining the spectral coefficients for the second pass. This process is repeated until the quantity $\sqrt{\mathbf{e}^H \mathbf{e}}$ either exceeds its value obtained in the previous pass or drops below a preset threshold of 10^{-16} , where \mathbf{e} is the difference between the original and reconstructed spatial signal column vectors.

6.4.5 Evaluation

We compare the accuracy of the formulated SHT with the SHT computed from the HEALPix quadrature in (6.7) and evaluate the reduction in number of samples achieved by the proposed sampling scheme. The formulated SHT is efficient, compared to the one associated with HEALPix, in the sense that it requires lesser number of samples.

Reduction in number of samples

Since our ring selection algorithm chooses iso-latitude rings from the HEALPix grid by minimizing the condition number of the matrix \mathbf{P}_m , we cannot analytically determine the exact reduction in the number of samples achieved by the proposed sampling scheme. However, we can work out the minimum guaranteed decrease in the number of samples which is presented in the following Lemma.

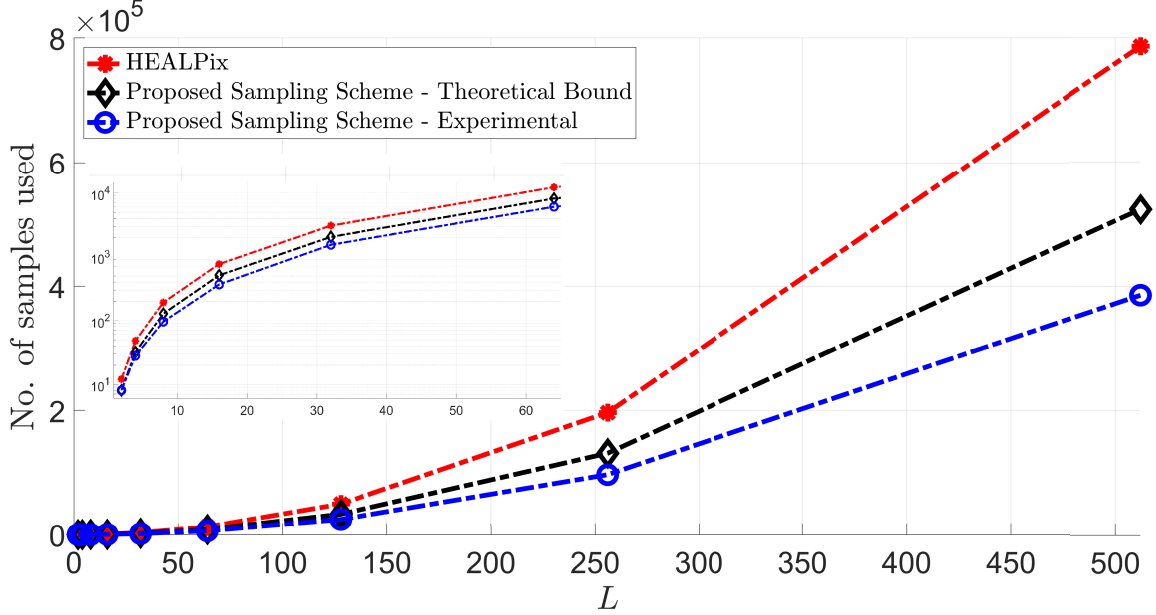


Figure 6-4: Number of samples used by HEALPix and the proposed sampling scheme, along with the theoretical bound established in Lemma 1, for the accurate computation of spherical harmonic transform of a signal bandlimited to degree $2 \leq L \leq 512$. Also shown is the magnified plot, in logarithmic scale, for bandlimits $L \leq 64$.

Lemma 1 (Lower-bound on the reduction in number of samples). *The proposed sampling scheme requires at least $3/2$ times less number of samples than HEALPix for the accurate computation of SHT of a signal, bandlimited to degree $L \leq 2N_{\text{side}}$.*

Proof. Since $L_{\text{max}} = 2N_{\text{side}}$ denotes the maximum bandlimit of the signal for a given HEALPix resolution parameter N_{side} , and the number of samples on the HEALPix grid is given by $N_{\text{pix}} = 12N_{\text{side}}^2$, we have $L_{\text{max}} = \sqrt{N_{\text{pix}}/3}$. As the proposed sampling scheme requires $L (\leq L_{\text{max}})$ iso-latitude rings of samples for the accurate computation of SHT, total number of samples in the proposed sampling scheme, denoted by N_{prop} , is given by $N_{\text{prop}} \leq L(4N_{\text{side}}) \leq L_{\text{max}}(4N_{\text{side}})$ or $N_{\text{pix}}/N_{\text{prop}} \geq 3/2$. \square

In Figure 6-4, we plot the number of samples used for computing SHT through the HEALPix quadrature, number of samples required to accurately compute SHT formulated for the proposed sampling scheme and the theoretical bound established in Lemma 1, at different values of bandlimit in the range $2 \leq L \leq 512$. It can be seen that beyond a rather small bandlimit of $L = 8$, the proposed sampling scheme requires about half the number of samples compared to HEALPix. Figure 6-5 shows a visual

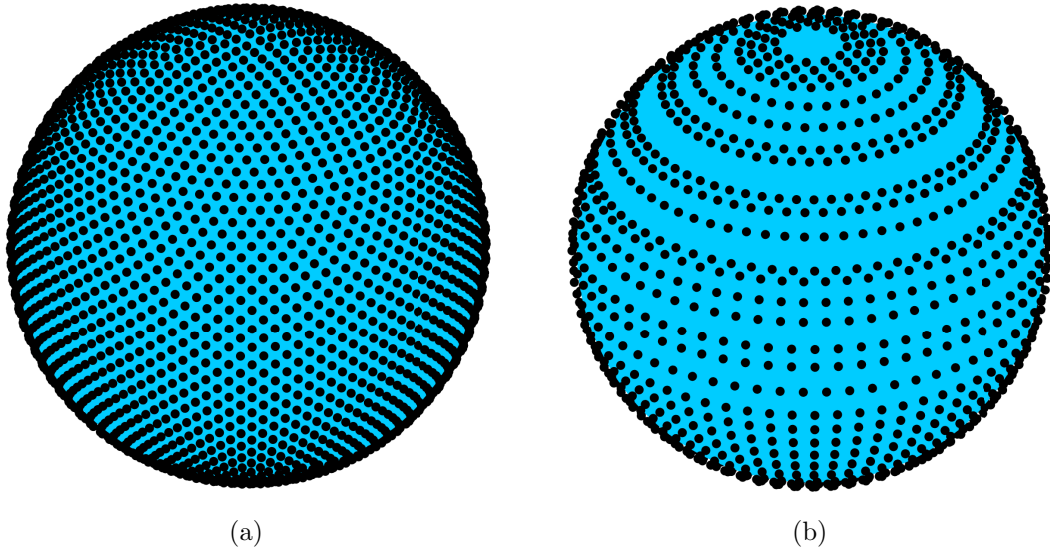


Figure 6-5: Visual comparison of sampling density between (a) HEALPix and (b) proposed sampling scheme, for bandlimit $L = 32$.

comparison of the number of samples used by HEALPix and the proposed sampling scheme to accurately compute the spherical harmonic transform at bandlimit $L = 32$.

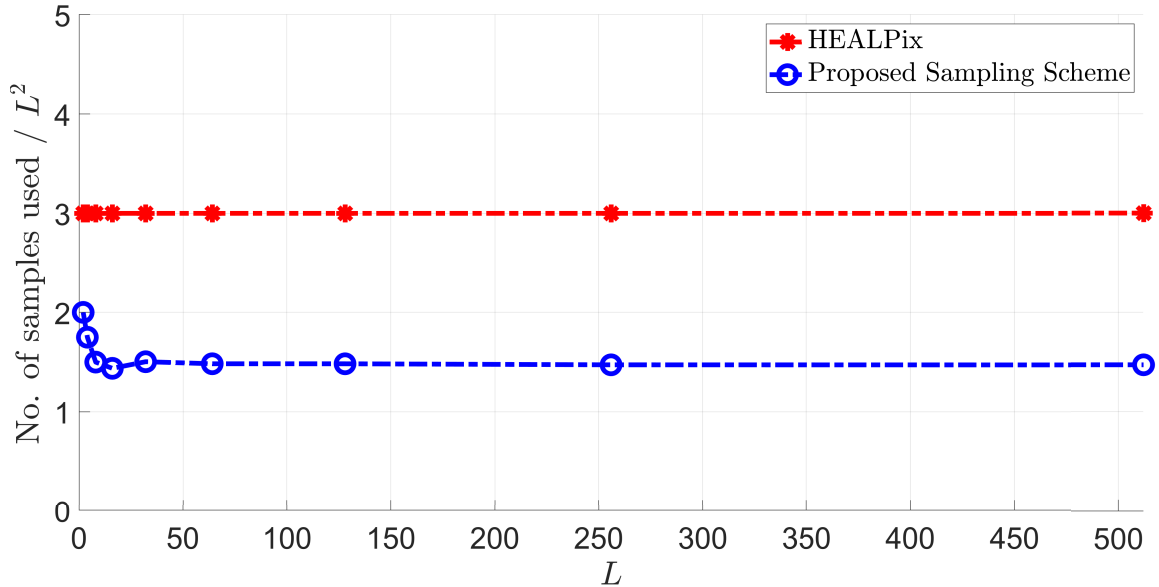


Figure 6-6: Number of samples used, in units of L^2 , for the computation of spherical harmonic transform of a signal, bandlimited to degree $2 \leq L \leq 512$. For $L = 2N_{\text{side}}$, HEALPix uses $3L^2$ samples, while the proposed sampling scheme requires at most $2L^2$ samples ($\sim 1.5L^2$ samples for $L \geq 8$) to compute the SHT.

Remark 8. We observe that for bandlimit $L = 2N_{\text{side}}$, HEALPix has $N_{\text{pix}} = 12N_{\text{side}}^2 = 3L^2$ samples on the sphere. From Lemma 1, the proposed sampling scheme uses at most $2L^2$ samples to accurately compute the spherical harmonic transform of a signal, bandlimited to degree L . This fact can be verified from Figure 6-6, which shows that for bandlimit $L \geq 8$, the proposed sampling scheme utilizes $\sim 1.5L^2$ samples, to compute the SHT of the signal.

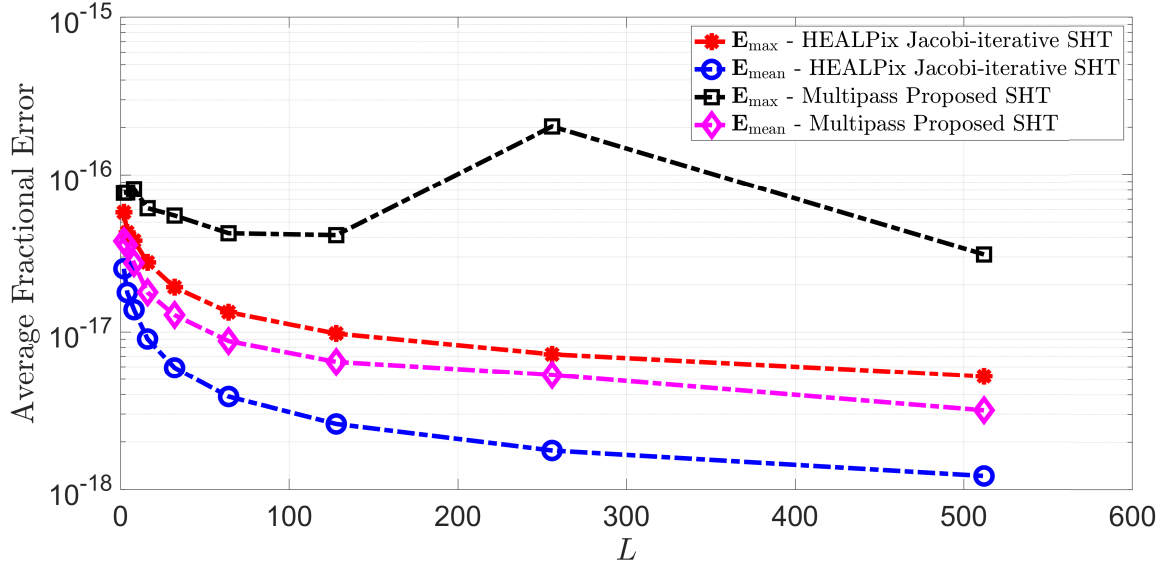


Figure 6-7: E_{max} and E_{mean} between spectral coefficients of the test and reconstructed signals, averaged over 50 realizations of the test signal, for bandlimits in the range $2 \leq L \leq 512$.

Accuracy analysis

SHT formulated for the proposed sampling scheme is evaluated on a test signal generated using spectral coefficients, $(f^T)_\ell^m$, uniformly distributed in the interval $(-1, 1)$ in real and imaginary parts. Denoting the reconstructed spectral coefficients by $(f^R)_\ell^m$, accuracy of the spherical harmonic transform is evaluated through the fractional maximum and mean errors, defined as

$$\begin{aligned}
 \mathbf{E}_{\text{max}} &\triangleq \frac{1}{\|f^T\|_{\mathbb{S}^2}} \max \left\{ |(f^T)_\ell^m - (f^R)_\ell^m| \right\}, \\
 \mathbf{E}_{\text{mean}} &\triangleq \frac{1}{\|f^T\|_{\mathbb{S}^2}} \frac{1}{L^2} \sum_{\ell=0}^{L-1} \sum_{m=-\ell}^{\ell} |(f^T)_\ell^m - (f^R)_\ell^m|.
 \end{aligned} \tag{6.20}$$

Spherical harmonic transform is computed for 50 different realizations of the test signal and the fractional errors are averaged over all realizations. Figure 6-7 shows the average fractional maximum error and average fractional mean error curves for the computation of SHT of the test signal, bandlimited to degree in the range $2 \leq L \leq 512$, using the proposed framework and the HEALPix quadrature rule in (6.7). It is evident that the proposed sampling scheme, although requires lesser number of samples, enables accurate computation of SHT with errors on the order of numerical precision.

Chapter 7

Multiscale analysis on the sphere

In some applications, it may be desirable to study scale-dependent characteristics of the signals by analyzing them at different resolutions. Such multiresolution (or multiscale) analysis has been extensively carried out for the 1D time domain signals using the framework of wavelet analysis [93, 94, 95], which has also been extended for signals defined on the sphere [78, 51, 79, 80, 82, 81, 83, 84, 85].

Unlike the Euclidean domain, the spherical domain is bounded and hence, as discussed in Chapter 6, can be partitioned into different pixels. If the partitioning scheme has the tendency to further divide the pixels into nested sub-pixels, the whole sphere can be partitioned into pixels of varying spatial extent. Such a hierarchical partitioning scheme provides an alternate way of formulating the framework of multiscale analysis, by finding signal representations in terms of basis functions which are localized within the pixels. Representing a signal in terms of such localized basis functions (for pixels of varying spatial extent) is similar in spirit to filtering the signal with wavelet functions of varying dilation. The localized basis functions for all the pixels at different scales can be collected together to form a multiscale dictionary, which is overcomplete by design. Unlike the wavelet coefficients, this dictionary is independent of the underlying signal and can be used to perform localized spatial (and spectral) analysis at different scales.

Slepian spatial-spectral concentration problem on the sphere, reviewed in Section 2.5, results in bandlimited and spatially well-optimally concentrated Slepian func-

tions, which can be used as localized basis functions for the partitioned regions on the sphere. These functions provide a useful way for accurate local signal representation within the pixels and have been previously used to construct a multiscale dictionary in [125]. However, [125] uses binary division of a cubed sphere to obtain multiscale pixels and does not present analytical computation of Slepian functions for the partitioned regions.

In this chapter, we propose a hierarchical partitioning scheme to divide the sphere into multiscale pixels, which are shown to have relatively simple mathematical representations, and employ the framework in [76] to obtain Slepian functions for these pixels on the sphere. We also consider HEALPix for hierarchical partitioning of the sphere at different resolutions, and present exact analytical expressions for the computation of Slepian functions for the resulting multiscale pixels. Due to complex mathematical representations of the boundaries of HEALPix pixels, such analytical computation is found to be a highly non-trivial task. Following the methodology in [125], we present two methods of constructing overcomplete multiscale dictionaries for both partitioning schemes, and analyze the dictionaries for the range and mutual coherence of their elements.

7.1 HEALPix

We present **H**ierarchical **E**qual **A**rea iso-**L**atitude iso-**L**ongitude **P**ixelization scheme, abbreviated as HEALPix, to partition the the sphere into disjoint, equal area pixels. Number of pixels on the sphere is determined by the resolution parameter $\mathfrak{L} = 0, 1, 2, \dots$, where $\mathfrak{L} = 0$, corresponds to the whole sphere. At $\mathfrak{L} = 1$, an iso-latitude ring at $\theta = \pi/2$ divides the sphere into two hemispheres and each hemisphere is further divided into two halves by iso-longitude rings at $\phi = 0, \pi$, for a total of four pixels¹. An increase in the resolution parameter by 1 partitions each pixel into four sub-pixels using systematic placement of iso-latitude and iso-longitude rings

¹Although referred as an iso-longitude ring, it is actually an iso-longitude semi-ring. Two semi-rings of a great circle are considered separately because they are specified by different longitudes.

described below. Hence, for a given resolution level \mathfrak{L} , the sphere is divided into $4^\mathfrak{L}$ or $2^{2\mathfrak{L}}$ disjoint pixels.

7.1.1 Placement of iso-latitude rings

An iso-latitude ring is placed at $\theta = \theta_k$ such that the spherical annulus formed by the iso-latitude rings at $\theta = \theta_{k-1}, \theta_{k+1}$ is equally divided in area. Since area of a spherical annulus bounded by $\theta = \theta_1, \theta_2$, and denoted by A_{θ_1, θ_2} , is given by

$$\begin{aligned} A_{\theta_1, \theta_2} &= 2\pi \int_{\theta_1}^{\theta_2} \sin \theta \, d\theta = 2\pi(\cos \theta_1 - \cos \theta_2) \\ &= 2\pi(z_1 - z_2), \end{aligned}$$

where $z_k = \cos \theta_k$, the condition for the placement of an iso-latitude ring at $\theta = \theta_k$ becomes

$$\frac{A_{\theta_{k-1}, \theta_{k+1}}}{2} = A_{\theta_k, \theta_{k+1}} \Rightarrow z_k = \frac{z_{k-1} + z_{k+1}}{2}.$$

Starting with $z_0 = 1, z_1 = 0, z_2 = -1$ at $\mathfrak{L} = 1$, we find that at a given resolution level \mathfrak{L} , there are $2^\mathfrak{L} - 1$ iso-latitude rings placed at positions given by (see Appendix B)

$$z_k = \left(1 - \frac{k}{2^{\mathfrak{L}-1}}\right), \quad 1 \leq k \leq 2^\mathfrak{L} - 1, \quad \mathfrak{L} \geq 1, \quad (7.1)$$

where $z_0 = 1, z_{2^\mathfrak{L}-1} = 0, z_{2^\mathfrak{L}} = -1$. Figure 7-1 shows the placement of iso-latitude rings for different values of the resolution parameter.

7.1.2 Placement of iso-longitude rings

Each equal area annulus is further divided into equal area pixels along ϕ by iso-longitude rings. An increase in resolution parameter \mathfrak{L} by 1 divides each pixel along longitude into two halves. Hence, for a given resolution parameter \mathfrak{L} , $2^\mathfrak{L}$ iso-longitude

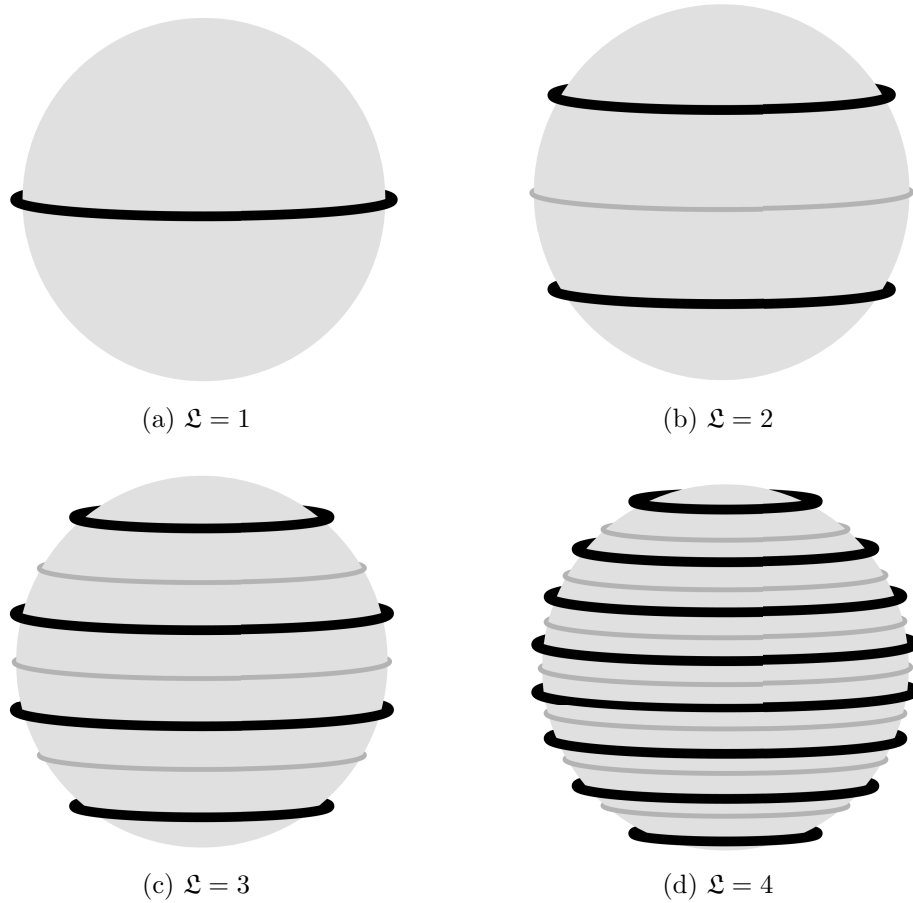


Figure 7-1: Placement of iso-latitude rings for HEALLPix at different resolutions.

rings are placed at the following positions (see Appendix B),

$$\phi_k = \frac{(k-1)\pi}{2^{\mathfrak{L}-1}}, \quad 1 \leq k \leq 2^{\mathfrak{L}}, \quad \mathfrak{L} \geq 1. \quad (7.2)$$

Figure 7-2 shows the placement of iso-longitude rings for different values of resolution parameter. Pixelization of the sphere under this scheme is shown in Figure 7-3 for different values of \mathfrak{L} . The resulting pixels are indexed in anticlockwise direction along longitude (starting at $\phi = 0$), and from north to south along colatitude.

7.1.3 Area of a pixel

HEALLPix partitions the sphere into equal area pixels. For $1 \leq k_1, k_2 \leq 2^{\mathfrak{L}}$, area of a pixel bounded by iso-latitude rings at $\theta = \theta_{k_1-1}, \theta_{k_1}$ and iso-longitude rings at

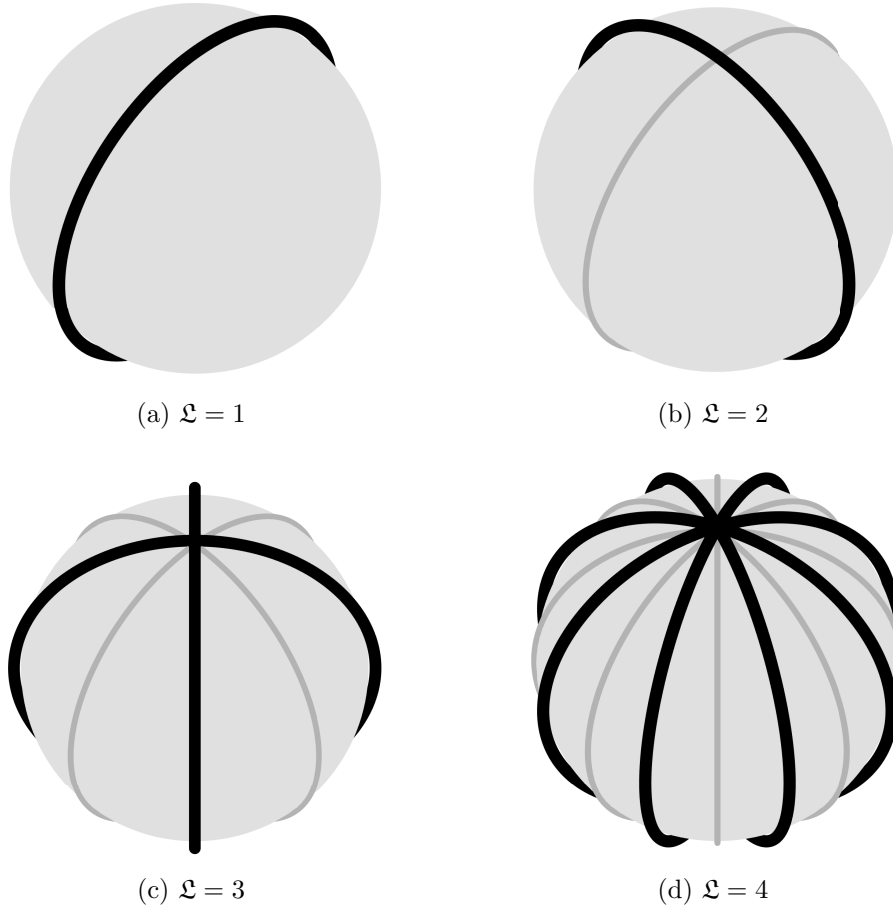


Figure 7-2: Placement of iso-longitude rings for HEALLPix at different resolutions.

$\phi = \phi_{k_2}, \phi_{k_2+1}$, at resolution level \mathcal{L} , is denoted by $A_{k_1, k_2}^{\mathcal{L}}$ and given as

$$\begin{aligned}
 A_{k_1, k_2}^{\mathcal{L}} &= \int_{\theta_{k_1-1}}^{\theta_{k_1}} \int_{\phi_{k_2}}^{\phi_{k_2+1}} \sin \theta \, d\theta d\phi \\
 &= (\phi_{k_2+1} - \phi_{k_2})(\cos \theta_{k_1-1} - \cos \theta_{k_1}) = \left((k_2 - (k_2 - 1)) \frac{\pi}{2^{\mathcal{L}-1}} \right) (z_{k_1-1} - z_{k_1}) \\
 &= \frac{\pi}{4^{\mathcal{L}-1}} = \text{constant} = A_{\mathcal{L}}. \tag{7.3}
 \end{aligned}$$

7.1.4 Pixel centers

For $1 \leq k_1, k_2 \leq 2^{\mathcal{L}}$, we represent the north-west, north-east, south-west and south-east vertices of a pixel, bounded by iso-latitude rings at $\theta = \theta_{k_1-1}, \theta_{k_1}$ and iso-longitude rings at $\phi = \phi_{k_2}, \phi_{k_2+1}$, as $\hat{\mathbf{x}}^{\text{nw}}(\theta_{k_1-1}, \phi_{k_2})$, $\hat{\mathbf{x}}^{\text{ne}}(\theta_{k_1-1}, \phi_{k_2+1})$, $\hat{\mathbf{x}}^{\text{sw}}(\theta_{k_1}, \phi_{k_2})$

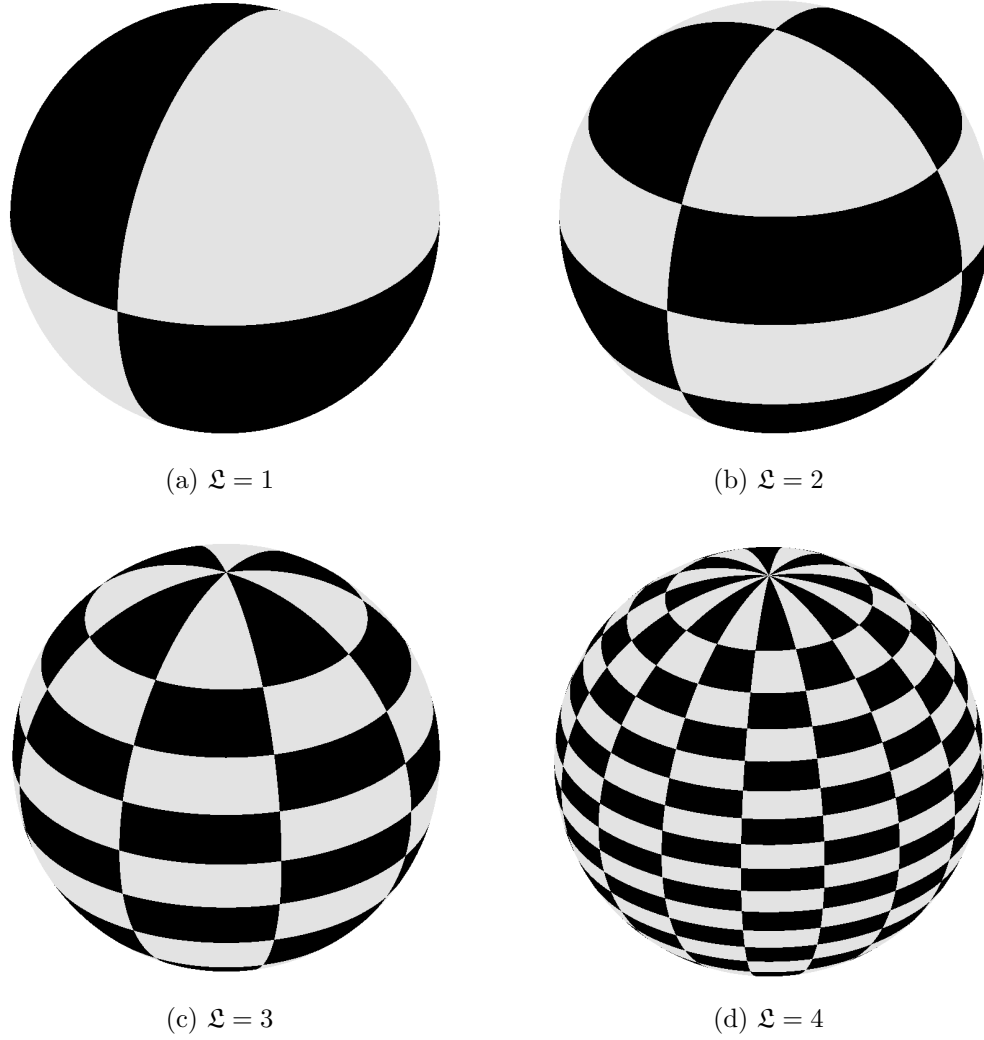


Figure 7-3: Hierarchical equal area iso-latitude iso-longitude pixelization of the sphere at different resolutions.

and $\hat{\mathbf{x}}^{\text{se}}(\theta_{k_1}, \phi_{k_2+1})$ respectively. Then, the pixel center, denoted by $\hat{\mathbf{x}}^0(\theta_{k_1}^0, \phi_{k_2}^0)$, can be defined as the mean of the pixel vertices, i.e.,

$$\theta_{k_1}^0 = \frac{\theta_{k_1-1} + \theta_{k_1}}{2}, \quad \phi_{k_2}^0 = \frac{\phi_{k_2} + \phi_{k_2+1}}{2}. \quad (7.4)$$

Alternately, we can define the pixel center so that it is equi-angular-distant from the pixel vertices, i.e.,

$$\hat{\mathbf{x}}^{\text{nw}}.\hat{\mathbf{x}}^0 = \hat{\mathbf{x}}^{\text{ne}}.\hat{\mathbf{x}}^0 = \hat{\mathbf{x}}^{\text{sw}}.\hat{\mathbf{x}}^0 = \hat{\mathbf{x}}^{\text{se}}.\hat{\mathbf{x}}^0, \quad (7.5)$$

where, using (2.7), we get the following expressions

$$\begin{aligned}
\hat{\mathbf{x}}^{\text{nw}} \cdot \hat{\mathbf{x}}^0 &= \cos \theta_{k_1-1} \cos \theta_{k_1}^0 + \sin \theta_{k_1-1} \sin \theta_{k_1}^0 \cos(\phi_{k_2} - \phi_{k_2}^0), \\
\hat{\mathbf{x}}^{\text{sw}} \cdot \hat{\mathbf{x}}^0 &= \cos \theta_{k_1} \cos \theta_{k_1}^0 + \sin \theta_{k_1} \sin \theta_{k_1}^0 \cos(\phi_{k_2} - \phi_{k_2}^0), \\
\hat{\mathbf{x}}^{\text{ne}} \cdot \hat{\mathbf{x}}^0 &= \cos \theta_{k_1-1} \cos \theta_{k_1}^0 + \sin \theta_{k_1-1} \sin \theta_{k_1}^0 \cos(\phi_{k_2+1} - \phi_{k_2}^0), \\
\hat{\mathbf{x}}^{\text{se}} \cdot \hat{\mathbf{x}}^0 &= \cos \theta_{k_1} \cos \theta_{k_1}^0 + \sin \theta_{k_1} \sin \theta_{k_1}^0 \cos(\phi_{k_2+1} - \phi_{k_2}^0).
\end{aligned} \tag{7.6}$$

From (7.6), it can be observed that the longitudinal contribution to the angular distance between pixel vertices and pixel center depends on the difference of ϕ_{k_2} and ϕ_{k_2+1} with $\phi_{k_2}^0$, which can be made constant by choosing $\phi_{k_2}^0$ as in (7.4), i.e.,

$$\begin{aligned}
\cos(\phi_{k_2+1} - \phi_{k_2}^0) &= \cos\left(\frac{\phi_{k_2+1} - \phi_{k_2}}{2}\right), \\
\cos(\phi_{k_2} - \phi_{k_2}^0) &= \cos\left(\frac{\phi_{k_2} - \phi_{k_2+1}}{2}\right) = \cos\left(\frac{\phi_{k_2+1} - \phi_{k_2}}{2}\right).
\end{aligned} \tag{7.7}$$

Solving the first two equations from the set of expressions in (7.6) results in the colatitude of the pixel center as²

$$\begin{aligned}
\theta_{k_1}^0 &= \tan^{-1} \left[\frac{1}{\cos(\phi_{k_2} - \phi_{k_2}^0)} \frac{\cos \theta_{k_1-1} - \cos \theta_{k_1}}{\sin \theta_{k_1} - \sin \theta_{k_1-1}} \right] \\
&= \tan^{-1} \left[\frac{1}{\cos\left(\frac{\phi_{k_2+1} - \phi_{k_2}}{2}\right)} \frac{\cos \theta_{k_1-1} - \cos \theta_{k_1}}{\sin \theta_{k_1} - \sin \theta_{k_1-1}} \right].
\end{aligned} \tag{7.8}$$

The angular distance between pixel vertices and pixel center is then given by

$$\hat{\mathbf{x}}^{\text{nw}} \cdot \hat{\mathbf{x}}^0 = \cos \theta_{k_1-1} \cos \theta_{k_1}^0 + \sin \theta_{k_1-1} \cos \theta_{k_1}^0 \left(\frac{\cos \theta_{k_1-1} - \cos \theta_{k_1}}{\sin \theta_{k_1} - \sin \theta_{k_1-1}} \right) \tag{7.9}$$

$$\begin{aligned}
&= \frac{\cos \theta_{k_1}^0}{\sin \theta_{k_1} - \sin \theta_{k_1-1}} (\sin \theta_{k_1} \cos \theta_{k_1-1} - \cos \theta_{k_1} \sin \theta_{k_1-1}) \\
&= \hat{\mathbf{x}}^{\text{sw}} \cdot \hat{\mathbf{x}}^0 = \hat{\mathbf{x}}^{\text{ne}} \cdot \hat{\mathbf{x}}^0 = \hat{\mathbf{x}}^{\text{se}} \cdot \hat{\mathbf{x}}^0.
\end{aligned} \tag{7.10}$$

Pixel centers, for these two methods, are shown in Figure 7-4.

²Solving the last two equations from the set of expressions in (7.6) yields the same result as given in (7.8).

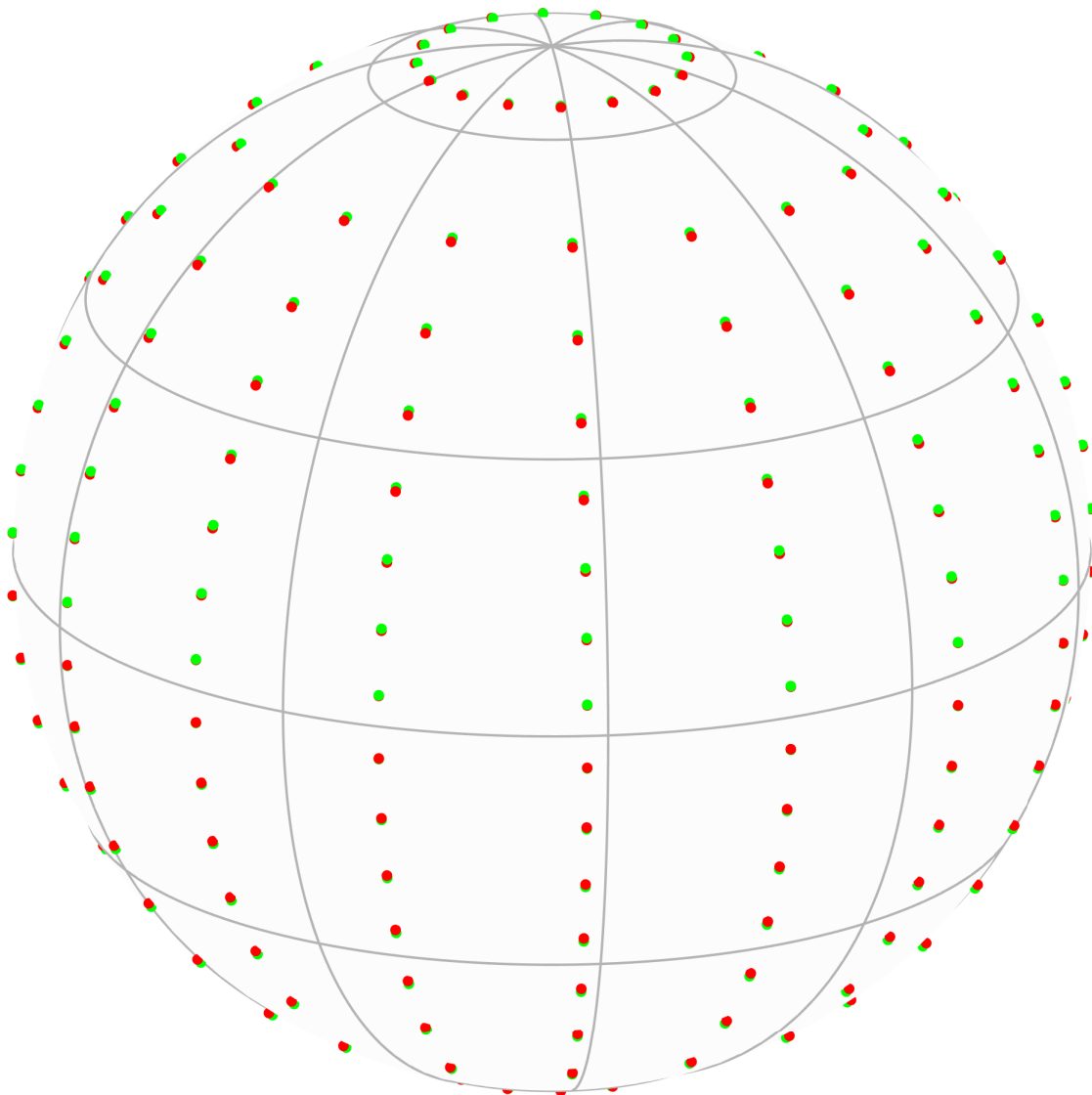


Figure 7-4: HEALLPix pixel centers shown as mean of the pixel vertices in green dots. Red dots show the pixel centers which are equi-angular-distant from the pixel vertices. Pixel centers have nearly the same position on the sphere for the two methods.

7.1.5 Quaternary tree structure

Since HEALLPix divides each pixel hierarchically into four sub-pixels, partitioning of the sphere has a quaternary tree structure as shown in Figure 7-5. Each node in the tree represents a pixel on the sphere. We define tree level as the depth (counted as number of tree edges) of the nodes from the root node and denote it by h_T . Root node, at tree level $h_T = 0$, represents the whole sphere, \mathbb{S}^2 . Nodes at tree level $h_T = 1$

represent pixels on the sphere at resolution $\mathfrak{L} = 1$. Hence, the tree level is given by the resolution parameter of the HEALLPix scheme, i.e., $h_T = \mathfrak{L}$. Maximum value of h_T is called the height of the tree and is given by $\mathfrak{H} = \mathfrak{L}_{\max}$. Nodes are labeled as $P(h_T, i_{h_T})$ where i_{h_T} is the index of the node at tree level h_T , which is given by $1 \leq i_{h_T} \leq 4^{h_T}$. Each parent node, representing a parent pixel, at tree level h_T is related to its child nodes, representing child pixels, at tree level $h_T + 1$ as follows

$$P(h_T, i_{h_T}) = \bigcup_{k=4i_{h_T}-3}^{4i_{h_T}} P(h_T + 1, k). \quad (7.11)$$

Since there are 4^{h_T} nodes at the tree level h_T , total number of nodes in the quaternary tree, denoted by n_P , is given by

$$n_P = \sum_{h_T=0}^{\mathfrak{H}} 4^{h_T} = \frac{(4^{\mathfrak{H}+1} - 1)}{3}. \quad (7.12)$$

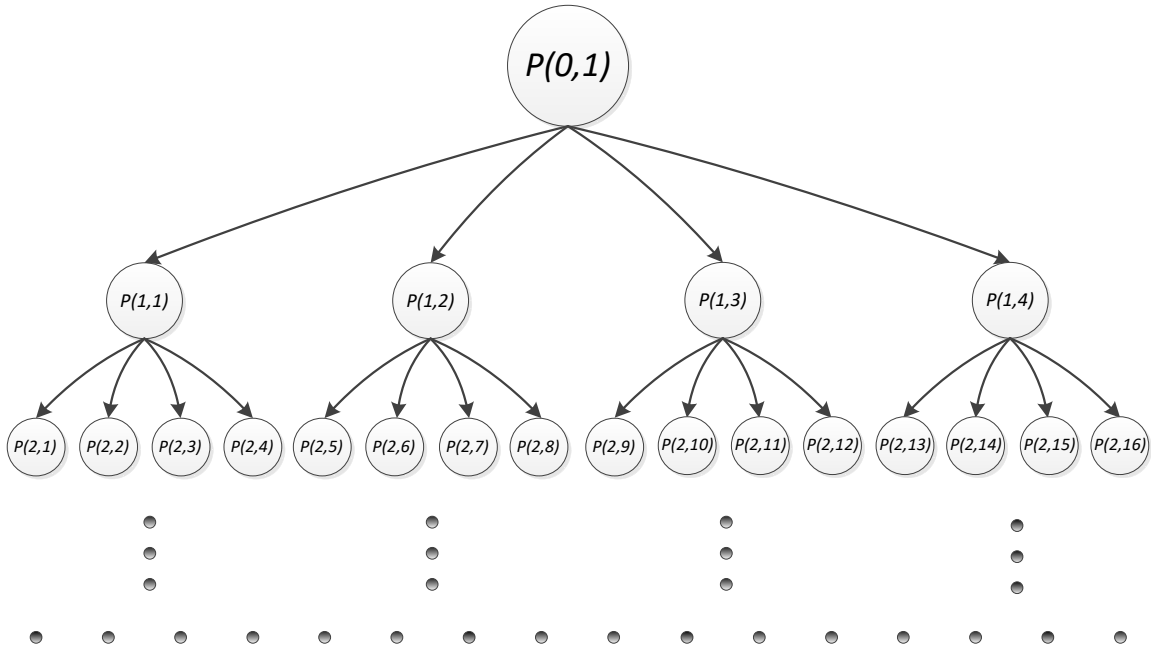


Figure 7-5: Quaternary tree representation for HEALLPix. Each node is represented as $P(h_T, i_{h_T})$ where $0 \leq h_T \leq \mathfrak{H}$ is the tree level and $1 \leq i_{h_T} \leq 4^{h_T}$ is the index of the node at tree level h_T . \mathfrak{H} is the maximum tree level, called height of the tree.

7.2 Overcomplete multiscale dictionary of Slepian functions

Bandlimited Slepian functions, which are solution (in the spectral domain) to the eigenvalue problem in (2.60), not only serve as basis functions for the space of bandlimited signals on the sphere \mathcal{H}_L , the first N_R bandlimited Slepian functions also form a (reduced) basis set for accurate representation of bandlimited signals, which are (energy) concentrated in a region R , where N_R , the spherical Shannon number, is a measure of the number of well-optimally concentrated Slepian functions in the region R . Hence, we can use this “reduced Slepian basis set” as localized basis for accurate representation of bandlimited signals within the HEALLPix pixels. Changing HEALLPix resolution changes the scale of pixelization and finding Slepian basis functions for these multiscale pixels lays the foundation for the framework of multiresolution analysis of signals on the sphere. In this section, we present two formulations to collect spectral representations of Slepian functions in an overcomplete multiscale dictionary.

As the number of well-optimally concentrated Slepian functions depends on the area of the pixel, pixels (or nodes representing pixels) at different resolutions (tree levels) will have different cardinality of the associated localized basis set. Therefore, Shannon number becomes a function of the tree level and is denoted by N_{h_T} . From (7.3), Shannon number for nodes at tree level h_T , denoted by N_{h_T} , is given by

$$N_{h_T} = \frac{A_{h_T} L^2}{4\pi} = \frac{L^2}{4^{\mathfrak{L}}} = \frac{L^2}{4^{h_T}}, \quad (7.13)$$

which is the same for all pixels represented by the nodes at tree level $h_T = \mathfrak{L}$.

The eigenvalue problem in (2.60) is solved for pixels represented by the nodes at a given tree level h_T to obtain N_{SF} number of well-optimally concentrated Slepian functions using (2.62), which are associated with the tree nodes representing respective pixels on the sphere. We present two methods of choosing the number of well-optimally concentrated Slepian functions to associate with each node in the tree.

Table 7.1: Height of the HEALLPix quaternary tree along with maximum HEALLPix resolution parameter, for fixed N_{SF} , at different values of bandlimit L and N_{SF} .

Bandlimit, L	N_{SF}	Tree height, \mathfrak{H}	$\mathfrak{L}_{\text{max}}$
4	2	1	1
8	4	2	2
16	8	2	2
32	16	3	3
64	32	3	3
128	50	4	4
256	64	5	5

7.2.1 Fixed N_{SF} for each tree node

We can choose to fix the cardinality of the localized basis set so that the pixels, represented by nodes in the tree at all tree levels, have the same number of well-optimally concentrated Slepian functions N_{SF} . Height of the HEALLPix tree, in this case, should be such that at least N_{SF} number of well-optimally concentrated Slepian functions are available for pixels represented by the nodes at tree level $h_{\text{T}} = \mathfrak{H}$, i.e.,

$$\begin{aligned}
 N_{\mathfrak{H}} &\geq N_{\text{SF}}, \\
 \mathfrak{H} &\leq \frac{1}{2} \log_2 \left(\frac{L^2}{N_{\text{SF}}} \right) \triangleq \left\lfloor \frac{1}{2} \log_2 \left(\frac{L^2}{N_{\text{SF}}} \right) \right\rfloor,
 \end{aligned} \tag{7.14}$$

where we have used (7.13) to get the final result. As height of the HEALLPix tree should be non-zero, number of well-optimally concentrated Slepian functions should satisfy the following constraint

$$\begin{aligned}
 \frac{1}{2} \log_2 \left(\frac{L^2}{N_{\text{SF}}} \right) &\geq 1, \\
 N_{\text{SF}} &\leq \frac{L^2}{4}.
 \end{aligned} \tag{7.15}$$

Table 7.1 lists some values of the tree height \mathfrak{H} and maximum HEALLPix resolution $\mathfrak{L}_{\text{max}}$ required to generate pixels corresponding to nodes at the tree height, for different values of N_{SF} and bandlimit L .

Table 7.2: Height of the HEALLPix quaternary tree along with maximum HEALLPix resolution parameter, for varying N_{SF} , at different bandlimits L .

Bandlimit, L	Tree height, \mathfrak{H}	$\mathfrak{L}_{\text{max}}$
4	2	2
8	3	3
16	4	4
32	5	5
64	6	6
128	7	7
256	8	8

7.2.2 Varying N_{SF} for nodes at different tree levels

Instead of choosing constant N_{SF} for all the nodes in the tree, we can vary N_{SF} across tree levels by setting it equal to the spherical Shannon number for pixels represented by the nodes at a given tree level, h_{T} , i.e.,

$$N_{\text{SF}} = N_{h_{\text{T}}} = \frac{L^2}{4^{h_{\text{T}}}}. \quad (7.16)$$

For this case, height of the tree should be such that at-least one well-optimally concentrated Slepian function is available for the pixels represented by nodes at tree level $h_{\text{T}} = \mathfrak{H}$, i.e.,

$$\begin{aligned} \frac{L^2}{4^{\mathfrak{H}}} &\geq 1, \\ \mathfrak{H} &\leq \log_2 L, \\ \mathfrak{H} &\triangleq \lfloor \log_2 L \rfloor. \end{aligned} \quad (7.17)$$

From (7.17), we also note that

$$\mathfrak{L}_{\text{max}} \triangleq \lfloor \log_2 L \rfloor. \quad (7.18)$$

Table 7.2 lists some values of the height of the tree \mathfrak{H} and maximum HEALLPix resolution parameter, for different values of bandlimit L , under this scheme.

7.2.3 Dictionary

Depending upon the choice, we find the height of the tree, either from (7.14) or (7.17), at a given bandlimit L , compute first N_{SF} number of eigenvectors using (2.60) (which are spectral domain representations of the bandlimited Slepian functions in (2.62)) for pixels represented by each node of the tree at tree level $0 \leq h_{\text{T}} \leq \mathfrak{H}$, and store them in an $L^2 \times n_{\mathfrak{D}}$ matrix \mathfrak{D} , called a dictionary, as

$$\mathfrak{D} = \left[\mathbf{d}_{(1,1)}^0, \mathbf{d}_{(1,2)}^0, \dots, \mathbf{d}_{(1,L^2)}^0, \mathbf{d}_{(1,1)}^1, \mathbf{d}_{(1,2)}^1, \dots, \mathbf{d}_{(1,N_{\text{SF}})}^1, \dots, \mathbf{d}_{(4^{\mathfrak{H}},1)}^{\mathfrak{H}}, \dots, \mathbf{d}_{(4^{\mathfrak{H}},N_{\text{SF}})}^{\mathfrak{H}} \right], \quad (7.19)$$

where

$$n_{\mathfrak{D}} = L^2 + \sum_{h_{\text{T}}=1}^{\mathfrak{H}} 4^{h_{\text{T}}} N_{\text{SF}} = \begin{cases} L^2 + \frac{4N_{\text{SF}}}{3}(4^{\mathfrak{H}} - 1), & \text{fixed } N_{\text{SF}}, \\ \sum_{h_{\text{T}}=0}^{\mathfrak{H}} 4^{h_{\text{T}}} (L^2/4^{h_{\text{T}}}) = (\mathfrak{H} + 1)L^2, & \text{varying } N_{\text{SF}} \end{cases} \quad (7.20)$$

is the size of the dictionary and represents the total number of Slepian functions in \mathfrak{D} . Dictionary element $\mathbf{d}_{(i_{h_{\text{T}}}, \alpha)}^{h_{\text{T}}}$ is the α^{th} spectral domain representation of the Slepian function (i.e., \mathbf{g}_{α} in (2.60)) for the pixel represented by the node at tree level h_{T} and index $i_{h_{\text{T}}}$. $\mathbf{d}_{(i_{h_{\text{T}}}, \alpha)}^{h_{\text{T}}}$ for $\alpha = 1, \dots, N_{\text{SF}}$ and $1 \leq i_{h_{\text{T}}} \leq 4^{h_{\text{T}}}$ represent well-optimally concentrated Slepian functions for all the pixels at HEALLPix resolution $\mathfrak{L} = h_{\text{T}}$. The dictionary in (7.19) is multiscale in nature because $\mathbf{d}_{(i_{h_{\text{T}}}, \alpha)}^{h_{\text{T}}}$, for different values of h_{T} , represents localized Slepian basis functions for pixels at different scales on the sphere. The dictionary is overcomplete because it contains $n_{\mathfrak{D}}$ number of localized Slepian basis functions, which for $\mathfrak{H} > 1$ is greater than L^2 , where L^2 is the number of basis functions required to represent a signal $f \in \mathcal{H}_L$ on the sphere.

Remark 9. We note that for the root node in Figure 7-5, which represents the whole sphere, Slepian matrix in (2.60) becomes identity and the corresponding Slepian functions become global spherical harmonic functions. Hence, for both methods of finding N_{SF} , the first L^2 elements of the dictionary, representing spherical harmonics, are the orthonormal vectors.

7.2.4 Computation of Slepian functions

Every node at tree level h_T represents a pixel at HEALPix resolution $\mathfrak{L} = h_T$, which is bounded by two co-latitude rings, θ_1, θ_2 and two longitude rings, ϕ_1, ϕ_2 . To compute the Slepian functions for a pixel, we solve for the elements of the matrix \mathbf{K} in (2.58), using the formulation given in [76], as

$$K_{\ell m, pq} = \sum_{m'=-\ell}^{\ell} F_{m', m}^{\ell} \sum_{q'=-p}^p F_{q', q}^p Q(m' + q') S(q - m), \quad (7.21)$$

where $F_{m', m}^{\ell}$, although defined in (4.8), is repeated here for convenience

$$F_{m', m}^{\ell} = (-i)^m \sqrt{\frac{2\ell + 1}{4\pi}} \Delta_{m', m}^{\ell} \Delta_{m', 0}^{\ell}, \quad \Delta_{m', m}^{\ell} \triangleq d_{m', m}^{\ell}(\pi/2), \quad (7.22)$$

and

$$Q(m) = \begin{cases} \frac{1}{4}(2im(\theta_2 - \theta_1)) + e^{2im\theta_1} - e^{2im\theta_2}, & |m| = 1, \\ \frac{1}{m^2 - 1} \left(e^{im\theta_1}(-\cos\theta_1 + im\sin\theta_1) + e^{im\theta_2}(\cos\theta_2 - im\sin\theta_2) \right), & |m| \neq 1, \end{cases}$$

$$S(m) = \begin{cases} \phi_2 - \phi_1, & m = 0, \\ \frac{i}{m}(e^{im\phi_1} - e^{im\phi_2}), & m \neq 0. \end{cases} \quad (7.23)$$

Figure 7-6 shows Slepian functions on the sphere, obtained using the Fourier expansion in (2.23), for different nodes in the HEALPix quaternary tree constructed for N_{SF} given by (7.16), at bandlimit $L = 16$ for which $\mathfrak{N} = 4$.

7.3 Analysis

We construct the dictionary using varying number of Slepian functions, i.e., $N_{\text{SF}} = N_{h_T}$, for which the height of the HEALPix quaternary tree and number of elements in the dictionary are given by (7.17) and (second expression in) (7.20) respectively. We assume that the bandlimit L is a power of 2 so that the Shannon number in (7.16)

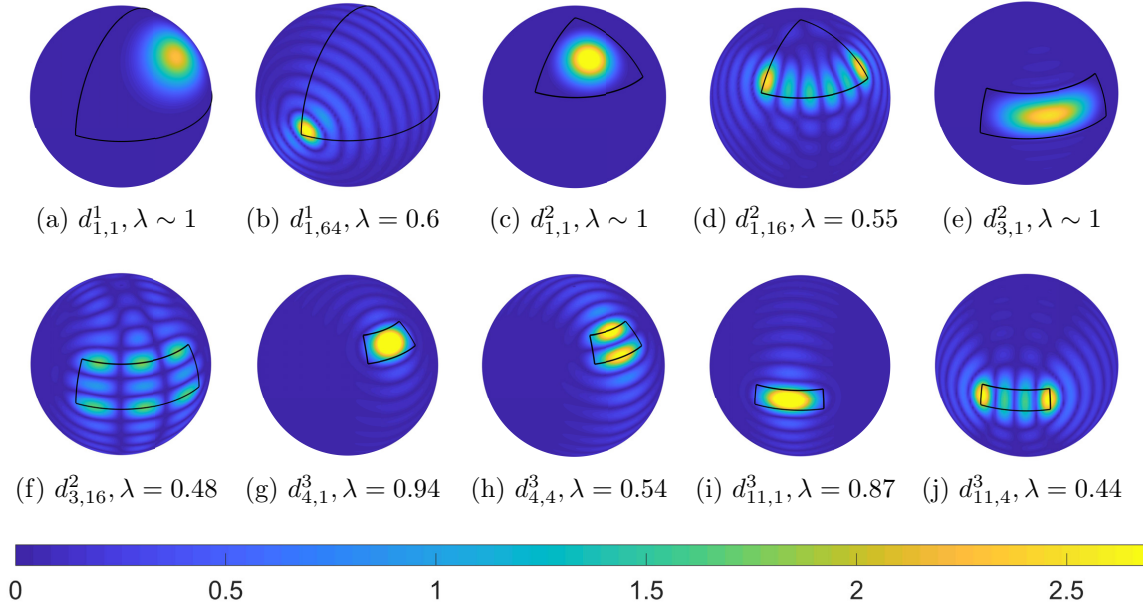


Figure 7-6: Magnitude of Slepian functions for different nodes in the HEALPix quaternary tree, constructed using (7.16) for bandlimit $L = 16$ and height $\mathfrak{H} = 4$. For each node, we show the most well-optimally concentrated and least well-optimally concentrated Slepian functions, where λ denotes the fractional energy concentration (see (2.57)). Boundary of the pixels is shown in black.

is an integer, which in turn gives the height of the tree in (7.17), and the maximum HEALPix resolution in (7.18), as $\log_2 L$. The resulting dictionary is overcomplete by design and hence, its elements do not make an orthogonal basis. This motivates the analysis for the range of the dictionary \mathfrak{D} , which is the vector space spanned by its elements, and mutual coherence, which is defined as magnitude of the inner product between dictionary elements.

7.3.1 Range of \mathfrak{D}

The utility of the dictionary \mathfrak{D} is in its ability to represent and reconstruct bandlimited signals concentrated within a pixel on the sphere. We analyze the range of the dictionary \mathfrak{D} by considering the following subset

$$\mathfrak{D}_k = \left\{ \mathbf{d}_{(i_{h_T}, \alpha)}^{h_T} \in \mathfrak{D} : h_T \in [1, \mathfrak{H}], \right. \\ \left. i_{h_T} = (k-1)4^{(h_T-1)} + 1, \dots, k4^{(h_T-1)}, \alpha = 1, \dots, N_{h_T} \right\}, \quad k \in [1, 4], \quad (7.24)$$

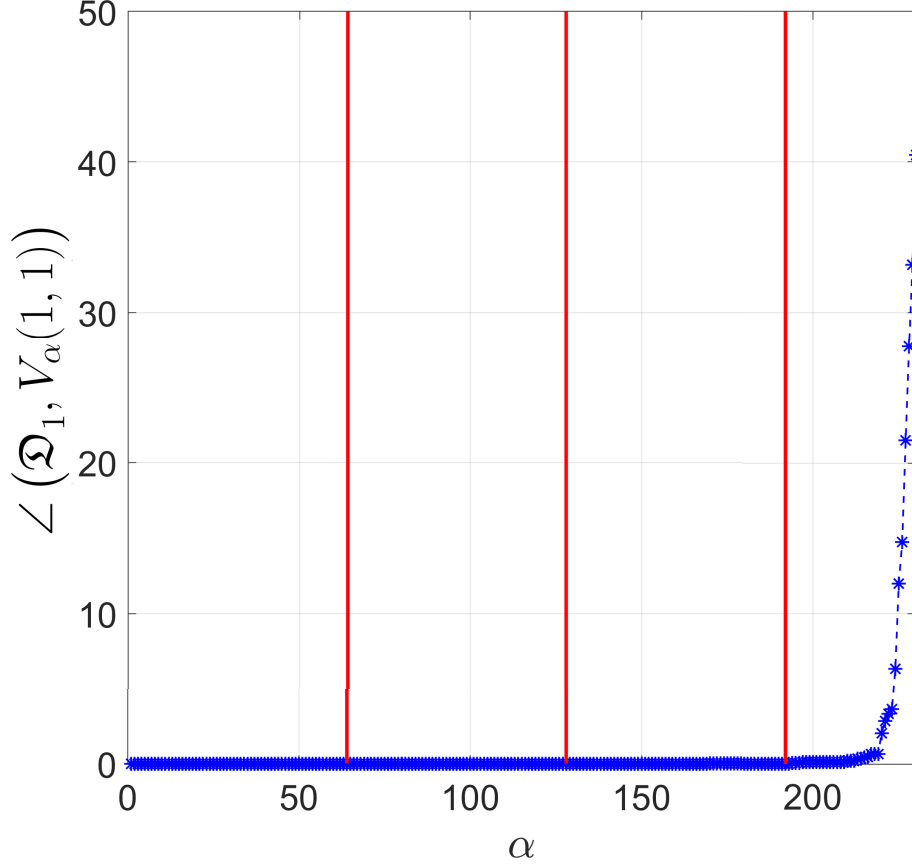


Figure 7-7: Angle (in degrees) between the range space of \mathfrak{D}_1 and $V_\alpha(1, 1)$ for different values of α and bandlimit $L = 16$ ($\mathfrak{N} = 4$). Thick red lines mark the integer multiples of Shannon number $N_1 = 64$.

i.e., \mathfrak{D}_k contains Slepian functions for the pixels represented by the node $P(1, k)$ and all its child nodes. Hence, the range space of \mathfrak{D}_k is the vector space spanned by the dictionary elements which are well-optimally concentrated within the pixels represented by the node $P(1, k)$ and all its child nodes. In order to analyze the range of \mathfrak{D}_k , for $k = 1$, we compare its range space to the vector space of bandlimited signals which are well-optimally concentrated within the pixel represented by the node $P(1, 1)$, i.e., we compare the range space of \mathfrak{D}_1 to that of the following matrix

$$V_\alpha(1, 1) = [\mathbf{d}_{(1,1)}^1, \dots, \mathbf{d}_{(1,\alpha)}^1], \quad \alpha \in [1, N_1], \quad N_1 = \frac{L^2}{4}, \quad (7.25)$$

by investigating the angle between them, where N_1 is the Shannon number at tree level $h_T = 1$ and $\mathbf{d}_{(1,\alpha)}^1$ is an element of the dictionary \mathfrak{D} in (7.19). For two subspaces,

having different dimensions, we define the angle as the maximum principle angle between them³. The results are shown in Figure 7-7 for bandlimit $L = 16$ and tree height $\mathfrak{H} = 4$. It can be seen that the elements of \mathfrak{D}_1 comfortably span the space of bandlimited signals which are well-optimally concentrated within pixel represented by the node $P(1, 1)$, since the angle $\angle(\mathfrak{D}_1, V_\alpha(1, 1))$ is essentially 0 for not only just the well-optimally concentrated Slepian functions, i.e., $\alpha \leq N_1$ but also for $N_1 \leq \alpha \leq 3N_1$.

7.3.2 Mutual coherence

Mutual coherence between the elements of the dictionary is defined as

$$M_C(\alpha, \beta) = \left| \left(\mathbf{d}_{(i_{h_T}, \alpha)}^{h_T} \right)^H \mathbf{d}_{(i_{h_T}, \beta)}^{h_T} \right|, \quad \alpha \neq \beta. \quad (7.26)$$

The dictionary \mathfrak{D} is required to be mutually incoherent, i.e., exhibit small mutual coherence, as this is of significant importance for the sparse representation of signals (e.g. [126, 127]). Figure 7-8 shows that the mutual coherence between most of the dictionary elements is negligibly small⁴, with the exception of the nodes which share their ancestors' pixels. Specifically, the dictionary elements $\mathbf{d}_{(1, \alpha)}^0, \mathbf{d}_{(1, \alpha)}^1, \mathbf{d}_{(1, \alpha)}^2, \mathbf{d}_{(1, \alpha)}^3, \dots$ tend to have large mutual coherence while the nodes representing disjoint pixels have negligibly small mutual coherence. In Figure 7-9, we sample the range of mutual coherence into bins and plot the cumulative fraction of the total number of absolute inner products between the dictionary elements, excluding self inner products, for different quaternary trees with height $\mathfrak{H} = 1, 2, 3, 4$ at corresponding bandlimit $L = 2, 4, 8, 16$. Arrow shows the direction in which the approximate knee of the curves is displaced with increasing values of the bandlimit L . It is observed that $\sim 96\%$ of the total number of inner products, for the tree with height $\mathfrak{H} = 4$, have magnitude less than 0.13. Hence, at bandlimit $L = 16$, only $\sim 4\%$ of the total number of inner products between dictionary elements contribute to mutual coherence $M_C \geq 0.13$. Table 7.3 tabulates the approximate knee for each curve in Figure 7-9.

³We use the *subspace* function in MATLAB to compute the angle between two subspaces.

⁴The first L^2 dictionary elements are orthonormal vectors which exhibit zero mutual coherence.

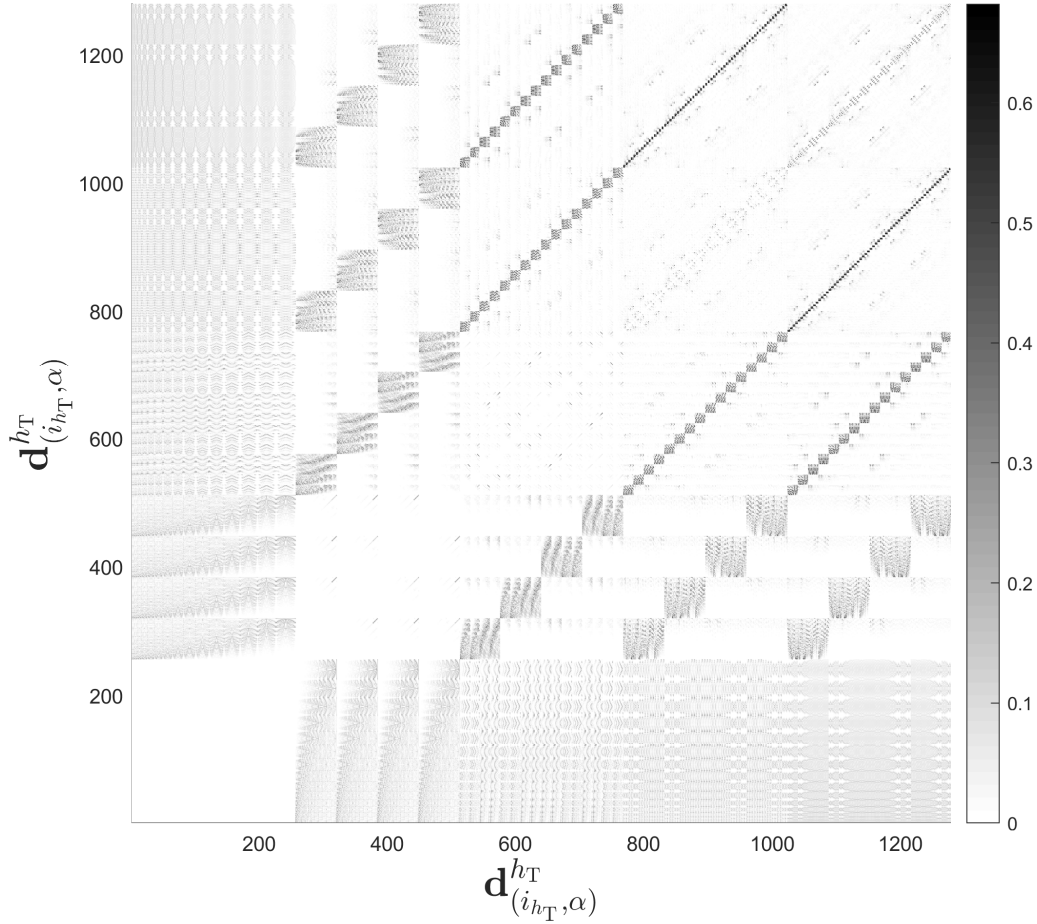


Figure 7-8: Mutual coherence between elements of the dictionary constructed for HEALLPix at bandlimit $L = 16$ ($\mathfrak{H} = 4$).

We can quantify the number of those inner products between the dictionary elements which result in significant mutual coherence⁵. Slepian functions computed for the child pixels exhibit large mutual coherence with those of their parent pixel, e.g., tracing the left-most ancestry of the tree in Figure 7-5, Slepian functions computed for the pixel represented by the root node $P(0, 1)$ exhibit large mutual coherence with the Slepian functions of the pixels represented by the child node $P(1, 1)$, the grandchild nodes $P(2, 1)$, $P(2, 2)$, $P(2, 3)$, $P(2, 4)$, the great grandchild nodes $P(3, 1)$, $P(3, 2)$, \dots , $P(3, 16)$ and so on. Noting that the number of Slepian functions associated with the root node $P(0, 1)$ is L^2 , number of those associated with the child

⁵The word “significant” is not used in its true sense, significant mutual coherence refers to absolute inner products between Slepian functions of the overlapping pixels.

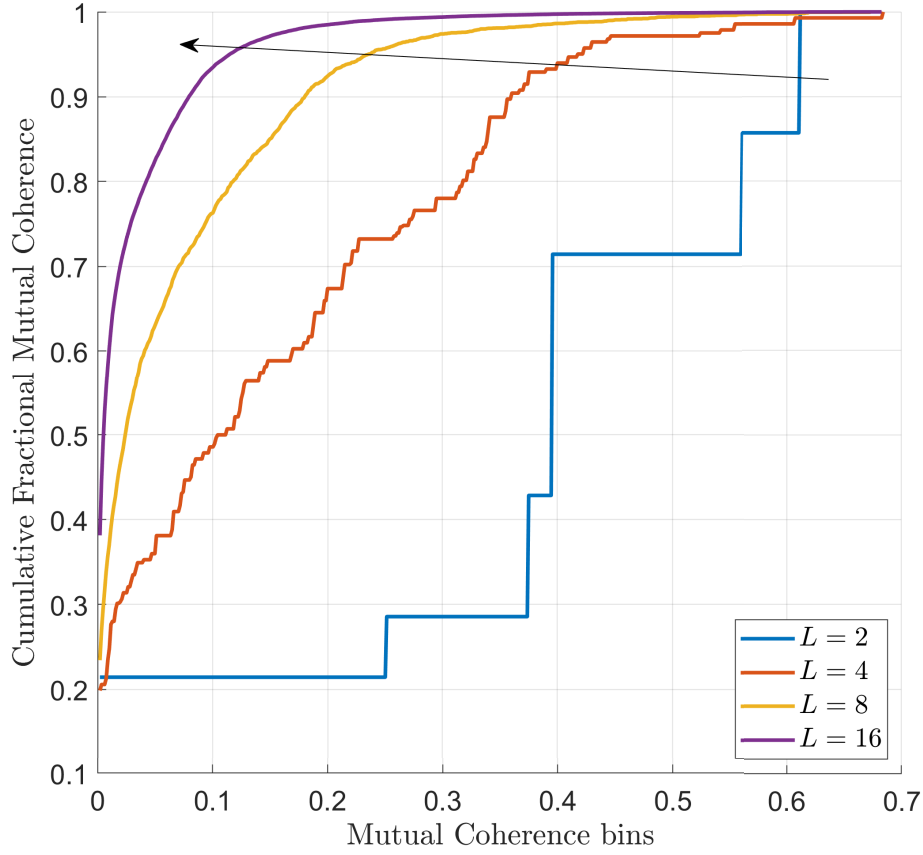


Figure 7-9: Cumulative fractional mutual coherence between dictionary elements, plotted against the range of mutual coherence values, for HEALLPix quaternary trees with height $\mathfrak{J} = 1, 2, 3, 4$, corresponding to bandlimit $L = 2, 4, 8, 16$. Arrow shows the direction in which the approximate knee of the curves is displaced with increasing values of L .

node $P(1, 1)$ is $L^2/4$, number of those associated with each of the grandchild nodes $P(2, 1), P(2, 2), P(2, 3), P(2, 4)$ is $L^2/16$ and so on, we can write the number of inner products resulting in significant mutual coherence as

$$\begin{aligned}
 N_{\text{sig}, M_C} &= 4 \sum_{J_1=1}^{\mathfrak{J}} L^2 4^{(J_1-1)} \frac{L^2}{4^{J_1}} + 4 \sum_{J_1=2}^{\mathfrak{J}} \frac{L^2}{4} 4^{(J_1-1)} \frac{L^2}{4^{J_1}} + \\
 &\quad 4^2 \sum_{J_1=3}^{\mathfrak{J}} \frac{L^2}{4^2} 4^{(J_1-2)} \frac{L^2}{4^{J_1}} + \dots + 4^{(\mathfrak{J}-1)} \frac{L^2}{4^{(\mathfrak{J}-1)}} 4 \frac{L^2}{4^{\mathfrak{J}}} \\
 &= \sum_{J_1=1}^{\mathfrak{J}} L^4 + \sum_{J_1=2}^{\mathfrak{J}} \frac{L^4}{4} + \sum_{J_1=3}^{\mathfrak{J}} \frac{L^4}{4^2} + \dots + \frac{L^4}{4^{(\mathfrak{J}-1)}} = \sum_{J_2=0}^{\mathfrak{J}-1} \frac{L^4 (\mathfrak{J} - J_2)}{4^{J_2}}, \quad (7.27)
 \end{aligned}$$

Table 7.3: Approximating the knee for each curve in Figure 7-9.

Bandlimit, L	Coordinates for knee of curves in Figure 7-9
2	(0.61, 0.86), i.e., $\sim 86\%$ of the total number of inner products result in mutual coherence ≤ 0.61
4	(0.4, 0.94), i.e., $\sim 94\%$ of the total number of inner products result in mutual coherence ≤ 0.4
8	(0.24, 0.95), i.e., $\sim 95\%$ of the total number of inner products result in mutual coherence ≤ 0.24
16	(0.13, 0.96), i.e., $\sim 96\%$ of the total number of inner products result in mutual coherence ≤ 0.13

where \mathfrak{H} is the height of the HEALLPix quaternary tree at bandlimit L . Ratio of the number of inner products resulting in significant mutual coherence to the total number of inner products between dictionary elements, excluding self inner products, i.e., of type $M_C(\alpha, \alpha)$, is given by

$$\frac{N_{\text{sig}, M_C}}{N_{\text{tot}, M_C}} = \frac{L^4 \left[\sum_{J_2=0}^{\mathfrak{H}-1} (\mathfrak{H} - J_2) 4^{-J_2} \right]}{0.5 * [(\mathfrak{H} + 1)^2 L^4 - (\mathfrak{H} + 1) L^2]} = \frac{2L^2 \left[\sum_{J_2=0}^{\mathfrak{H}-1} (\mathfrak{H} - J_2) 4^{-J_2} \right]}{(\mathfrak{H} + 1) [(\mathfrak{H} + 1) L^2 - 1]}. \quad (7.28)$$

Figure 7-10, which plots this ratio for HEALLPix quaternary tree with different heights, shows that the fraction of total number of inner products between dictionary elements, resulting in significant mutual coherence, decreases with increasing height of the tree. For a HEALLPix quaternary tree with height $\mathfrak{H} = 4$, at bandlimit $L = 16$, $\sim 39\%$ of the total number of inner products between dictionary elements result in significant mutual coherence.

It must be noted that “significant” mutual coherence is computed as the magnitude of inner product between those dictionary elements which are associated with nodes representing overlapping pixels on the sphere. At small bandlimits, spatial concentration of bandlimited Slepian functions within the pixels is relatively poor, hence, inner product between the dictionary elements associated with nodes representing non-overlapping pixels can also be significant, due to greater leakage (i.e., small associated eigenvalues) for even the well-optimally concentrated Slepian functions. This is apparent from the curves in Figure 7-9 for bandlimits $L = 2, 4$.

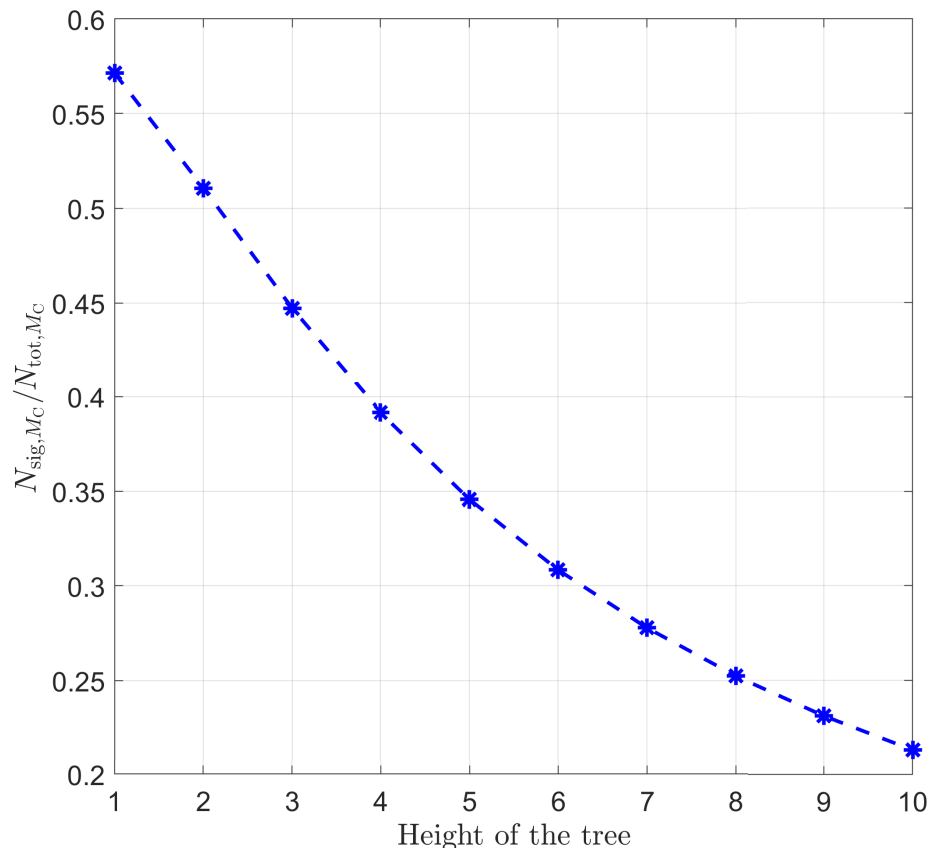


Figure 7-10: Fraction of total number of inner products between HEALPix dictionary elements which result in significant mutual coherence.

7.4 Multiscale analysis for HEALPix

HEALPix scheme, proposed in the previous section, generates pixels with boundaries having simple mathematical representations, which makes the computation of Slepian functions a relatively simple task. In this section, we present exact analytical expressions for the computation of bandlimited Slepian functions for the pixels generated using HEALPix [57], which was reviewed in Section 6.2.1. HEALPix pixels have much more complex mathematical expressions for the boundaries, which makes the computation of Slepian functions a highly non-trivial task. We exploit rotational symmetries between different HEALPix pixels to find appropriate rotation angles, and employ Wigner- D functions to develop an efficient framework for the computation of Slepian functions. We propose convergence criterion for infinite series expansions employed in the framework and construct an overcomplete multiscale

dictionary of Slepian functions, which is analyzed for the range and mutual coherence of its elements. However, before presenting the mathematical formulation for the computation of surface integrals over HEALPix pixels, we review the geometry of HEALPix in detail.

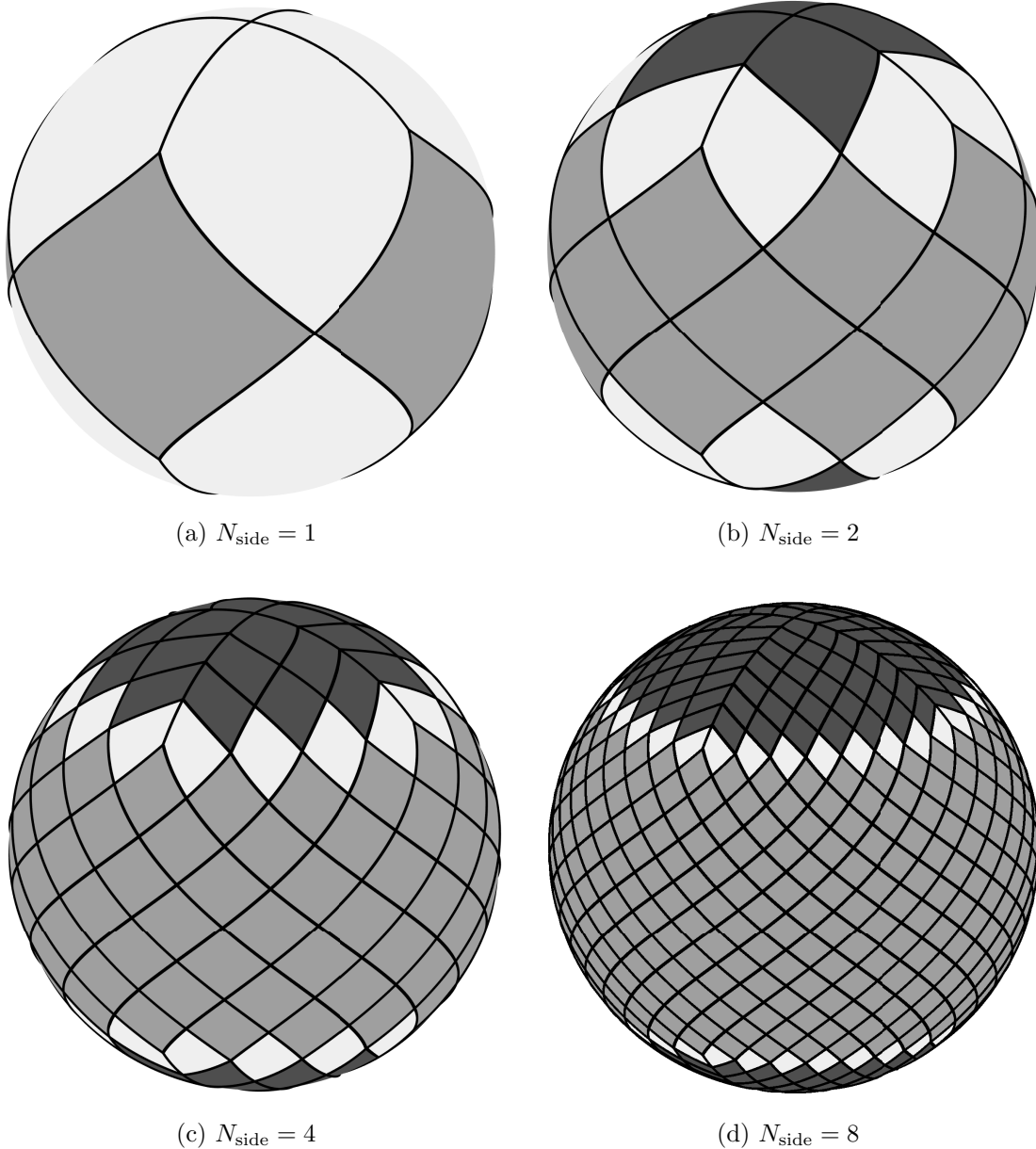


Figure 7-11: Hierarchical equal area iso-latitude pixelization of the sphere at different resolutions. Light shade of gray represents pixels at the boundary of polar and equatorial zones whereas dark and medium shades of gray represent pixels in the polar and equatorial zones respectively. Pixel boundaries are shown in black.

7.4.1 Geometry of HEALPix

As reviewed in Section 6.2.1, HEALPix divides the whole sphere into 12 equal area pixels at the base-resolution, i.e., $N_{\text{side}} = 1$. Increasing the resolution level by one step divides each pixel into 4 sub-pixels, resulting in $N_{\text{pix}} = 12N_{\text{side}}^2$ pixels, which are divided into three zones, namely *north polar* ($\cos \theta \geq 2/3$), *equatorial* ($-2/3 < \cos \theta < 2/3$) and *south polar* ($\cos \theta \leq -2/3$). Partitioning of the sphere under HEALPix is shown in Figure 7-11 for different values of N_{side} . We treat pixels which are centered on the iso-latitude rings at $\cos \theta = \pm 2/3$ separately from polar and equatorial pixels and refer to them as north-polar-equatorial and south polar-equatorial pixels respectively (these pixels are shown in the lightest shade of gray in Figure 7-11). Hence, in the context of this work, HEALPix pixels are divided into five zones, namely *north polar* (NP), *north polar-equatorial* (NPE), *equatorial* (EQ), *south polar-equatorial* (SPE) and *south polar* (SP).

Pixel Indexing

There are two schemes which can be adopted for indexing HEALPix pixels, namely the *ring* scheme and the *nested* scheme [57]. We choose the ring scheme, in which pixels are indexed in anticlockwise direction along longitude (starting from $\phi = 0$), and from north to south along colatitude. Ring index, denoted by \mathbf{p} , for pixels in the five zones on HEALPix grid, is given by

$$\begin{aligned}
 \text{NP} &: 1 \leq \mathbf{p} \leq 2N_{\text{side}}(N_{\text{side}} - 1), \\
 \text{NPE} &: 2N_{\text{side}}(N_{\text{side}} - 1) < \mathbf{p} \leq 2N_{\text{side}}(N_{\text{side}} + 1), \\
 \text{EQ} &: 2N_{\text{side}}(N_{\text{side}} + 1) < \mathbf{p} \leq N_{\text{side}}(10N_{\text{side}} - 2), \\
 \text{SPE} &: N_{\text{side}}(10N_{\text{side}} - 2) < \mathbf{p} \leq N_{\text{side}}(10N_{\text{side}} + 2), \\
 \text{SP} &: N_{\text{side}}(10N_{\text{side}} + 2) < \mathbf{p} \leq N_{\text{pix}}.
 \end{aligned} \tag{7.29}$$

Given a pixel indexed by $\mathbf{p} \in \{1, 2, \dots, N_{\text{pix}}\}$, we further refine the indexing using the “row kind” (r , which indexes the pixel along colatitude) and “column kind” (c ,

which indexes the pixel along longitude) indices as

$$r = \begin{cases} \left\lceil \frac{-1 + \sqrt{1 + 2\mathbf{p}}}{2} \right\rceil, & \text{NP,} \\ 1, & \text{NPE,} \\ \left\lceil \frac{\mathbf{p} - 2N_{\text{side}}(N_{\text{side}} + 1)}{4N_{\text{side}}} \right\rceil, & \text{EQ,} \\ 1, & \text{SPE,} \\ \left\lceil \frac{-1 + \sqrt{1 + 2(N_{\text{side}}(N_{\text{side}} - 1) - \mathbf{p}_s + 1)}}{2} \right\rceil, & \text{SP,} \end{cases} \quad (7.30)$$

$$c = \begin{cases} \mathbf{p} - 2r(r - 1), & \text{NP,} \\ \mathbf{p} - 2N_{\text{side}}(N_{\text{side}} - 1), & \text{NPE,} \\ \mathbf{p} - 2N_{\text{side}}(N_{\text{side}} + 1) - 4N_{\text{side}}(r - 1), & \text{EQ,} \\ \mathbf{p} - N_{\text{side}}(10N_{\text{side}} - 2), & \text{SPE,} \\ \mathbf{p}_s - 2(N_{\text{side}} - r - 1)(N_{\text{side}} + r), & \text{SP,} \end{cases} \quad (7.31)$$

where $\mathbf{p}_s = \mathbf{p} - N_{\text{side}}(10N_{\text{side}} + 2)$. Note that for south polar pixels, row index decreases from $N_{\text{side}} - 1$ to 1 as the colatitude increases towards π .

Diametrically opposite pixels

Every pixel in the southern hemisphere has a diametrically opposite pixel in the northern hemisphere. Denoting the row and column indices of the equatorial pixels in the southern hemisphere by $r^{\text{eq,S}}$ and $c^{\text{eq,S}}$ respectively, we note that

$$\begin{aligned} r^{\text{eq,N}} &= 2N_{\text{side}} - r^{\text{eq,S}}, \\ c^{\text{eq,N}} &= \begin{cases} (c^{\text{eq,S}} + 2N_{\text{side}}) \bmod 4N_{\text{side}}, & \text{if } (c^{\text{eq,S}} + 2N_{\text{side}}) \bmod 4N_{\text{side}} \neq 0, \\ 4N_{\text{side}}, & \text{otherwise,} \end{cases} \end{aligned} \quad (7.32)$$

where $r^{\text{eq,N}}$ and $c^{\text{eq,N}}$ are the row and column indices of the equatorial pixels in the northern hemisphere. Denoting the row and column indices of the north polar

and north polar-equatorial pixels by $r^{\text{p},\text{N}}$, $c^{\text{p},\text{N}}$ and $r^{\text{pe},\text{N}}$, $c^{\text{pe},\text{N}}$ respectively, similar expressions can be obtained as

$$r^{\text{p},\text{N}} = r^{\text{p},\text{S}},$$

$$c^{\text{p},\text{N}} = \begin{cases} (c^{\text{p},\text{S}} + 2r^{\text{p},\text{S}}) \bmod 4r^{\text{p},\text{N}}, & \text{if } (c^{\text{p},\text{S}} + 2r^{\text{p},\text{S}}) \bmod 4r^{\text{p},\text{N}} \neq 0, \\ 4r^{\text{p},\text{N}}, & \text{otherwise,} \end{cases} \quad (7.33)$$

and

$$r^{\text{pe},\text{N}} = r^{\text{pe},\text{S}} = 1,$$

$$c^{\text{pe},\text{N}} = \begin{cases} (c^{\text{pe},\text{S}} + 2N_{\text{side}}) \bmod 4N_{\text{side}}, & \text{if } (c^{\text{pe},\text{S}} + 2N_{\text{side}}) \bmod 4N_{\text{side}} \neq 0, \\ 4N_{\text{side}}, & \text{otherwise,} \end{cases} \quad (7.34)$$

where $r^{\text{p},\text{S}}$, $c^{\text{p},\text{S}}$ and $r^{\text{pe},\text{S}}$, $c^{\text{pe},\text{S}}$ are row and column indices of the pixels in the south polar and south polar-equatorial zones respectively.

Pixel Boundaries

Polar pixels have non-linear boundaries. Defining c^{pz} as the cyclic polar zone column index, i.e.,

$$c^{\text{pz}} \triangleq \begin{cases} c \bmod r, & c \bmod r \neq 0, \\ r, & c \bmod r = 0, \end{cases} \quad (7.35)$$

for r and c given in (7.30) and (7.31) respectively, north polar pixel boundaries are given by the following expressions [57],

$$\phi = \begin{cases} \pi E_{u\ell}^{\text{pz}} / (a^{\text{pz}} \sin(\theta/2)) + \Delta\phi, & \text{(upper left),} \\ \pi/2 - \pi E_{\ell\ell}^{\text{pz}} / (a^{\text{pz}} \sin(\theta/2)) + \Delta\phi, & \text{(lower left),} \\ \pi E_{\ell r}^{\text{pz}} / (a^{\text{pz}} \sin(\theta/2)) + \Delta\phi, & \text{(lower right),} \\ \pi/2 - \pi E_{ur}^{\text{pz}} / (a^{\text{pz}} \sin(\theta/2)) + \Delta\phi, & \text{(upper right),} \end{cases} \quad (7.36)$$

where $a^{\text{pz}} = 2\sqrt{6}N_{\text{side}}$, $E_{ul}^{\text{pz}} = c^{\text{pz}} - 1$, $E_{\ell\ell}^{\text{pz}} = r - c^{\text{pz}} + 1$, $E_{\ell r}^{\text{pz}} = c^{\text{pz}}$, $E_{ur}^{\text{pz}} = r - c^{\text{pz}}$,

$$\Delta\phi \triangleq \begin{cases} (\pi/2) \left(\left\lceil \frac{c}{r} \right\rceil - 1 \right), & \text{for NP/SP pixels,} \\ (\pi/2) \left(\left\lceil \frac{c}{N_{\text{side}}} \right\rceil - 1 \right), & \text{for NPE/SPE pixels,} \end{cases} \quad (7.37)$$

and the subscripts, denoting upper left, lower left, lower right and upper right, describe the respective sides of the pixel boundary with respect to the center of the pixel. Similarly, south polar pixel boundaries are given by

$$\phi = \begin{cases} \pi E_{ul}^{\text{pz}} / (a^{\text{pz}} \cos(\theta/2)) + \Delta\phi, & \text{(lower left),} \\ \pi/2 - \pi E_{\ell\ell}^{\text{pz}} / (a^{\text{pz}} \cos(\theta/2)) + \Delta\phi, & \text{(upper left),} \\ \pi E_{\ell r}^{\text{pz}} / (a^{\text{pz}} \cos(\theta/2)) + \Delta\phi, & \text{(upper right),} \\ \pi/2 - \pi E_{ur}^{\text{pz}} / (a^{\text{pz}} \cos(\theta/2)) + \Delta\phi, & \text{(lower right),} \end{cases} \quad (7.38)$$

which can be easily derived from (7.36) by replacing θ with $\pi - \theta$.

Equatorial pixels have linear boundaries which are given by the following expressions [57]

$$\cos\theta = \begin{cases} 2/3 - E_{ul}^{\text{ez}} a^{\text{ez}} + b\phi, & \text{(upper left),} \\ 2/3 - E_{\ell\ell}^{\text{ez}} a^{\text{ez}} - b\phi, & \text{(lower left),} \\ 2/3 - E_{\ell r}^{\text{ez}} a^{\text{ez}} + b\phi, & \text{(lower right),} \\ 2/3 - E_{ur}^{\text{ez}} a^{\text{ez}} - b\phi, & \text{(upper right),} \end{cases} \quad (7.39)$$

where $a^{\text{ez}} = 4/3N_{\text{side}}$, $b = 8/3\pi$, $E_{ul}^{\text{ez}} = c^{\text{ez}} - 1$, $E_{\ell\ell}^{\text{ez}} = r - (c^{\text{ez}} - 1)$, $E_{\ell r}^{\text{ez}} = c^{\text{ez}}$, $E_{ur}^{\text{ez}} = r - c^{\text{ez}}$, and c^{ez} is defined as

$$c^{\text{ez}} \triangleq c + \lfloor r/2 \rfloor. \quad (7.40)$$

Polar-equatorial pixels are shared between polar and equatorial zones. Hence, their boundaries can be derived from (7.36), (7.38) and (7.39). Defining c^{pe} as the

cyclic column index for the polar-equatorial zone, i.e.,

$$c^{\text{pe}} = \begin{cases} c \bmod N_{\text{side}}, & c \bmod N_{\text{side}} \neq 0, \\ N_{\text{side}}, & c \bmod N_{\text{side}} = 0, \end{cases} \quad (7.41)$$

for c given in (7.31), boundaries for the north polar-equatorial pixels are given by

$$\begin{aligned} \phi &= \begin{cases} \pi E_{ul}^{\text{npe}} / (a^{\text{pz}} \sin(\theta/2)) + \Delta\phi, & \text{(upper left)}, \\ \pi/2 - \pi E_{ur}^{\text{npe}} / (a^{\text{pz}} \sin(\theta/2)) + \Delta\phi, & \text{(upper right)}, \end{cases} \\ \cos \theta &= \begin{cases} 2/3 - E_{\ell\ell}^{\text{npe}} a^{\text{ez}} - b\phi, & \text{(lower left)}, \\ 2/3 - E_{\ell r}^{\text{npe}} a^{\text{ez}} + b\phi, & \text{(lower right)}, \end{cases} \end{aligned} \quad (7.42)$$

where $E_{ul}^{\text{npe}} = c^{\text{pe}} - 1$, $E_{ur}^{\text{npe}} = N_{\text{side}} - c^{\text{pe}}$, $E_{\ell\ell}^{\text{npe}} = 1 - c$ and $E_{\ell r}^{\text{npe}} = c$. Similarly, boundaries for the south polar-equatorial pixels are given by

$$\begin{aligned} \cos \theta &= \begin{cases} 2/3 - E_{ul}^{\text{spe}} a^{\text{ez}} + b\phi, & \text{(upper left)}, \\ 2/3 - E_{ur}^{\text{spe}} a^{\text{ez}} - b\phi, & \text{(upper right)}, \end{cases} \\ \phi &= \begin{cases} \pi E_{\ell\ell}^{\text{spe}} / (a^{\text{pz}} \cos(\theta/2)) + \Delta\phi, & \text{(lower left)}, \\ \pi/2 - \pi E_{\ell r}^{\text{spe}} / (a^{\text{pz}} \cos(\theta/2)) + \Delta\phi, & \text{(lower right)}, \end{cases} \end{aligned} \quad (7.43)$$

where $E_{ul}^{\text{spe}} = N_{\text{side}} + c - 1$, $E_{ur}^{\text{spe}} = N_{\text{side}} - c$, $E_{\ell\ell}^{\text{spe}} = c^{\text{pe}} - 1$ and $E_{\ell r}^{\text{spe}} = N_{\text{side}} - c^{\text{pe}}$.

7.5 Slepian functions for HEALPix pixels

Slepian functions are computed from (2.62) in which the spectral coefficients are obtained as eigenvectors of the Slepian matrix \mathbf{K} in (2.60). From (2.53), elements of the Slepian matrix, given in (2.58), can be written as

$$K_{\ell m, pq}(r, c) = \sum_{m'=-\ell}^{\ell} F_{m', m}^{\ell} \sum_{q'=-p}^p F_{q', q}^p G_{mq, m'q'}(r, c), \quad (7.44)$$

where $F_{m',m}^\ell$ is given in (7.22),

$$G_{mq,m'q'}(r, c) = \int_{R(r,c)} e^{i(q-m)\phi} \sin \theta e^{i(m'+q')\theta} d\theta d\phi \quad (7.45)$$

is the Slepian sub-integral and $R(r,c)$ is the region bounded by the HEALPix pixel indexed by row index r and column index c .

7.5.1 North polar pixels

To speed up computation, we compute the Slepian matrix elements for the north polar pixels in the first longitudinal quadrant only, i.e., for $0 \leq \phi \leq \pi/2$. For pixels in the other three longitudinal quadrants, Slepian matrix elements are obtained from the matrix elements computed for the pixels in the first longitudinal quadrant. Hence for a north polar pixel with index $1 \leq \mathbf{p} \leq 2N_{\text{side}}(2N_{\text{side}} - 1)$, we get

$$\begin{aligned} K_{\ell m, pq}(r, c) &= \int_{R(r,c)} \overline{Y_\ell^m(\theta, \phi)} Y_p^q(\theta, \phi) \sin \theta d\theta d\phi \\ &= \int_{R(r, c^{\text{pz}})} (\mathcal{D}(0, 0, -\Delta\phi) \overline{Y_\ell^m} Y_p^q)(\theta, \phi) \sin \theta d\theta d\phi \\ &= \sum_{m'=-\ell}^{\ell} \overline{D_{m',m}^\ell(0, 0, -\Delta\phi)} \sum_{q'=-p}^p D_{q',q}^p(0, 0, -\Delta\phi) \int_{R(r, c^{\text{pz}})} \overline{Y_\ell^{m'}(\theta, \phi)} Y_p^{q'}(\theta, \phi) \sin \theta d\theta d\phi \\ &= e^{-i(m-q)\Delta\phi} K_{\ell m, pq}(r, c^{\text{pz}}), \end{aligned} \quad (7.46)$$

where we have used the spectral representation of rotated spherical harmonics in (4.6) along with the following identity

$$d_{m,n}^\ell(0) \triangleq \delta_{m,n}, \quad (7.47)$$

to obtain the final result, r and c are the row and column indices of the north polar pixel indexed by \mathbf{p} , c^{pz} is defined in (7.35) and $\Delta\phi$ is given in (7.37). Here $K_{\ell m, pq}(r, c^{\text{pz}})$ denote the Slepian matrix elements for the pixel which can be rotated into the pixel, with ring index \mathbf{p} , by an angle $\Delta\phi$ around the z -axis. Matrix elements $K_{\ell m, pq}(r, c^{\text{pz}})$

are computed using (7.44), in which the Slepian sub-integral is given by

$$G_{mq,m'q'}(r, c^{\text{pz}}) = \int_{\theta_{r-1}}^{\theta_r} \int_{\frac{\pi}{2} - \frac{\pi E_{ur}^{\text{pz}}}{a^{\text{pz}} \sin \frac{\theta}{2}}^{\frac{\pi}{2} - \frac{\pi E_{ur}^{\text{pz}}}{a^{\text{pz}} \sin \frac{\theta}{2}}} e^{i(q-m)\phi} \sin \theta e^{i(m'+q')\theta} d\phi d\theta + \int_{\theta_r}^{\theta_{r+1}} \int_{\frac{\pi}{2} - \frac{\pi E_{\ell r}^{\text{pz}}}{a^{\text{pz}} \sin \frac{\theta}{2}}^{\frac{\pi}{2} - \frac{\pi E_{\ell r}^{\text{pz}}}{a^{\text{pz}} \sin \frac{\theta}{2}}} e^{i(q-m)\phi} \sin \theta e^{i(m'+q')\theta} d\phi d\theta, \quad (7.48)$$

where we have used the pixel boundaries in (7.36) (with $\Delta\phi = 0$) to obtain the integration limits on ϕ and θ_r is the colatitude of the iso-latitude ring that the pixel is centered on, given by

$$\theta_r = \cos^{-1} \left(1 - \frac{r^2}{3N_{\text{side}}^2} \right), \quad 1 \leq r \leq N_{\text{side}} - 1. \quad (7.49)$$

We present an analytical expression for the Slepian sub-integral in (7.48) in the following theorem.

Theorem 8. *Let $G_{mq,m'q'}(r, c^{\text{pz}})$ be an integral of the form given in (7.48), where r is the row index of the pixel, c^{pz} is given by (7.35) in which c is the column index of the pixel, θ_r is the colatitude given in (7.49), and $a^{\text{pz}} = 2\sqrt{6}N_{\text{side}}$, $E_{ul}^{\text{pz}} = c^{\text{pz}} - 1$, $E_{\ell\ell}^{\text{pz}} = r - c^{\text{pz}} + 1$, $E_{\ell r}^{\text{pz}} = c^{\text{pz}}$, $E_{ur}^{\text{pz}} = r - c^{\text{pz}}$. Then,*

$$G_{mq,m'q'}(r, c^{\text{pz}}) = \begin{cases} \frac{-4e^{i\nu}}{(q-m)} \sum_{J_1=0}^{2|M|} \binom{2|M|}{J_1} (S_M i)^{J_1} \left(F^{\text{pz}}(J_1, M, A^{\text{pz}}, B^{\text{pz}}, \nu, \Gamma_u, \theta_{r-1}, \theta_r) - F^{\text{pz}}(J_1, M, D^{\text{pz}}, C^{\text{pz}}, \nu, \Gamma_l, \theta_r, \theta_{r+1}) \right), & m \neq q, \\ \frac{\pi}{2} \left(\frac{C_1(M, \theta_{r-1}, \theta_r) - C_1(M, \theta_r, \theta_{r+1})}{1-M^2} \right) + \frac{4}{1-4M^2} \times \\ \left(C_2\left(M, \frac{\pi E_{ul}^{\text{pz}}}{a^{\text{pz}}}, -\frac{\pi E_{ur}^{\text{pz}}}{a^{\text{pz}}}, \theta_{r-1}, \theta_r\right) + C_2\left(M, -\frac{\pi E_{\ell\ell}^{\text{pz}}}{a^{\text{pz}}}, \frac{\pi E_{\ell r}^{\text{pz}}}{a^{\text{pz}}}, \theta_r, \theta_{r+1}\right) \right), & m = q, M \neq \pm 1, \\ \frac{\pi}{2} \left(C_3(M, \theta_{r-1}, \theta_r) - C_3(M, \theta_r, \theta_{r+1}) \right) + \frac{4}{1-4M^2} \times \\ \left(C_2\left(M, \frac{\pi E_{ul}^{\text{pz}}}{a^{\text{pz}}}, -\frac{\pi E_{ur}^{\text{pz}}}{a^{\text{pz}}}, \theta_{r-1}, \theta_r\right) + C_2\left(M, -\frac{\pi E_{\ell\ell}^{\text{pz}}}{a^{\text{pz}}}, \frac{\pi E_{\ell r}^{\text{pz}}}{a^{\text{pz}}}, \theta_r, \theta_{r+1}\right) \right), & m = q, M = \pm 1, \end{cases} \quad (7.50)$$

where $M \triangleq m' + q'$, $\nu = (q - m)\pi/4$, the functions F^{pz} , C_1 , C_2 and C_3 are given by

$$\begin{aligned}
 F^{\text{pz}}(J_1, M, A, B, \nu, \Gamma_u, \theta_1, \theta_2) &= \sum_{J_2=0}^{\Gamma_u} \binom{|M| - J_1/2}{J_2} \frac{(-1)^{J_2}}{(J_1 + 2J_2 + 2)!} \times \\
 &\left(\sum_{J_3=0}^{(J_1+2J_2+1)} (-1)^{\lceil \frac{J_3+1}{2} \rceil} (J_1 + 2J_2 + 1 - J_3)! \left[(B)^{J_3} W_{(J_3 \bmod 2)}(J_1, J_2, J_3, B, \nu, \theta_1, \theta_2) - \right. \right. \\
 &\left. \left. (A)^{J_3} W_{(J_3 \bmod 2)}(J_1, J_2, J_3, A, -\nu, \theta_1, \theta_2) \right] \right) + (-1)^{\lfloor \frac{J_1+2J_2+2}{2} \rfloor} \left[(B)^{(J_1+2J_2+2)} \times \right. \\
 &\left. W_{(\mathbf{f}_{J_1, J_2})}(J_1, J_2, B, \nu, \theta_1, \theta_2) - (A)^{(J_1+2J_2+2)} W_{(\mathbf{f}_{J_1, J_2})}(J_1, J_2, A, -\nu, \theta_1, \theta_2) \right], \quad (7.51)
 \end{aligned}$$

$$\begin{aligned}
 C_1(M, \theta_1, \theta_2) &= \left[e^{iM\theta} (iM \sin \theta - \cos \theta) \right]_{\theta_1}^{\theta_2}, \\
 C_2(M, A, B, \theta_1, \theta_2) &= (B - A) \left[e^{iM\theta} \left(\sin \frac{\theta}{2} + 2iM \cos \frac{\theta}{2} \right) \right]_{\theta_1}^{\theta_2}, \quad (7.52) \\
 C_3(M, \theta_1, \theta_2) &= \left[-\frac{1}{4} \cos 2\theta + s_M \frac{i}{2} \theta - s_M \frac{i}{4} \sin 2\theta \right]_{\theta_1}^{\theta_2}.
 \end{aligned}$$

Here $\binom{2|M|}{J_1}$ is binomial coefficient, $\binom{|M| - J_1/2}{J_2}$ is generalized binomial coefficient, $\mathbf{f}_{J_1, J_2} = 2 + [(J_1 + 2J_2 + 3) \bmod 2]$, the constants are given by

$$\begin{aligned}
 A^{\text{pz}} &= \frac{\pi(q - m)E_{ul}^{\text{pz}}}{a^{\text{pz}}}, & B^{\text{pz}} &= -\frac{\pi(q - m)E_{ur}^{\text{pz}}}{a^{\text{pz}}}, \\
 C^{\text{pz}} &= -\frac{\pi(q - m)E_{\ell\ell}^{\text{pz}}}{a^{\text{pz}}}, & D^{\text{pz}} &= \frac{\pi(q - m)E_{\ell r}^{\text{pz}}}{a^{\text{pz}}},
 \end{aligned} \quad (7.53)$$

$$s_M = \begin{cases} 1, & M \geq 0, \\ -1, & M < 0, \end{cases} \quad (7.54)$$

summation limits, Γ_u for upper half and Γ_l for lower half of the pixel, are given by

$$\Gamma_u = \Gamma_l = \begin{cases} |M| - J_1/2, & J_1 \bmod 2 = 0, \\ \infty, & J_1 \bmod 2 = 1, \end{cases} \quad (7.55)$$

and the functions $W_{(\cdot)}(\cdot)$ are defined as

$$W_{(0)}(\mathbf{J}_1, \mathbf{J}_2, \mathbf{J}_3, w, v, \theta_1, \theta_2) = \left[\frac{\sin \left(w \csc \frac{\theta}{2} + v \right) - i(-1)^{J_3} \cos \left(w \csc \frac{\theta}{2} + v \right)}{\left(\csc \frac{\theta}{2} \right)^{(J_1+2J_2+2-J_3)}} \right]_{\theta_1}^{\theta_2}, \quad (7.56)$$

$$W_{(1)}(\mathbf{J}_1, \mathbf{J}_2, \mathbf{J}_3, w, v, \theta_1, \theta_2) = \left[\frac{\cos \left(w \csc \frac{\theta}{2} + v \right) - i(-1)^{J_3} \sin \left(w \csc \frac{\theta}{2} + v \right)}{\left(\csc \frac{\theta}{2} \right)^{(J_1+2J_2+2-J_3)}} \right]_{\theta_1}^{\theta_2}, \quad (7.57)$$

$$W_{(2)}(\mathbf{J}_1, \mathbf{J}_2, w, v, \theta_1, \theta_2) = C_i(w, v, \theta_1, \theta_2) - i(-1)^{(J_1+2J_2+2)} S_i(w, v, \theta_1, \theta_2), \quad (7.58)$$

$$W_{(3)}(\mathbf{J}_1, \mathbf{J}_2, w, v, \theta_1, \theta_2) = S_i(w, v, \theta_1, \theta_2) - i(-1)^{(J_1+2J_2+2)} C_i(w, v, \theta_1, \theta_2), \quad (7.59)$$

where the functions $S_i(w, v, \theta_1, \theta_2)$ and $C_i(w, v, \theta_1, \theta_2)$ are given by the following expressions

$$S_i(w, v, \theta_1, \theta_2) = \begin{cases} \cos v T_S \left(w, \csc \left(\frac{\theta_1}{2} \right), \csc \left(\frac{\theta_2}{2} \right) \right) + \\ \quad \sin v T_C \left(w, \csc \left(\frac{\theta_1}{2} \right), \csc \left(\frac{\theta_2}{2} \right) \right), & w \neq 0, \\ \sin v \ln \left(\frac{\csc(\theta_2/2)}{\csc(\theta_1/2)} \right), & w = 0, \end{cases} \quad (7.60)$$

$$C_i(w, v, \theta_1, \theta_2) = \begin{cases} \cos v T_C \left(w, \csc \left(\frac{\theta_1}{2} \right), \csc \left(\frac{\theta_2}{2} \right) \right) - \\ \quad \sin v T_S \left(w, \csc \left(\frac{\theta_1}{2} \right), \csc \left(\frac{\theta_2}{2} \right) \right), & w \neq 0, \\ \cos v \ln \left(\frac{\csc(\theta_2/2)}{\csc(\theta_1/2)} \right), & w = 0, \end{cases} \quad (7.61)$$

in which T_S and T_C are the Maclaurin series expansions of the sine and cosine inte-

grals, i.e.,

$$T_S(w, u_1, u_2) = \sum_{k_S=0}^{\infty} \frac{(-1)^{k_S} w^{2k_S+1}}{(2k_S+1)!} \left(\frac{u_2^{2k_S+1} - u_1^{2k_S+1}}{2k_S+1} \right), \quad (7.62)$$

$$T_C(w, u_1, u_2) = \ln \left(\frac{u_2}{u_1} \right) + \sum_{k_C=1}^{\infty} \frac{(-1)^{k_C} w^{2k_C}}{(2k_C)!} \left(\frac{u_2^{2k_C} - u_1^{2k_C}}{2k_C} \right). \quad (7.63)$$

Proof. See Appendix C for the proof of Theorem 8 and Section 7.7 for convergence criterion of the infinite series expansions. \square

7.5.2 Equatorial pixels (centered either above or at equator)

We take advantage of the rotational symmetry of the equatorial pixels centered on a given iso-latitude ring and compute the Slepian matrix for only the first pixel in an iso-latitude ring (i.e., the pixel with column index $c = 1$). Slepian matrix for an equatorial pixel, centered above or at equator, with row index r and column index $c > 1$ is then obtained as

$$\begin{aligned} K_{\ell m, pq}(r, c) &= \int_{R_{(r,c)}} \overline{Y_{\ell}^m(\theta, \phi)} Y_p^q(\theta, \phi) \sin \theta d\theta d\phi \\ &= \int_{R_{(r,1)}} \left(\mathcal{D} \left(0, 0, \frac{\pi(1-c)}{2N_{\text{side}}} \right) \overline{Y_{\ell}^m} Y_p^q \right) (\theta, \phi) \sin \theta d\theta d\phi \\ &= \sum_{m'=-\ell}^{\ell} \overline{D_{m',m}^{\ell} \left(0, 0, \frac{\pi(1-c)}{2N_{\text{side}}} \right)} \sum_{q'=-p}^p D_{q',q}^p \left(0, 0, \frac{\pi(1-c)}{2N_{\text{side}}} \right) \times \\ &\quad \int_{R_{(r,1)}} \overline{Y_{\ell}^{m'}(\theta, \phi)} Y_p^{q'}(\theta, \phi) \sin \theta d\theta d\phi \\ &= e^{\frac{-i(m-q)\pi(c-1)}{2N_{\text{side}}}} K_{\ell m, pq}(r, 1), \end{aligned} \quad (7.64)$$

where $R_{(r,1)}$ is the region bounded by the pixel with row index r and column index 1, $\pi(c-1)/2N_{\text{side}}$ is the rotational symmetry between the pixels with same row indices and columns indices c and 1 respectively, and we have used (4.6), (7.47) to obtain the final result. Slepian matrix elements $K_{\ell m, pq}(r, 1)$ are computed from (7.44) in which

the Slepian sub-integral is given by

$$\begin{aligned}
 G_{mq,m'q'}(r, 1) = & \int_{\theta_{r-1}}^{\theta_r} \int_{\left(\cos \theta - \frac{2}{3} + \frac{4E^{\text{ez}}}{3N_{\text{side}}}\right)/b}^{\left(\frac{2}{3} - \frac{4E^{\text{ez}}}{3N_{\text{side}}} - \cos \theta\right)/b} e^{i(q-m)\phi} \sin \theta e^{i(m'+q')\theta} d\phi d\theta + \\
 & \int_{\theta_r}^{\theta_{r+1}} \int_{\left(\frac{2}{3} - \frac{4E^{\text{ez}}}{3N_{\text{side}}} - \cos \theta\right)/b}^{\left(\cos \theta - \frac{2}{3} + \frac{4E^{\text{ez}}}{3N_{\text{side}}}\right)/b} e^{i(q-m)\phi} \sin \theta e^{i(m'+q')\theta} d\phi d\theta, \quad (7.65)
 \end{aligned}$$

where (7.39) have been used to obtain the integration limits on ϕ and

$$\theta_r = \cos^{-1} \left(\frac{2}{3} \left(1 - \frac{r}{N_{\text{side}}} \right) \right), \quad 1 \leq r \leq 2N_{\text{side}} - 1 \quad (7.66)$$

is the colatitude of the iso-latitude ring that the pixel is centered on. Analytical expression for the Slepian sub-integral in (7.65) is presented in the following theorem.

Theorem 9. *Let $G_{mq,m'q'}(r, 1)$ be an integral of the form given in (7.65), where r is the row index of the pixel and θ_r is the colatitude given in (7.66). Then,*

$$\begin{aligned}
 G_{mq,m'q'}(r, 1) = & \left\{ \begin{aligned} & \frac{2}{(q-m)} \sum_{J_1=0}^{|M|} \binom{|M|}{J_1} (s_M i)^{J_1} \left(F^{\text{ez}}(J_1, M, A^{\text{ez}}, B^{\text{ez}}, \mu, \Gamma_u, \theta_{r-1}, \theta_r) \right. \\ & \quad \left. - F^{\text{ez}}(J_1, M, D^{\text{ez}}, C^{\text{ez}}, \mu, \Gamma_l, \theta_r, \theta_{r+1}) \right), \quad m \neq q, \\ & \frac{1}{b(1-M^2)} [C_4(M, A^{\text{ez}}, B^{\text{ez}}, \theta_{r-1}, \theta_r) - C_4(M, C^{\text{ez}}, D^{\text{ez}}, \theta_r, \theta_{r+1})] \\ & - \frac{2}{b(4-M^2)} [C_5(M, \theta_{r-1}, \theta_r) - C_5(M, \theta_r, \theta_{r+1})], \quad m = q, M \neq \pm 1, \pm 2, \\ & \frac{1}{b} [C_6(M, A^{\text{ez}}, B^{\text{ez}}, \theta_{r-1}, \theta_r) - C_6(M, C^{\text{ez}}, D^{\text{ez}}, \theta_r, \theta_{r+1})] \\ & - \frac{2}{b(4-M^2)} [C_5(M, \theta_{r-1}, \theta_r) - C_5(M, \theta_r, \theta_{r+1})], \quad m = q, M = \pm 1, \\ & \frac{1}{b(1-M^2)} [C_4(M, A^{\text{ez}}, B^{\text{ez}}, \theta_{r-1}, \theta_r) - C_4(M, C^{\text{ez}}, D^{\text{ez}}, \theta_r, \theta_{r+1})] \\ & - \frac{1}{b} [C_7(M, \theta_{r-1}, \theta_r) + C_7(M, \theta_r, \theta_{r+1})], \quad m = q, M = \pm 2, \end{aligned} \right. \quad (7.67)
 \end{aligned}$$

where $M \triangleq m' + q'$, $\mu = (q - m)/b$ and functions F^{ez} , C_4 , C_5 , C_6 , C_7 are given by

$$\begin{aligned}
 F^{\text{ez}}(J_1, M, A, B, \mu, \Gamma_u, \theta_1, \theta_2) &= e^{\frac{i\mu}{2}(B-A)} \sum_{J_2=0}^{\Gamma_u} \binom{J_1/2}{J_2} (-1)^{J_2} \times \\
 &\sum_{J_3=1}^{(2J_2+|M|-J_1+1)} (-1)^{\lceil \frac{J_3+1}{2} \rceil} \mu^{-J_3} \frac{(2J_2 + |M| - J_1)!}{(2J_2 + |M| - J_1 + 1 - J_3)!} \times \\
 &\begin{cases} [(\cos \theta)^{(2J_2+|M|-J_1+1-J_3)} \cos(\mu(\cos \theta - \frac{A+B}{2}))]_{\theta_1}^{\theta_2}, & J_3 \text{ odd,} \\ [(\cos \theta)^{(2J_2+|M|-J_1+1-J_3)} \sin(\mu(\cos \theta - \frac{A+B}{2}))]_{\theta_1}^{\theta_2}, & J_3 \text{ even,} \end{cases} \quad (7.68)
 \end{aligned}$$

$$\begin{aligned}
 C_4(M, A, B, \theta_1, \theta_2) &= (A + B) \left[e^{iM\theta} (iM \sin \theta - \cos \theta) \right]_{\theta_1}^{\theta_2}, \\
 C_5(M, \theta_1, \theta_2) &= \left[e^{iM\theta} \left(\frac{iM}{2} \sin 2\theta - \cos 2\theta \right) \right]_{\theta_1}^{\theta_2}, \\
 C_6(M, A, B, \theta_1, \theta_2) &= (A + B) \left[-\frac{1}{4} \cos 2\theta + s_M \frac{i}{2} \theta - s_M \frac{i}{4} \sin 2\theta \right]_{\theta_1}^{\theta_2}, \\
 C_7(M, \theta_1, \theta_2) &= \left[-\frac{1}{8} \cos 4\theta + s_M \frac{i}{2} \theta - s_M \frac{i}{8} \sin 4\theta \right]_{\theta_1}^{\theta_2}. \quad (7.69)
 \end{aligned}$$

Here, $\binom{|M|}{J_1}$ is binomial coefficient, $\binom{J_1/2}{J_2}$ is generalized binomial coefficient,

$$s_M = \begin{cases} 1, & M \geq 0, \\ -1, & M < 0, \end{cases} \quad (7.70)$$

and the constants are defined by pixel parameters, i.e.,

$$\begin{aligned}
 A^{\text{ez}} &= \frac{2}{3} - E_{ul}^{\text{ez}} a^{\text{ez}}, & B^{\text{ez}} &= \frac{2}{3} - E_{ur}^{\text{ez}} a^{\text{ez}}, \\
 C^{\text{ez}} &= \frac{2}{3} - E_{\ell\ell}^{\text{ez}} a^{\text{ez}}, & D^{\text{ez}} &= \frac{2}{3} - E_{lr}^{\text{ez}} a^{\text{ez}}, \quad (7.71)
 \end{aligned}$$

for $a^{\text{ez}} = 4/3N_{\text{side}}$, $b = 8/3\pi$, $E_{ul}^{\text{ez}} = c^{\text{ez}} - 1$, $E_{\ell\ell}^{\text{ez}} = r - (c^{\text{ez}} - 1)$, $E_{lr}^{\text{ez}} = c^{\text{ez}}$, $E_{ur}^{\text{ez}} = r - c^{\text{ez}}$ and $c^{\text{ez}} = 1 + \lfloor r/2 \rfloor$. The summation limits Γ_u and Γ_l (for the upper and lower halves of the pixel respectively) are given by

$$\Gamma_u = \Gamma_l = \begin{cases} J_1/2, & J_1 \bmod 2 = 0, \\ \infty, & J_1 \bmod 2 = 1. \end{cases} \quad (7.72)$$

Proof. See Appendix C for the proof of Theorem 9 and Section 7.7 for convergence criterion of the infinite series expansion. \square

Remark 10. An alternative formulation of the Slepian sub-integral $G_{mq,m'q'}(r, 1)$ in (7.67), for the case when $m \neq q$, can be obtained as

$$\begin{aligned} G_{mq,m'q'}(r, 1) = & F^{\text{ez}}(B^{\text{ez}}, M, b, -\mu, \theta_{r-1}, \theta_r) - F^{\text{ez}}(A^{\text{ez}}, M, b, \mu, \theta_{r-1}, \theta_r) + \\ & F^{\text{ez}}(D^{\text{ez}}, M, b, \mu, \theta_r, \theta_{r+1}) - F^{\text{ez}}(C^{\text{ez}}, M, b, -\mu, \theta_r, \theta_{r+1}), \end{aligned} \quad (7.73)$$

for $M \triangleq m' + q'$, $\mu = (q - m)/b$ and

$$\begin{aligned} F^{\text{ez}}(A, M, b, \mu, \theta_1, \theta_2) = & \frac{(\theta_1 - \theta_2)}{2b\mu} e^{-i\mu A} \left(i^{M+1} J_{M+1}(\mu) * \varepsilon(M+1; \theta_1, \theta_2) - \right. \\ & \left. i^{M-1} J_{M-1}(\mu) * \varepsilon(M-1; \theta_1, \theta_2) \right), \end{aligned} \quad (7.74)$$

where $J_M(\mu)$ is the Bessel function of first kind and order M , evaluated at μ , $*$ denotes the Euclidean domain convolution,

$$\varepsilon(M; \theta_1, \theta_2) = e^{iM\left(\frac{\theta_1 + \theta_2}{2}\right)} \text{sinc} \left[M \left(\frac{\theta_2 - \theta_1}{2} \right) \right], \quad (7.75)$$

and

$$\text{sinc}(x) \triangleq \sin x/x \quad (7.76)$$

is the sinc function. We refer the reader to Appendix C for the derivation of (7.73) and for details on computing the convolution of $J_M(\mu)$ and $\varepsilon(M, \theta_1, \theta_2)$. In the rest of this work, we use the results in Theorem 9 to compute the Slepian sub-integral for equatorial pixels.

7.5.3 North polar-equatorial pixels

North polar-equatorial pixels are located at the boundary of north polar and equatorial zones, i.e., their upper and lower halves are located in the north polar and equatorial zones respectively. Exploiting the rotational symmetry between pixels, Slepian matrix is computed for pixels with column index $c \leq N_{\text{side}}$. For a pixel with column index $c > N_{\text{side}}$, Slepian matrix elements are given by

$$\begin{aligned} K_{\ell m, pq}(r, c) &= \int_{R(r, c)} \overline{Y_\ell^m(\theta, \phi)} Y_p^q(\theta, \phi) \sin \theta d\theta d\phi \\ &= \int_{R(r, c^{\text{pe}})} (\mathcal{D}(0, 0, -\Delta\phi) \overline{Y_\ell^m} Y_p^q)(\theta, \phi) \sin \theta d\theta d\phi = e^{-i(m-q)\Delta\phi} K_{\ell m, pq}(r, c^{\text{pe}}), \quad r = 1, \end{aligned} \quad (7.77)$$

where again (4.6), (7.47) have been used to obtain the final result, c is the column index of the pixel, c^{pe} is defined in (7.41), and $\Delta\phi$, given in (7.37), is the rotational symmetry between pixels with column indices c and c^{pe} . Since, north polar-equatorial pixels are shared between the north polar and equatorial zones, we can use the results presented in Theorem 8 and Theorem 9 to compute the Slepian matrix elements $K_{\ell m, pq}(r, c^{\text{pe}})$ from (7.44), by formulating the Slepian sub-integral as

$$\begin{aligned} G_{mq, m'q'}(r, c^{\text{pe}}) &= \int_{\theta_{r-1}}^{\theta_r} \int_{\frac{\frac{\pi}{2} + \frac{B^{\text{nppe}}}{(q-m)\sin\frac{\theta}{2}}}{\frac{A^{\text{nppe}}}{(q-m)\sin\frac{\theta}{2}}} e^{i(q-m)\phi} \sin \theta e^{iM\theta} d\phi d\theta + \\ &\quad \int_{\theta_r}^{\theta_{r+1}} \int_{\frac{(C^{\text{nppe}} - \cos \theta)}{b}}^{\frac{(\cos \theta - D^{\text{nppe}})}{b}} e^{i(q-m)\phi} \sin \theta e^{i(m'+q')\theta} d\phi d\theta, \quad r = 1, \end{aligned} \quad (7.78)$$

where

$$\theta_k = \begin{cases} \cos^{-1} \left(1 - \frac{(N_{\text{side}}-1)^2}{3N_{\text{side}}^2} \right), & k = r - 1, \\ \cos^{-1} \left(\frac{2}{3} \right), & k = r, \\ \cos^{-1} \left(\frac{2}{3} \left(1 - \frac{1}{N_{\text{side}}} \right) \right), & k = r + 1, \end{cases} \quad (7.79)$$

and the constants are given by

$$\begin{aligned} A^{\text{npe}} &= \frac{\pi(q-m)E_{ul}^{\text{npe}}}{a^{\text{pz}}}, & B^{\text{npe}} &= -\frac{\pi(q-m)E_{ur}^{\text{npe}}}{a^{\text{pz}}}, \\ C^{\text{npe}} &= \frac{2}{3} - E_{\ell\ell}^{\text{npe}}a^{\text{ez}}, & D^{\text{npe}} &= \frac{2}{3} - E_{\ell r}^{\text{npe}}a^{\text{ez}}, \end{aligned} \quad (7.80)$$

for pixel parameters b , a^{pz} , a^{ez} , E_{ul}^{npe} , E_{ur}^{npe} , $E_{\ell\ell}^{\text{npe}}$ and $E_{\ell r}^{\text{npe}}$ defined in Section 7.4.1. We note that A^{npe} , B^{npe} and C^{npe} , D^{npe} are defined in a similar way as in Theorem 8 and Theorem 9 respectively. Hence, the first and second integral in (7.78) correspond to the first integral in (7.48) and second integral in (7.65). Therefore, an analytical expression for the Slepian sub-integral in (7.78) can be directly obtained from Theorem 8 and Theorem 9 as

$$\begin{aligned} G_{mq,m'q'}(1, c^{\text{pe}}) &= \\ &\left\{ \begin{aligned} &\frac{-4e^{i\nu}}{(q-m)} \sum_{J_1=0}^{2|M|} \binom{2|M|}{J_1} (s_M i)_{J_1}^J F^{\text{pz}}(J_1, M, A^{\text{npe}}, B^{\text{npe}}, \nu, \Gamma_u, \theta_0, \theta_1) - \\ &\frac{2}{(q-m)} \sum_{J_1=0}^{|M|} \binom{|M|}{J_1} (s_M i)_{J_1}^{J_1} F^{\text{ez}}(J_1, M, D^{\text{npe}}, C^{\text{npe}}, \mu, \Gamma_l, \theta_1, \theta_2), & m \neq q, \\ &\frac{\pi}{2(1-M^2)} C_1(M, \theta_0, \theta_1) + \frac{2}{b(4-M^2)} C_5(M, \theta_1, \theta_2) + \\ &\frac{4}{(1-4M^2)} C_2\left(M, \frac{\pi E_{ul}^{\text{npe}}}{a^{\text{pz}}}, -\frac{\pi E_{ur}^{\text{npe}}}{a^{\text{pz}}}, \theta_0, \theta_1\right) - \\ &\frac{1}{b(1-M^2)} C_4(M, C^{\text{npe}}, D^{\text{npe}}, \theta_1, \theta_2), & m = q, M \neq \pm 1, \pm 2, \\ &\frac{\pi}{2} C_3(M, \theta_0, \theta_1) + \frac{2}{b(4-M^2)} C_5(M, \theta_1, \theta_2) + \\ &\frac{4}{(1-4M^2)} C_2\left(M, \frac{\pi E_{ul}^{\text{npe}}}{a^{\text{pz}}}, -\frac{\pi E_{ur}^{\text{npe}}}{a^{\text{pz}}}, \theta_0, \theta_1\right) \\ &-\frac{1}{b} C_6(M, C^{\text{npe}}, D^{\text{npe}}, \theta_1, \theta_2), & m = q, M = \pm 1, \\ &\frac{\pi}{2(1-M^2)} C_1(M, \theta_0, \theta_1) + \frac{1}{b} C_7(M, \theta_1, \theta_2) + \\ &\frac{4}{(1-4M^2)} C_2\left(M, \frac{\pi E_{ul}^{\text{npe}}}{a^{\text{pz}}}, -\frac{\pi E_{ur}^{\text{npe}}}{a^{\text{pz}}}, \theta_0, \theta_1\right) \\ &-\frac{1}{b(1-M^2)} C_4(M, C^{\text{npe}}, D^{\text{npe}}, \theta_1, \theta_2), & m = q, M = \pm 2, \end{aligned} \right. \quad (7.81) \end{aligned}$$

where F^{pz} , M , ν , s_M , Γ_u , C_1 , C_2 , C_3 are given in Theorem 8 and F^{ez} , μ , Γ_l , C_4 , C_5 , C_6 , C_7 are given in Theorem 9.

7.5.4 Pixels centered below equator

From (2.18), we note that $P_\ell^m(-z) = (-1)^{\ell+m} P_\ell^m(z)$. Hence, spherical harmonics for the diametrically opposite (antipodal) pixels satisfy the following relation

$$Y_\ell^m(\pi - \theta, \pi + \phi) = (-1)^\ell Y_\ell^m(\theta, \phi), \quad (7.82)$$

where $(\pi - \theta, \pi + \phi)$ is antipodal to a point (θ, ϕ) on the sphere. Since every pixel in the southern hemisphere is diametrically opposite to some pixel in the northern hemisphere, we can use the indexing in (7.32), (7.33) and (7.34) to directly find the Slepian matrix elements for the southern equatorial, south polar and south polar-equatorial pixels as

$$\begin{aligned} K_{\ell m, pq}(r^{\text{eq,S}}, c^{\text{eq,S}}) &= (-1)^{\ell+p} K_{\ell m, pq}(r^{\text{eq,N}}, c^{\text{eq,N}}), \\ K_{\ell m, pq}(r^{\text{p,S}}, c^{\text{p,S}}) &= (-1)^{\ell+p} K_{\ell m, pq}(r^{\text{p,N}}, c^{\text{p,N}}), \\ K_{\ell m, pq}(r^{\text{pe,S}}, c^{\text{pe,S}}) &= (-1)^{\ell+p} K_{\ell m, pq}(r^{\text{pe,N}}, c^{\text{pe,N}}), \end{aligned} \quad (7.83)$$

where $K_{\ell m, pq}(r^{\text{eq,N}}, c^{\text{eq,N}})$, $K_{\ell m, pq}(r^{\text{p,N}}, c^{\text{p,N}})$ and $K_{\ell m, pq}(r^{\text{pe,N}}, c^{\text{pe,N}})$ are the Slepian matrix elements for the northern equatorial, north polar and north polar-equatorial pixels, given in (7.64), (7.46) and (7.77) respectively.

7.6 Multiscale dictionary of Slepian functions for HEALPix

We compute spectral coefficients of the Slepian functions as eigenvectors of the Slepian matrix using the formulations given in Section 7.5.1, Section 7.5.2, Section 7.5.3 and Section 7.5.4 for north polar pixels, equatorial pixels, north-polar-equatorial pixels and pixels centered below equator respectively, at different resolutions of HEALPix partitioning scheme. As in Section 7.1.5, we associate a quaternary tree structure with HEALPix, in which tree levels and tree height are denoted by h_T and \mathfrak{H} respectively. Root node, at tree level $h_T = 0$, represents the whole sphere. Every node in the tree,

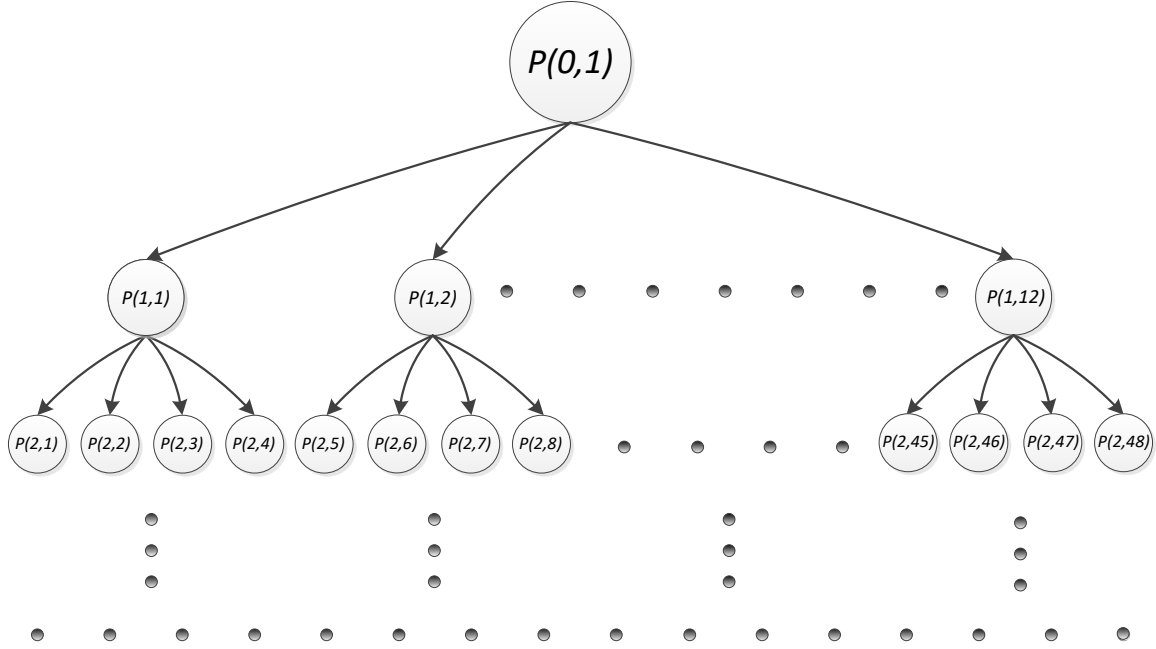


Figure 7-12: Quaternary tree representation for HEALPix scheme. Each node is represented as $P(h_T, i_{h_T})$ where $h_T \in [0, \mathfrak{H}]$ is the tree level and i_{h_T} is the index of the node at tree level h_T . \mathfrak{H} is the maximum tree level, called height of the tree.

at tree level $h_T \geq 1$, represents one of the HEALPix pixels at resolution given by

$$\begin{aligned} N_{\text{side}} &= 2^{h_T-1}, \quad h_T \geq 1, \\ h_T &= 1 + \log_2 N_{\text{side}}. \end{aligned} \quad (7.84)$$

Height of the tree is the maximum tree level, which relates to the maximum HEALPix resolution $N_{\text{side}}^{\text{max}}$ as

$$\mathfrak{H} = 1 + \log_2 N_{\text{side}}^{\text{max}}, \quad \mathfrak{H} \geq 1. \quad (7.85)$$

At a given tree level $h_T \geq 1$, there are $12N_{\text{side}}^2 = 3(4^{h_T})$ nodes which are indexed by i_{h_T} as

$$i_{h_T} = \begin{cases} 1, & h_T = 0, \\ 1, 2, \dots, 3(4^{h_T}), & 1 \leq h_T \leq \mathfrak{H}. \end{cases} \quad (7.86)$$

As before, each node is labeled as $P(h_T, i_{h_T})$, i.e., by its tree level and its index at that tree level. Given a parent node, denoted by $P(h_T, i_{h_T})$, its four child nodes in the tree can be found as $P(h_T + 1, k)$, $4i_{h_T} - 3 \leq k \leq 4i_{h_T}$. Total number of nodes in the quaternary tree is given by

$$n_P = 1 + \sum_{h_T=1}^5 3(4^{h_T}) = 4^{(5+1)} - 3. \quad (7.87)$$

Since nodes in the quaternary tree represent HEALPix pixels at resolution given by (7.84), we can relate cardinality of the reduced Slepian basis set, i.e., the spherical Shannon number, with the tree level as

$$N_{h_T} = \frac{A_{h_T} L^2}{4\pi} = \frac{L^2}{3(4^{h_T})}, \quad h_T \geq 1, \quad (7.88)$$

where

$$A_{h_T} = \frac{4\pi}{3(4^{h_T})}, \quad h_T \geq 1 \quad (7.89)$$

is the area of the pixel represented by a node at tree level h_T .

7.6.1 Construction of overcomplete multiscale dictionary

To facilitate multiresolution analysis, i.e., signal analysis at different scales on the sphere, we associate L^2 number of orthonormal vectors (which are spectral representations of spherical harmonic basis functions) with the root node at $h_T = 0$ and N_{SF} number of spectral representations of well-optimally concentrated Slepian functions, computed as eigenvectors of (2.60), with each of the nodes in the quaternary tree at tree levels $h_T \geq 1$. Set of all such spectral representations, associated with all the nodes in the tree, makes an overcomplete multiscale dictionary \mathfrak{D} , which is given by,

$$\mathfrak{D} = \left[\mathbf{d}_{1,1}^0, \mathbf{d}_{1,2}^0, \dots, \mathbf{d}_{1,L^2}^0, \mathbf{d}_{1,1}^1, \mathbf{d}_{1,2}^1, \dots, \mathbf{d}_{1,N_{\text{SF}}}^1, \dots, \right. \\ \left. \mathbf{d}_{1,1}^5, \mathbf{d}_{1,2}^5, \dots, \mathbf{d}_{1,N_{\text{SF}}}^5, \dots, \mathbf{d}_{3(4^5),1}^5, \dots, \mathbf{d}_{3(4^5),N_{\text{SF}}}^5 \right], \quad (7.90)$$

Table 7.4: Height of the HEALPix quaternary tree along with maximum HEALPix resolution, for fixed N_{SF} , at different values of bandlimit L and N_{SF} .

Bandlimit, L	N_{SF}	Tree height, \mathfrak{H}	N_{side}^{\max}
4	1	1	1
8	3	1	1
16	5	2	2
32	7	2	2
64	8	3	4
128	9	4	8
256	10	5	16

where, as before, $\mathbf{d}_{i_{h_{\text{T}}}, \alpha}^{h_{\text{T}}}$ is \mathbf{g}_{α} computed from (2.60) for the pixel represented by the node at tree level h_{T} and index $i_{h_{\text{T}}}$. Size of the dictionary $n_{\mathfrak{D}}$ depends on the number of spectral eigenvectors \mathbf{g}_{α} for each node in the quaternary tree, i.e., N_{SF} , which again can be chosen in the following two ways.

Fixed N_{SF} for each tree node

We can associate a fixed number of localized Slepian functions with each of the nodes in the HEALPix quaternary tree by keeping N_{SF} constant for all the nodes in the tree. Hence, from (7.88), we observe that the number of well-optimally concentrated Slepian functions for nodes at tree level $h_{\text{T}} = \mathfrak{H}$ should be greater than N_{SF} , i.e., $N_{\text{SF}} \leq N_{\mathfrak{H}}$, from which we obtain

$$\mathfrak{H} \leq \frac{1}{2} \log_2 \left(\frac{L^2}{3N_{\text{SF}}} \right) \triangleq \left\lfloor \frac{1}{2} \log_2 \left(\frac{L^2}{3N_{\text{SF}}} \right) \right\rfloor, \quad (7.91)$$

where again we have chosen \mathfrak{H} to be the greatest integer which is smaller than or equal to $(1/2) \log_2(L^2/(3N_{\text{SF}}))$. Since \mathfrak{H} has to be positive, we note that

$$N_{\text{SF}} \leq \frac{L^2}{12}. \quad (7.92)$$

Hence, given the bandlimit L , N_{SF} can be chosen to be any number as long as the inequality in (7.92) is satisfied. From (7.87), it can be seen that size of the resulting

dictionary is given by

$$n_{\mathfrak{D}} = L^2 + N_{\text{SF}}(4^{(\mathfrak{H}+1)} - 4). \quad (7.93)$$

Table 7.4 lists some values of the tree height \mathfrak{H} and maximum HEALPix resolution for different values of N_{SF} and bandlimit L .

Varying N_{SF} for nodes at different tree levels

Instead of choosing constant N_{SF} for all the nodes in the tree, we can vary N_{SF} across tree levels by choosing it equal to spherical Shannon number for pixels represented by the nodes at a given tree level, h_{T} , i.e.,

$$N_{\text{SF}} = N_{h_{\text{T}}} = \frac{L^2}{3(4^{h_{\text{T}}})}, \quad h_{\text{T}} \geq 1. \quad (7.94)$$

Now height of the tree should be such that $N_{\mathfrak{H}} \geq 1$, which gives

$$\begin{aligned} \mathfrak{H} &\leq \frac{1}{2} \log_2 \left(\frac{L^2}{3} \right), \\ \mathfrak{H} &\triangleq \left\lfloor \frac{1}{2} \log_2 \left(\frac{L^2}{3} \right) \right\rfloor, \quad \mathfrak{H} \geq 1, \end{aligned} \quad (7.95)$$

where again we have chosen \mathfrak{H} to be the greatest integer which is smaller than or equal to $(1/2) \log_2(L^2/3)$. Size of the resulting dictionary is then given by

$$n_{\mathfrak{D}} = L^2 + \sum_{h_{\text{T}}=1}^{\mathfrak{H}} N_{h_{\text{T}}} 3(4^{h_{\text{T}}}) = (\mathfrak{H} + 1)L^2. \quad (7.96)$$

Table 7.5 lists some values of the tree height \mathfrak{H} and maximum HEALPix resolution for different values of bandlimit L under this scheme.

Remark 11. *We note that spherical Shannon number at tree level h_{T} , i.e., $N_{h_{\text{T}}}$, may differ from (7.88) when rounded to the nearest integer, due to which, the actual size of the dictionary may be different from that given in (7.96).*

Table 7.5: Height of the HEALPix quaternary tree along with maximum HEALPix resolution, for varying N_{SF} , at different bandlimits L .

Bandlimit, L	Tree height, \mathfrak{H}	$N_{\text{side}}^{\text{max}}$
4	1	1
8	2	2
16	3	4
32	4	8
64	5	16
128	6	32
256	7	64

7.7 Numerical considerations

Analytical formulations of the Slepian sub-integrals for the polar, equatorial and polar-equatorial pixels, presented in Section 7.5, depend on infinite series expansions. In this section, we present convergence criteria to truncate such expansions for the accurate computation of Slepian sub-integrals.

7.7.1 Generalized binomial series expansions

Generalized binomial series expansion in (C.9) indexed by J_2 is infinite when J_1 is odd, as can be seen from (7.55). Considering the integral in (C.10), infinite series indexed by J_2 is terminated at Γ_u , for each odd value of J_1 at a given M , when

$$\left| 4 \times 2 \times 2\sqrt{2}|M| \binom{2|M|}{J_1} \binom{|M| - \frac{J_1}{2}}{\Gamma_u} u_r^{(-J_1 - 2\Gamma_u - 2)} \right| \leq \text{tol}, \quad \Gamma_u > J_2^{\text{pz}_o}, \quad (7.97)$$

for the upper half of the north polar pixel, i.e., $\theta_{r-1} \leq \theta \leq \theta_r$, where $u \triangleq \csc(\theta/2)$, tol is a preset tolerance and $J_2^{\text{pz}_o}$ is determined by the maximum value of the generalized binomial coefficient $\binom{|M| - J_1/2}{J_2}$, i.e.,

$$J_2^{\text{pz}_o} = \begin{cases} \lceil |M|/2 - J_1/4 \rceil, & |M| - J_1/2 + 0.5 \text{ even,} \\ \lfloor |M|/2 - J_1/4 \rfloor, & |M| - J_1/2 + 0.5 \text{ odd.} \end{cases} \quad (7.98)$$

The truncation criterion in (7.97) estimates the integral (over the upper half of the pixel) in (C.10) by an upper bound, given by

$$2\sqrt{2} \int_{u_{r-1}}^{u_r} \frac{1}{u^{(J_1+2\Gamma_u+3)}} du < 2\sqrt{2} \frac{1}{u_r^{(J_1+2\Gamma_u+2)}}, \quad (7.99)$$

where the factor of $2\sqrt{2}$ is an upper bound on the magnitude of the trigonometric term in the integrand in (C.10). Moreover, for each value of M , there are $|M|$ odd values for the summation index J_1 and hence, a factor of $|M|$ is included in (7.97) to ensure that the compounded error is within the preset tolerance.

Similarly, for the lower half of the pixel, i.e., $\theta_r \leq \theta \leq \theta_{r+1}$, infinite series indexed by J_2 in (C.10) is terminated at Γ_l when

$$\left| 4 \times 2 \times 2\sqrt{2}|M| \binom{2|M|}{J_1} \binom{|M| - \frac{J_1}{2}}{\Gamma_l} u_{r+1}^{(-J_1-2\Gamma_l-2)} \right| \leq \text{tol}, \quad \Gamma_l > J_2^{\text{pzo}}, \quad (7.100)$$

where the integral in (C.10), over lower half of the pixel, has been estimated by the following upper bound

$$2\sqrt{2} \int_{u_r}^{u_{r+1}} \frac{1}{u^{(J_1+2\Gamma_l+3)}} du < 2\sqrt{2} \frac{1}{u_{r+1}^{(J_1+2\Gamma_l+2)}}. \quad (7.101)$$

An additional factor of 2 in (7.97) and (7.100) takes into account the compounding effect of the truncation for the upper and lower halves of the pixel respectively.

For the equatorial pixels, generalized binomial series expansion in (C.27) has an infinite series indexed by J_2 for each odd value of J_1 at a given M , as can be seen from (7.72), which, considering the integral in (C.29), is terminated at Γ_u and Γ_l , for the upper and lower halves of the pixel respectively, when

$$\begin{aligned} \left| 2 \times 2 \times \left\lceil \frac{|M|}{2} \right\rceil \binom{|M|}{J_1} \binom{J_1/2}{\Gamma_u} u_{r-1}^{(2\Gamma_u+|M|-J_1+1)} \right| &\leq \text{tol}, \quad \Gamma_u > J_2^{\text{ezo}}, \\ \left| 2 \times 2 \times \left\lceil \frac{|M|}{2} \right\rceil \binom{|M|}{J_1} \binom{J_1/2}{\Gamma_l} u_{\Gamma_l}^{(2\Gamma_l+|M|-J_1+1)} \right| &\leq \text{tol}, \quad \Gamma_l > J_2^{\text{ezo}}, \end{aligned} \quad (7.102)$$

where an additional factor of $2 \lceil |M|/2 \rceil$ takes into account the compounding effect of

the truncation for the upper and lower halves of the pixel⁶, $u \triangleq \cos \theta$, tol is the preset tolerance,

$$u_{\Gamma_l} = \begin{cases} \cos(\theta_r), & r < N_{\text{side}}, \\ \cos(\theta_{r+1}), & r = N_{\text{side}}, \end{cases} \quad (7.103)$$

and $J_2^{\text{ez}_o}$ is determined by the maximum value of the generalized binomial coefficient $\binom{J_1/2}{J_2}$, i.e.,

$$J_2^{\text{ez}_o} = \begin{cases} \lceil J_1/4 \rceil, & J_1/2 + 0.5 \text{ even}, \\ \lfloor J_1/4 \rfloor, & J_1/2 + 0.5 \text{ odd}. \end{cases} \quad (7.104)$$

Truncation criterion in (7.102) estimates the magnitude of the integral in (C.29) over the upper half of the pixel by the following upper bound

$$\begin{aligned} \left| \int_{u_{r-1}}^{u_r} u^{(2J_2+|M|-J_1)} \sin \left[\mu \left(u - \frac{A^{\text{ez}} + B^{\text{ez}}}{2} \right) \right] du \right| &< \left| \int_{u_{r-1}}^{u_r} u^{(2J_2+|M|-J_1)} du \right| \\ &< \left| \frac{u_r^{(2J_2+|M|-J_1+1)} - u_{r-1}^{(2J_2+|M|-J_1+1)}}{(2J_2 + |M| - J_1 + 1)} \right| \\ &< \left| u_{r-1}^{(2J_2+|M|-J_1+1)} \right|, \end{aligned} \quad (7.105)$$

and the lower half of the pixel by the upper bound given below

$$\begin{aligned} \left| \int_{u_r}^{u_{r+1}} u^{(2J_2+|M|-J_1)} \sin \left[\mu \left(u - \frac{C^{\text{ez}} + D^{\text{ez}}}{2} \right) \right] du \right| &< \left| \int_{u_r}^{u_{r+1}} u^{(2J_2+|M|-J_1)} du \right| \\ &< \left| \frac{1}{(2J_2 + |M| - J_1 + 1)} \left(u_{r+1}^{(2J_2+|M|-J_1+1)} - u_r^{(2J_2+|M|-J_1+1)} \right) \right| \\ &\leq \begin{cases} \left| u_r^{(2J_2+|M|-J_1+1)} \right|, & r < N_{\text{side}}, \\ \left| u_{r+1}^{(2J_2+|M|-J_1+1)} \right|, & r = N_{\text{side}}, \end{cases} \end{aligned} \quad (7.106)$$

where $\mu = (q - m)/b$.

⁶There are $\lceil |M|/2 \rceil$ odd values for the summation index J_1 , for each value of M , in the expression given in (C.29).

7.7.2 Infinite Maclaurin series expansions

Infinite Maclaurin series expansions in (7.62) and (7.63), indexed by k_S and k_C respectively, are truncated at T_1 and T_2 when

$$\begin{aligned} & \left[16\sqrt{2}N_t \times \max \left\{ \binom{2|M|}{J_1} \left| \binom{|M| - \frac{J_1}{2}}{J_2} \right| \frac{Q_{\text{pz}}^{(J_1+2J_2+2)}}{(J_1+2J_2+2)!} \right\} \right] \left| \frac{w^{2T_1+1} (u_2^{2T_1+1} - u_1^{2T_1+1})}{(2T_1+1)(2T_1+1)!} \right| \leq \text{tol}, \\ & \left[16\sqrt{2}N_t \times \max \left\{ \binom{2|M|}{J_1} \left| \binom{|M| - \frac{J_1}{2}}{J_2} \right| \frac{Q_{\text{pz}}^{(J_1+2J_2+2)}}{(J_1+2J_2+2)!} \right\} \right] \left| \frac{w^{2T_2} (u_2^{2T_2} - u_1^{2T_2})}{2T_2(2T_2)!} \right| \leq \text{tol}, \end{aligned} \quad (7.107)$$

where the first term on the left hand side takes into account the compounding of truncation error, in which

$$N_t = \begin{cases} (4(L-1)+1) \times \max \{ \Gamma_{u_{\max}} + 1, 2(L-1) + 1 \}, & \theta \in [\theta_{r-1}, \theta_r], \\ (4(L-1)+1) \times \max \{ \Gamma_{l_{\max}} + 1, 2(L-1) + 1 \}, & \theta \in [\theta_r, \theta_{r+1}] \end{cases} \quad (7.108)$$

is an upper bound on number of terms in the double summation indexed by J_1, J_2 ,

$$Q_{\text{pz}} = \begin{cases} \max \{ |A^{\text{pz}}|, |B^{\text{pz}}| \}, & \theta \in [\theta_{r-1}, \theta_r], \\ \max \{ |C^{\text{pz}}|, |D^{\text{pz}}| \}, & \theta \in [\theta_r, \theta_{r+1}], \end{cases} \quad (7.109)$$

which depends on the pixel boundary parameters and tol is the preset tolerance. Here, $\Gamma_{u_{\max}}$ and $\Gamma_{l_{\max}}$ are the maximum number of terms in truncated series for different values of M and J_1 for the upper and lower halves of the north polar pixel respectively. Additional factor of $4\sqrt{2}$ takes into account the compounding of truncation error of the infinite Maclaurin series in real and imaginary parts of the integral in (C.10).

7.8 Analysis

We construct the overcomplete multiscale dictionary of Slepian functions at bandlimit $L = 32$ using (7.94), which gives the height of the HEALPix quaternary tree to be $\mathfrak{H} = 4$ and maximum HEALPix resolution parameter $N_{\text{side}}^{\max} = 8$. As an illustration,

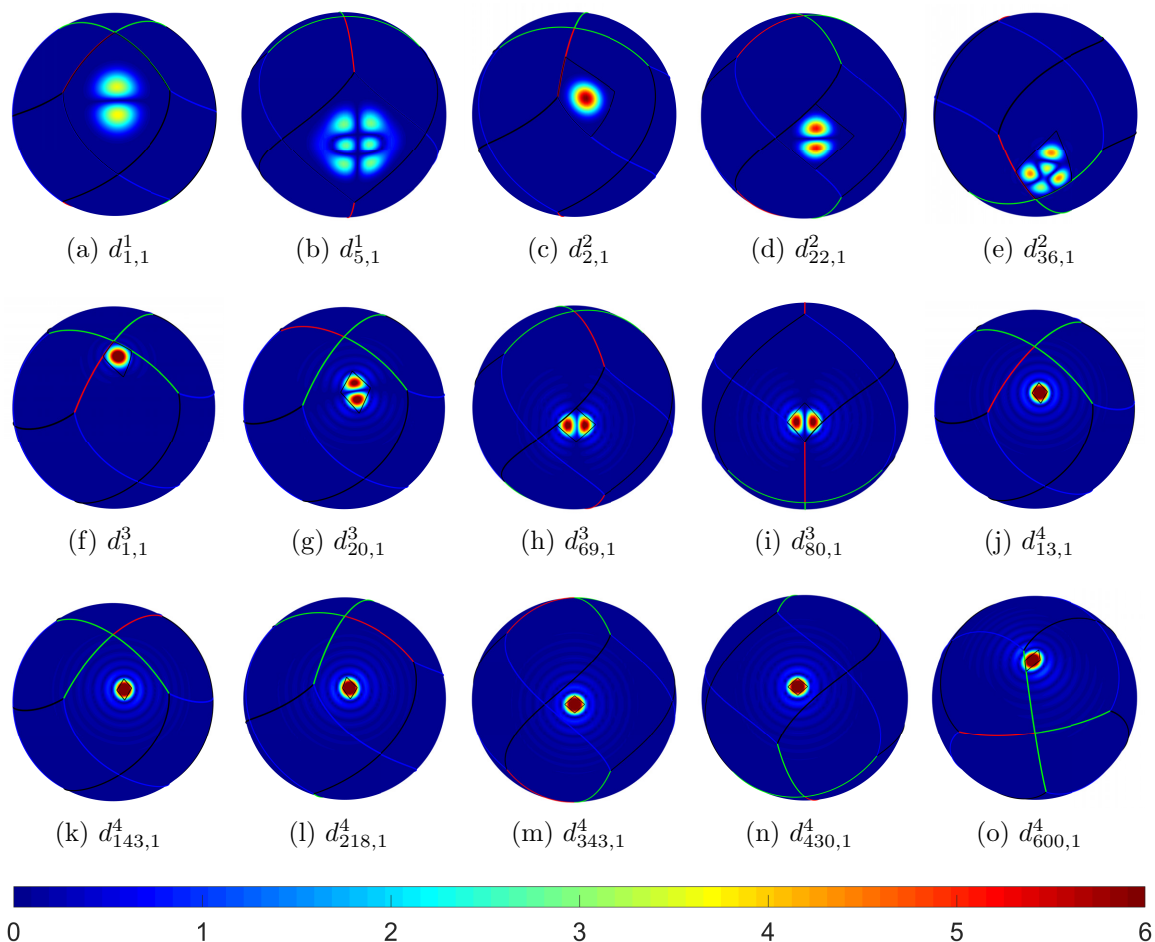


Figure 7-13: Magnitude of most well-optimally concentrated Slepian functions for different nodes in the HEALPix quaternary tree, constructed for bandlimit $L = 32$ ($\mathfrak{N} = 4$). Thick green, red, black and blue lines mark the boundaries of HEALPix base-resolution pixels, where the red line also indicates the $\phi = 0$ great circle arc. Boundary of the pixels is shown in black.

Figure 7-13 shows dictionary elements in the spatial domain, obtained using (2.62), for pixels represented by different nodes in the HEALPix quaternary tree.

7.8.1 Range of \mathfrak{D}

We verify the span of the elements of dictionary by comparing the range space of the subset \mathfrak{D}_k , given in (7.24) for $k \in [1, 12]$, with the range space of the following matrix

$$V_\alpha(1, k) = [\mathbf{d}_{(k,1)}^1, \dots, \mathbf{d}_{(k,\alpha)}^1], \quad \alpha \in [1, N_1], \quad N_1 = \frac{L^2}{12}, \quad k \in [1, 12], \quad (7.110)$$

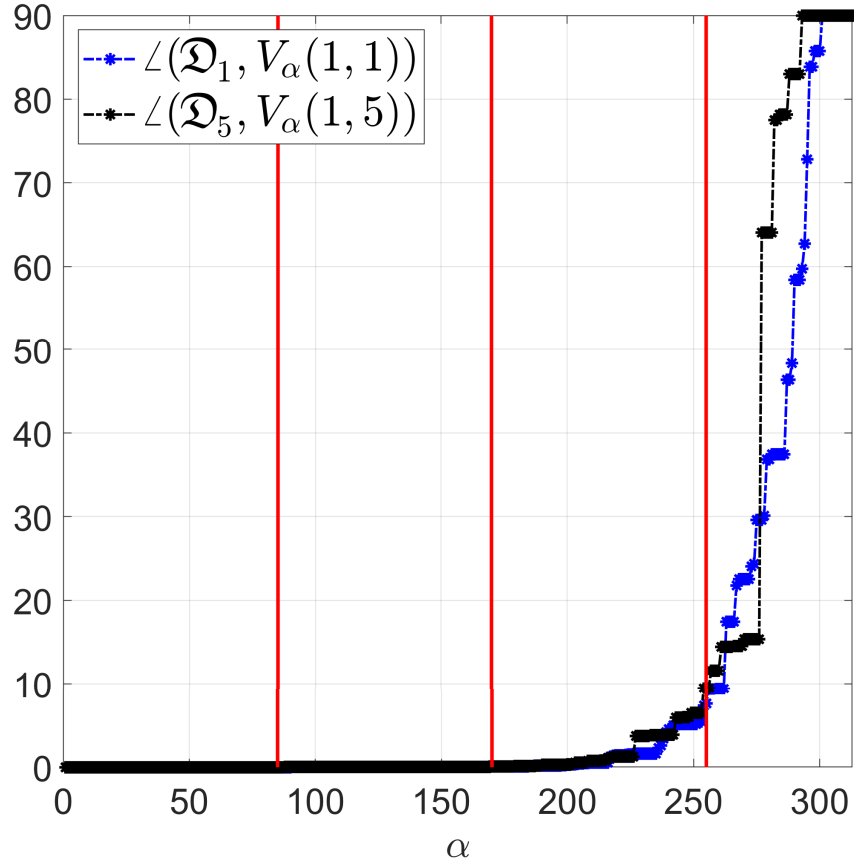


Figure 7-14: Angle (in degrees) between the range spaces of \mathfrak{D}_1 , $V_\alpha(1, 1)$ and \mathfrak{D}_5 , $V_\alpha(1, 5)$, for different values of α at bandlimit $L = 32$ ($\mathfrak{H} = 4$). Thick red lines mark the integer multiples of Shannon number $N_1 = 85$.

where N_1 is the Shannon number for pixels represented by the nodes at tree level $h_T = 1$ and $\mathbf{d}_{(k,\alpha)}^1$ is an element of the dictionary \mathfrak{D} in (7.90). Range space of the matrix $V_\alpha(1, k)$ represents the vector space of bandlimited signals which are well-optimally concentrated within the pixel represented by the node $P(1, k)$. As before, the range space of \mathfrak{D}_k is compared to that of $V_\alpha(1, k)$ by analyzing the maximum principle angle between them⁷. Figure 7-14 shows the results of this comparison for the pixels represented by the nodes $P(1, 1)$ and $P(1, 5)$. The respective dictionary elements can be seen to comfortably, if not strictly, span the space of bandlimited signals which are optimally concentrated within pixels represented by the nodes $P(1, 1)$ and $P(1, 5)$, since the angle is essentially 0 for not just the well-optimally concentrated Slepian functions, i.e., $\alpha \leq N_1$ but also for $N_1 \leq \alpha \leq 2N_1$.

⁷Please refer to Footnote 3 on page 185 for more details.

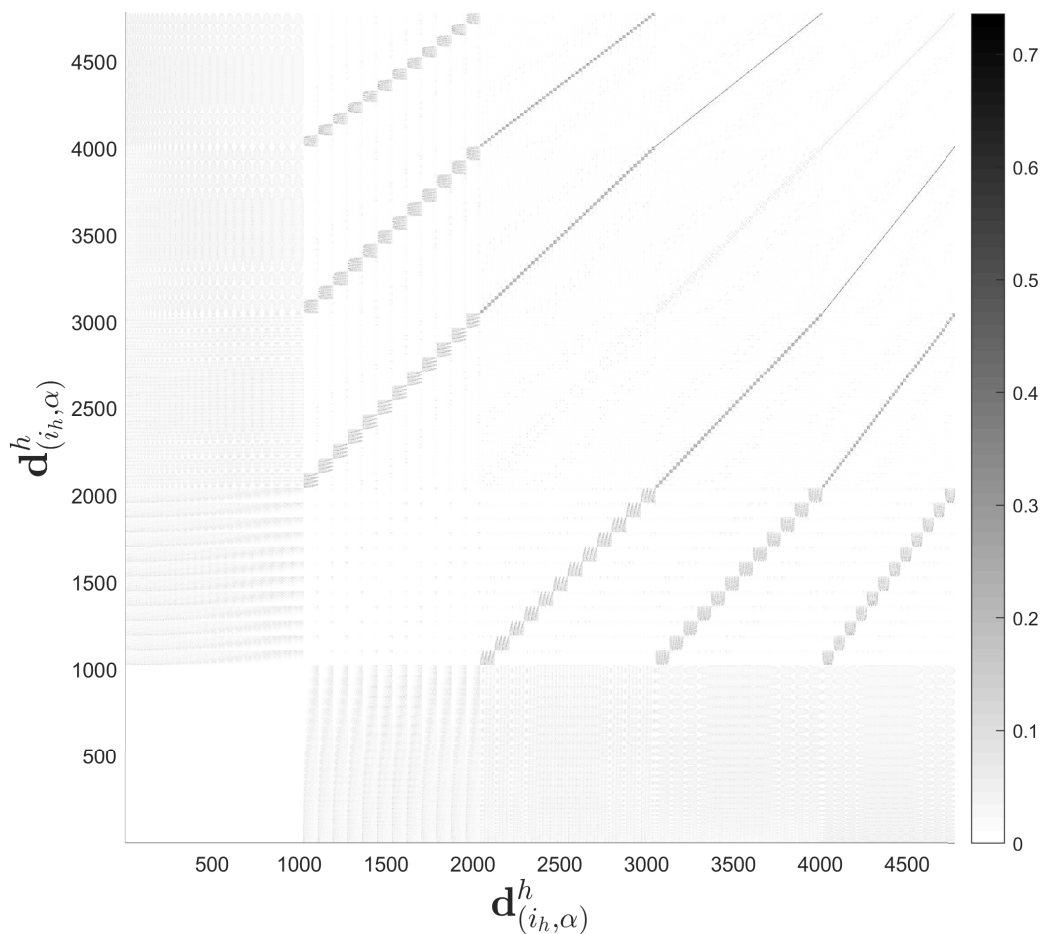


Figure 7-15: Mutual coherence between elements of the dictionary constructed for HEALPix at bandlimit $L = 32$ ($\mathfrak{J} = 4$).

7.8.2 Mutual coherence

Mutual coherence, defined in (7.26), is computed for the overcomplete multiscale dictionary of Slepian functions for HEALPix, and is shown in Figure 7-15 as a surface plot of the absolute inner products between the dictionary elements, from which it can be observed that mutual coherence between most of the dictionary elements is very small. The first L^2 elements of the dictionary are orthonormal vectors, which exhibit zero mutual coherence. The pixels which share overlapping regions on the sphere tend to exhibit relatively large mutual coherence. As the resolution of HEALPix partitioning scheme is increased, fraction of such overlapping pixels is reduced. This can be seen from Figure 7-16, which shows the cumulative fractional mutual coherence

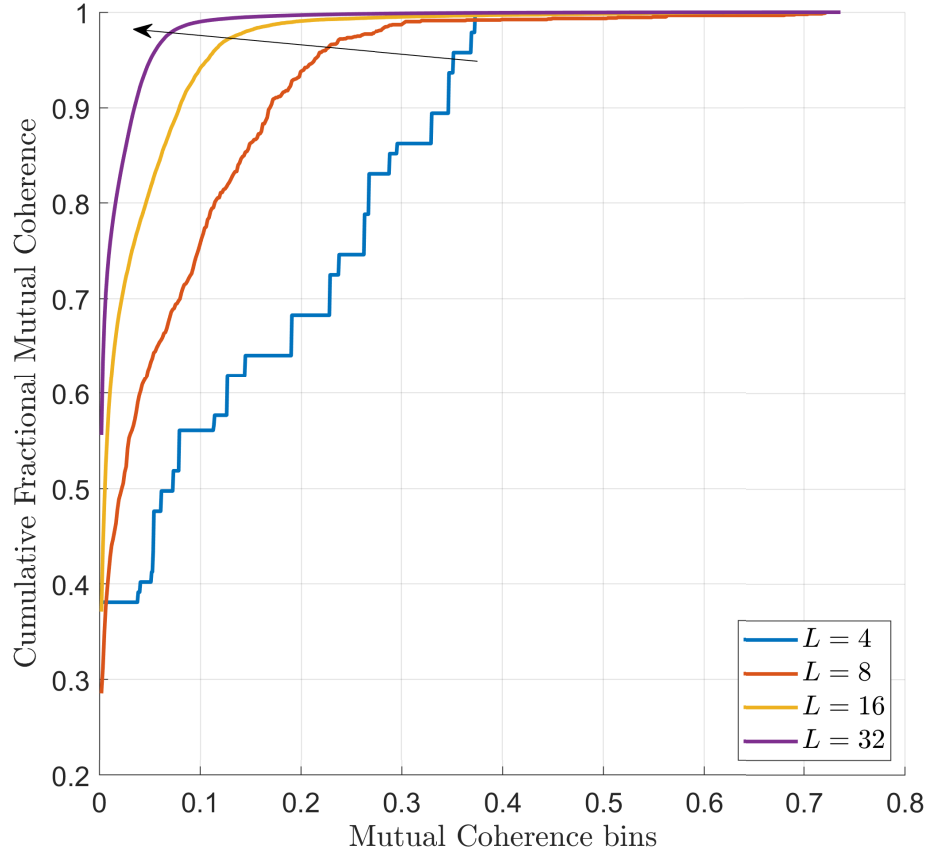


Figure 7-16: Cumulative fractional mutual coherence between dictionary elements, plotted against the range of mutual coherence values, for HEALPix quaternary trees at bandlimit $L = 4, 8, 16, 32$, having corresponding height $\mathfrak{H} = 1, 2, 3, 4$. Arrow shows the direction in which the approximate knee of the curves is displaced with increasing values of L .

at various bandlimits. Increasing the bandlimit L increases height of the HEALPix

Table 7.6: Approximating the knee for each curve in Figure 7-16.

Bandlimit, L	Coordinates for knee of the curves in Figure 7-16
4	$(0.35, 0.96)$, i.e., $\sim 96\%$ of the total number of inner products result in mutual coherence ≤ 0.35
8	$(0.24, 0.97)$, i.e., $\sim 97\%$ of the total number of inner products result in mutual coherence ≤ 0.24
16	$(0.13, 0.97)$, i.e., $\sim 97\%$ of the total number of inner products result in mutual coherence ≤ 0.13
32	$(0.07, 0.98)$, i.e., $\sim 98\%$ of the total number of inner products result in mutual coherence ≤ 0.07

quaternary tree according to (7.95), which increases the maximum resolution of the

HEALPix partitioning scheme, thus, increasing the fraction of dictionary elements exhibiting small mutual coherence.

Table 7.6 lists the approximate coordinates for the knee of curves in Figure 7-16, which shows that at bandlimit $L = 32$, $\sim 98\%$ of the total number of inner products between dictionary elements, excluding self inner products, have magnitude less than 0.07, indicating that only $\sim 2\%$ of the total number of inner products between dictionary elements result in mutual coherence $M_C \geq 0.07$.

Chapter 8

Summary and future work

This dissertation has been concerned with the development of novel techniques for signal processing on the sphere. In this chapter, we give a brief summary of the work presented in this dissertation, along with potential research directions for future.

8.1 Summary of dissertation

We have proposed novel signal filtering and estimation methods in the joint domain using spatially localized spherical harmonic transform and scale-discretized wavelet transform, assuming the noise to be a realization of a zero-mean and anisotropic process on the sphere. We have also designed axisymmetric and directional optimal window signals to enhance the performance of signal filtering and estimation framework in the joint spatial-spectral domain and the joint $\mathbb{SO}(3)$ -spectral domain respectively, where these joint domain representations are enabled by spatially localized spherical harmonic transform. The effectiveness of these methods have been demonstrated on bandlimited Earth and Mars topography maps.

In the context of localized signal analysis, we have formulated a framework for analytical evaluation of integral of signals, and analytical computation of bandlimited Slepian functions, to support localized analysis over simple spherical polygons, and have provided illustrations using bandlimited Earth and Mars topography maps. We have also proposed a joint spatial-Slepian domain representation for spherical sig-

nals through the novel spatial-Slepian transform. The joint spatial-Slepian domain representation is given by the spatial-Slepian coefficients, which have been shown to exhibit better spatial localization compared to scale-discretized wavelet coefficients. Spatial-Slepian coefficients have been further employed to detect the presence of hidden (extremely weak) localized variations in the signal, and to formulate a framework for linear transformations in the joint spatial-Slepian domain. These transformations have been specified by a spatial-Slepian transformation kernel, special forms of which have been used to provide illustrations on a bandlimited Mars topography map.

Finally, we have proposed Hierarchical Equal Area iso-Latitude iso-Longitude Pixelization (HEALLPix) scheme and have used it to construct an overcomplete multiscale dictionary of localized (spectral domain) Slepian functions on the sphere. We have also considered HEALPix and have proposed a sampling scheme, which uses a subset of HEALPix samples, for efficient and accurate computation of spherical harmonic transform of bandlimited signals. Moreover, we have presented a framework for the analytical computation of bandlimited Slepian functions for multiscale HEALPix pixels by exploiting rotational symmetries between pixels, and using Wigner- D functions of appropriate rotation angles, for efficient computation. Localized spectral representations of bandlimited Slepian functions, computed for HEALPix pixels at different scales, have been collected to form another overcomplete multiscale dictionary of localized basis functions. The two dictionaries have been shown to span the space of bandlimited signals, with negligibly small mutual coherence between most of their respective elements.

8.2 Future research directions

A number of potential research directions stem from different studies carried out in this dissertation, as listed below.

- Instead of designing optimal filters in the joint domain through minimum mean-square error criterion, optimal filters can be designed by minimizing variance of the spectral estimate of the signal in the joint domain. Performance of the

such filters can be compared with the results presented in this dissertation.

- Since the mean-square error can be written as sum of the variance and bias-squared of the spectral estimate [128], a weighted mean-square error (where weights sum to 1) can be used to design joint domain optimal filters. The weights can be adjusted to further optimize the performance of the filters.
- A framework, similar to that of multiscale optimal filtering using scale-discretized wavelet transform, can also be formulated for other wavelet transforms on the sphere available in the literature.
- Spatially localized spherical harmonic transform can be extended for signal analysis on the ball¹. The resulting joint domain representation can be used to design joint domain filters for signal estimation on the ball.
- Multiscale optimal filtering can be extended to filter signals on the ball using the framework of wavelet analysis on the ball, presented in [130].
- The framework of localized signal analysis over simple spherical polygons can be extended to compute vector Slepian functions over polygons for localized analysis of vector fields on the sphere.
- The framework of localized variation analysis using spatial-Slepian transform has been illustrated on a synthetic data set. This framework can be applied to real data sets from medical imaging for the diagnosis of different anomalies. This framework can also be used for cosmological data sets to detect localized spatial variations across time.
- Using the framework of Slepian spatial-spectral concentration problem on the ball [129], spatial-Slepian transform can be extended to analyze signals on the ball.

¹A ball is defined as the set $\mathbb{B}^3 \triangleq \mathbb{R}^+ \times \mathbb{S}^2$, where \mathbb{R}^+ represents the half-real line domain, i.e., $[0, \infty)$, and \mathbb{S}^2 is the surface of the sphere [129].

- In the context of analytical computation of Slepian functions over spherical right-angled triangles and HEALPix pixels, a framework for analytical computation of Slepian functions over spherically elliptical regions can be formulated.
- The overcomplete multiscale dictionaries of Slepian functions can be used to formulate a framework of multiresolution analysis on the sphere to perform
 - i. multiscale feature extraction,
 - ii. localized spectral analysis at different scales.

Furthermore, these dictionaries can be used for optimal filtering of signals and for the solution of ill-posed inverse problems on the sphere such as:

- i. signal inpainting,
 - ii. signal deconvolution,
 - iii. sparse representation of signals.
- Referring again to the framework of Slepian spatial-spectral concentration problem on the ball [129], overcomplete multiscale dictionaries of Slepian functions can be constructed for signal analysis on the ball.

Appendix A

A.1 Integration of $e^{iq\phi}e^{im\theta}$ over spherical right-angled triangle in standard orientation

Integration in (4.9) can be expressed as four separate integrals over θ and ϕ , using (4.20), as

$$\begin{aligned}
 \mathbb{I}(\mathbf{q}, \mathbf{m}, \theta_{b,t}, \phi_{c,t}) &= \int_{\phi=0}^{\phi_{c,t}} \int_{\theta=\tan^{-1}(\mathbf{k}_t/\sin(\phi_{c,t}-\phi))}^{\pi/2} e^{iq\phi} e^{im\theta} d\theta d\phi \\
 &= \begin{cases} \int_{\phi=0}^{\phi_{c,t}} \left(\frac{\pi}{2} - \tan^{-1} \left(\frac{\mathbf{k}_t}{\sin(\phi_{c,t}-\phi)} \right) \right) d\phi, & \mathbf{q} = 0, \mathbf{m} = 0, \\ \int_{\phi=0}^{\phi_{c,t}} \frac{1}{i\mathbf{m}} \left(i^{\mathbf{m}} - e^{im \tan^{-1} \left(\frac{\mathbf{k}_t}{\sin(\phi_{c,t}-\phi)} \right)} \right) d\phi, & \mathbf{q} = 0, \mathbf{m} \neq 0, \\ \int_{\phi=0}^{\phi_{c,t}} e^{iq\phi} \left(\frac{\pi}{2} - \tan^{-1} \left(\frac{\mathbf{k}_t}{\sin(\phi_{c,t}-\phi)} \right) \right) d\phi, & \mathbf{q} \neq 0, \mathbf{m} = 0, \\ \int_{\phi=0}^{\phi_{c,t}} \frac{e^{iq\phi}}{i\mathbf{m}} \left(i^{\mathbf{m}} - e^{im \tan^{-1} \left(\frac{\mathbf{k}_t}{\sin(\phi_{c,t}-\phi)} \right)} \right) d\phi, & \mathbf{q} \neq 0, \mathbf{m} \neq 0, \end{cases} \\
 &= \begin{cases} \mathbb{I}(0, 0, \theta_{b,t}, \phi_{c,t}), & \mathbf{q} = 0, \mathbf{m} = 0, \\ \frac{i^{\mathbf{m}} \phi_{c,t}}{i\mathbf{m}} - \frac{1}{i\mathbf{m}} S(0, \mathbf{m}, \theta_{b,t}, \phi_{c,t}), & \mathbf{q} = 0, \mathbf{m} \neq 0, \\ \frac{\pi(e^{iq\phi_{c,t}}-1)}{2i\mathbf{q}} - Q(\mathbf{q}, \theta_{b,t}, \phi_{c,t}), & \mathbf{q} \neq 0, \mathbf{m} = 0, \\ \frac{-i^{\mathbf{m}}(e^{iq\phi_{c,t}}-1)}{m\mathbf{q}} - \frac{1}{i\mathbf{m}} S(\mathbf{q}, \mathbf{m}, \theta_{b,t}, \phi_{c,t}), & \mathbf{q} \neq 0, \mathbf{m} \neq 0, \end{cases} \tag{A.1}
 \end{aligned}$$

where the functions Q and S are given by

$$Q(\mathbf{q}, \theta_{b,t}, \phi_{c,t}) = \int_{\phi=0}^{\phi_{c,t}} e^{i\mathbf{q}\phi} \tan^{-1} \left(\frac{\mathbf{k}_t}{\sin(\phi_{c,t} - \phi)} \right) d\phi, \quad (\text{A.2})$$

$$S(\mathbf{q}, \mathbf{m}, \theta_{b,t}, \phi_{c,t}) = \int_{\phi=0}^{\phi_{c,t}} e^{i\mathbf{q}\phi} e^{i\mathbf{m} \tan^{-1} \left(\frac{\mathbf{k}_t}{\sin(\phi_{c,t} - \phi)} \right)} d\phi. \quad (\text{A.3})$$

The integral in (A.1) is solved for different cases of \mathbf{q} and \mathbf{m} .

A.1.1 $\mathbf{q} = 0, \mathbf{m} = 0, 0 \leq \theta_{b,t} < \pi/4$:

Let $\phi = \phi_1$ be the angle at which $\sin(\phi_{c,t} - \phi)/\mathbf{k}_t = 1$. Then

$$\phi_1 = \phi_{c,t} - \sin^{-1}(\mathbf{k}_t). \quad (\text{A.4})$$

Since $|\sin(\phi_{c,t} - \phi)/\mathbf{k}_t| \geq 1$ for $0 \leq \phi \leq \phi_1$ and $|\sin(\phi_{c,t} - \phi)/\mathbf{k}_t| < 1$ for $\phi_1 < \phi \leq \phi_{c,t}$, we can break $\mathbb{I}(0, 0, \theta_{b,t}, \phi_{c,t})$ in (A.1) into two integrals as

$$\begin{aligned} \mathbb{I}(0, 0, \theta_{b,t}, \phi_{c,t}) &= \int_{\phi=0}^{\phi_{c,t}} \left(\frac{\pi}{2} - \tan^{-1} \left(\frac{\mathbf{k}_t}{\sin(\phi_{c,t} - \phi)} \right) \right) d\phi \\ &= \int_{\phi=0}^{\phi_1} \left(\frac{\pi}{2} - \tan^{-1} \left(\frac{\mathbf{k}_t}{\sin(\phi_{c,t} - \phi)} \right) \right) d\phi + \int_{\phi=\phi_1}^{\phi_{c,t}} \tan^{-1} \left(\frac{\sin(\phi_{c,t} - \phi)}{\mathbf{k}_t} \right) d\phi \\ &= \frac{\pi}{2} \phi_1 + \mathbf{k}_t \int_{\mathbf{k}_t/\sin(\phi_{c,t} - \phi_1)}^{\mathbf{k}_t/\sin \phi_{c,t}} \frac{\tan^{-1}(y_1)}{y_1 \sqrt{y_1^2 - \mathbf{k}_t^2}} dy_1 + \mathbf{k}_t \int_0^{\sin(\phi_{c,t} - \phi_1)/\mathbf{k}_t} \frac{\tan^{-1}(y_2)}{\sqrt{1 - (y_2 \mathbf{k}_t)^2}} dy_2, \end{aligned} \quad (\text{A.5})$$

where, in the last equality, we have used the substitutions $y_1 = \mathbf{k}_t/\sin(\phi_{c,t} - \phi)$ and $y_2 = \sin(\phi_{c,t} - \phi)/\mathbf{k}_t$. Expanding $\tan^{-1}(\cdot)$ in Taylor series as

$$\tan^{-1}(y_1) = \sum_{n_1=0}^{\infty} \frac{(-1)^{n_1}}{(2n_1 + 1)} y_1^{2n_1+1} = \sum_{n_1=0}^{\infty} \frac{(-1)^{n_1} \mathbf{k}_t^{2n_1+1}}{(2n_1 + 1) \sin^{2n_1+1}(\phi_{c,t} - \phi)}, \quad (\text{A.6})$$

and

$$\tan^{-1}(y_2) = \sum_{n_2=0}^{\infty} \frac{(-1)^{n_2}}{(2n_2 + 1)} y_2^{2n_2+1} = \sum_{n_2=0}^{\infty} \frac{(-1)^{n_2}}{\mathbf{k}_t^{2n_2+1} (2n_2 + 1)} \sin^{2n_2+1}(\phi_{c,t} - \phi), \quad (\text{A.7})$$

we can rewrite $\mathbb{I}(0, 0, \theta_{b,t}, \phi_{c,t})$ as

$$\begin{aligned} \mathbb{I}(0, 0, \theta_{b,t}, \phi_{c,t}) &= \frac{\pi}{2}\phi_1 + \sum_{n_1=0}^{\infty} \frac{\mathbf{k}_t(-1)^{n_1}}{(2n_1+1)} \int_{\frac{\mathbf{k}_t}{\sin(\phi_{c,t}-\phi_1)}}^{\frac{\mathbf{k}_t}{\sin\phi_{c,t}}} \frac{y_1^{2n_1-1}}{\sqrt{1-(\mathbf{k}_t/y_1)^2}} dy_1 + \\ &\quad \sum_{n_2=0}^{\infty} \frac{\mathbf{k}_t(-1)^{n_2}}{(2n_2+1)} \int_0^{\frac{\sin(\phi_{c,t}-\phi_1)}{\mathbf{k}_t}} \frac{y_2^{2n_2+1}}{\sqrt{1-(y_2\mathbf{k}_t)^2}} dy_2. \end{aligned} \quad (\text{A.8})$$

The denominator in the two integrands in the last expression can be expanded in the following generalized binomial series

$$\left(1 - (\mathbf{k}_t/y_1)^2\right)^{-1/2} = \sum_{J_1=0}^{\infty} \binom{-1/2}{J_1} (-1)^{J_1} \mathbf{k}_t^{2J_1} \frac{1}{y_1^{2J_1}}, \quad (\text{A.9})$$

$$\left(1 - (y_2\mathbf{k}_t)^2\right)^{-1/2} = \sum_{J_2=0}^{\infty} \binom{-1/2}{J_2} (-1)^{J_2} \mathbf{k}_t^{2J_2} y_2^{2J_2}, \quad (\text{A.10})$$

where $\binom{-1/2}{J_1}$ and $\binom{-1/2}{J_2}$ are generalized binomial coefficients. Therefore,

$$\begin{aligned} \mathbb{I}(0, 0, \theta_{b,t}, \phi_{c,t}) &= \frac{\pi}{2}\phi_1 + \sum_{n_1=0}^{\infty} \frac{\mathbf{k}_t(-1)^{n_1}}{(2n_1+1)} \sum_{J_1=0}^{\infty} \binom{-1/2}{J_1} (-1)^{J_1} \mathbf{k}_t^{2J_1} \times \\ &\quad \int_{\frac{\mathbf{k}_t}{\sin(\phi_{c,t}-\phi_1)}}^{\frac{\mathbf{k}_t}{\sin\phi_{c,t}}} y_1^{2n_1-1-2J_1} dy_1 + \sum_{n_2=0}^{\infty} \frac{\mathbf{k}_t(-1)^{n_2}}{(2n_2+1)} \sum_{J_2=0}^{\infty} \binom{-1/2}{J_2} (-1)^{J_2} \mathbf{k}_t^{2J_2} \int_0^{\frac{\sin(\phi_{c,t}-\phi_1)}{\mathbf{k}_t}} y_2^{2n_2+1+2J_2} dy_2 \\ &= \frac{\pi}{2}\phi_1 + \sum_{n_1=0}^{\infty} \frac{\mathbf{k}_t(-1)^{n_1}}{(2n_1+1)} W_1(\theta_{b,t}, \phi_{c,t}, \phi_1, n_1) + \sum_{n_2=0}^{\infty} \frac{\mathbf{k}_t(-1)^{n_2}}{(2n_2+1)} W_2(\theta_{b,t}, \phi_{c,t}, \phi_{c,t} - \phi_1, n_2), \end{aligned} \quad (\text{A.11})$$

where the final expression is a consequence of the following simple result

$$\int_{y_a}^{y_b} y^{(a+b)} dy = \begin{cases} \left[y^{(a+b+1)} / (a+b+1) \right]_{y_a}^{y_b}, & a+b \neq -1, \\ \left[\ln y \right]_{y_a}^{y_b}, & a+b = -1, \end{cases} \quad (\text{A.12})$$

and W_1, W_2 are given in (4.27), (4.28) respectively. We refer the reader to Section 4.2.5 for the truncation of infinite series indexed by n_1, n_2, J_1 and J_2 .

A.1.2 $\mathbf{q} = 0, \mathbf{m} = 0, \pi/4 \leq \theta_{b,t} < \pi/2$

For this case

$$|\sin(\phi_{c,t} - \phi)/\mathbf{k}_t| \leq 1, \quad (\text{A.13})$$

hence, we can write $\mathbb{I}(0, 0, \theta_{b,t}, \phi_{c,t})$ as

$$\begin{aligned} \mathbb{I}(0, 0, \theta_{b,t}, \phi_{c,t}) &= \int_{\phi=0}^{\phi_{c,t}} \left(\frac{\pi}{2} - \tan^{-1} \left(\frac{\mathbf{k}_t}{\sin(\phi_{c,t} - \phi)} \right) \right) d\phi \\ &= \int_0^{\sin \phi_{c,t}/\mathbf{k}_t} \mathbf{k}_t \frac{\tan^{-1}(y)}{\sqrt{1 - (y\mathbf{k}_t)^2}} dy, \end{aligned} \quad (\text{A.14})$$

where, in the last equality, we have used the substitution $y = \sin(\phi_{c,t} - \phi)/\mathbf{k}_t$. Using the expansion in (A.7) and expanding the denominator of the integrand above in the following generalized binomial series

$$\left(1 - (y\mathbf{k}_t)^2\right)^{-1/2} = \sum_{J_2=0}^{\infty} \binom{-1/2}{J_2} (-1)^{J_2} \mathbf{k}_t^{2J_2} y^{2J_2}, \quad (\text{A.15})$$

$\mathbb{I}(0, 0, \theta_{b,t}, \phi_{c,t})$ can be solved as

$$\begin{aligned} \mathbb{I}(0, 0, \theta_{b,t}, \phi_{c,t}) &= \sum_{n_3=0}^{\infty} \frac{(-1)^{n_3} \mathbf{k}_t}{(2n_3 + 1)} \sum_{J_2=0}^{\infty} \binom{-1/2}{J_2} (-1)^{J_2} \mathbf{k}_t^{2J_2} \int_0^{\frac{\sin \phi_{c,t}}{\mathbf{k}_t}} y^{2n_3+1+2J_2} dy \\ &= \sum_{n_3=0}^{\infty} \frac{(-1)^{n_3} \mathbf{k}_t}{(2n_3 + 1)} W_2(\theta_{b,t}, \phi_{c,t}, \phi_{c,t}, n_3), \end{aligned} \quad (\text{A.16})$$

where $\binom{-1/2}{J_2}$ is the generalized binomial coefficient and W_2 is given in (4.28). We refer the reader to (4.40) for the truncation of alternating series indexed by n_3 and to (4.41) for the truncation of infinite series indexed by J_2 in (A.15).

A.1.3 $\mathbf{q} = 0, \mathbf{m} \neq 0, \mathbf{q} \neq 0, \mathbf{m} = 0$ and $\mathbf{q} \neq 0, \mathbf{m} \neq 0$

For all other cases, integral $\mathbb{I}(\mathbf{q}, \mathbf{m}, \theta_{b,t}, \phi_{c,t})$ depends either on the function Q or the function S .

Evaluating the function $Q(\mathbf{q}, \theta_{b,t}, \phi_{c,t})$:

Substituting $u = \phi_{c,t} - \phi$ in (A.2), we get

$$\begin{aligned} Q(\mathbf{q}, \theta_{b,t}, \phi_{c,t}) &= -e^{iq\phi_{c,t}} \int_{u=\phi_{c,t}}^0 e^{-iqu} \tan^{-1} \left(\frac{\mathbf{k}_t}{\sin u} \right) du \\ &= -e^{iq\phi_{c,t}} \int_{\phi=-\phi_{c,t}}^0 e^{iq\phi} \tan^{-1} \left(\frac{\mathbf{k}_t}{\sin \phi} \right) d\phi. \end{aligned} \quad (\text{A.17})$$

Expanding the complex exponential function in binomial series as

$$\begin{aligned} e^{iq\phi} &= (\cos \phi + s_{\mathbf{q}} i \sin \phi)^{|\mathbf{q}|} \\ &= \sum_{n_0=0}^{|\mathbf{q}|} \binom{|\mathbf{q}|}{n_0} A(\mathbf{q}, n_0) (\cos \phi)^{n_0} (\sin \phi)^{|\mathbf{q}|-n_0}, \end{aligned} \quad (\text{A.18})$$

and performing integration by parts, $Q(\mathbf{q}, \theta_{b,t}, \phi_{c,t})$ becomes

$$\begin{aligned} Q(\mathbf{q}, \theta_{b,t}, \phi_{c,t}) &= -\frac{e^{iq\phi_{c,t}}}{i\mathbf{q}} \left(e^{-iq\phi_{c,t}} \tan^{-1} \left(\frac{\mathbf{k}_t}{\sin \phi_{c,t}} \right) - \frac{\pi}{2} + \right. \\ &\quad \left. \mathbf{k}_t \sum_{n_0=0}^{|\mathbf{q}|} \binom{|\mathbf{q}|}{n_0} A(\mathbf{q}, n_0) \int_{-\phi_{c,t}}^0 \frac{(\cos \phi)^{n_0+1} (\sin \phi)^{|\mathbf{q}|-n_0}}{\sin^2 \phi + \mathbf{k}_t^2} d\phi \right), \end{aligned} \quad (\text{A.19})$$

where $A(\mathbf{q}, n_0)$ is defined in (4.26) and

$$s_{\mathbf{q}} = \begin{cases} +1, & \mathbf{q} \geq 0, \\ -1, & \mathbf{q} < 0. \end{cases} \quad (\text{A.20})$$

Now we observe that

$$\begin{aligned} \int \frac{(\cos \phi)^{n_0+1} (\sin \phi)^{|\mathbf{q}|-n_0}}{\sin^2 \phi + \mathbf{k}_t^2} d\phi &= \frac{(\sin \phi)^{(1+|\mathbf{q}|-n_0)}}{\mathbf{k}_t^2 (1 + |\mathbf{q}| - n_0)} \times \\ &F_1 \left(\frac{(1 + |\mathbf{q}| - n_0)}{2}, \frac{-n_0}{2}, 1, \frac{(3 + |\mathbf{q}| - n_0)}{2}; \sin^2 \phi, -\frac{\sin^2 \phi}{\mathbf{k}_t^2} \right), \end{aligned} \quad (\text{A.21})$$

where F_1 is the Appell F_1 hypergeometric function, which can be used to formulate the integral in (A.19) as

$$\begin{aligned}
 Q(\mathbf{q}, \theta_{b,t}, \phi_{c,t}) &= -\frac{e^{iq\phi_{c,t}}}{iq} \left(e^{-iq\phi_{c,t}} \tan^{-1} \left(\frac{\mathbf{k}_t}{\sin \phi_{c,t}} \right) - \frac{\pi}{2} \right) - \\
 &\quad \frac{e^{iq\phi_{c,t}} \mathbf{k}_t}{iq} \sum_{n_0=0}^{|\mathbf{q}|} \binom{|\mathbf{q}|}{n_0} A(\mathbf{q}, n_0) W_3(n_0, \mathbf{q}, \theta_{b,t}, \phi_{c,t}), \quad (\text{A.22})
 \end{aligned}$$

where W_3 is given in (4.29).

Evaluating the function $S(\mathbf{q}, \mathbf{m}, \theta_{b,t}, \phi_{c,t})$:

Substituting $u = \phi_{c,t} - \phi$ in (A.3), we get

$$\begin{aligned}
 S(\mathbf{q}, \mathbf{m}, \theta_{b,t}, \phi_{c,t}) &= -\int_{u=\phi_{c,t}}^0 e^{iq\phi_{c,t}} e^{-iqu} e^{im \tan^{-1} \left(\frac{\mathbf{k}_t}{\sin u} \right)} du \\
 &= e^{iq\phi_{c,t}} \int_{\phi=-\phi_{c,t}}^0 e^{iq\phi} e^{-im \tan^{-1} \left(\frac{\mathbf{k}_t}{\sin \phi} \right)} d\phi. \quad (\text{A.23})
 \end{aligned}$$

We note that

$$\begin{aligned}
 e^{-im \tan^{-1} \left(\frac{\mathbf{k}_t}{\sin \phi} \right)} &= e^{-s_m i |\mathbf{m}| \tan^{-1} \left(\frac{\mathbf{k}_t}{\sin \phi} \right)} \\
 &= \left(\frac{1}{\sqrt{1 + \frac{\mathbf{k}_t^2}{\sin^2 \phi}}} - s_m i \frac{\mathbf{k}_t / \sin \phi}{\sqrt{1 + \frac{\mathbf{k}_t^2}{\sin^2 \phi}}} \right)^{|\mathbf{m}|} \\
 &= \left(\frac{1}{\sqrt{\sin^2 \phi + \mathbf{k}_t^2}} (-\sin \phi) - s_m i \frac{\mathbf{k}_t / \sin \phi}{\sqrt{\sin^2 \phi + \mathbf{k}_t^2}} (-\sin \phi) \right)^{|\mathbf{m}|} \\
 &= \frac{(-1)^{|\mathbf{m}|} \mathbf{k}_t^{|\mathbf{m}|}}{(\sin^2 \phi + \mathbf{k}_t^2)^{|\mathbf{m}|/2}} \sum_{r=0}^{|\mathbf{m}|} \binom{|\mathbf{m}|}{r} (-1)^{|\mathbf{m}|-r} A(\mathbf{m}, r) (\sin \phi)^r \mathbf{k}_t^{-r}, \quad (\text{A.24})
 \end{aligned}$$

where s_m is defined in (A.20), $\sqrt{\sin^2 \phi} = -\sin \phi$ because $\sin \phi < 0$ over the range of integration and $A(\mathbf{m}, r)$ is defined in (4.26). Using (A.18) and (A.24), the integral in (A.23) becomes

$$\begin{aligned}
 S(\mathbf{q}, \mathbf{m}, \theta_{b,t}, \phi_{c,t}) &= e^{iq\phi_{c,t}} \sum_{n_0=0}^{|\mathbf{q}|} \binom{|\mathbf{q}|}{n_0} A(\mathbf{q}, n_0) \sum_{r=0}^{|\mathbf{m}|} (-1)^r \times \\
 &\quad \binom{|\mathbf{m}|}{r} A(\mathbf{m}, r) \mathbf{k}_t^{|\mathbf{m}|-r} \int_{\phi=-\phi_{c,t}}^0 \frac{(\cos \phi)^{n_0} (\sin \phi)^{|\mathbf{q}|-n_0+r}}{(\sin^2 \phi + \mathbf{k}_t^2)^{|\mathbf{m}|/2}} d\phi, \quad (\text{A.25})
 \end{aligned}$$

A.1 Integration of $e^{iq\phi}e^{im\theta}$ over spherical right-angled triangle in standard orientation

in which the integral can be written in terms of AppellF₁ hypergeometric function as

$$\int \frac{(\cos \phi)^{n_0} (\sin \phi)^{|\mathbf{q}|-n_0+r}}{(\sin^2 \phi + \mathbf{k}_t^2)^{|\mathbf{m}|/2}} d\phi = \frac{(\sin \phi)^{1+|\mathbf{q}|-n_0+r}}{\mathbf{k}_t^{|\mathbf{m}|} (1 + |\mathbf{q}| - n_0 + r)} \times$$

$$F_1 \left(\frac{(1 + |\mathbf{q}| - n_0 + r)}{2}, \frac{1 - n_0}{2}, \frac{|\mathbf{m}|}{2}, \frac{(3 + |\mathbf{q}| - n_0 + r)}{2}, \sin^2 \phi, -\frac{\sin^2 \phi}{\mathbf{k}_t^2} \right).$$
(A.26)

Therefore,

$$S(\mathbf{q}, \mathbf{m}, \theta_{b,t}, \phi_{c,t}) = e^{iq\phi_{c,t}} \sum_{n_0=0}^{|\mathbf{q}|} \binom{|\mathbf{q}|}{n_0} A(\mathbf{q}, n_0) \sum_{r=0}^{|\mathbf{m}|} (-1)^r \binom{|\mathbf{m}|}{r} \times$$

$$A(\mathbf{m}, r) \mathbf{k}_t^{|\mathbf{m}|-r} W_4(n_0, r, \mathbf{q}, |\mathbf{m}|, \theta_{b,t}, \phi_{c,t}), \quad (\text{A.27})$$

where W_4 is given in (4.30).

Appendix B

B.1 Placement of iso-latitude rings for HEALLPix

An iso-latitude ring is placed at $\theta = \theta_k$ such that area of the spherical annulus bounded by iso-latitude rings at $\theta = \theta_{k-1}, \theta_{k+1}$, denoted by $A_{\theta_{k-1}, \theta_{k+1}}$, is divided into two equal area sub-annuli, i.e.,

$$\frac{A_{\theta_{k-1}, \theta_{k+1}}}{2} = A_{\theta_{k-1}, \theta_k} = A_{\theta_k, \theta_{k+1}}, \quad (\text{B.1})$$

where

$$A_{\theta_{k-1}, \theta_{k+1}} = \int_{\theta_{k-1}}^{\theta_{k+1}} \int_{\phi=0}^{2\pi} \sin \theta \, d\theta = 2\pi(\cos \theta_{k-1} - \cos \theta_{k+1}) = 2\pi(z_{k-1} - z_{k+1}), \quad (\text{B.2})$$

and $z_k = \cos \theta_k$. Hence, the condition for placement of an iso-latitude ring at $\theta = \theta_k$ becomes

$$2\pi(z_{k-1} - z_k) = 2\pi(z_k - z_{k+1}) \Rightarrow z_k = \frac{(z_{k-1} + z_{k+1})}{2}. \quad (\text{B.3})$$

At $\mathfrak{L} = 0$, there is no partitioning of the sphere and the whole sphere can be considered a spherical annulus bounded by (trivial) iso-latitude rings at $\theta = 0, \pi$ or equivalently, at $z_0 = 1$ and $z_1 = -1$. At $\mathfrak{L} = 1$, an iso-latitude ring is placed such that the spherical annulus at resolution level $\mathfrak{L} = 0$ is divided into two equal area spherical annuli. As a result, there are 3 iso-latitude rings dividing the sphere into 2 equal area spherical annuli. At $\mathfrak{L} = 2$, two more iso-latitude rings are placed such that each of the two

spherical annuli at resolution level $\mathfrak{L} = 1$ are further divided into two equal area spherical annuli, resulting in 5 iso-latitude rings dividing the sphere into 4 equal area spherical annuli. Therefore, at a given resolution level \mathfrak{L} , there are $2^\mathfrak{L} + 1$ (or $2^\mathfrak{L} - 1$, excluding trivial iso-latitude rings) iso-latitude rings, indexed by $k = 0, 1, \dots, 2^\mathfrak{L}$ from top to bottom, dividing the sphere into $2^\mathfrak{L}$ equal area annuli which satisfy

$$\begin{aligned} A_{\theta_j, \theta_{j+1}} &= A_{\theta_k, \theta_{k+1}}, \quad \forall j, k = 0, 1, \dots, 2^\mathfrak{L}, \\ 2\pi(z_j - z_{j+1}) &= 2\pi(z_k - z_{k+1}), \quad \forall j, k = 0, 1, \dots, 2^\mathfrak{L}, \\ \Rightarrow (z_k - z_{k+1}) &= \text{constant} = A_{\text{SA}}, \quad \forall k = 0, 1, \dots, 2^\mathfrak{L}, \end{aligned} \quad (\text{B.4})$$

from which we get the following relations for position of iso-latitude rings at HEALPix resolution \mathfrak{L}

$$\begin{aligned} z_0 &= 1 = 1 - 0 \cdot A_{\text{SA}}, \\ z_0 - z_1 &= A_{\text{SA}} \Rightarrow z_1 = 1 - A_{\text{SA}}, \\ z_1 - z_2 &= A_{\text{SA}} \Rightarrow z_2 = 1 - 2A_{\text{SA}}, \\ &\vdots \\ z_{2^\mathfrak{L}-1} - z_{2^\mathfrak{L}} &= A_{\text{SA}} \Rightarrow z_{2^\mathfrak{L}} = 1 - 2^\mathfrak{L}A_{\text{SA}} = 1. \end{aligned} \quad (\text{B.5})$$

The (constant) area of the spherical annuli can be obtained from the last expression in (B.5) as

$$A_{\text{SA}} = \frac{2}{2^\mathfrak{L}} = \frac{1}{2^{\mathfrak{L}-1}}. \quad (\text{B.6})$$

Hence, the positions of iso-latitude rings, at HEALPix resolution \mathfrak{L} , can be compactly written as

$$z_k = \left(1 - \frac{k}{2^{\mathfrak{L}-1}}\right), \quad 0 \leq k \leq 2^\mathfrak{L}, \quad \mathfrak{L} \geq 1, \quad (\text{B.7})$$

where $k = 0, 2^\mathfrak{L}$ represents the position of trivial iso-latitude rings at $\theta = 0, \pi$ respectively.

B.2 Placement of iso-longitude rings for HEALLPix

Since area of the region between two iso-longitude rings at $\phi = \phi_1, \phi_2$, denoted by A_{ϕ_1, ϕ_2} , is given by

$$A_{\phi_1, \phi_2} = \int_{\phi_1}^{\phi_2} \int_{\theta=0}^{\pi} \sin \theta \, d\theta d\phi = 2(\phi_2 - \phi_1), \quad (\text{B.8})$$

iso-longitude rings must be equiangular in order to obtain equal area partitioning of the sphere along longitude as well.

There is no partitioning of the sphere at resolution level $\mathfrak{L} = 0$ and so, the whole sphere is considered as one region along longitude. At $\mathfrak{L} = 1$, the sphere is divided into two halves by placing 2 equiangular iso-longitude rings at $\phi = 0, \pi$. At $\mathfrak{L} = 2$, each of the two halves are further divided into two equal area regions by 2 more iso-longitude rings, resulting in 4 equiangular iso-longitude rings at $\phi = 0, \pi/2, \pi, 3\pi/2$, dividing the sphere into 4 equal area regions along longitude. Therefore, at a given resolution level \mathfrak{L} , there are $2^{\mathfrak{L}}$ equiangular iso-longitude rings, indexed by $k = 1, 2, \dots, 2^{\mathfrak{L}}$ in anticlockwise direction, dividing the sphere into $2^{\mathfrak{L}}$ equal area regions satisfying

$$\begin{aligned} A_{\phi_j, \phi_{j+1}} &= A_{\phi_k, \phi_{k+1}}, \quad \forall j, k = 1, 2, \dots, 2^{\mathfrak{L}}, \\ 2(\phi_{j+1} - \phi_j) &= 2(\phi_{k+1} - \phi_k), \quad \forall j, k = 1, 2, \dots, 2^{\mathfrak{L}}, \\ \Rightarrow (\phi_{k+1} - \phi_k) &= \text{constant} = A_{\text{LONG}}, \quad \forall k = 1, 2, \dots, 2^{\mathfrak{L}}, \end{aligned} \quad (\text{B.9})$$

from which we get the following expressions for the position of iso-longitude rings at HEALLPix resolution \mathfrak{L}

$$\begin{aligned} \phi_1 = 0 &\Rightarrow \phi_1 = 0 \cdot A_{\text{LONG}}, \\ \phi_2 - \phi_1 &= A_{\text{LONG}} \Rightarrow \phi_2 = A_{\text{LONG}}, \\ &\vdots \\ \phi_{2^{\mathfrak{L}}} - \phi_{2^{\mathfrak{L}}-1} &= A_{\text{LONG}} \Rightarrow \phi_{2^{\mathfrak{L}}} = (2^{\mathfrak{L}} - 1) A_{\text{LONG}}, \\ \phi_{2^{\mathfrak{L}+1}} - \phi_{2^{\mathfrak{L}}} &= A_{\text{LONG}}, \quad \phi_{2^{\mathfrak{L}+1}} = \phi_1 = 2\pi, \end{aligned} \quad (\text{B.10})$$

where the last relation is a consequence of periodicity in longitude, solving which gives us the (constant) area of the divided regions along longitude as

$$A_{\text{LONG}} = \frac{2\pi}{2^{\mathfrak{L}}}. \quad (\text{B.11})$$

So, the positions of iso-longitude rings, at HEALLPix resolution \mathfrak{L} , can be compactly written as

$$\phi_k = (k-1)A_{\text{LONG}} = \frac{2\pi(k-1)}{2^{\mathfrak{L}}} = \frac{\pi(k-1)}{2^{\mathfrak{L}-1}}, \quad 1 \leq k \leq 2^{\mathfrak{L}}, \mathfrak{L} \geq 1. \quad (\text{B.12})$$

Appendix C

C.1 Evaluating Slepian sub-integral for HEALPix north polar pixels

Defining $M \triangleq (m' + q')$ and the constants as

$$\begin{aligned} A^{\text{pz}} &= \frac{\pi(q-m)E_{ul}^{\text{pz}}}{a^{\text{pz}}}, & B^{\text{pz}} &= -\frac{\pi(q-m)E_{ur}^{\text{pz}}}{a^{\text{pz}}}, \\ C^{\text{pz}} &= -\frac{\pi(q-m)E_{\ell\ell}^{\text{pz}}}{a^{\text{pz}}}, & D^{\text{pz}} &= \frac{\pi(q-m)E_{\ell r}^{\text{pz}}}{a^{\text{pz}}}, \end{aligned} \quad (\text{C.1})$$

where a^{pz} , E_{ul}^{pz} , E_{ur}^{pz} , $E_{\ell\ell}^{\text{pz}}$ and $E_{\ell r}^{\text{pz}}$, which determine the shape and position of the pixel, are defined in Section 7.4.1, we rewrite the Slepian sub-integral in (7.48) as

$$\begin{aligned} G_{mq,m'q'}(r, c^{\text{pz}}) &= \int_{\theta_{r-1}}^{\theta_r} \int_{\frac{\pi}{2} + \frac{B^{\text{pz}}}{(q-m)\sin\frac{\theta}{2}}}^{\frac{\pi}{2} + \frac{A^{\text{pz}}}{(q-m)\sin\frac{\theta}{2}}} e^{i(q-m)\phi} \sin\theta e^{iM\theta} d\phi d\theta + \\ &\quad \int_{\theta_r}^{\theta_{r+1}} \int_{\frac{\pi}{2} + \frac{C^{\text{pz}}}{(q-m)\sin\frac{\theta}{2}}}^{\frac{\pi}{2} + \frac{D^{\text{pz}}}{(q-m)\sin\frac{\theta}{2}}} e^{i(q-m)\phi} \sin\theta e^{iM\theta} d\phi d\theta. \end{aligned} \quad (\text{C.2})$$

Analytical expressions for the Slepian sub-integral in (C.2) can be derived for two different cases of $q - m$.

C.1.1 $q - m \neq 0$:

Integrating (C.2) over ϕ results in the following expression

$$\begin{aligned}
 G_{mq,m'q'}(r, c^{\text{pz}}) &= \int_{\theta_{r-1}}^{\theta_r} \sin \theta e^{iM\theta} \frac{e^{i(q-m)\frac{\pi}{2}} e^{iB^{\text{pz}} \csc \frac{\theta}{2}} - e^{iA^{\text{pz}} \csc \frac{\theta}{2}}}{i(q-m)} d\theta + \\
 &\quad \int_{\theta_r}^{\theta_{r+1}} \sin \theta e^{iM\theta} \frac{e^{iD^{\text{pz}} \csc \frac{\theta}{2}} - e^{i(q-m)\frac{\pi}{2}} e^{iC^{\text{pz}} \csc \frac{\theta}{2}}}{i(q-m)} d\theta \\
 &= \frac{-8e^{i\nu}}{(q-m)} \left(\int_{u_{r-1}}^{u_r} \left[\frac{\sqrt{u^2-1}}{u} + s_M \frac{i}{u} \right]^{2|M|} \frac{\cos \Upsilon u \sin(\tau u + \nu) + i \sin \Upsilon u \sin(\tau u + \nu)}{u^3} du \right. \\
 &\quad \left. - \int_{u_r}^{u_{r+1}} \left[\frac{\sqrt{u^2-1}}{u} + s_M \frac{i}{u} \right]^{2|M|} \frac{\cos \chi u \sin(\psi u + \nu) + i \sin \chi u \sin(\psi u + \nu)}{u^3} du \right), \quad (\text{C.3})
 \end{aligned}$$

where we have used the substitution $u = \csc(\theta/2)$,

$$s_M = \begin{cases} 1, & M \geq 0, \\ -1, & M < 0, \end{cases} \quad (\text{C.4})$$

and the constants are given by

$$\begin{aligned}
 \tau &= \frac{(B^{\text{pz}} - A^{\text{pz}})}{2}, & \Upsilon &= \frac{(B^{\text{pz}} + A^{\text{pz}})}{2}, \\
 \psi &= \frac{(C^{\text{pz}} - D^{\text{pz}})}{2}, & \chi &= \frac{(C^{\text{pz}} + D^{\text{pz}})}{2},
 \end{aligned} \quad (\text{C.5})$$

$$\nu = (q-m) \frac{\pi}{4}. \quad (\text{C.6})$$

Expanding $\left[\frac{\sqrt{u^2-1}}{u} + s_M \frac{i}{u} \right]^{2|M|}$ as the following binomial series

$$\left[\frac{\sqrt{u^2-1}}{u} + s_M \frac{i}{u} \right]^{2|M|} = \frac{1}{u^{2|M|}} \sum_{J_1=0}^{2|M|} \binom{2|M|}{J_1} (s_M i)^{J_1} (u^2 - 1)^{\frac{1}{2}(2|M|-J_1)}, \quad (\text{C.7})$$

and using the following sum-product formulae for sine and cosine functions [121],

$$\begin{aligned}
 2 \cos(a) \sin(b) &= (\sin(a+b) - \sin(a-b)), \\
 2 \sin(a) \sin(b) &= (\cos(a-b) - \cos(a+b)),
 \end{aligned} \quad (\text{C.8})$$

we can rewrite $G_{mq,m'q'}(r, c^{\text{pz}})$ as

$$\begin{aligned}
 G_{mq,m'q'}(r, c^{\text{pz}}) &= \frac{-8e^{i\nu}}{(q-m)} \sum_{J_1=0}^{2|M|} \binom{2|M|}{J_1} (s_M i)^{J_1} \left[\int_{u_{r-1}}^{u_r} \frac{(u^2-1)^{(|M|-J_1/2)}}{u^{3+2|M|}} \frac{1}{2} \times \right. \\
 &\left. \left(\sin\{(\Upsilon+\tau)u+\nu\} - \sin\{(\Upsilon-\tau)u-\nu\} + i \cos\{(\Upsilon-\tau)u-\nu\} - \right. \right. \\
 &\left. \left. i \cos\{(\Upsilon+\tau)u+\nu\} \right) du - \int_{u_r}^{u_{r+1}} \frac{(u^2-1)^{(|M|-J_1/2)}}{u^{3+2|M|}} \frac{1}{2} \left(\sin\{(\chi+\psi)u+\nu\} - \right. \right. \\
 &\left. \left. \sin\{(\chi-\psi)u-\nu\} + i \cos\{(\chi-\psi)u-\nu\} - i \cos\{(\chi+\psi)u+\nu\} \right) du \right].
 \end{aligned}$$

Expanding $(u^2-1)^{(|M|-J_1/2)}$ further in a generalized binomial series as

$$\begin{aligned}
 (u^2-1)^{(|M|-J_1/2)} &= \sum_{J_2=0}^{\Gamma_u} \binom{|M|-J_1/2}{J_2} (-1)^{J_2} (u^2)^{(|M|-J_1/2-J_2)}, \quad u \in [u_{r-1}, u_r], \\
 (u^2-1)^{(|M|-J_1/2)} &= \sum_{J_2=0}^{\Gamma_l} \binom{|M|-J_1/2}{J_2} (-1)^{J_2} (u^2)^{(|M|-J_1/2-J_2)}, \quad u \in [u_r, u_{r+1}],
 \end{aligned} \tag{C.9}$$

Slepian sub-integral becomes

$$\begin{aligned}
 G_{mq,m'q'}(r, c^{\text{pz}}) &= \frac{-4e^{i\nu}}{(q-m)} \sum_{J_1=0}^{2|M|} \binom{2|M|}{J_1} (s_M i)^{J_1} \left[\sum_{J_2=0}^{\Gamma_u} \binom{|M|-J_1/2}{J_2} (-1)^{J_2} \times \right. \\
 &\int_{u_{r-1}}^{u_r} \frac{1}{u^{(J_1+2J_2+3)}} \left(\sin\{(\Upsilon+\tau)u+\nu\} - \sin\{(\Upsilon-\tau)u-\nu\} + i \cos\{(\Upsilon-\tau)u-\nu\} - \right. \\
 &\left. i \cos\{(\Upsilon+\tau)u+\nu\} \right) du - \sum_{J_2=0}^{\Gamma_l} \binom{|M|-J_1/2}{J_2} (-1)^{J_2} \int_{u_r}^{u_{r+1}} \frac{1}{u^{(J_1+2J_2+3)}} \left(\sin\{(\chi+\psi)u+\nu\} \right. \\
 &\left. - \sin\{(\chi-\psi)u-\nu\} + i \cos\{(\chi-\psi)u-\nu\} - i \cos\{(\chi+\psi)u+\nu\} \right) du \Big], \tag{C.10}
 \end{aligned}$$

where Γ_u and Γ_l are given by

$$\Gamma_u = \Gamma_l = \begin{cases} |M| - J_1/2, & J_1 \bmod 2 = 0, \\ \infty, & J_1 \bmod 2 = 1. \end{cases} \tag{C.11}$$

Here $\binom{2|M|}{J_1}$ is binomial coefficient and $\binom{|M|-J_1/2}{J_2}$ is generalized binomial coefficient. Through integration by parts, the integral $\int_{u_1}^{u_2} \frac{\sin(xu+y)}{u^{(J_1+2J_2+3)}} du$ can be formulated as

$$\begin{aligned} & \int_{u_1}^{u_2} \frac{\sin(xu+y)}{u^{(J_1+2J_2+3)}} du = \\ & \sum_{J_3=0}^{(J_1+2J_2+1)} (-1)^{\lceil \frac{J_3+1}{2} \rceil} \frac{(J_1+2J_2+1-J_3)! x^{J_3}}{(J_1+2J_2+2)!} \left[\begin{aligned} & \left[\frac{\sin(xu+y)}{u^{(J_1+2J_2+2-J_3)}} \right]_{u_1}^{u_2}, \quad J_3 \bmod 2 = 0 \\ & \left[\frac{\cos(xu+y)}{u^{(J_1+2J_2+2-J_3)}} \right]_{u_1}^{u_2}, \quad J_3 \bmod 2 = 1 \end{aligned} \right] + \\ & (-1)^{\lfloor \frac{J_1+2J_2+2}{2} \rfloor} \frac{x^{(J_1+2J_2+2)}}{(J_1+2J_2+2)!} \left[\begin{aligned} & \int_{u_1}^{u_2} \frac{\cos(xu+y)}{u} du, \quad (J_1+2J_2+3) \bmod 2 = 0 \\ & \int_{u_1}^{u_2} \frac{\sin(xu+y)}{u} du, \quad (J_1+2J_2+3) \bmod 2 = 1 \end{aligned} \right]. \quad (\text{C.12}) \end{aligned}$$

Similarly, $\int_{u_1}^{u_2} \frac{\cos(xu+y)}{u^{(J_1+2J_2+3)}} du$ can be integrated by parts to get the following expression

$$\begin{aligned} & \int_{u_1}^{u_2} \frac{\cos(xu+y)}{u^{(J_1+2J_2+3)}} du = \\ & \sum_{J_3=0}^{(J_1+2J_2+1)} (-1)^{\lceil \frac{J_3+2}{2} \rceil} \frac{(J_1+2J_2+1-J_3)! x^{J_3}}{(J_1+2J_2+2)!} \left[\begin{aligned} & \left[\frac{\cos(xu+y)}{u^{(J_1+2J_2+2-J_3)}} \right]_{u_1}^{u_2}, \quad J_3 \bmod 2 = 0 \\ & \left[\frac{\sin(xu+y)}{u^{(J_1+2J_2+2-J_3)}} \right]_{u_1}^{u_2}, \quad J_3 \bmod 2 = 1 \end{aligned} \right] + \\ & (-1)^{\lfloor \frac{J_1+2J_2+3}{2} \rfloor} \frac{x^{(J_1+2J_2+2)}}{(J_1+2J_2+2)!} \left[\begin{aligned} & \int_{u_1}^{u_2} \frac{\sin(xu+y)}{u} du, \quad (J_1+2J_2+3) \bmod 2 = 0 \\ & \int_{u_1}^{u_2} \frac{\cos(xu+y)}{u} du, \quad (J_1+2J_2+3) \bmod 2 = 1 \end{aligned} \right]. \quad (\text{C.13}) \end{aligned}$$

Furthermore, the integrals $\int_{u_1}^{u_2} \frac{\sin(xu+y)}{u} du$, $\int_{u_1}^{u_2} \frac{\cos(xu+y)}{u} du$ can be solved as

$$\begin{aligned} \int_{u_1}^{u_2} \frac{\sin(xu+y)}{u} du &= \begin{cases} \cos y \int_{u_1}^{u_2} \frac{\sin au}{u} du + \sin y \int_{u_1}^{u_2} \frac{\cos au}{u} du, & a \neq 0, \\ \sin y \ln\left(\frac{u_2}{u_1}\right), & a = 0, \end{cases} \\ &= \begin{cases} \cos y T_S(a, u_1, u_2) + \sin y T_C(a, u_1, u_2), & a \neq 0, \\ \sin y \ln\left(\frac{u_2}{u_1}\right), & a = 0, \end{cases} \quad (\text{C.14}) \end{aligned}$$

and

$$\begin{aligned}
 \int_{u_1}^{u_2} \frac{\cos(xu + y)}{u} du &= \begin{cases} \cos y \int_{u_1}^{u_2} \frac{\cos au}{u} du - \sin y \int_{u_1}^{u_2} \frac{\sin au}{u} du, & a \neq 0, \\ \cos y \ln\left(\frac{u_2}{u_1}\right), & a = 0, \end{cases} \\
 &= \begin{cases} \cos y T_C(a, u_1, u_2) - \sin y T_S(a, u_1, u_2), & a \neq 0, \\ \cos y \ln\left(\frac{u_2}{u_1}\right), & a = 0, \end{cases} \quad (\text{C.15})
 \end{aligned}$$

where T_S and T_C are the Maclaurin series expansions given in (7.62) and (7.63) respectively. Putting together (C.15), (C.14), (C.13), (C.12) and noting that $(-1)^{\lceil \frac{J_3+2}{2} \rceil} = (-1)^{J_3} (-1)^{\lceil \frac{J_3+1}{2} \rceil}$, $(-1)^{\lfloor \frac{J_1+2J_2+3}{2} \rfloor} = (-1)^{(J_1+2J_2+2)} (-1)^{\lfloor \frac{J_1+2J_2+2}{2} \rfloor}$, Slepian sub-integral in (C.10) is formulated as

$$\begin{aligned}
 G_{mq,m'q'}(r, c^{\text{pz}}) &= \frac{-4e^{i\nu}}{(q-m)} \sum_{J_1=0}^{2|M|} \binom{2|M|}{J_1} (s_M i)^{J_1} \times \\
 &\quad \left(F^{\text{pz}}(J_1, M, A^{\text{pz}}, B^{\text{pz}}, \nu, \Gamma_u, \theta_{r-1}, \theta_r) - F^{\text{pz}}(J_1, M, D^{\text{pz}}, C^{\text{pz}}, \nu, \Gamma_l, \theta_r, \theta_{r+1}) \right), \quad (\text{C.16})
 \end{aligned}$$

where F^{pz} is given in (7.51).

C.1.2 $q - m = 0$:

For this case, Slepian sub-integral in (C.2) takes the following simpler form,

$$\begin{aligned}
 G_{mq,m'q'}(r, c^{\text{pz}}) &= \frac{\pi}{2} \int_{\theta_{r-1}}^{\theta_r} e^{iM\theta} \sin \theta d\theta - \frac{2\pi}{a^{\text{pz}}} (E_{ul}^{\text{pz}} + E_{ur}^{\text{pz}}) \int_{\theta_{r-1}}^{\theta_r} e^{iM\theta} \cos \frac{\theta}{2} d\theta - \\
 &\quad \frac{\pi}{2} \int_{\theta_r}^{\theta_{r+1}} e^{iM\theta} \sin \theta d\theta + \frac{2\pi}{a^{\text{pz}}} (E_{\ell\ell}^{\text{pz}} + E_{\ell r}^{\text{pz}}) \int_{\theta_r}^{\theta_{r+1}} e^{iM\theta} \cos \frac{\theta}{2} d\theta. \quad (\text{C.17})
 \end{aligned}$$

Performing integration by parts, we conclude that

$$\int_{\theta_1}^{\theta_2} e^{ix\theta} \cos y\theta d\theta = \frac{y}{y^2 - x^2} \left[e^{ix\theta} \left(\sin y\theta + \frac{ix}{y} \cos y\theta \right) \right]_{\theta_1}^{\theta_2}, \quad (\text{C.18})$$

$$\int_{\theta_1}^{\theta_2} e^{ix\theta} \sin y\theta \, d\theta = \frac{y}{y^2 - x^2} \left[-e^{ix\theta} \left(\cos y\theta - \frac{ix}{y} \sin y\theta \right) \right]_{\theta_1}^{\theta_2}, \quad x \neq \pm y, \quad (\text{C.19})$$

and

$$\int_{\theta_1}^{\theta_2} e^{\pm iy\theta} \sin y\theta \, d\theta = \frac{1}{4y} (\cos 2y\theta_1 - \cos 2y\theta_2) \pm \frac{i}{2} (\theta_2 - \theta_1) \mp \frac{i}{4y} (\sin 2y\theta_2 - \sin 2y\theta_1). \quad (\text{C.20})$$

As a result, $G_{mq,m'q'}(r, c^{\text{pz}})$ in (C.17) becomes

$$G_{mq,m'q'}(r, c^{\text{pz}}) = \begin{cases} \frac{\pi}{2} \left(\frac{C_1(M, \theta_{r-1}, \theta_r) - C_1(M, \theta_r, \theta_{r+1})}{1-M^2} \right) + \\ \frac{4}{1-4M^2} \left(C_2 \left(M, \frac{\pi E_{ul}^{\text{pz}}}{a^{\text{pz}}}, -\frac{\pi E_{ur}^{\text{pz}}}{a^{\text{pz}}}, \theta_{r-1}, \theta_r \right) + \right. \\ \left. C_2 \left(M, -\frac{\pi E_{\ell\ell}^{\text{pz}}}{a^{\text{pz}}}, \frac{\pi E_{\ell r}^{\text{pz}}}{a^{\text{pz}}}, \theta_r, \theta_{r+1} \right) \right), & M \neq \pm 1, \\ \frac{\pi}{2} \left(C_3(M, \theta_{r-1}, \theta_r) - C_3(M, \theta_r, \theta_{r+1}) \right) + \\ \frac{4}{1-4M^2} \left(C_2 \left(M, \frac{\pi E_{ul}^{\text{pz}}}{a^{\text{pz}}}, -\frac{\pi E_{ur}^{\text{pz}}}{a^{\text{pz}}}, \theta_{r-1}, \theta_r \right) + \right. \\ \left. C_2 \left(M, -\frac{\pi E_{\ell\ell}^{\text{pz}}}{a^{\text{pz}}}, \frac{\pi E_{\ell r}^{\text{pz}}}{a^{\text{pz}}}, \theta_r, \theta_{r+1} \right) \right), & M = \pm 1, \end{cases} \quad (\text{C.21})$$

where the functions C_1 , C_2 and C_3 are given in (7.52).

C.2 Evaluating Slepian sub-integral for HEALPix equatorial pixels

Defining $M \triangleq (m' + q')$ and the constants as

$$\begin{aligned} A^{\text{ez}} &= \frac{2}{3} - E_{ul}^{\text{ez}} a^{\text{ez}}, & B^{\text{ez}} &= \frac{2}{3} - E_{ur}^{\text{ez}} a^{\text{ez}}, \\ C^{\text{ez}} &= \frac{2}{3} - E_{\ell\ell}^{\text{ez}} a^{\text{ez}}, & D^{\text{ez}} &= \frac{2}{3} - E_{\ell r}^{\text{ez}} a^{\text{ez}}, \end{aligned} \quad (\text{C.22})$$

where a^{ez} , E_{ul}^{ez} , E_{ur}^{ez} , $E_{\ell\ell}^{\text{ez}}$ and $E_{\ell r}^{\text{ez}}$, which determine the shape and position of the pixel, are defined in Section 7.4.1, we rewrite the Slepian sub-integral in (7.65) as

$$\begin{aligned}
 G_{mq,m'q'}(r, 1) = & \int_{\theta_{r-1}}^{\theta_r} \int_{\frac{(\cos \theta - A^{\text{ez}})}{b}}^{\frac{(B^{\text{ez}} - \cos \theta)}{b}} e^{i(q-m)\phi} \sin \theta e^{i(m'+q')\theta} d\phi d\theta \\
 & + \int_{\theta_r}^{\theta_{r+1}} \int_{\frac{(C^{\text{ez}} - \cos \theta)}{b}}^{\frac{(\cos \theta - D^{\text{ez}})}{b}} e^{i(q-m)\phi} \sin \theta e^{i(m'+q')\theta} d\phi d\theta. \quad (\text{C.23})
 \end{aligned}$$

We derive analytical expressions for $G_{mq,m'q'}(r, 1)$ for two different cases of $q - m$.

C.2.1 $q - m \neq 0$:

Integrating (C.23) over ϕ , we get

$$\begin{aligned}
 G_{mq,m'q'}(r, 1) = & \frac{2}{(q-m)} \left[e^{\frac{i\mu(B^{\text{ez}} - A^{\text{ez}})}{2}} \int_{u_{r-1}}^{u_r} \left[u + s_M i \sqrt{1-u^2} \right]^{|M|} \times \right. \\
 & \left. \sin \left(\mu u - \mu \frac{A^{\text{ez}} + B^{\text{ez}}}{2} \right) du - e^{\frac{i\mu(C^{\text{ez}} - D^{\text{ez}})}{2}} \int_{u_r}^{u_{r+1}} \left[u + s_M i \sqrt{1-u^2} \right]^{|M|} \times \right. \\
 & \left. \sin \left(\mu u - \mu \frac{C^{\text{ez}} + D^{\text{ez}}}{2} \right) du \right], \quad (\text{C.24})
 \end{aligned}$$

where we have used the substitution $u = \cos \theta$, s_M is defined in (C.4) and $\mu \triangleq (q-m)/b$. Expanding $\left[u + i s_M \sqrt{1-u^2} \right]^{|M|}$ in binomial series as

$$\left[u + i s_M \sqrt{1-u^2} \right]^{|M|} = \sum_{J_1=0}^{|M|} \binom{|M|}{J_1} u^{(|M|-J_1)} (s_M i)^{J_1} (1-u^2)^{J_1/2}, \quad (\text{C.25})$$

we can rewrite the Slepian sub-integral for equatorial pixels as

$$\begin{aligned}
 G_{mq,m'q'}(r, 1) = & \frac{2}{(q-m)} \sum_{J_1=0}^{|M|} \binom{|M|}{J_1} (s_M i)^{J_1} \left[e^{\frac{i\mu(B^{\text{ez}} - A^{\text{ez}})}{2}} \int_{u_{r-1}}^{u_r} u^{(|M|-J_1)} (1-u^2)^{J_1/2} \times \right. \\
 & \left. \sin \left(\mu u - \mu \frac{A^{\text{ez}} + B^{\text{ez}}}{2} \right) du - e^{\frac{i\mu(C^{\text{ez}} - D^{\text{ez}})}{2}} \int_{u_r}^{u_{r+1}} u^{(|M|-J_1)} (1-u^2)^{J_1/2} \times \right. \\
 & \left. \sin \left(\mu u - \mu \frac{C^{\text{ez}} + D^{\text{ez}}}{2} \right) du \right]. \quad (\text{C.26})
 \end{aligned}$$

The term $(1 - u^2)^{J_1/2}$ inside the integral can further be expanded using generalized binomial series as

$$\begin{aligned} (1 - u^2)^{J_1/2} &= \sum_{J_2=0}^{\Gamma_u} \binom{J_1/2}{J_2} (-1)^{J_2} u^{2J_2}, \quad u \in [u_{r-1}, u_r], \\ (1 - u^2)^{J_1/2} &= \sum_{J_2=0}^{\Gamma_l} \binom{J_1/2}{J_2} (-1)^{J_2} u^{2J_2}, \quad u \in [u_r, u_{r+1}], \end{aligned} \quad (\text{C.27})$$

where Γ_u and Γ_l are given by

$$\Gamma_u = \Gamma_l = \begin{cases} J_1/2, & J_1 \bmod 2 = 0, \\ \infty, & J_1 \bmod 2 = 1. \end{cases} \quad (\text{C.28})$$

Here $\binom{|M|}{J_1}$ is binomial coefficient and $\binom{J_1/2}{J_2}$ is generalized binomial coefficient.

Putting (C.27) in (C.26), we get

$$\begin{aligned} G_{mq,m'q'}(r, 1) &= \frac{2}{q - m} \sum_{J_1=0}^{|M|} \binom{|M|}{J_1} (s_M i)^{J_1} \times \\ &\left[\sum_{J_2=0}^{\Gamma_u} \binom{J_1/2}{J_2} (-1)^{J_2} e^{\frac{i\mu(B^{ez} - A^{ez})}{2}} \int_{u_{r-1}}^{u_r} u^{(2J_2 + |M| - J_1)} \sin\left(\mu u - \mu \frac{A^{ez} + B^{ez}}{2}\right) du \right. \\ &\left. - \sum_{J_2=0}^{\Gamma_l} \binom{J_1/2}{J_2} (-1)^{J_2} e^{\frac{i\mu(C^{ez} - D^{ez})}{2}} \int_{u_r}^{u_{r+1}} u^{(2J_2 + |M| - J_1)} \sin\left(\mu u - \mu \frac{C^{ez} + D^{ez}}{2}\right) du \right], \end{aligned} \quad (\text{C.29})$$

in which the integral $\int_{u_1}^{u_2} u^{(2J_2 + |M| - J_1)} \sin(\mu(u - y)) du$ can be solved through integration by parts to obtain the following expression

$$\begin{aligned} \int_{u_1}^{u_2} u^{(2J_2 + |M| - J_1)} \sin(\mu(u - y)) du &= \sum_{J_3=1}^{(2J_2 + |M| - J_1 + 1)} (-1)^{\lceil \frac{J_3 + 1}{2} \rceil} \mu^{-J_3} \times \\ &\frac{(2J_2 + |M| - J_1)!}{(2J_2 + |M| - J_1 + 1 - J_3)!} \times \begin{cases} \left[u^{(2J_2 + |M| - J_1 + 1 - J_3)} \sin(\mu(u - y)) \right]_{u_1}^{u_2}, & J_3 \bmod 2 = 0, \\ \left[u^{(2J_2 + |M| - J_1 + 1 - J_3)} \cos(\mu(u - y)) \right]_{u_1}^{u_2}, & J_3 \bmod 2 = 1. \end{cases} \end{aligned} \quad (\text{C.30})$$

Using (C.30) in (C.29), Slepian sub-integral for equatorial pixels becomes

$$G_{mq,m'q'}(r, 1) = \frac{2}{(q-m)} \sum_{J_1=0}^{|M|} \binom{|M|}{J_1} (s_M i)^{J_1} \times \left(F^{\text{ez}}(J_1, M, A^{\text{ez}}, B^{\text{ez}}, \mu, \Gamma_u, \theta_{r-1}, \theta_r) - F^{\text{ez}}(J_1, M, D^{\text{ez}}, C^{\text{ez}}, \mu, \Gamma_l, \theta_r, \theta_{r+1}) \right), \quad (\text{C.31})$$

where F^{ez} is given in (7.68).

Alternate Formulation in terms of Bessel Function

We can write (C.23) in an alternate manner as

$$G_{mq,m'q'}(r, 1) = \frac{-1}{2(q-m)} \left[e^{i\mu B^{\text{ez}}} \left(\int_{\theta_{r-1}}^{\theta_r} e^{i(M+1)\theta} e^{-i\mu \cos \theta} d\theta - \int_{\theta_{r-1}}^{\theta_r} e^{i(M-1)\theta} e^{-i\mu \cos \theta} d\theta \right) - e^{-i\mu A^{\text{ez}}} \left(\int_{\theta_{r-1}}^{\theta_r} e^{i(M+1)\theta} e^{i\mu \cos \theta} d\theta - \int_{\theta_{r-1}}^{\theta_r} e^{i(M-1)\theta} e^{i\mu \cos \theta} d\theta \right) + e^{-i\mu D^{\text{ez}}} \left(\int_{\theta_r}^{\theta_{r+1}} e^{i(M+1)\theta} e^{i\mu \cos \theta} d\theta - \int_{\theta_r}^{\theta_{r+1}} e^{i(M-1)\theta} e^{i\mu \cos \theta} d\theta \right) - e^{i\mu C^{\text{ez}}} \left(\int_{\theta_r}^{\theta_{r+1}} e^{i(M+1)\theta} e^{-i\mu \cos \theta} d\theta - \int_{\theta_r}^{\theta_{r+1}} e^{i(M-1)\theta} e^{-i\mu \cos \theta} d\theta \right) \right], \quad (\text{C.32})$$

where again $\mu = (q-m)/b$. Now using the following Jacobi-Anger expansion

$$e^{i\mu \cos \theta} = \sum_{n_1=-\infty}^{\infty} i^{n_1} J_{n_1}(\mu) e^{-in_1\theta}, \quad (\text{C.33})$$

where $J_{n_1}(\mu)$ is the Bessel function of first kind and order n_1 , evaluated at $\mu = (q-m)/b$, and solving the integral of the form $\int_{\theta_1}^{\theta_2} e^{iM\theta} e^{i\mu \cos \theta} d\theta$ as

$$\begin{aligned} \int_{\theta_1}^{\theta_2} e^{iM\theta} e^{i\mu \cos \theta} d\theta &= \int_{\theta_1}^{\theta_2} e^{iM\theta} \sum_{n_1=-\infty}^{\infty} i^{n_1} J_{n_1}(\mu) e^{-in_1\theta} d\theta \\ &= \sum_{n_1=-\infty}^{\infty} i^{n_1} J_{n_1}(\mu) \frac{e^{i(M-n_1)\theta_2} - e^{i(M-n_1)\theta_1}}{i(M-n_1)} \\ &= (\theta_2 - \theta_1) i^M J_M(\mu) * \varepsilon(M; \theta_1, \theta_2), \end{aligned} \quad (\text{C.34})$$

where $\varepsilon(M; \theta_1, \theta_2)$ is defined in (7.75) and $*$ denotes the Euclidean domain convolution, Slepian sub-integral for the equatorial pixels can be reformulated as

$$G_{mq,m'q'}(r, 1) = F^{\text{ez}}(B^{\text{ez}}, M, b, -\mu, \theta_{r-1}, \theta_r) - F^{\text{ez}}(A^{\text{ez}}, M, b, \mu, \theta_{r-1}, \theta_r) + \\ F^{\text{ez}}(D^{\text{ez}}, M, b, \mu, \theta_r, \theta_{r+1}) - F^{\text{ez}}(C^{\text{ez}}, M, b, -\mu, \theta_r, \theta_{r+1}), \quad (\text{C.35})$$

where F^{ez} is defined in (7.68).

We note that both $J_{n_1}(\cdot)$ and $\varepsilon(n_2; \cdot, \cdot)$ have infinite mathematical support due to which their convolution will have infinite support. However, we observe that $J_{n_1}(\cdot)$ is a much rapidly decreasing function compared to $\varepsilon(n_2; \cdot, \cdot)$ and hence, essentially determines the mathematical support of their convolution. The Jacobi-Anger expansion in (C.33) is truncated when $|J_{n_1}(\cdot)| \leq \text{tol}$, where tol is a preset tolerance. Denoting the lower and upper bounds on n_1 by n_1^l and n_1^u respectively, we truncate $\varepsilon(n_2; \cdot, \cdot)$ as

$$n_2^l = -2(L - 1) - 1 - n_1^l, \quad (\text{C.36}) \\ n_2^u = 2(L - 1) + 1 - n_1^u,$$

where n_2^l and n_2^u are the values of n_2 at which $\varepsilon(n_2; \cdot, \cdot)$ is truncated in the negative and positive directions respectively, and we have used the fact that $M_{\min} = -2(L - 1)$ and $M_{\max} = 2(L - 1)$ in (7.74).

C.2.2 $q - m = 0$:

For this case, $G_{mq,m'q'}(r, 1)$ in (C.23) is given by the following simplified expression

$$G_{mq,m'q'}(r, 1) = \frac{1}{b} \left[(B^{\text{ez}} + A^{\text{ez}}) \int_{\theta_{r-1}}^{\theta_r} e^{iM\theta} \sin \theta d\theta - \int_{\theta_{r-1}}^{\theta_r} e^{iM\theta} \sin 2\theta d\theta + \right. \\ \left. \int_{\theta_r}^{\theta_{r+1}} e^{iM\theta} \sin 2\theta d\theta - (D^{\text{ez}} + C^{\text{ez}}) \int_{\theta_r}^{\theta_{r+1}} e^{iM\theta} \sin \theta d\theta \right], \quad (\text{C.37})$$

which can be easily solved, using (C.19) and (C.20), to get the expressions in (7.67).

Bibliography

- [1] J. Princen and A. Bradley, “Analysis/synthesis filter bank design based on time domain aliasing cancellation,” *IEEE Trans. Acoust., Speech, Signal Process.*, vol. 34, no. 5, pp. 1153–1161, Oct. 1986.
- [2] G. Boudreaux-Bartels and T. Parks, “Time-varying filtering and signal estimation using Wigner distribution synthesis techniques,” *IEEE Trans. Acoust., Speech, Signal Process.*, vol. 34, no. 3, pp. 442–451, June 1986.
- [3] J. D. Scargle, “Studies in astronomical time series analysis. II - statistical aspects of spectral analysis of unevenly spaced data,” *Astrophys. J.*, vol. 263, pp. 835–853, Dec. 1982.
- [4] A. J. Jerri, “The Shannon sampling theorem—its various extensions and applications: A tutorial review,” *Proc. IEEE*, vol. 65, no. 11, pp. 1565–1596, Nov. 1977.
- [5] F. Hlawatsch, W. Kozek, and W. Krattenthaler, “Time-frequency subspaces and their application to time-varying filtering,” in *Proc. IEEE Int. Conf. Acoust., Speech, Signal Process., ICASSP’1990*, Apr. 1990, vol. 3, pp. 1607–1610.
- [6] W. Kozek and F. Hlawatsch, “A comparative study of linear and nonlinear time-frequency filters,” in *Proc. IEEE-SP Int. Symp. Time-Freq., Time-Scale Anal., 1992.*, Oct. 1992, pp. 163–166.
- [7] L. Cohen, *Time-frequency analysis: Theory and applications*, Prentice-Hall Inc., 1995.
- [8] J. G. Proakis and D. K. Manolakis, *Digital Signal Processing: Principles, Algorithms, and Applications*, Prentice-Hall Inc., New Jersey, USA, fourth edition, 2006.
- [9] L. Cohen, “Time-frequency distributions-a review,” *Proc. IEEE*, vol. 77, no. 7, pp. 941–981, July 1989.
- [10] M. Mojiri, M. Karimi-Ghartemani, and A. Bakhshai, “Time-domain signal analysis using adaptive notch filter,” *IEEE Trans. Signal Process.*, vol. 55, no. 1, pp. 85–93, Jan. 2007.

-
- [11] C. Knapp and G. Carter, "The generalized correlation method for estimation of time delay," *IEEE Trans. Acoust., Speech, Signal Process.*, vol. 24, no. 4, pp. 320–327, Aug. 1976.
- [12] D. J. Thomson, "Spectrum estimation and harmonic analysis," *Proc. IEEE*, vol. 70, no. 9, pp. 1055–1096, Sept. 1982.
- [13] A. M. Sayeed and D. L. Jones, "Optimal detection using bilinear time-frequency and time-scale representations," *IEEE Trans. Signal Process.*, vol. 43, no. 12, pp. 2872–2883, Dec. 1995.
- [14] D. Griffin and J. Lim, "Signal estimation from modified short-time Fourier transform," *IEEE Trans. Acoust., Speech, Signal Process.*, vol. 32, no. 2, pp. 236–243, Apr. 1984.
- [15] B. Vidakovic and C. B. Lozoya, "On time-dependent wavelet denoising," *IEEE Trans. Signal Process.*, vol. 46, no. 9, pp. 2549–2554, Sept. 1998.
- [16] H. L. V. Trees, K. L. Bell, and (with) Z. Tian, *Detection, Estimation, and Modulation Theory: Detection, Estimation, and Linear Modulation Theory*, John Wiley & Sons Inc., New Jersey, USA, second edition, 2013.
- [17] S. S. Kang and M. H. Lee, "An expanded 2D DCT algorithm based on convolution," *IEEE Transactions on Consumer Electronics*, vol. 39, no. 3, pp. 159–165, Aug. 1993.
- [18] X. Wang, "Moving window-based double haar wavelet transform for image processing," *IEEE Trans. Image Process.*, vol. 15, no. 9, pp. 2771–2779, Sept. 2006.
- [19] H. Lin, J. Si, and G. P. Abousleman, "Orthogonal rotation-invariant moments for digital image processing," *IEEE Trans. Image Process.*, vol. 17, no. 3, pp. 272–282, Mar. 2008.
- [20] F. J. Simons and D. V. Wang, "Spatiospectral concentration in the cartesian plane," *Intern. J. Geo-math.*, vol. 2, no. 1, pp. 1–36, Apr. 2011.
- [21] S. Stanković and I. Orović, "An approach to 2D signals recovering in compressive sensing context," *Circuits Syst. Signal Process.*, vol. 36, pp. 1700–1713, 2017.
- [22] T. S. Pollock, T. D. Abhayapala, and R. A. Kennedy, "Introducing space into MIMO capacity calculations," *J. Telecommun. Syst.*, vol. 24, no. 2, pp. 415–436, Oct. 2003.
- [23] Q. Nadeem, A. Kammoun, M. Debbah, and M. S. Alouini, "A generalized spatial correlation model for 3D mimo channels based on the Fourier coefficients of power spectrums," *IEEE Trans. Signal Process.*, vol. 63, no. 14, pp. 3671–3686, July 2015.

- [24] R. A. Kennedy, Z. Khalid, and Y. F. Alem, "Spatial correlation from multipath with 3D power distributions having rotational symmetry," in *Proc. IEEE Int. Conf. Sig. Process. and Comm. Sys., ICSPCS*, Carrara, VIC, Australia, Dec. 2013.
- [25] Y. F. Alem, Z. Khalid, and R. A. Kennedy, "3D spatial fading correlation for uniform angle of arrival distribution," *IEEE Commun. Lett.*, vol. 19, no. 6, pp. 1073–1076, June 2015.
- [26] S. Yan, H. Sun, U. P. Svensson, X. Ma, and J. M. Hovem, "Optimal modal beamforming for spherical microphone arrays," *IEEE Trans. Audio, Speech, Language Process.*, vol. 19, no. 2, pp. 361–371, Feb. 2011.
- [27] R. Ng, R. Ramamoorthi, and P. Hanrahan, "Triple product wavelet integrals for all-frequency relighting," *ACM Trans. Graph.*, vol. 23, no. 3, pp. 477–487, Aug. 2004.
- [28] P.-M. Lam, C.-S. Leung, and T.-T. Wong, "Noise-resistant fitting for spherical harmonics," *IEEE Transactions on Visualization and Computer Graphics*, vol. 12, pp. 254–265, 2006.
- [29] S. Nadeem, Z. Su, W. Zeng, A. Kaufman, and X. Gu, "Spherical parameterization balancing angle and area distortions," *IEEE Transactions on Visualization and Computer Graphics*, vol. 23, no. 6, pp. 1663–1676, June 2017.
- [30] H. Johansen-Berg and T. E. J. Behrens, *Diffusion MRI: From quantitative measurement to in-vivo neuroanatomy*, Academic Press, San Diego, USA, second edition, 2013.
- [31] A. P. Bates, Z. Khalid, and R. A. Kennedy, "An optimal dimensionality sampling scheme on the sphere with accurate and efficient spherical harmonic transform for diffusion MRI," *IEEE Signal Process. Lett.*, vol. 23, no. 1, pp. 15–19, Jan. 2016.
- [32] W. Zhang, M. Zhang, R. A. Kennedy, and T. D. Abhayapala, "On high-resolution head-related transfer function measurements: An efficient sampling scheme," *IEEE Trans. Audio, Speech, Language Process.*, vol. 20, no. 2, pp. 575–584, Feb. 2012.
- [33] A. P. Bates, Z. Khalid, and R. A. Kennedy, "Novel sampling scheme on the sphere for head-related transfer function measurements," *IEEE/ACM Trans. Audio, Speech, Language Process.*, vol. 23, no. 6, pp. 1068–1081, June 2015.
- [34] A. H. Moore, C. Evers, and P. A. Naylor, "Direction of arrival estimation in the spherical harmonic domain using subspace pseudointensity vectors," *IEEE/ACM Trans. Audio, Speech, Language Process.*, vol. 25, no. 1, pp. 178–192, Jan. 2017.

- [35] H. Liu, Y. Fang, and Q. Huang, “Efficient representation of head-related transfer functions with combination of spherical harmonics and spherical wavelets,” *IEEE Access*, vol. 7, pp. 78214–78222, June 2019.
- [36] M. A. Wieczorek and F. J. Simons, “Localized spectral analysis on the sphere,” *Geophys. J. Int.*, vol. 162, no. 3, pp. 655–675, Sept. 2005.
- [37] M. A. Wieczorek and F. J. Simons, “Minimum variance multitaper spectral estimation on the sphere,” *J. Fourier Anal. Appl.*, vol. 13, no. 6, pp. 665–692, 2007.
- [38] F. A. Dahlen and F. J. Simons, “Spectral estimation on a sphere in geophysics and cosmology,” *Geophys. J. Int.*, vol. 174, pp. 774–807, Sept. 2008.
- [39] D. W. Ritchie and G. J. L. Kemp, “Fast computation, rotation, and comparison of low resolution spherical harmonic molecular surfaces,” *J. Comput. Chem.*, vol. 20, no. 4, pp. 383–395, 1999.
- [40] M. Johansson and V. Veryazov, “Automatic procedure for generating symmetry adapted wavefunctions,” *J. Cheminform.*, vol. 9, no. 8, Feb. 2017.
- [41] B. D. Wandelt, E. Hivon, and K. M. Górski, “Cosmic microwave background anisotropy power spectrum statistics for high precision cosmology,” *Phys. Rev. D.*, vol. 64, no. 8, Oct. 2001.
- [42] E. Hivon, K. M. Górski, C. B. Netterfield, B. P. Crill, S. Prunet, and F. Hansen, “Master of the cosmic microwave background anisotropy power spectrum: a fast method for statistical analysis of large and complex cosmic microwave background data sets,” *Astrophys. J.*, vol. 567, pp. 2–17, Mar. 2002.
- [43] D. N. Spergel, R. Bean, O. Doré, M. R. Nolta, C. L. Bennett, J. Dunkley, G. Hinshaw, N. Jarosik, E. Komatsu, L. Page, H. V. Peiris, L. Verde, M. Halpern, R. S. Hill, A. Kogut, M. Limon, S. S. Meyer, N. Odegard, G. S. Tucker, J. L. Weiland, E. Wollack, and E. L. Wright, “Three-year Wilkinson Microwave Anisotropy Probe (WMAP) observations: Implications for cosmology,” *The Astrophysical Journal Supplement Series*, vol. 170, no. 2, pp. 377–408, 2007.
- [44] D. Marinucci, D. Pietrobon, A. Balbi, P. Baldi, P. Cabella, G. Kerkycharian, P. Natoli, D. Picard, and N. Vittorio, “Spherical needlets for cosmic microwave background data analysis,” *Monthly Notices Roy. Astron. Soc.*, vol. 383, no. 2, pp. 539–545, Jan. 2008.
- [45] F. Lanusse, A. Rassat, and J.-L. Starck, “3D galaxy clustering with future wide-field surveys: Advantages of a spherical Fourier-Bessel analysis,” *Astron. & Astrophys.*, vol. 578, no. A10, pp. 1–12, May 2015.
- [46] J. Bobin, F. Sureau, and J.-L. Starck, “Cosmic microwave background reconstruction from the WMAP and Planck PR2 data,” *Astron. & Astrophys.*, vol. 591, no. A50, pp. 1–12, July 2016.

- [47] D. Saadeh, S. M. Feeney, A. Pontzen, V. P. Hiranya, and J. D. McEwen, “A framework for testing isotropy with the cosmic microwave background,” *Monthly Notices Roy. Astron. Soc.*, vol. 462, no. 2, pp. 1802–1811, Oct. 2016.
- [48] N. Jarosik, C. L. Bennett, J. Dunkley, B. Gold, M. R. Greason, M. Halpern, R. S. Hill, G. Hinshaw, A. Kogut, E. Komatsu, D. Larson, M. Limon, S. S. Meyer, M. R. Nolta, N. Odegard, L. Page, K. M. Smith, D. N. Spergel, G. S. Tucker, J. L. Weiland, E. Wollack, and E. L. Wright, “Seven-year Wilkinson Microwave Anisotropy Probe (WMAP) observations: Sky maps, systematic errors, and basic results,” *Astrophys. J.*, vol. 192, no. 2, pp. 1–14, 2011.
- [49] Planck Collaboration I., “*Planck* 2018 results. I. Overview and the cosmological legacy of *Planck*,” *Astron. & Astrophys.*, vol. 641, no. A1, Sept. 2019.
- [50] M. Simons, S. C. Solomon, and B. H. Hager, “Localization of gravity and topography: constraints on the tectonics and mantle dynamics of Venus,” *Geophys. J. Int.*, vol. 131, pp. 24–44, Oct. 1997.
- [51] F. Freeden and U. Windheuser, “Combined spherical harmonic and wavelet expansion – a future concept in the Earth’s gravitational determination,” *Appl. Comput. Harm. Anal.*, vol. 4, no. 1, pp. 1–37, Jan. 1997.
- [52] S. E. Smrekar, R. Comstock, and F. S. Anderson, “A gravity survey of type 2 coronae on Venus,” *J. Geophys. Res.*, vol. 108, no. E8, pp. 9–1–9–17, Aug. 2003.
- [53] C. V. Voorhies, T. J. Sabaka, and M. Purucker, “On magnetic spectra of Earth and Mars,” *J. Geophys. Res.*, vol. 107, pp. 1–1–1–10, June 2002.
- [54] T. Hoogenboom, S. E. Smrekar, F. S. Anderson, and G. Houseman, “Admittance survey of type 1 coronae on Venus,” *J. Geophys. Res.*, vol. 109, no. 2, pp. 1–19, Mar. 2004.
- [55] E. Galanti, Y. Kaspi, F. J. Simons, D. Durante, M. Parisi, and S. J. Bolton, “Determining the depth of Jupiter’s great red spot with Juno: A Slepian approach,” *The Astrophysical Journal Letters*, vol. 874, no. 2, Apr. 2019.
- [56] J. R. Driscoll and D. M. Healy, Jr., “Computing Fourier transforms and convolutions on the 2-sphere,” *Adv. Appl. Math.*, vol. 15, no. 2, pp. 202–250, June 1994.
- [57] K. M. Górski, E. Hivon, A. J. Banday, B. D. Wandelt, F. K. Hansen, M. Reinecke, and M. Bartelmann, “HEALPix: A Framework for High-Resolution Discretization and Fast Analysis of Data Distributed on the Sphere,” *Astrophys. J.*, vol. 622, pp. 759–771, Apr. 2005.
- [58] A. G. Doroshkevich, P. D. Naselsky, O. V. Verkhodanov, D. I. Novikov, V. I. Turchaninov, I. D. Novikov, P. R. Christensen, and L.-Y. Chiang, “Gauss –

- Legendre Sky Pixelization (GLESP) for CMB maps,” *Int. J. Mod. Phys. D.*, vol. 14, no. 02, pp. 275–290, Feb. 2005.
- [59] J. D. McEwen and Y. Wiaux, “A novel sampling theorem on the sphere,” *IEEE Trans. Signal Process.*, vol. 59, no. 12, pp. 5876–5887, Dec. 2011.
- [60] Z. Khalid, R. A. Kennedy, and J. D. McEwen, “An optimal-dimensionality sampling scheme on the sphere with fast spherical harmonic transforms,” *IEEE Trans. Signal Process.*, vol. 62, no. 17, pp. 4597–4610, Sept. 2014.
- [61] B. D. Wandelt and K. M. Górski, “Fast convolution on the sphere,” *Phys. Rev. D.*, vol. 63, pp. 123002, May 2001.
- [62] P. Sadeghi, R. A. Kennedy, and Z. Khalid, “Commutative anisotropic convolution on the 2-sphere,” *IEEE Trans. Signal Process.*, vol. 60, no. 12, pp. 6697–6703, Dec. 2012.
- [63] R. A. Kennedy, T. A. Lamahewa, and L. Wei, “On azimuthally symmetric 2-sphere convolution,” *Digital Signal Processing*, vol. 5, no. 11, pp. 660–666, Sept. 2011.
- [64] R. A. Kennedy and P. Sadeghi, *Hilbert Space Methods in Signal Processing*, Cambridge University Press, Cambridge, UK, Mar. 2013.
- [65] Y. Wiaux, L. Jacques, P. Vielva, and P. Vanderghenst, “Fast directional correlation on the sphere with steerable filters,” *Astrophys. J.*, vol. 652, no. 1, pp. 820–832, Nov. 2006.
- [66] I. Sasgen, Z. Martinec, and K. Fleming, “Wiener optimal filtering of GRACE data,” *Studia Geophysica et Geodaetica*, vol. 50, no. 4, pp. 499–508, 2006.
- [67] J. D. McEwen, M. P. Hobson, and A. N. Lasenby, “Optimal filters on the sphere,” *IEEE Trans. Signal Process.*, vol. 56, no. 8, pp. 3813–3823, Aug. 2008.
- [68] Z. Khalid, S. Durrani, R. A. Kennedy, and P. Sadeghi, “On the construction of low-pass filters on the unit sphere,” in *Proc. IEEE Int. Conf. Acoust., Speech, Signal Process., ICASSP’2011*, Prague, Czech Republic, May 2011, pp. 4356–4359.
- [69] J. D. McEwen, S. M. Feeney, M. C. Johnson, and H. V. Peiris, “Optimal filters for detecting cosmic bubble collisions,” *Phys. Rev. D.*, vol. 85, no. 10, pp. 103502, May 2012.
- [70] R. Klees, E. A. Revtova, B. C. Gunter, P. Ditmar, E. Oudman, H. C. Winsemius, and H. H. G. Savenije, “The design of an optimal filter for monthly GRACE gravity models,” *Geophys. J. Int.*, vol. 175, no. 2, pp. 417–432, 2008.
- [71] R. Arora and H. Parthasarathy, “Optimal estimation and detection in homogeneous spaces,” *IEEE Trans. Signal Process.*, vol. 58, no. 5, pp. 2623–2635, May 2010.

- [72] P. Sadeghi, R. A. Kennedy, and Z. Khalid, “Minimum mean square error equalization on the 2-sphere,” in *2014 IEEE Workshop on Statistical Signal Processing (SSP)*. IEEE, 2014, pp. 101–104.
- [73] A. Albertella, F. Sansò, and N. Sneeuw, “Band-limited functions on a bounded spherical domain: the Slepian problem on the sphere,” *J. Geodesy*, vol. 73, no. 9, pp. 436–447, June 1999.
- [74] F. J. Simons, F. A. Dahlen, and M. A. Wieczorek, “Spatiospectral concentration on a sphere,” *SIAM Rev.*, vol. 48, no. 3, pp. 504–536, 2006.
- [75] F. J. Simons and F. A. Dahlen, “Spherical Slepian functions and the polar gap in geodesy,” *Geophys. J. Int.*, vol. 166, no. 3, pp. 1039–1061, Sept. 2006.
- [76] A. P. Bates, Z. Khalid, and R. A. Kennedy, “Slepian spatial-spectral concentration problem on the sphere: Analytical formulation for limited colatitude-longitude spatial region,” *IEEE Trans. Signal Process.*, vol. 65, no. 6, pp. 1527–1537, Mar. 2017.
- [77] A. P. Bates, Z. Khalid, and R. A. Kennedy, “Efficient computation of Slepian functions for arbitrary regions on the sphere,” *IEEE Trans. Signal Process.*, vol. 65, no. 16, pp. 4379–4393, Aug. 2017.
- [78] F. J. Narcowich and J. D. Ward, “Non-stationary wavelets on the m-sphere for scattered data,” *Appl. Comput. Harm. Anal.*, vol. 3, no. 4, pp. 324–336, Oct. 1996.
- [79] J.-P. Antoine and P. Vandergheynst, “Wavelets on the n-sphere and related manifolds,” *J. Math. Phys.*, vol. 39, pp. 3987–4008, 1998.
- [80] J.-P. Antoine and P. Vandergheynst, “Wavelets on the 2-sphere: A group-theoretical approach,” *Appl. Comput. Harm. Anal.*, vol. 7, no. 3, pp. 262–291, Nov. 1999.
- [81] J.-L. Starck, Y. Moudden, P. Abrial, and M. Nguyen, “Wavelets, ridgelets and curvelets on the sphere,” *Astron. & Astrophys.*, vol. 446, pp. 1191–1204, Feb. 2006.
- [82] Y. Wiaux, L. Jacques, and P. Vandergheynst, “Correspondence principle between spherical and Euclidean wavelets,” *Astrophys. J.*, vol. 632, no. 1, pp. 15–28, Oct. 2005.
- [83] Y. Wiaux, J. D. McEwen, P. Vandergheynst, and O. Blanc, “Exact reconstruction with directional wavelets on the sphere,” *Monthly Notices Roy. Astron. Soc.*, vol. 388, no. 2, pp. 770–788, Aug. 2008.
- [84] B. Leistedt, J. D. McEwen, P. Vandergheynst, and Y. Wiaux, “S2LET: A code to perform fast wavelet analysis on the sphere,” *Astron. & Astrophys.*, vol. 558, no. A128, pp. 1–9, Oct. 2013.

-
- [85] J. D. McEwen, C. Durastanti, and Y. Wiaux, “Localisation of directional scale-discretised wavelets on the sphere,” *Appl. Comput. Harm. Anal.*, vol. 44, no. 1, pp. 59–88, Jan. 2018.
- [86] F. Hlawatsch, G. Matz, H. Kirchauer, and W. Kozek, “Time-frequency formulation, design, and implementation of time-varying optimal filters for signal estimation,” *IEEE Trans. Signal Process.*, vol. 48, no. 5, pp. 1417–1432, May 2000.
- [87] Z. Khalid, R. A. Kennedy, P. Sadeghi, and S. Durrani, “Spatio-spectral formulation and design of spatially-varying filters for signal estimation on the 2-sphere,” in *Proc. Wavelets and Sparsity XV, SPIE international symposium on optics and photonics, invited contribution*, San Diego, California, United States, Aug. 2013.
- [88] Z. Khalid, S. Durrani, P. Sadeghi, and R. A. Kennedy, “Spatio-spectral analysis on the sphere using spatially localized spherical harmonics transform,” *IEEE Trans. Signal Process.*, vol. 60, no. 3, pp. 1487–1492, Mar. 2012.
- [89] D. Slepian and H. O. Pollak, “Prolate spheroidal wave functions, Fourier analysis and uncertainty—I,” *Bell Syst. Tech. J.*, vol. 40, no. 1, pp. 43–63, Jan. 1961.
- [90] H. J. Landau and H. O. Pollak, “Prolate spheroidal wave functions, Fourier analysis and uncertainty—II,” *Bell Syst. Tech. J.*, vol. 40, no. 1, pp. 65–84, Jan. 1961.
- [91] D. Slepian, “Prolate spheroidal wave functions, Fourier analysis and uncertainty—IV: Extensions to many dimensions; generalized prolate spheroidal functions,” *Bell Syst. Tech. J.*, vol. 40, pp. 3009–3057, Nov. 1964.
- [92] C. E. Shannon, “Communication in the presence of noise,” in *Proc. of the IEEE*, Feb. 1998, vol. 86, pp. 447–457.
- [93] S. G. Mallat, “A theory for multiresolution signal decomposition: the wavelet representation,” *IEEE Trans. Pattern Anal. Mach. Intell.*, vol. 11, no. 7, pp. 674–693, July 1989.
- [94] I. Daubechies, “The wavelet transform, time-frequency localization and signal analysis,” *IEEE Trans. Inf. Theory*, vol. 36, no. 5, pp. 961–1005, Sept. 1990.
- [95] S. G. Mallat, *A Wavelet Tour of Signal Processing*, Academic Press, Massachusetts, USA, third edition, 2009.
- [96] B. T. T. Yeo, W. Ou, and P. Golland, “On the construction of invertible filter banks on the 2-sphere,” *IEEE Trans. Image Process.*, vol. 17, no. 3, pp. 283–300, Mar. 2008.

- [97] B. O'Neill, *Elementary Differential Geometry, Revised Second Edition*, Academic Press, second edition, 2006.
- [98] Z. Khalid, R. A. Kennedy, S. Durrani, P. Sadeghi, Y. Wiaux, and J. D. McEwen, "Fast directional spatially localized spherical harmonic transform," *IEEE Trans. Signal Process.*, vol. 61, no. 9, pp. 2192–2203, May 2013.
- [99] T. Risbo, "Fourier transform summation of Legendre series and D-functions," *J. Geodesy*, vol. 70, no. 7, pp. 383–396, July 1996.
- [100] S. Trapani and J. Navaza, "Calculation of spherical harmonics and Wigner d functions by FFT. Applications to fast rotational matching in molecular replacement and implementation into AMoRe," *Acta Cryst. A*, vol. 62, no. 4, pp. 262–269, July 2006.
- [101] Z. Khalid, S. Durrani, P. Sadeghi, and R. A. Kennedy, "Concentration uncertainty principles for signals on the unit sphere," in *Proc. IEEE Int. Conf. Acoustics, Speech and Signal Processing, ICASSP'2012*, Kyoto, Japan, Mar. 2012, pp. 3717–3720.
- [102] M. Tegmark, D. H. Hartmann, M. S. Briggs, and C. A. Meegan, "The angular power spectrum of BATSE 3B gamma-ray bursts," *Astrophys. J.*, vol. 468, pp. 214–224, Sept. 1996.
- [103] K.-I. Seon, "Smoothing of all-sky survey map with Fisher-von Mises function," *J. Korean Phys. Soc.*, vol. 48, no. 3, pp. 331–334, Mar.–Apr. 2006.
- [104] N. J. Vilenkin, *Special Functions and the Theory of Group Representations, Volume 22 of Translations of mathematical monographs*, American Mathematical Soc., Rhode Island, USA, 1968.
- [105] P. J. Kostelec and D. N. Rockmore, "FFTs on the rotation group," *J. Fourier Anal. and Appl.*, vol. 14, pp. 145–179, 2008.
- [106] Z. Khalid, P. Sadeghi, R. A. Kennedy, and S. Durrani, "Spatially varying spectral filtering of signals on the unit sphere," *IEEE Trans. Signal Process.*, vol. 61, no. 3, pp. 530–544, Feb. 2013.
- [107] J.-L. Starck and A. Bijaoui, "Filtering and deconvolution by the wavelet transform," *Signal Processing*, vol. 35, pp. 195–211, 1994.
- [108] O. Renaud, J.-L. Starck, and F. Murtagh, "Wavelet-based combined signal filtering and prediction," *IEEE Transactions on Systems, Man, and Cybernetics, Part B (Cybernetics)*, vol. 35, no. 6, pp. 1241–1251, Dec. 2005.
- [109] J.-L. Starck and F. Murtagh, "Multiscale entropy filtering," *Signal Processing*, vol. 76, no. 2, pp. 147–165, July 1999.

-
- [110] M. K. Chung, K. M. Dalton, L. Shen, A. C. Evans, and R. J. Davidson, “Weighted Fourier series representation and its application to quantifying the amount of gray matter,” *IEEE Trans. Med. Imag.*, vol. 26, no. 4, pp. 566–581, Apr. 2007.
- [111] W. Freeden and M. Schreiner, “Non-orthogonal expansions on the sphere,” *Math. Methods in the Appl. Sciences*, vol. 18, no. 2, pp. 83–120, Feb. 1995.
- [112] B. N. Delaunay, “On the empty sphere. In memory of Georges Voronoi,” *Report of the academy of sciences of the USSR. Mathematical and natural sciences class*, no. 6, pp. 793–800, 1934, (in French).
- [113] M. R. Garey, D. S. Johnson, F. P. Preparata, and R. E. Tarjan, “Triangulating a simple polygon,” *Inform. Process. Lett.*, vol. 7, pp. 175–179, June 1978.
- [114] A. Fournier and D. Y. Montuno, “Triangulating simple polygons and equivalent problems,” *ACM Trans. on Graphics*, vol. 3, pp. 153–174, Apr. 1984.
- [115] K. L. Clarkson, R. T. Tarjan, and C. J. Van Wyk, “A fast Las Vegas algorithm for triangulating a simple polygon,” *Discrete and Computational Geometry*, vol. 4, pp. 423–432, Oct. 1989.
- [116] B. Chazelle, “Triangulating a simple polygon in linear time,” *Discrete and Computational Geometry*, vol. 6, pp. 485–524, Sept. 1991.
- [117] R. Seidel, “A simple and fast incremental randomized algorithm for computing trapezoidal decompositions and for triangulating polygons,” *Computational Geometry: Theory and Applications*, vol. 1, pp. 51–64, July 1991.
- [118] N. M. Amato, M. T. Goodrich, and E. A. Ramos, “A randomized algorithm for triangulating a simple polygon in linear time,” *Discrete and Computational Geometry*, vol. 26, pp. 245–265, Jan. 2001.
- [119] R. J. Renka, “Algorithm 772: Stripack: Delaunay triangulation and Voronoi diagram on the surface of a sphere,” *ACM Trans. on Mathematical Software*, vol. 23, no. 3, pp. 416–434, Sept. 1997.
- [120] A. Saalfeld, “Delaunay triangulations and stereographic projections,” *Cartography and Geographic Information Science*, vol. 26, no. 4, pp. 289–296, 1999.
- [121] J. Stewart, *Calculus: Early Transcendentals*, Brooks/Cole, Belmont, CA, USA, seventh edition, 2012.
- [122] J. D. McEwen, P. Vandergheynst, and Y. Wiaux, “On the computation of directional scale-discretized wavelet transforms on the sphere,” in *Proc. Wavelets and Sparsity XV, SPIE international symposium on optics and photonics, invited contribution*, San Diego, California, United States, Sept. 2013, vol. 8858.

- [123] J. D. McEwen, M. P. Hobson, and A. N. Lasenby, “A directional continuous wavelet transform on the sphere,” *Arxiv preprint astro-ph/0609159*, 2006.
- [124] W. Shukowsky, “A quadrature formula over the sphere with application to high resolution spherical harmonic analysis,” *J. Geodesy*, vol. 60, no. 1, pp. 1–14, Mar. 1986.
- [125] F. J. Simons, I. Loris, E. Brevdo, and I. C. Daubechies, “Wavelets and wavelet-like transforms on the sphere and their application to geophysical data inversion,” in *Wavelets and Sparsity XIV*. International Society for Optics and Photonics, 2011, vol. 8138, pp. 224 – 238, SPIE.
- [126] R. Gribonval and M. Nielsen, “Sparse representations in unions of bases,” *IEEE Trans. Inf. Theory*, vol. 49, no. 12, pp. 3320–3325, Dec. 2003.
- [127] J. A. Tropp and A. C. Gilbert, “Signal recovery from random measurements via orthogonal matching pursuit,” *IEEE Trans. Inf. Theory*, vol. 53, no. 12, pp. 4655–4666, Dec. 2007.
- [128] D. D. Wackerly, W. Mendenhall, and R. L. Scheaffer, *Mathematical Statistics with Applications*, Thomson Brooks/Cole, Belmont, CA, USA, seventh edition, 2008.
- [129] Z. Khalid, R. A. Kennedy, and J. D. McEwen, “Slepian spatial-spectral concentration on the ball,” *Appl. Comput. Harm. Anal.*, vol. 40, pp. 470–504, May 2016.
- [130] B. Leistedt and J. D. McEwen, “Exact wavelets on the ball,” *IEEE Trans. Sig. Proc.*, vol. 60, no. 12, pp. 6257–6269, 2012.